CdTe solar cells: growth phenomena and device performance

Jonathan Major

CdTe solar cells: growth phenomena and device performance

By Jonathan Major, MPhys

A thesis presented in candidature for the degree of Doctor of Philosophy in the University of Durham
Department of Physics
June 2008

Abstract

A systematic study is presented on the control of CdTe and CdS layers during their growth, with the understanding gained being implemented in the production of solar cells with enhanced performance. In particular the growth mechanisms for close space sublimation (CSS) – grown CdTe were evaluated as a function of processing gas (N_2, O_2 and H_2) and nitrogen pressure. Films were shown to form via the Volmer-Weber growth mode with films deposited under nitrogen showing well defined crystal facets. Inclusion of oxygen in the deposition ambient produced islands of a rounded morphology, reduced size and increased number density, whilst hydrogen was shown to increase the island number density and the level of substrate coverage. Growth mechanisms were deduced from the morphologies observed at different stages of growth by ex-situ AFM and SEM and by comparison with growth literature, especially the work of P. Barna. Nucleation density, step flow and impurity incorporation are all invoked in the discussion.Factors influencing the cell performance were evaluated with the aid of a optical beam induced current (OBIC) and external quantum efficiency (EQE) system built as part of this work and having the capacity to measure EQE or OBIC maps with a resolution of 12.5μm. The system was used to evaluate the photovoltaic response of CdTe/CdS devices as a function of wavelength with the impact of the nitric-phosphoric acid (NP) etch on the back surface, the uniformity of CdTe/CdS devices deposited by different methods and the effect of absorber layer thickness of PV uniformity being assessed.

The performance of CdTe/CdS devices was evaluated as a function of variables that could be influenced by growth of the CdTe and CdS layers. The use of lower substrate temperature and the incorporation oxygen in CdS increased V_{oc} from 0.51 to 0.65V is discussed. Oxygen in the CdTe was also shown to influence the junction position and hence efficiency, while oxygen in the CdS layer was also shown to be vital for the formation of hetero-junctions. The CdTe grain size was shown to be significantly increased for deposition under higher nitrogen pressures (Grain diameter = $[0.027P + 0.9]$μm, where P is the pressure in Torr), with the average grain diameters being 0.94μm at 2Torr and 5.63μm at 200Torr. Device performance was improved as a result with the peak device efficiency being increased from 2.1% at 2Torr to 14.1% at 100Torr. The series resistance was shown to be minimised for larger grain size, owing to the reduced contribution of grain boundaries. Suggestions for the fabrication of high efficiency solar cells are given with reference to the efficiency limiting factor.

Declaration

I declare that with the exception of those procedures listed below all the work presented in this thesis was carried out by the candidate. I also declare that none of this work has previously been submitted for any degree and that it is not being submitted for any other degree.

MOCVD Samples reported in Chapter 6 were provided by Dr V. Barrioz, Department of Chemistry, University of Wales, Bangor.

XRD measurements included in Chapter 8 were performed by Dr G. Zoppi, Northumbria University, Newcastle.

Acknowledgement

I would like to offer my heartfelt thanks to my supervisor Professor Ken Durose for his support and expert guidance throughout my time here. I would also like to thank him for the countless hours of proof reading and his valiant attempt to teach me the difference between Cumbrian and English.

My thanks also to the long suffering technical staff of the Physics Department, in particular Norman Thompson and David Pattinson.

A large number of people have worked within, or around, the research group during my time here who I would like to thank for there friendship and for making this an enjoyable place to work; Guillaume Zoppi, Keriya "K" Mam, Chris Hodgson, Martin Archbold, Mahieddine Emziane, Ben Cantwell, Yuri Proskuryakov, Tom Hindmarch, Justus Oldenburg, Ben Taele, Mohammed Al Turkestani, Jiang, Rob Treharne, Aktar Rind and Paul Scott.

This work was carried out as part of the Supergen PV21 project and my thanks are offered to the all the team members who have worked on the project for their collective wisdom and insight. In particular thanks go to consortium members Vincent Barrioz, for the growth of MOCVD devices featured in this work, and to Guillaume Zoppi, for his help with the XRD characterisation of devices. My thanks also to the Engineering and Physical Sciences Research Council who funded this work.

Finally, this thesis is dedicated to my parents, who have supported me in everything I've ever done, and to Claire, who has always encouraged, loved and mocked me in equal measure. Without you all this thesis wouldn't have been written.

CONTENTS

Acronyms

AFM – Atomic force microscopy

CBD – Chemical bath deposition

CSS – Close space sublimation

EBIC – Electron beam induced current

EDX – Energy dispersive X-ray analysis

EQE – External quantum efficiency

FTO – Fluorine doped tin oxide

IQE – Internal quantum efficiency

ITO – Indium tin oxide

J-V – Current voltage analysis

LBIC – Light/laser beam induced current

MOCVD – Metal-organic chemical vapour deposition

MOVPE – Metal-organic vapour phase epitaxy

OBIC – Optical beam induced current

PV - Photovoltaic

PVD – Physical vapour deposition

QE – Quantum efficiency

SEM – Secondary electron microscope

SIMS – Secondary ion mass spectrometry

TCO – Transparent conducting oxide

XRD – X-ray diffraction

1 Introduction

Public concern over the environmental impact of fossil fuels has never been greater, with terms such as "global warming", "carbon footprint" and "climate change" becoming part of the common vocabulary. The interest in renewable energy has grown considerably as a result, with the need for an abundant and clean source of electricity being apparent. There are numerous renewable sources capable of generating significant amounts of electricity such as wind, biomass, geothermal and hydroelectricity, however 80% of the world current power generation is still based upon fossil fuels[1]. Whilst the aforementioned technologies have the capacity to contribute towards global energy production, none have the unmatched potential of solar energy. Solar radiation incident upon the Earth's surface is the most abundant source of energy on the planet, with around 1.08×10^{14} kW of energy reaching the surface. Solar cells directly convert this solar radiation into electrical power via the photovoltaic (PV) effect, using a semiconductor *p-n* junction. Solar cells generate no pollution in operation, with a small amount of heat being the only by-product. It is estimated that covering an area comprising 0.1% of the Earth's surface with 10% efficient solar cells would generate 3000 GW, four times the world's total current generating capacity. Solar energy is therefore seen as the most likely candidate to replace fossil fuels as the world's principle method of electrical power generation. However, due to the current high cost of solar power in comparison to other sources, electrical power generation by PV is estimated to comprise less than 1% of the world's energy production at present. The main goal of current solar cell research is to reduce the cost of photovoltaic power generation, so as to make it a viable alternative to fossil fuels.

Currently the majority of solar modules produced for industrial, space and domestic application are based on silicon homo-junctions, the most well established solar cell technology. While these modules are capable of high levels of efficiency (with up to 22% being reported for a $0.8m^2$ area[2]) the systems are intrinsically expensive, owing to the high cost of the silicon used. As a result, alternative technologies based upon thin-film materials have received a great deal of interest, due to the vast reduction in material costs. One of the most promising of these materials is cadmium telluride (CdTe), owing to its

near ideal optical bandgap for solar energy conversion and a high optical absorption coefficient. There are often concerns over the use of CdTe based solar cells, due to the potential health and environmental issues related to the use of cadmium based materials. However, research into the life cycle of solar cells has shown that CdTe based devices contribute significantly less cadmium to the environment per kWh of power generation than for fossil fuels and even silicon solar cells[3] (owing to the fact that burning fossil fuels emits cadmium and that silicon device fabrication uses more electrical power). Unlike in silicon devices where a large thickness of material (typically 100 - 200μm thickness) is required for sufficient optical absorption, CdTe is able to be utilised as a very thin layer (<8μm), leading to significant reductions for the cost of cell production. Because CdTe solar cell technology is less developed, module efficiencies are low (maximum of 10.7%[2]) in comparison to silicon, but the benefits for cost reduction more than compensate for this efficiency deficit. As may be expected, laboratory-scale devices perform at a superior level to commercial modules, with >16% efficiency being reported for 1cm^2 devices[4]. However, this is still someway short of the maximum efficiency predicted for CdTe/CdS solar cells, which has been estimated as ~30%. It is clear therefore that a great deal of further research needs to be undertaken in order to help realise the full potential of CdTe/CdS devices.

The outstanding issues in the continuing development of CdTe/CdS solar cells are:-

a) Grain size and grain boundary effects. The films are polycrystalline; Sites *et al*[5] estimated that 2/3 of the performance loss in CdTe is due to polycrystallinity, with recombination, segregation of impurities and leakage current being important (see Chapter 4 and 8).

b) Optical loss. Absorption in the CdS window layer does not contribute to photocurrent (see Chapter 6).

c) Control of the junction position and the electrical field profile. Doping is controlled by diffusion and depends upon the interaction of point defects, interdiffused layers and intentional/unintentionally introduced impurities (see Chapters 6 and 8).

d) Contacts. The work function of *p*-type CdTe is 5.8eV which exceeds the work functions of the common metals. Contacts to *p*-type CdTe are therefore

rectifying and present a resistive barrier. The thermodynamic stability of contacts is therefore an issue.

This thesis, while touching on all of the above issues (albeit incidentally) has the issue of polycrystallinity as its central theme. The approach has focused on close space sublimation (CSS), one of the most widely used techniques for the deposition of CdTe thin films for high efficiency solar cells. Owing to the technique's high rate of deposition and ability to deposit uniform films over large areas, it is also highly suited to industrial manufacturing[6]. However, despite the large volume of work reported based upon CdTe/CdS devices deposited by CSS, very little attention has been paid to the growth of CdTe films at a more fundamental level. As a result the focus of this work was to investigate the early stages of growth of CdTe thin films deposited by CSS, in order to develop the understanding of the material as it is the early stages of growth that influences coverage, grain size and grain structure most profoundly. The knowledge gained from this study was then used to inform the research scale production of CdTe/CdS devices, in order to improve the device performance. Characterisation included optical beam induced current (OBIC) measurements, since spatially resolved effects were considered important.

The basic outline of this thesis is as follows: Firstly, the basic principles of photovoltaic power generation are discussed in Chapter 2. Chapter 3 contains a discussion of the structure and performance of CdTe/CdS solar cells, while the principal theories and mechanisms of thin film nucleation and growth are outlined in Chapter 4. In Chapter 5 the experimental techniques used in this thesis are described prior to the discussion of results which are ordered in the following manner:

i) Chapter 6 – reports the construction and operation of a spectrally resolved OBIC system and its use in the characterisation of CdTe/CdS devices.

ii) Chapter 7 – reports a study into the growth mechanisms of CdTe deposited by close space sublimation (CSS) on different substrates and under different deposition conditions.

iii) Chapter 8 – reports the growth and performance of CdTe/CdS devices, fabricated using techniques informed by the work presented in Chapter 7.

1.1 References for Chapter 1

1 *2007 Survey of Energy Resources*, *http://www.worldenergy.org/documents/ser2007_final_online_version_1.pdf, accessed April 2008.*

2 M. A. Green, K. Emery, Y. Hishikawa, and W. Warta, Progress in Photovoltaics: Research and Applications **16**, 61-67 (2008).

3 V. M. Fthenakis and H. C. Kim, Thin Solid Films **515**, 5961-5963 (2007).

4 X. Wu, Solar Energy **77**, 803-814 (2004).

5 J. R. Sites, J. E. Granata, and J. F. Hiltner, Solar Energy Materials and Solar Cells **55**, 43-50 (1998).

6 D. Bonnet, Materials Research Society Symposium Proceedings **1012**, 249-258 (2007).

2 Photovoltaic devices

2.1 Introduction

A photovoltaic (PV) device transforms incident light photons into electrical energy and forms the basis of solar cell technology. The discovery of PV is widely attributed to Bequerel in 1839, who observed a photocurrent produced by light upon an electrolyte solution. Whilst numerous solar cell type structures were developed as a result of this discovery (for example a 1% efficient device was reported based on selenium and copper oxide in 1914), the first true forerunner of the modern solar cell device was not developed until 1954, when Chapin, Fuller and Pearson[1] produced a ~6% efficient device based on a silicon junction.

This chapter outlines the basic principles of the photovoltaic effect and the behaviour of *p-n* junctions (Section 2.2), as well as the performance of solar cell devices and the determination of basic solar cell performance parameters (Section 2.3). Finally a brief description of common solar cell device materials is presented (Section 2.4).

2.2 Semiconductors and the photovoltaic effect

2.2.1 Types of semiconductor

The three principal conductivity types of semiconductor are shown in fig.2.1. In a pure, or intrinsic, semiconductor (fig.2.1a) the concentration of electrons in the conduction band is equal to the concentration of holes in the valence band and the Fermi level (E_F) is in the middle of the bandgap. In n-type doping (fig.2.1b) the addition of donor impurities (e.g. group V elements such as phosphorous are used for *n*-type doping of silicon) shifts the Fermi level closer to the conduction band, and leads to the formation of a donor level (E_D). Alternatively, in *p*-type doping (fig.2.1c) the addition of electron acceptor impurities (e.g. group III elements such as boron are used in silicon) leads to the formation of an acceptor level (E_A), and the Fermi level is shifted closer to the valence band (see for example Sze[2]).

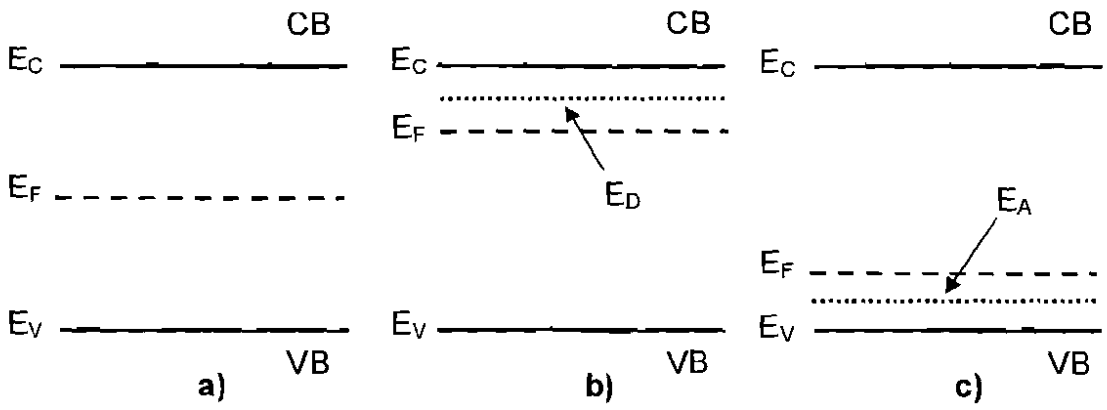

Figure 2.1: Energy level diagrams for various conduction types of semiconductor a) an intrinsic semiconductor, b) an extrinsic *n*-type semiconductor, with marked electron donor level E_D and c) an extrinsic *p*-type semiconductor, with marked electron acceptor level E_A.

2.2.2 The photovoltaic effect

The photovoltaic effect principally operates via two separate mechanisms: Firstly, an electron in the valence band is excited across the bandgap by an incident photon of sufficient energy, leading to the formation of an electron-hole pair. Secondly, the electron-hole pair must then be separated by an electric field before the charges recombine, in order for a photocurrent to be collected. The effect that light has when incident on an ideal semiconductor principally depends upon the bandgap of the material, E_g, and the energy of incident photons, hv. The possible outcomes of this interaction are listed below in terms of these values:

i) For photons with energy less than the material bandgap ($hv < E_g$), no excitation across the bandgap may occur as the photons have insufficient energy. However, in the case of non-ideal semiconductors, where some inter-band states may be present, excitation of electrons from the valence band, into these states may occur.

ii) For photons of energy, $E_g \leq hv < 2E_g$, an electron from the valence band is excited across the bandgap leading to the formation of an electron-hole pair.

iii) For photons of energy, $h\nu \geq 2E_g$, "impact ionisation" may occur, whereby after promotion across the bandgap the excited electron still retains sufficient energy to create further electron hole pairs.

As previously mentioned, in order for a photocurrent to be collected the generated carriers must be separated by an electric field. This can be achieved, either by the formation of an internal electric field, or by the application of an external bias voltage. In the case of solar cells, an internal electric field is created by the formation of a semiconductor *p-n* junction or by a Schottky barrier. These junctions are discussed in the following section.

2.3 Semiconductor junctions

The theory of semiconductor junctions is treated in a number of texts, see for example Bube[3], Sze[2] or Nelson[4]. Nevertheless, given the central importance of junction phenomena to photoconductive devices, the main concepts are outlined in this section.

Of the common junction types the *p-n* junction is the most important in PV technology. It may be described as follows: When *p*-type and *n*-type materials are brought together a *p-n* junction is formed and the Fermi levels align. Electrons pass from the *n*-type layer into the *p*-type, with holes moving in the opposite direction. The electrons crossing from the *n*-type to *p*-type region leave behind a region of positive charge, and the *n*-type region close to the interface is depleted of mobile electrons. Due to the flow of electrons crossing into the *p*-type regions a negative charge is set up close to the junction in this region and an electric field is thus established across the junction in which carriers may drift. This forms the basis of charge separation by a semiconductor *p-n* junction.

The three main types of junction, homo-junctions, hetero-junctions and Schottky-junctions, will now be discussed in turn.

2.3.1 Homo-junction

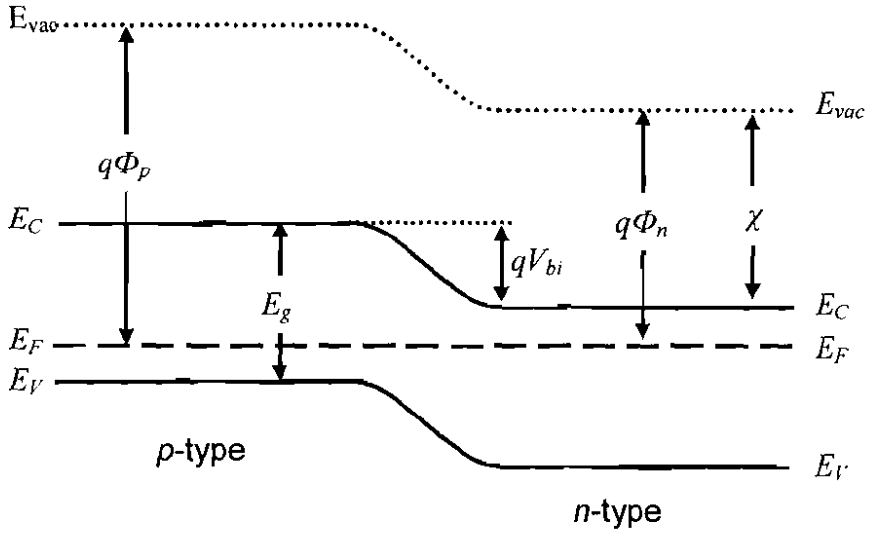

Figure 2.2: Semiconductor homo-junction band diagram. The *p-n* junction is formed between two differently doped layers of the same material. Φ_n and Φ_p are the work function of the *n* and *p*-type regions respectively, E_g and χ are the material bandgap and electron affinity and V_{bi} is the built-in junction potential.

Homo-junctions are the easiest junctions to treat theoretically as they are formed between *p*-type and *n*-type portions of the same material, as shown in fig.2.2. Junctions of this type are usually formed by diffusing a dopant into a single piece of material, producing *n*-type and *p*-type regions by overcompensating for the existing doping. Due to the bandgaps of the two regions being identical, homo-junctions have the advantage of having no barriers within the band structure (as is common with hetero-junctions) which may block the flow of electrons. Whereas the *p-n* homo-junction is the basis of the silicon PV industry, use of homo-junctions for the more highly absorbing compound semiconductor CdTe and the chalcopyrites – is not successful. Since their absorption coefficients are ~100 times greater than for silicon, much of the absorption is close to their surface. Hence, even though a *p-n* homo-junction may be engineered close to the surface, a heavy penalty is paid in terms of surface recombination. These materials are therefore exploited in hetero-junctions (see Section 2.3.3).

2.3.2 Schottky junction

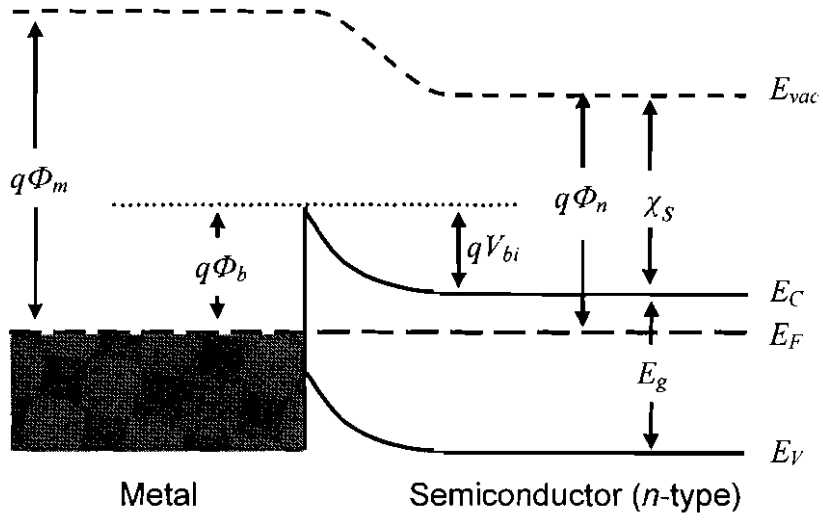

Figure 2.3: Schottky junction band diagram. The junction is formed between an *n*-type semiconductor of work function Φ_n and a metal of work function Φ_m, leading to a Schottky barrier of height Φ_b being formed. E_g is the bandgap of the semiconductor, χ_s is the electron affinity and V_{bi} is the built-in junction potential.

A Schottky junction is a rectifying junction formed when a semiconductor and metal are brought into contact. This is typically achieved by deposition of a thin metal layer onto a semiconductor substrate. The junction is considered to arise due to charge flow induced by the difference in the work functions of the materials, with the sign of the barrier field depending on the direction of the current flow. Fig.2.3 shows a Schottky junction formed between a metal and an *n*-type semiconductor. If the metal is sufficiently thin to allow significant optical transmission, then Schottky junctions may act as photocurrent collectors. However, their importance is greater in the field of semiconductor contacts (see Section 3.2.7). For electrons flowing from the semiconductor into the metal the barrier height is given by $qV_{bi} = q(\Phi_m - \Phi_n)$, but for transport from the metal to the semiconductor the barrier is given by Φ_b (Schottky barrier height) which may be determined by $\Phi_b = \Phi_m - \chi_s$.

2.3.3 Hetero-junction

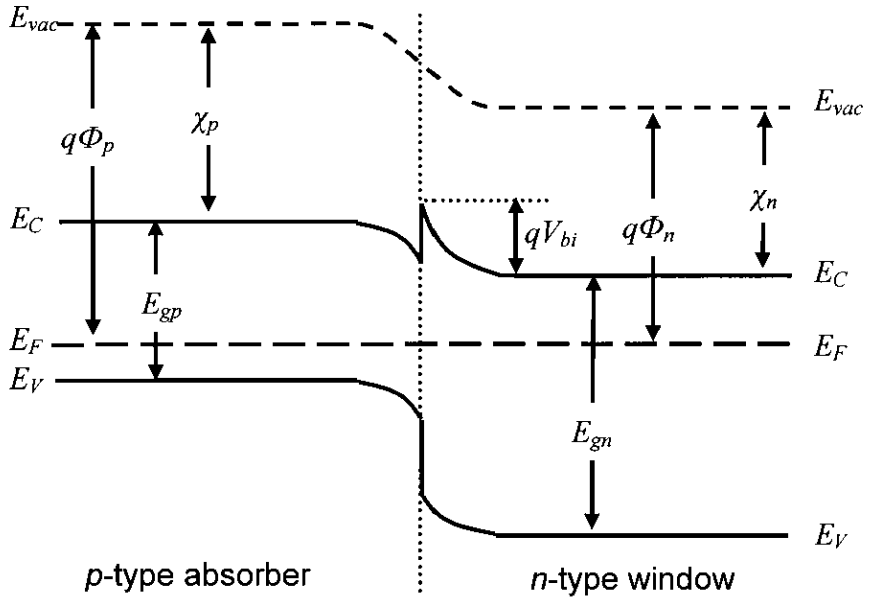

Figure 2.4: Band diagram of a hetero-junction formed between *p* and *n*-type layers of different semiconductor materials, where the *p*-type (absorber) layer has a smaller bandgap than the *n*-type (window) layer ($E_{gp}<E_{gn}$). The *n*-type and *p*-type semiconductors have work functions of Φ_n and Φ_p, and electron affinities of χ_n and χ_p respectively, while V_{bi} is the built-in junction potential. Typical Φ, χ and E_g values for CdTe/CdS hetero-junctions are given in table 2.1.

Hetero-junctions are formed between two different semiconductor materials that have different bandgaps. In the case of hetero-junction solar cells there is typically an *n*-type window layer with a large bandgap and a *p*-type absorber layer of a lower bandgap. This allows incident photons with energy below that of the window layer bandgap (photon energy < E_{gn}), to pass through and reach the absorber layer, generating carriers near the junction region. This eliminates the need for the junction to be positioned close to the surface, as is required in both homo-junctions and Schottky junctions. The hetero-junction band diagram is somewhat more complicated than that of a homo-junction cell, but a good approximation is made by the Anderson model (see for example Fahrenbruch and Bube[5], where a complete discussion of the model is provided). Due to the differences in the bandgap and the electron affinity values of the materials, discontinuities may arise in the conduction and valence bands. As is shown in fig.2.4 this can lead to "spikes"

being formed in the conduction band, which provide a barrier to the flow of carriers and can thus limit the collection efficiency of the junction.

Material (300K)	E_g (eV)	χ (eV)	Φ (eV)
CdTe	1.47	4.5	5.97
CdS	2.42	4.5	4.79

Table 2.1: Material parameters for a CdTe/CdS hetero-junction.

2.4 J-V characteristics of solar cell devices

2.4.1 The ideal device

Current density-voltage (*J-V*) analysis is an important characterisation technique for solar cells and is the standard method by which the cell efficiency is determined. The current generated by a device is measured as a function of applied bias (usually in the -1V to +1V range) in either the dark, or under illumination (typically AM1.5 illumination, see Section 2.4.2). As well as the device efficiency, standard device performance parameters such as the fill factor (*FF*), the open circuit voltage (V_{oc}) and the short circuit current density (J_{sc}) may also be determined from "light" *J-V* measurements under standard illumination. This section describes the performance of an ideal solar cell and the determination of these parameters from the *J-V* curve of such a device.

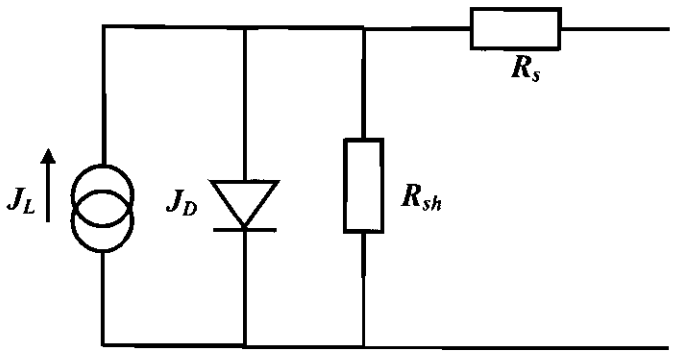

Figure 2.5: Equivalent circuit for a solar cell, including a current generator with light generated current density J_L, a diode with dark current density J_D, shunt resistance R_{sh} and a series resistance R_s.

The equivalent circuit diagram for a photovoltaic cell[3] is shown in fig.2.5. The circuit consists of a diode representing the *p-n* junction, as well as series and shunt resistances to account for the resistivity of the layers and any leakage currents respectively. However, for an ideal device the resistances are deemed to have no impact on performance and it is thus assumed that $R_s = 0$ and $R_{sh} = \infty$ (the impact of finite shunt and series resistances are discussed in Section 2.4.2). In the case of an ideal device, and when the device is in the dark, the diode current density (J) may be determined as a function of voltage using the Schockley diode equation[2]:

$$J = J_0(e^{qV/AkT} - 1) \quad (2.1)$$

where q is the charge of an electron, k is Boltzman's constant, T is the temperature, J_0 is the reverse saturation current density (a constant related to material properties), and A is the diode ideality factor .When the device is place under a light source a light generated current density term (J_L) is added to the equation:

$$J = J_0(e^{qV/AkT} - 1) - J_L \quad (2.2)$$

Typical light and dark J-V curves for an ideal device are shown in fig.2.6, these represent direct plots of equations 2.1 and 2.2. The standard device performance parameters (J_{sc} and V_{oc}) are marked on the light curve, along with the maximum power rectangle including the maximum power point P_{mp} and the associated current density and voltage values J_{mp} and V_{mp}.

The standard device performance parameters are typically determined from light J-V curves. The calculation of each of these parameters is now discussed in turn:

Short circuit current density

The short circuit current density (J_{sc}) is the current generated by the device under no applied bias, seen as the y-intercept in fig.2.6. From equation 2.2 for an ideal diode, when no bias is applied ($V = 0$) the J_0 term becomes zero and the short circuit current density is equivalent to J_L.

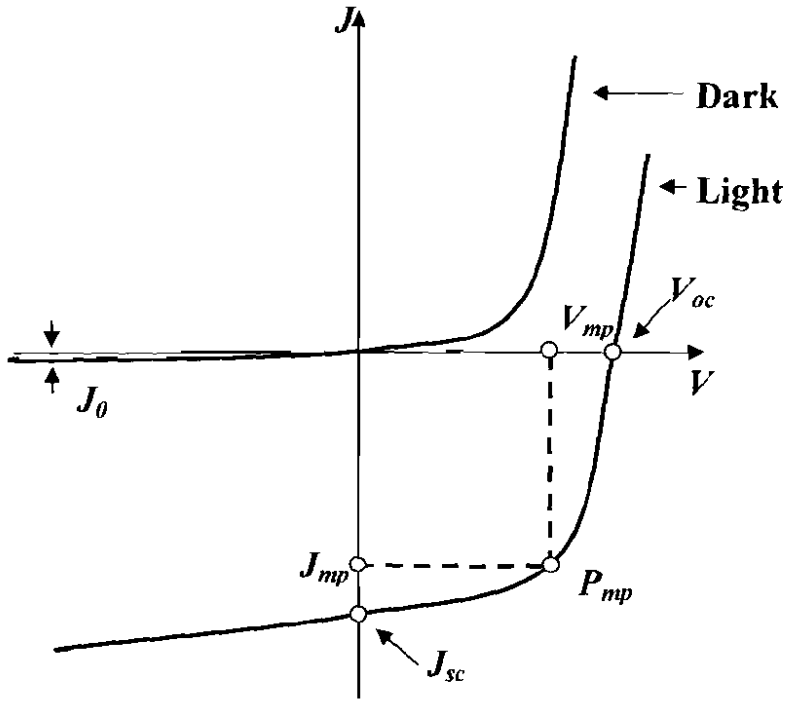

Figure 2.6: Ideal diode *J-V* curves for measurement in the dark and under illumination.

Open circuit voltage

The open circuit voltage (V_{oc}) of a device is defined as the applied bias at which no current flows through the device, determined from the *x*-intercept of the light *J-V* curve. The V_{oc} for an ideal cell may also be determined from equation 2.2 by setting the condition that $J = 0$. Rearranging the equation gives:

$$V_{oc} = \frac{AkT}{q} \ln\left[\frac{J_L}{J_0} + 1\right] \tag{2.3}$$

It can be seen from equation 2.3 that V_{oc} is a function of both the dark and light generated current density terms, as well as the diode quality factor A.

Fill factor

The fill factor (*FF*) is a measure of the "squareness" of the curve, with higher values tending towards a square response (i.e. $P_{mp} = J_{sc} \times V_{oc}$), and lower values tending toward a straight line. The fill factor is defined as a ratio of the size of the maximum power rectangle, to the power rectangle formed by the product of the short current density and open circuit voltage:

$$FF = \frac{P_{mp}}{J_{sc}V_{oc}} = \frac{J_{mp}V_{mp}}{J_{sc}V_{oc}} \tag{2.4}$$

Efficiency

The device efficiency (η) is defined as the ratio of the maximum power generated by the device (P_{mp}), to the power of the radiation incident upon it (P_s):

$$\eta = \frac{P_{mp}}{P_s} = \frac{V_{oc}J_{sc}FF}{P_s} \tag{2.5}$$

Efficiency values are typically determined using AM1.5 illumination.

2.4.2 The solar spectrum and non-ideal device losses

The previous section discussed the performance of an ideal photovoltaic device, and the determination of the standard device performance parameters. This section provides a brief discussion on real device performance; firstly the impact of the solar spectrum upon device performance is described, followed by a brief description of the impact of finite shunt and series resistances upon the device *J-V* characteristics.

2.4.2.1 The solar spectrum

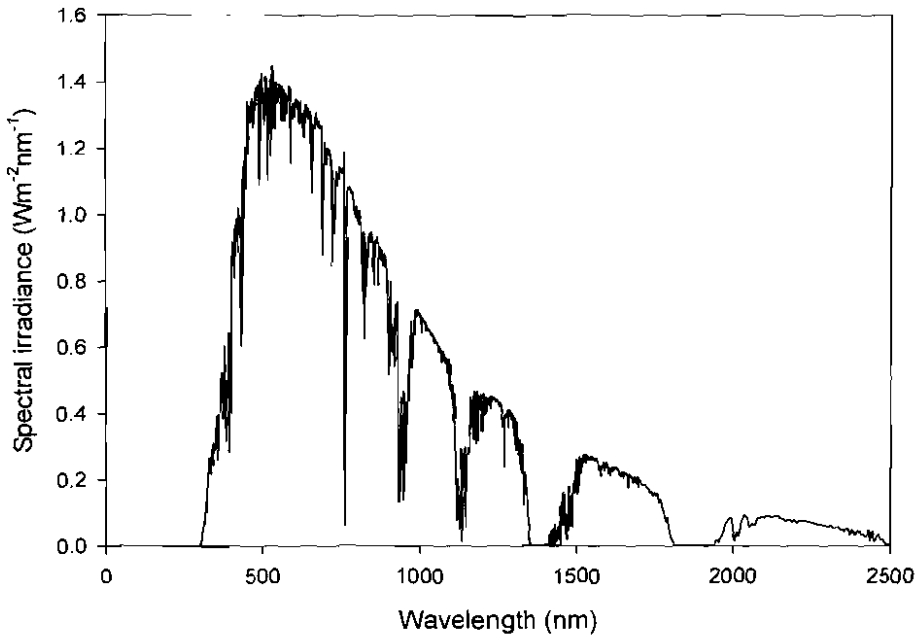

Figure 2.7: The AM 1.5 spectrum (source: ASTM E-891 reference table[6])

The solar spectrum can be approximated by a black body emitting at a temperature of 6050K[3]. However, the spectrum is attenuated by a number of factors such as variation in temperature across the Sun's surface, Fraunhofer absorption lines and the effect of both the Sun's and Earth's atmospheres. Whilst the other attenuations are assumed to be constant, the attenuation provided by the Earth's atmosphere will vary dependent upon the path length of the light through the atmosphere, with a longer path length leading to greater attenuation. This path length is commonly described in terms of "air mass" (AM), with AM0 corresponding to the solar spectrum outside of the Earths atmosphere and AM1 representing the solar spectrum incident at the equator, the shortest path length to the surface. For temperate climates the AM1.5 solar spectrum is used as an approximation (as shown in fig.2.7), which corresponds to the spectrum at an angle of 45° from the vertical. For the purposes of standardised device testing an intensity of 100mW/cm^2 is used in combination with the AM1.5 spectrum. All device efficiency results reported in this thesis have been determined in this manner, using the apparatus described in Section 5.4.1.

2.4.2.2 Fundamental losses

Because light from the Sun is incident upon the Earth over a range of wavelengths, solar cells must be designed with the solar spectrum in mind. The bandgap of the absorber plays a key role in determining the maximum power (and thus efficiency) that may be generated by a solar cell. It is intuitive to see that materials with very large or very small bandgaps will lead to a low level of power generation; in the case of the former because the portion of the solar spectrum absorbed is small, leading to low photocurrent being generated, and in the later because the generated voltage is too small (V_{mp} is always less than E_g for a material). Consequently there is a trade off to be made between the voltage that the device is capable of producing and the fraction of the solar spectrum it is capable of absorbing light from. This leads to the definition of an ideal bandgap for semiconductors of around 1.4eV, where the theoretical conversion efficiency for a single band photoconductor is around 33%[4]. The maximum theoretical conversion efficiency as a function of the material bandgap is shown in fig.2.8. The bandgaps of common solar cell materials have been marked for reference.

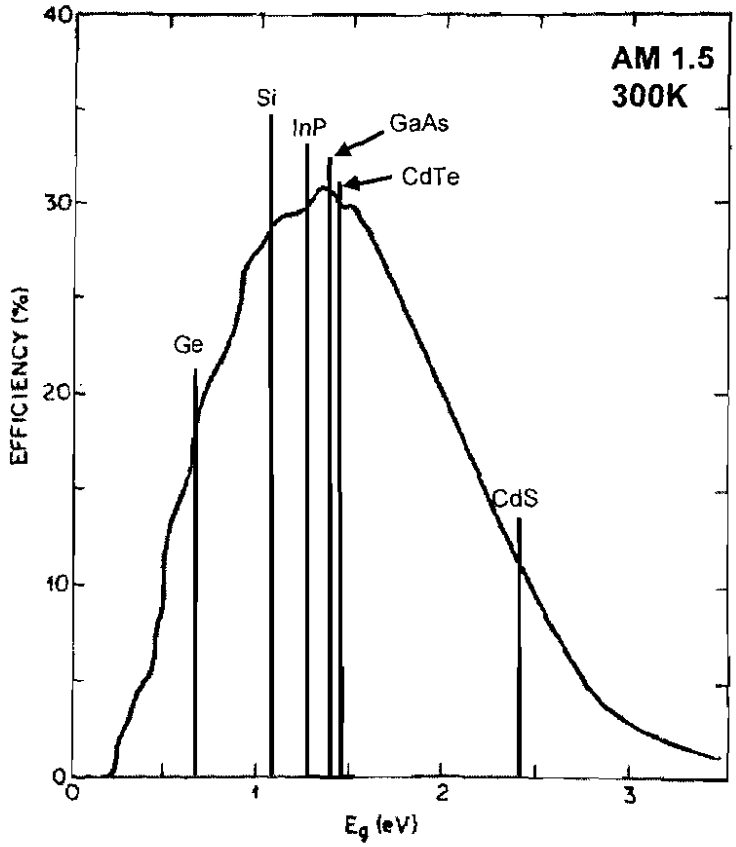

Figure 2.8: Maximum theoretical conversion efficiency as a function of bandgap under AM 1.5 illumination[7]. Common solar cell device materials have been marked for reference.

2.4.2.3 Resistance losses

In Section 2.3.1 the equivalent circuit for an ideal cell (fig.2.5) was defined as having resistances of $R_s = 0$ and $R_{sh} = \infty$. Clearly for a real device this will not be the case, and the shunt and series resistance will thus impact upon the device performance and the shape of *J-V* curves. The series resistance arises as a result of the resistivity of the device layers towards current flow and any resistivity at interfaces with the device contacts. Poor quality contacts to layers with high resistivity, leads to an increase in the series resistance of devices. The shunt resistance arises due to leakage pathways through the cell, typically as a result of grain boundaries or pinholes in the material. Cells with a large number of these leakage pathways are expected to have a significantly reduced shunt resistance and

device performance will be hindered as a result. These two resistance terms may be incorporated into equation 2.2 as follows[5]:

$$J = J_0(e^{(qV-JR_s)/AkT} - 1) + \frac{(V - JR_s)}{R_{sh}} - J_L \qquad (2.6)$$

A representation of the *J-V* characteristics of a cell for various values of R_{sh} and R_s is shown in fig.2.9.

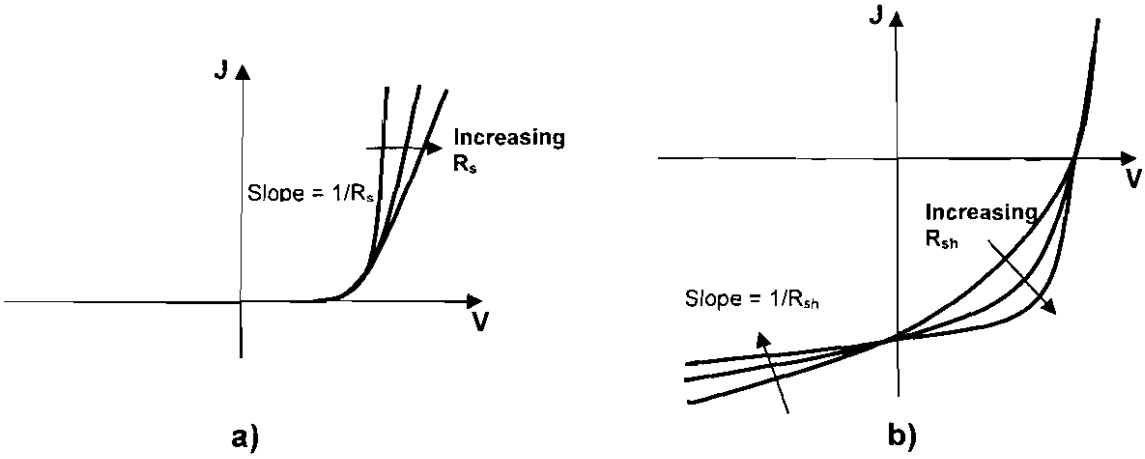

Figure 2.9: The effect of a) series resistance (R_s) and b) shunt resistance (R_{sh}), on the *J-V* characteristics of a solar cell.

Series resistance

It can be seen from fig.2.9a, that R_s dominates the shape of the curve under forward bias, with a decrease in R_s leading to a steeper gradient in the forward bias region. A reduction in the series resistance is usually found to improve the fill factor of a device and improve the overall performance. An estimate for R_s may be determined from the gradient of the straight line portion of the curve under forward bias. In this region the slope is approximately equivalent to $1/R_s$.

Shunt resistance

Fig.2.9b shows the effect of shunt resistance on the *J-V* curve. Increasing the R_{sh} value leads to a reduction in the gradient of the curve under reverse bias, and typically an improvement in the fill factor of the device. An estimate for R_{sh} may be determined from

the gradient of the straight line portion of the curve under reverse bias. In this region the slope is approximately equal to $1/R_{sh}$.

2.5 Solar cell device materials

There are numerous photovoltaic materials commonly used in the production of solar cells. This section provides a brief review of the principle absorber layer materials currently being used.

2.5.1 Silicon

Silicon is the most established and widely used solar cell material and device technology, owing to its abundance and the large depth of material knowledge gained from the electronics industry. Si based devices are highly developed and as a result high efficiencies of up to 24.7%[8] have been achieved using single crystal Si wafers. However, as Si has an indirect bandgap (photon absorption is phonon assisted[2]) of 1.1eV, it has a relatively low absorption coefficient and thus a large thickness of Si is required for high levels of light absorption (~200μm). Because of this, and the high purity of material required (due to the need for a long minority carrier diffusion length), devices based around single crystal Si cells are inherently expensive in comparison to other photovoltaic devices. A lower cost alternative to single crystal Si is the use of polycrystalline Si. Although cheaper than the single crystal material, polycrystalline Si tends to yield lower efficiency devices, due to the negative impact of grain boundaries within the material.

2.5.2 III-V materials

There are two group III-V technologies that are commonly used for the production of solar cells, gallium arsenide (GaAs) and indium phosphide (InP). Both have direct bandgaps of 1.43eV and 1.34eV respectively, making them both highly suited as solar absorbers. Device efficiencies of up to 25.1% for GaAs and 21.9% for InP have been reported[8]. The major limitation to these materials is seen as the scarcity of Ga and toxicity of As in GaAs devices and the high In cost for InP devices. III-V devices therefore find niche applications for space cells and concentrator devices.

2.5.3 Thin film material

Due to the prohibitively high materials cost of silicon base devices, devices utilising photovoltaic thin films present an attractive alternative and offer significant cost reduction. This section briefly describes the three principle thin film technologies currently being researched, hydrogenated amorphous silicon, copper indium diselenide and cadmium telluride.

2.5.3.1 Hydrogenated amorphous silicon

Hydrogenated amorphous silicon (a-Si:H) is distinctly different to the single crystal or polycrystalline forms of the material, with it having a direct bandgap of approximately 1.7eV (although the bandgap may range from 1.6eV to 1.8eV, depending upon how the material is deposited). As a result the absorption coefficient of a-Si:H is typically an order of magnitude larger than for bulk silicon and therefore only thin films of the material are required to provide a good level of absorption. Single junction a-Si:H devices with efficiency of up to 9.5% have thus far been reported[8], although the technology is still produced in low volume in comparison to single crystal and polycrystalline Si technologies. A large amount of research has been carried out on this material, but concerns about stability and low production efficiency have limited its success.

2.5.3.2 Copper indium diselenide

Copper indium diselenide (CIS) is a highly promising thin film absorber material due to its direct bandgap of 1.04eV, meaning a large portion of the spectrum is easily absorbed. However, the bandgap of the material may also be controlled (in the range 1.0eV to 1.7eV) by the substitution of gallium for indium, leading the formation of copper indium gallium diselenide (CIGS). By incorporation of gallium, the bandgap can be optimised for the solar spectrum and efficiencies of up to 19.9% have thus far been reported for CIGS based devices[8]. This represents the highest reported efficiency for any thin film device. Module efficiencies of up to 13.4% are reported and there is presently an intensive research and industrialisation effort.

2.5.3.3 Cadmium telluride

Cadmium telluride (CdTe) is a polycrystalline material that has long been recognised as a promising thin film absorber layer, owing to its near-ideal direct bandgap of 1.5eV and its high optical absorption coefficient (a 1 μm layer will typically absorb >90% of incident photons). It is usually paired with a CdS window layer to form hetero-junction device structures. The first such device was reported in 1972 by Bonnet and Rabenhorst[9], with a device conversion efficiency of ~5% being achieved. Current state of the art devices are far more developed, with laboratory scale devices reaching efficiencies of up to 16.5%[10]. Presently a number of research challenges are being addressed in the CdTe field and, in parallel, large scale production is being initiated.

The growth and characterisation of CdTe layers and CdTe/CdS solar cells is the subject of this work. Full details of the CdTe/CdS device structure are provided in Chapter 3, along with an explanation for the function of each layer and the various processing steps used during device fabrication.

2.6 References for Chapter 2

1 D. M. Chapin, C. S. Fuller, and G. L. Pearson, Journal of Applied Physics **25,** 676-677 (1954).

2 S. M. Sze, *Semiconductor Devices Physics and Technology*, John Wiley & Sons, New York, 1985.

3 R. H. Bube, *Photovoltaic Materials*, Imperial College Press, London, 1998.

4 J. Nelson, *The Physics of Solar Cells*, Imperial College Press, Singapore, 2003.

5 A. L. Fahrenbruch and R. H. Bube, *Fundamentals of Solar Cells*, Academic Press, New York, 1983.

6 *ASTM E-891 AM 1.5 Reference Table* NREL, http://rredc.nrel.gov/solar/spectra/am1.5/

7 C. H. Henry, Journal of Applied Physics **51,** 4494-4500 (1980).

8 M. A. Green, K. Emery, Y. Hishikawa, and W. Warta, Progress in Photovoltaics: Research and Applications **16,** 61-67 (2008).

9 D. Bonnet and H. Rabenhorst, in *9th IEEE Photovoltaic Specialists Conference* (Silver Springs, Maryland, 1972), 129-132.

10 X. Wu, Solar Energy **77,** 803-814 (2004).

3 CdTe/CdS solar cells

3.1 Introduction

Owing to its near ideal bandgap and high optical absorption coefficient, CdTe is seen as a highly suited absorber layer for solar cells, as explained briefly in Chapter 2. The use of CdTe homo-junction devices is not practical due to the high rate of surface recombination and research into these structures is not pursued. Since the early 1970's, following the work of Bonnet and Rabenhorst[1], CdTe has primarily been used with CdS as a hetero-junction partner and this has become the standard arrangement for CdTe based devices.

In this chapter the structure of the CdTe/CdS solar cells, which form the basis of this work, is discussed. The role of each layer and its importance to the performance of the completed device is described, along with role of the back contact and the activation and etching steps. Finally a brief review of the state of the art for research scale CdTe/CdS devices is given.

3.2 Device structure

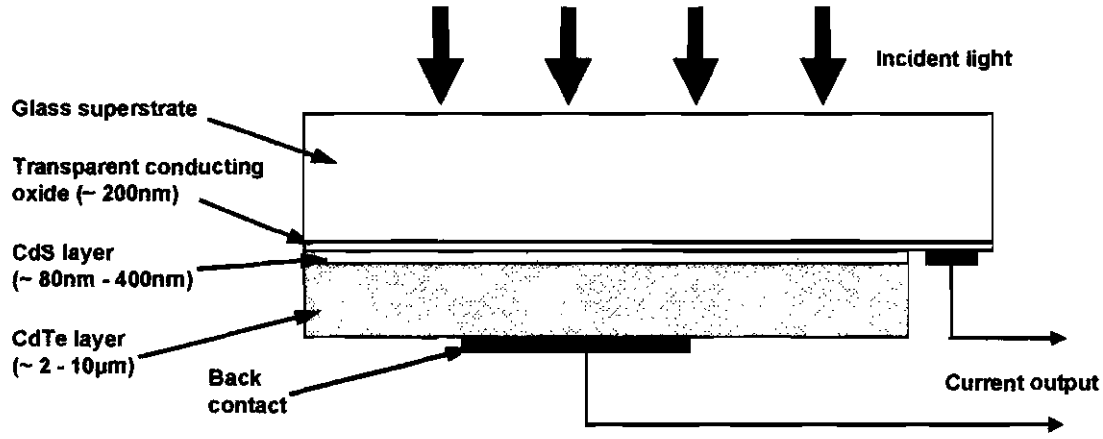

Figure 3.1: Structure of a CdTe/CdS solar cell in the 'superstrate' configuration.

The CdTe/CdS solar cells reported in this work were prepared in the superstrate geometry, shown in fig.3.1. In this arrangement all deposition takes place on a glass

substrate, which then becomes the transparent front surface in the completed device. Although CdTe/CdS devices are sometimes prepared in the substrate configuration[2] (where the deposition substrate becomes the opaque device back surface) the superstrate configuration is by far the most common device geometry encountered.

The fabrication of a superstrate CdTe/CdS solar cell may be briefly summarised as follows:

I. A transparent conducting oxide (TCO) layer is deposited onto a glass substrate to act as the front contact to the device.
II. A CdS window layer is then deposited onto the TCO/glass structure.
III. The CdTe absorber layer is deposited onto the CdS layer leading to the formation of the *p*-CdTe/*n*-CdS junction.
IV. The CdTe/CdS/TCO/glass structure is then subjected to a cadmium chloride ($CdCl_2$) "activation" step. A thin (typically 50-200nm) $CdCl_2$ layer is deposited onto the CdTe back surface, before the entire structure is annealed. This step may be done with or without the presence of oxygen.
V. The CdTe layer is etched to provide a suitable surface for the back contact to be applied.
VI. A back contact metallisation is applied to the device.

The following sections provide a brief discussion of each device layer or processing step, with the common materials or techniques for each being described. The specific conditions or materials used for devices reported in this work may be found in either Chapter 5 or the appropriate results chapter.

3.2.1 Glass substrate

For superstrate configuration devices a glass substrate is used, with all subsequent layers being deposited on this substrate. It is therefore important to choose a suitable glass type that will withstand the deposition temperatures used for the various layers. Commonly used types of glass are soda-lime, aluminosilicate and borosilicate glass, which have melting temperatures 695°C, 820°C and 915°C respectively. For most

deposition methods soda-lime glass is acceptable and it is widely used in production. Although soda-lime glass is used widely in research also, when higher than usual deposition temperatures are under investigation i.e. >500°C, it is found to be necessary to use aluminosilicate or borosilicate glass structures. The thickness of the glass substrates is also an important parameter to consider, as some incident light will be absorbed by the glass[3]. This attenuation will be increased for thicker substrates, so it is often preferable to minimise the substrate thickness whilst maintaining thermal and mechanical stability. It is also important to consider the possible effect of impurities when selecting a substrate, as it has been shown that significant impurity diffusion into the CdTe and CdS layers from the glass may occur as a result of the deposition processes[4]. As a result, at least one manufacturer applies a sputtered SiO_2 coating to the glass prior to the deposition of the transparent conductor layers.

Details of the soda-lime and aluminosilicate substrates used in this work are described in Section 5.2.4.

3.2.2 Transparent conducting oxide front contact

Numerous types and combinations of TCO layers are reported for CdTe/CdS devices: the formation of a good device front contact is essential to the production of a high efficiency device. The principle requirements of a TCO are that it be highly optically transparent and highly conductive, with an optical transmission of >80% and a sheet resistance of <10Ω/□ typically being considered suitable. The most commonly used TCOs are based on oxides of tin or indium, typically in the form of fluorine doped tin oxide (FTO) or indium doped tin oxide (ITO), both of which are most successfully deposited by reactive sputtering. Of the two, ITO has the lower sheet resistance and is as such the preferable material. However it has often been found to be unsuitable for high temperature deposition methods, owing to indium diffusion from the ITO layer[5]. This problem is overcome by the use a diffusion "blocking" layer (typically un-doped tin oxide) between the ITO and CdS layers[6]. Alternatively the more thermally stable FTO can be used in place of the ITO. Other, more novel, TCO layers have also been reported. Of particular promise is cadmium stannate (Cd_2SnO_4)[7,8] which has been shown to be

capable of producing highly efficient devices as it is more conductive and more transparent than standard TCOs[9].

Details of the ITO and FTO transparent conductors used in this work are given in Section 5.2.4.

3.2.3 Cadmium sulphide window layer

In the majority of CdTe based solar cells the *n*-type window layer is cadmium sulphide (CdS). CdS is a naturally *n*-type material, so requires no doping under most growth conditions and can be used for device fabrication in its as-grown state. It has a wide bandgap (~2.4eV) at room temperature, meaning it is transparent to light at wavelengths above ~520nm. Although the *n*-CdS/ *p*-CdTe device is in principle a hetero-junction solar cell, experimentally it is found that carriers generated by absorption in the CdS are not collected: This may be demonstrated simply from external quantum efficiency (EQE) curves which show a deficiency in the short wavelength region of the spectrum (the reader is referred to Section 6.2.2 for further information). It is therefore advantageous for device performance, to minimise the CdS absorption. This is usually achieved by using thin (<100nm) CdS layers, which has been shown to significantly improve the current generation for incident light wavelengths of <520nm[10]. However, the reduction of CdS thickness may lead to the formation of pinholes in the material which, whilst increasing the device J_{sc}, may lead to a loss of V_{oc} and device performance. This is ascribed to the formation of CdTe/ITO interfaces which are inferior to the CdTe/CdS junction[11] and thus reduce the photovoltage and fill factor. This loss may be minimised by a reduction in the CdS grain size[12] which increases the substrate coverage at lower CdS thickness, allowing significantly thinner films to be used. For this reason it is preferable to have dense CdS films with a small grain size. The manner by which CdS is deposited will principally determine its grain structure and morphology. A wide range of techniques have been investigated including chemical bath deposition (CBD)[13], sputtering[14], metal organic chemical vapour deposition (MOCVD)[15] and close space sublimation (CSS)[16]. The higher temperature techniques such as CSS tend to produce films of a larger grain size than the low temperature techniques such as CBD[17].

The devices reported in this work were fabricated using CdS deposited by both CBD, using the method outlined in Section 5.2.2, and by CSS, using a wide range of deposition conditions (see Chapter 8). Evaluation of the growth mechanisms of the semiconductor layers was chosen as one of the themes of the present work given their impact on grain structure and morphology.

3.2.4 Cadmium telluride absorber layer

p-type cadmium telluride (CdTe) is the absorber layer in CdTe/CdS solar cells, it has a high optical absorption coefficient (> 5 x 10^5 cm^{-2}), with a 2μm layer absorbing around 99% of photons incident on the junction that have an energy > 1.5eV. This means significantly less material is required than for silicon based devices, where absorber layers of >200μm thickness are routinely used. It is preferable for cost reduction purposes to use a thin absorber layer (<2μm), however problems may be encountered upon reducing the CdTe layer thickness, due to the formation of pinholes as a result of non-homogeneities in thin CdTe layers. This may lead to shunting and results in significant loss of device performance. To compensate for this thicker CdTe absorber layers of 5-8μm are often used, both in research and industrially.

The following sections outline some of the primary issues that need to be considered during CdTe device fabrication, i) the CdTe grain size and grain boundary effects, ii) doping of the CdTe layer and iii) the junction position.

3.2.4.1 CdTe grain size and grain boundaries

Thin film CdTe is a polycrystalline material and the boundaries between single crystal grains may thus have a significant impact upon the photovoltaic performance of CdTe/CdS devices. There is expected to be a high defect density (e.g. dangling bonds, lattice dislocations) at the grain boundaries, as well as the possibility that impurities may segregate there. Grain boundaries in semiconductors are therefore generally expected to act as strong recombination centres, due to the introduction of deep energy levels within the bandgap resulting from the high defect concentration[18]. Grain boundaries may also act as barriers to current transport[19] or cause significant leakage current owing to low resistance paths forming as a result of the granular structure[20]. It is therefore

advantageous to device performance to minimise the impact of grain boundaries by maximising the grain size of CdTe films. The grain size of CdTe films is known to strongly depend on the deposition temperature[21], with the largest grained films usually being produced by high temperature deposition methods, particularly CSS. The majority of high efficiency devices reported typically utilise CdTe layers deposited by CSS[8,21] although good quality CdTe layers are also deposited by a number of different methods such as pulsed laser deposition[22], MOCVD[15], sputtering[23], screen printing[24] and electrodeposition[25].

3.2.4.2 Doping of CdTe

CdTe conductivity and carrier concentration play a vital role in determining the junction position and field in *p-n* junction devices. A brief description of intrinsic and extrinsic doping phenomena in CdTe is therefore included, followed by a description of the phenomena of particular relevance to CdTe/CdS solar cells.

Intrinsic doping

It is generally accepted that the Cd and Te vacancies in CdTe are native defects that are active in the doping [26]. The doubly positively charged Cd vacancy ($V_{Cd}^{\cdot\cdot}$) is an acceptor in CdTe. At high temperature the vapour pressure of Cd exceeds that of Te over the solid and the resulting excess of Te therefore promotes *n*-type conductivity. Conversely, an excess of Cd introduces doubly negatively charged Te vacancies ($V_{Te}^{\cdot\cdot}$), these acting as donors. Interstitials of Cd and Te (Cd_i, Te_i) might also be expected to be electrically active, but there is less evidence of their activity than for vacancy centers in CdTe[26].

Extrinsic doping

Both *n*-type and *p*-type extrinsic (impurity) doping of CdTe has been explored extensively. For II-VI semiconductors including CdTe, donors are selected from groups III and VII (these being incorporated on the II and VI sites respectively), whilst acceptors are selected from groups I and V (these being incorporated on the II and VI sites respectively). Of the *n*-type dopants, Cl and In are widely reported while Ga and Al are

well known[5,27,28]. For *p*-type doping, Ag, and Cu are well known as effective dopants while the *p*-type activity of Na, Li, As and Au is also reported[26].

In addition to the above, iso-electronic doping on the group VI site is also known for CdTe, with O_{Te} being known as an acceptor, presumably on account of its greater electronegativity than Te.

Extrinsic dopants are known to act with native defects: this may lead to compensation phenomena. For example, highly resistive CdTe is required for use in radiation detectors. However, growth at high temperatures encourages the formation of a significant density of Cd vacancy acceptors ($V_{Cd}^{\cdot\cdot}$). Industrially this is compensated by the deliberate addition of Cl as a donor. In the case of *p*-doping it is found experimentally that there is an upper limit to the acceptor carrier concentration achievable. This is understood to be limited by the formation of a native compensating donor defect[29].

CdTe solar cells

For the case of CdTe in solar cells, Basol[30] empirically developed a post-growth treatment involving Cl ("activation") which is essential for high-performance PV operation. While Cl_{Te} is known as a donor, it is understood that Cl doping is compatible with the operation of the *n*-CdS/*p*-CdTe solar cell. While the exact microscopic mechanism has not been fully determined, it is likely that the native population of $V_{Cd}^{\cdot\cdot}$ is stabilised by the formation of a complex with Cd i.e. $(V_{Cd}^{\cdot\cdot}\text{-}V_{Te}^{\cdot})^{\cdot}$, this being a single acceptor complex[31]. Many authors report that oxygen incorporation has a significant beneficial effect in CdTe solar cells, presumably due to its role as an iso-electronic acceptor[32].

Cu-doping of the back contact surface of the CdTe is widely used to promote the formation of a p^+ layer, hence reducing contact resistance[33]. However, Cu is a fast diffuser in CdTe and has been implicated in causing instability in the devices, possibly by *p*-doping of the CdS layer. Many European laboratories are therefore presently working on Cu-free processes.

In attempts to grown hetero-structures with a controlled doping profile, MOCVD has been used to grow CdTe:As. While the *p*-doping by this route has been demonstrated in

test structures[29], its use in CdTe/CdS solar cells gave poor device performance. Hence As-doping was combined with Cl treatment in an empirical attempt to achieve good diode characteristics. This approach proved to be successful and is the subject of ongoing research at Bangor University, including efforts to understand the doping phenomena and compensation. Material of this type is reported in Section 6.4.3 and the growth in Section 5.2.3.

Finally it should be mentioned that since the industry standard for CdTe purity is 99.999% (for reasons of cost), the material is relatively impure by semiconductor standards. Emziane reported extensively on the origin and impact of unintentional impurities in CdTe solar cells and their origin in for example the TCO/glass[34], the $CdCl_2$ used for activation[35] and the CdTe feedstock itself[36].

3.2.4.3 Un-optimised device structures and impurities

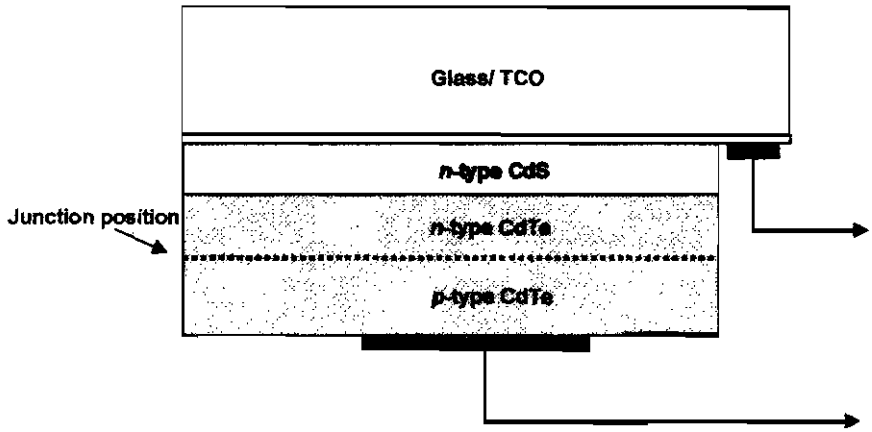

Figure 3.2: Structure of a buried homo-junction CdTe/CdS device

In cases where the doping is not properly controlled, or impurities within the layer have led to unintentional doping, buried homo-junctions (*n*-CdTe/ *p*-CdTe, fig.3.2) may form which are deleterious to device performance due to high levels of surface recombination. Whilst it is assumed that the device retains a *p-n* junction, as shown in fig.3.2, it may in fact be the case that a *p-i-n* structure has been formed, with an intrinsic or weakly doped CdTe region located between the CdS and *p*-type CdTe regions.

The formation of buried homo-junctions is the subject of work presented in Chapters 6 and 8, and the reader is thus referred there for further information.

In this work CdTe layers have been deposited by the CSS technique. The details of the specific deposition system used may be found in Section 5.2, whilst a review of CSS CdTe growth may be found in Section 4.6. Chapter 7 presents an exhaustive investigation of the nucleation and growth mechanics of CdTe films. The insight gained was exploited in the fabrication of devices, e.g. as a function of grain size, in Chapter 8.

3.2.5 Cadmium chloride activation step

As mentioned in Section 3.2.4.2, post-growth treatment with Cl is essential in promoting high performance in CdTe solar cells. The chlorine species is most commonly provided by cadmium chloride ($CdCl_2$), with a layer being applied to the CdTe back surface either by drying from a solution ($CdCl_2$ in methanol) or directly by vacuum evaporation. After deposition of the $CdCl_2$ layer the device is annealed in order to diffuse the Cl species into the CdTe layer. Whilst the annealing process is usually separate from the $CdCl_2$ deposition, numerous in-situ $CdCl_2$ treatments have also been reported[37,38] where the device structure is annealed during the $CdCl_2$ deposition.

$CdCl_2$ treatment is considered to have an important effect on doping as outlined in the previous section. Indeed it is essential in the formation of a structure displaying good diode characteristics. In addition to the direct electrical effects, $CdCl_2$ treatment promotes profound physical effects including i) enhancement of intermixing between the CdTe and CdS[39], and ii) promoting of grain growth and recrystallisation in small grained films[40] (a brief review on the effects of recrystallisation resulting from post growth annealing is presented in Section 4.6.2.3). It is important that the $CdCl_2$ treatment is correctly optimised as under treatment will lead to an incomplete activation of the junction, whilst over treatment may lead to delamination of the films from the substrate. The treatment is optimised by adjusting the time and temperature of the annealing, or by changing the thickness of the deposited $CdCl_2$ layer.

3.2.6 Intermixing between CdTe and CdS layers

At the interface between the CdTe and CdS layers there is typically an intermixed region consisting of the solid solutions resulting from Te diffusion into the CdS layer (forming $CdS_{1-y}Te_y$[41]), and S diffusion into the CdTe layer (forming CdS_xTe_{1-x} alloy[42]). The level of intermixing between the layers is dependent on a number of factors, such as the CdTe deposition temperature (higher temperature leads to greater intermixing), CdS grain size (smaller CdS grains lead to greater intermixing) and the $CdCl_2$ activation step (treatment promotes further intermixing). The performance of the cell is to some extent determined by the level of intermixing, with an optimised level being expected to increase the photovoltage and fill factor[6]. The amount of intermixing may also affect the spectral response of CdTe/CdS devices, due to variations in the bandgap of the intermixed layers. Its influence on the spectral response of CdTe/CdS devices is discussed more fully in Section 6.2.2 with reference to the effects of interdiffusion on specific parts of the EQE response.

3.2.7 Back contact

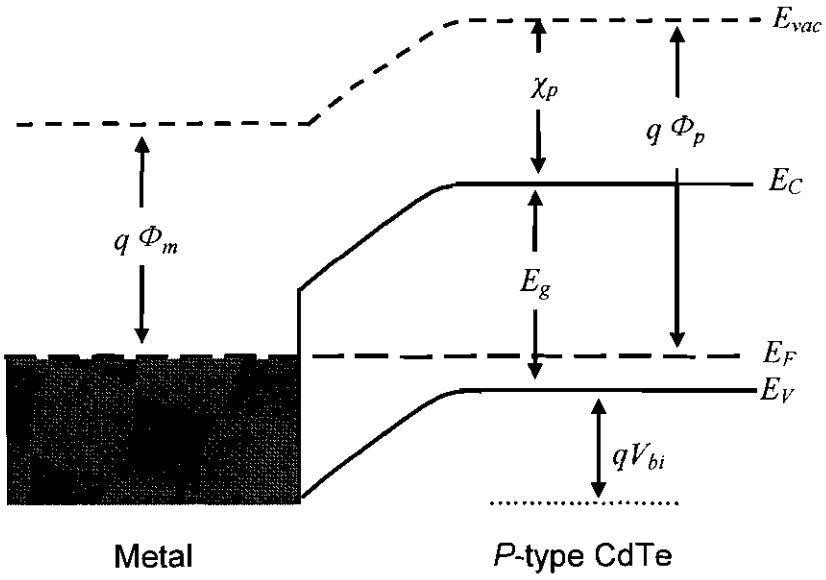

Figure 3.3: Metal/ *p*-CdTe contact band diagram showing the work functions of the metal and semiconductor (Φ_m and Φ_p) and the electron affinity of the semiconductor χ_p.

Because of the high work function of *p*-CdTe (due to its high electron affinity, see fig.3.3) a metal of a suitably high work function is required in order to form a good ohmic contact. As the majority of metals do not permit this, metal back contacts usually form Schottky barriers with CdTe. This leads to the formation of a diode opposing the CdTe/CdS junction, thus reducing device performance[43] and contributing to series resistance. Two strategies are reported in the literature to overcome this fundamental problem:

a) Use of a p^+ doped layer at the contact (back) surface of the CdTe. This heavy doping has the effect of reducing the width of the electron barrier, hence encouraging tunnelling. Experimentally this is achieved by the use of Cu-containing contact materials (as copper is a known *p*-type dopant, Section 3.2.4.2) such as Cu/graphite, Cu/Mo, Au/Cu and pure Au contacts. The copper containing materials, whilst yielding good quality contacts, and in many cases improving device performance (increasing Cu concentration has been shown to improve fill factor[44]), may also lead to shunting within devices due to diffusion of the copper along grain boundaries and into the CdS layer[45]. Other techniques have also been reported that attempt to generate a p^+ back contact layer, for example Barrioz et al[46] reported the use of high levels of arsenic doping for this purpose.

b) Use of a more appropriate junction i.e. involving a CdTe/semiconductor or CdTe/semi-metal junction. Most often this is achieved by creating a Te-rich layer on the CdTe back surface through chemical etching. However, this also leads to enhanced *p*-type character at the back surface, due to the creation of cadmium vacancies (Section 3.2.4.1). Fritsche et al[47] attributed the formation of a good quality contact to this doping, as it was found that vacuum deposited Te layers on the back surface lead to poorer quality contacts, whereas the formation of a Te rich layer by etching produced good quality contacts. Two different etching solutions are commonly used; a bromine-methanol solution and a nitric-phosphoric acid (NP) solution. Whist both are effective, the NP etch is often found to be a more aggressive treatment and to preferably etch grain boundaries[48].

Details of the etching and metallization procedure used in this work are given in Section 5.2.6.

3.3 High efficiency CdTe/CdS devices

η (%)	J_{sc} (mA/cm^2)	FF (%)	V_{oc} (mV)	R_{sh} (Ωcm^2)	R_s (Ωcm^2)
16.5	25.86	74.45	845.0	3-5 x 10^3	~1

Table 3.1: Performance parameters for Wu's[8] world record CdTe/CdS device, recorded for a ~1cm^2 back contact.

The highest efficiency currently reported for a CdTe/CdS solar cell stands at 16.5%[8], and the performance parameters for this device are given in table 3.1. This device incorporated a number of novel materials to improve the device efficiency: The front contact was provided by cadmium stannate ($CdSnO_4$ or CTO) rather than the standard ITO or FTO, as this was found more optically transparent and more conductive. A highly resistive zinc tin oxide (ZTO) buffer layer was then deposited on top of the CTO, this being added to prevent the formation of localised CdTe/TCO junctions which would reduce device performance. Rather than standard polycrystalline CdS films, what was termed as a nanostructured CdS:O film was used[49]. This was deposited by rf magnetron sputtering, at room temperature and in the presence of an O_2/Ar ambient. The resulting films were found to have high O_2 concentration and small grain size of < 5nm. The bandgap of the material was also found to be increased for greater O_2 concentrations, reaching a value of 3.17eV for deposition in a 5% oxygen deposition ambient. This allowed a greater portion of the incident solar spectrum to be utilised and resulted in significant current generation for wavelengths <400nm. As a result of these innovations the device was found to have exceptionally high values for the fill factor (74.45%) and the V_{oc} (845mV). The CdTe layer in this device was deposited by CSS, which is the most common deposition technology for CdTe layers in high efficiency solar cells. Whilst devices of 15.8% efficiency have been reported that utilise CdS deposited by both CBD[50] and CSS[21], and a device with 16% efficiency has been reported based on MOCVD deposited CdS[51], all these devices are based upon CdTe layers by CSS.

3.4 References for Chapter 3

1 D. Bonnet and H. Rabenhorst, in *Conference Record of the Ninth IEEE Photovoltaic Specialists Conference* (Silver Springs, Maryland, 1972), 129-132.

2 N. Romeo, A. Bosio, and V. Canevari, Intemational Journal of Sustainable Energy **12,** 183-186 (1992).

3 J. R. Sites, Solar Energy Materials and Solar Cells **75,** 243-251 (2003).

4 M. Emziane, K. Durose, D. P. Halliday, N. Romeo, and A. Bosio, Thin Solid Films **511-512,** 66-70 (2006).

5 D. Bonnet, Thin Solid Films **361,** 547-552 (2000).

6 D. Bonnet, in *Clean Electricity From Photovoltaics*, edited by M. D. Archer and R. Hill (Imperial College Press, Singapore, 2001).

7 C. S. Ferekides, R. Mamazza, U. Balasubramanian, and D. L. Morel, Thin Solid Films **480-481,** 224-229 (2005).

8 X. Wu, Solar Energy **77,** 803-814 (2004).

9 X. Wu, P. Sheldon, T. J. Coutts, D. H. Rose, W. P. Mulligan, and H. R. Moutinho, in *NREL/SNL Photovoltaics Program Review - Proceedings of the 14th Conference: A Joint Meeting*, edited by C. E. Witt, M. AlJassim, and J. M. Gee (1997), 693-702.

10 J. E. Granata, J. R. Sites, G. ContrerasPuente, and A. D. Compaan, in *Conference Record of the Twenty Fifth IEEE Photovoltaic Specialists Conference* (Washington D.C., 1996), 853-856.

11 C. S. Ferekides, D. Marinskiy, S. Marinskaya, B. Tetali, D. Oman, and D. L. Morel, in *Conference Record of the Twenty Fifth IEEE Photovoltaic Specialists Conference*, (Washington D.C., 1996), 751-756.

12 C. S. Ferekides, K. Dugan, V. Ceekala, J. Killian, D. Oman, R. Swaminathan, and D. L. Morel, in *Conference Record of the IEEE First World Conference on Photovoltaic Energy Conversion/Conference Record of the Twenty Fourth IEEE Photovoltaic Specialists Conference*, (Hawaii, 1994), 99-102.

13 M. D. Archbold, D. P. Halliday, K. Durose, T. P. A. Hase, D. S. Boyle, S. Mazzamuto, N. Romeo, and A. Bosio, Thin Solid Films **515,** 2954-2957 (2007).

[14] A. D. Compaan, A. Gupta, S. Lee, S. Wang, and J. Drayton, Solar Energy **77,** 815-822 (2004).

[15] G. Zoppi, K. Durose, S. J. C. Irvine, and V. Barrioz, Semiconductor Science and Technology **21,** 763-770 (2006).

[16] A. R. Davies, J. R. Sites, R. A. Enzenroth, W. S. Sampath, and K. L. Barth, Materials Research Society Symposium Proceedings **1012,** 157-162 (2007).

[17] D. Albin, D. Rose, R. Dhere, D. Levi, L. Woods, A. Swartzlander, and P. Sheldon, in *Conference Record of the Twenty Sixth IEEE Photovoltaic Specialists Conference*, (Anaheim, 1997), 367-370.

[18] A. Morales-Acevedo, Solar Energy Materials and Solar Cells **90,** 678-685 (2006).

[19] K. Durose, D. Boyle, A. Abken, C. J. Ottley, P. Nollet, S. Degrave, M. Burgelman, R. Wendt, J. Beier, and D. Bonnet, Physica Status Solidi B-Basic Research **229,** 1055-1064 (2002).

[20] J. R. Sites, J. E. Granata, and J. F. Hiltner, Solar Energy Materials and Solar Cells **55,** 43-50 (1998).

[21] C. S. Ferekides, D. Marinskiy, V. Viswanathan, B. Tetali, V. Palekis, P. Selvaraj, and D. L. Morel, Thin Solid Films **361,** 520-526 (2000).

[22] A. Bylica, P. Sagan, I. Virt, A. Bester, I. Stefaniuk, and M. Kuzma, Thin Solid Films **511,** 439-442 (2006).

[23] A. D. Compaan, A. Gupta, S. Y. Lee, S. L. Wang, and J. Drayton, Solar Energy **77,** 815-822 (2004).

[24] N. Nakayama, H. Matsumoto, A. Nakano, S. Ikegami, H. Uda, and T. Yamashita, Japanese Journal of Applied Physics **19,** 703-712 (1980).

[25] W. Song, D. Mao, Y. Zhu, J. Tang, and J. U. Trefny, in *Conference Record of the Twenty Fifth IEEE Photovoltaic Specialists Conference*, (Washington D.C., 1996), 873-876.

[26] P. Capper, in *Narrow-gap II-VI Compounds for Optoelectronic and Electromagnetic Applications*, edited by P. Capper (Chapman and Hall, London, 1997).

[27] W. F. Mohamed and M. A. Shehathah, Renewable Energy **21,** 141-152 (2000).

[28] E. Watson and D. Shaw, Journal of Physics C-Solid State Physics **16,** 515-537 (1983).

[29] G. Zoppi, PhD Thesis, Durham University, 2005.

[30] B. M. Basol, International Journal of Sustainable Energy **12,** 25-35 (1992).

[31] M. Laasch, R. Schwarz, W. Joerger, C. Eiche, M. Fiederle, K. W. Benz, and K. Grasza, Journal of Crystal Growth **146,** 125-129 (1995).

[32] K. Akimoto, H. Okuyama, M. Ikeda, and Y. Mori, Applied Physics Letters **60,** 91-93 (1992).

[33] J. Zhou, X. Wu, A. Duda, G. Teeter, and S. H. Demtsu, Thin Solid Films **515,** 7364-7369 (2007).

[34] M. Emziane, K. Durose, D. P. Halliday, A. Bosio, and N. Romeo, Applied Physics Letters **87** (2005).

[35] M. Emziane, K. Durose, N. Romeo, A. Bosio, and D. P. Halliday, Thin Solid Films **480,** 377-381 (2005).

[36] M. Emziane, K. Durose, A. Bosio, N. Romeo, and D. P. Halliday, Journal of Materials Science **40,** 1327-1331 (2005).

[37] V. Barrioz, S. J. C. Irvine, E. W. Jones, R. L. Rowlands, and D. A. Lamb, Thin Solid Films **515,** 5808-5813 (2007).

[38] P. D. Paulson and V. Dutta, Thin Solid Films **370,** 299-306 (2000).

[39] I. Clemminck, M. Burgelman, M. Casteleyn, J. Depoorter, and A. Vervaet, in *Conference Record of the Twenty Second IEEE Photovoltaic Specialists Conference*, (Las Vegas, 1991),1114-1119.

[40] B. E. McCandless, L. V. Moulton, and R. W. Birkmire, Progress in Photovoltaics **5,** 249-260 (1997).

[41] J. P. Enriquez, E. G. Barojas, R. S. Gonzalez, and U. Pal, Solar Energy Materials and Solar Cells **91,** 1392-1397 (2007).

[42] K. Ohata, J. Saraie, and T. Tanaka, Japanese Journal of Applied Physics **12,** 1641-1642 (1973).

[43] A. Niemegeers and M. Burgelman, Journal of Applied Physics **81,** 2881-2886 (1997).

[44] A. O. Pudov, M. Gloeckler, S. H. Demtsu, J. R. Sites, K. L. Barth, R. A. Enzenroth, and W. S. Sampath, in *Conference Record of the Twenty-Ninth IEEE Photovoltaic Specialists Conference* (New Orleans, 2002), 760-763.

[45] D. L. Batzner, R. Wendt, A. Romeo, H. Zogg, and A. N. Tiwari, Thin Solid Films **361,** 463-467 (2000).

[46] V. Barrioz, Y. Y. Proskuryakov, E. W. Jones, J. D. Major, S. J. C. Irvine, K. Durose, and D. A. Lamb, Materials Research Society Symposium Proceedings **1012,** 367-372 (2007).

[47] J. Fritsche, D. Kraft, A. Thissen, T. Mayer, A. Klein, and W. Jaegermann, Thin Solid Films **403,** 252-257 (2002).

[48] H. R. Moutinho, R. G. Dhere, C. S. Jiang, M. M. Al-Jassim, and L. L. Kazmerski, in *Conference Record of the Nineteenth European Photovoltaic Solar Energy Conference and Exhibition* (Paris, 2004), 1-4.

[49] X. Wu, Y. Yan, R. G. Dhere, Y. Zhang, J. Zhou, C. Perkins, and B. To, Physica Status Solidi (c) **1,** 1062-1066 (2004).

[50] J. Britt and C. Ferekides, Applied Physics Letters **62,** 2851-2852 (1993).

[51] T. Aramoto, S. Kumazawa, H. Higuchi, T. Arita, S. Shibutani, T. Nishio, J. Nakajima, M. Tsuji, A. Hanafusa, T. Hibino, K. Omura, H. Ohyama, and M. Murozono, Japanese Journal of Applied Physics Part 1-Regular Papers Short Notes & Review Papers **36,** 6304-6305 (1997).

4 Growth mechanisms of polycrystalline thin films

4.1 Introduction

The microstructural properties of a thin film will be dependent upon the processes that govern its formation and may be very different from that of the bulk material. The early stages of film formation, nucleation and growth up to the point of coverage of the substrate, are of particular importance. Use of different temperatures, pressures or impurities may alter the early growth mechanism and produce films of differing quality. In the case of polycrystalline thin films such as CdTe, the size, morphology and structure of grains that comprise the material will be determined by the nucleation of the film. Understanding these early growth processes and how they may be manipulated, may therefore offer a route to controlling the grain structure within polycrystalline thin films.

This chapter presents the accepted models for the growth of thin films, including thermodynamic and atomistic models of nucleation. Due to the detailed and wide ranging nature of the theories of nucleation and growth, a complete review is not possible within these pages. The focus within this chapter is therefore placed on topics that relate directly to the growth of CdTe thin films and assist in subsequent explanation of the experimental results presented in Chapters 7 and 8. For a wider description of growth and nucleation phenomena, the reader is referred to the numerous book length reviews on the subject[1-9].

4.2 Thin film growth modes

The three well known and distinct modes of thin film crystal growth are shown in fig.4.1. The mode by which a given material will grow is dependent on the difference in chemical potentials between film-film and film-substrate atomic interactions. Each growth mode will now be discussed in turn.

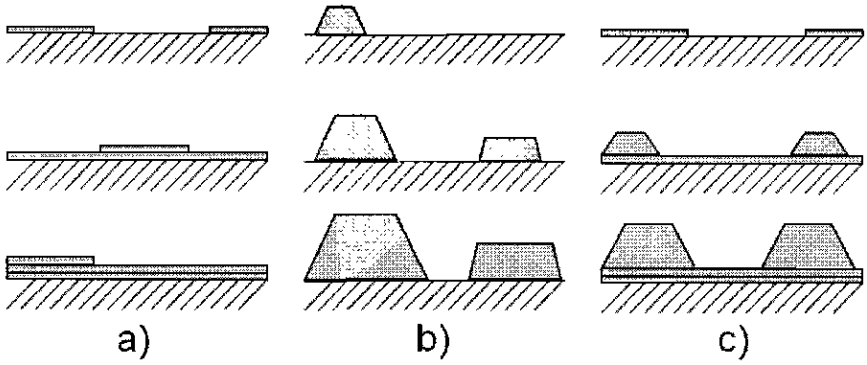

Figure 4.1: Three thin film crystal growth modes a) Frank-van der Merwe or 'layer-by-layer' mode, b) Volmer-Weber or 'island' mode and c) Stranski-Krastanov or 'layer-plus-island' mode.

4.2.1 Frank-van der Merwe growth

'Layer-by-layer' or Frank- van der Merwe growth (fig.4.1a) occurs when the binding energy between an atom and the surface is greater than that between individual atoms within a layer. In this case nucleation is two dimensional, leading to the formation of planar sheets. After formation of a complete monolayer, a second less tightly bound monolayer forms on top. The 'layer-by-layer' growth mode will be sustained providing the decrease in binding energy with thickness is continuous and approaches toward the bulk crystal value of the deposited material.

4.2.2 Volmer-Weber growth

In the 'island' or Volmer-Weber growth mode (fig.4.1b), the binding energy between adatoms is stronger than their binding to the surface. In this case three dimensional clusters nucleate on the surface and grow to form island structures. A wide range of thin film systems display this growth mode including CdTe/GaAs[10], NiTi/Silicon nitride[11] and Cu/Si[12]. The Volmer-Weber mechanism is assumed to be the principal growth mode of most polycrystalline thin films.

4.2.3 Stranski-Krastanov growth

An intermediate case between the 'layer-by-layer' and 'island' growth modes is the Stranski-Krastanov mode (fig.4.1c). After an initial number of monolayers have formed the monotonic decrease in binding energy (a requirement for 'layer-by-layer' growth to be sustained) is interrupted. Island growth then takes place on top of the monolayers leading to the 'layer-plus-island' structure. The onset of Stranski-

Krastanov growth is usually ascribed to the accumulation of strain in the growing film due to film-substrate lattice mismatch. Energy deposited at the surface when this strain is released triggers the island formation. This growth mode has been observed in numerous systems including metal-metal[13] and metal-semiconductor[14] layers and has been exploited in growing quantum dot structures[15].

A considerable part of this thesis (Chapters 7 and 8) is concerned with the details of the early stages of growth of CdTe on both polycrystalline transparent conductors, and CdS by close-space sublimation (CSS). There it is demonstrated that growth proceeds by the 'island' mechanism, incidentally confirming the findings of other authors (e.g. Belgaev *et al*[16]). Accordingly the overview and detailed descriptions of film formation that now follow (Sections 4.3 - 4.5) are centred on the Volmer-Weber mechanism of nucleation and the processes that follow it in order to form a complete film.

4.3 Film formation processes

Here a brief overview is presented to provide a context for the detailed descriptions of nucleation and film formation processes that follow in Sections 4.4 and 4.5.

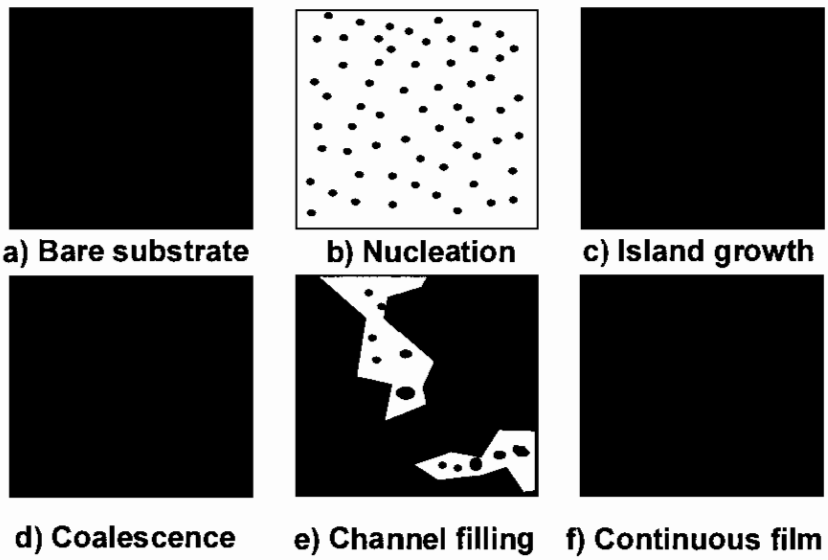

Figure 4.2: Growth processes of thin films by the Volmer-Weber mechanism.

Polycrystalline thin film growth via the 'island' (Volmer-Weber) mechanism may be divided into three stages, i) nucleation, ii) early and iii) late stages of growth that

collectively lead to the formation of a complete film[17]. Fig.4.2 illustrates a typical sequence of distinct stages that occur during polycrystalline thin film growth from the vapour[18], which proceeds as follows: Firstly, an initial set of nuclei is formed on the surface by deposition from the vapour (fig.4.2b, Section 4.4). Those nuclei that are stable (to re-evaporation) continue to grow by addition of material from the vapour and by the surface diffusion of adatoms. The islands become enlarged, but the distribution remains unchanged as no further nucleation occurs at this stage (fig.4.2c, Section 4.5.1). As these islands continue to grow they come into contact with one-another and coalescence processes begin to occur (fig.4.2d, Section 4.5.3). During this period further nucleation is assumed not to occur, since established islands capture, and incorporate, the majority of adatoms incident upon the surface. When islands reach a certain size they no longer completely coalesce and re-order, due to the slow rate at which the process occurs for larger islands. A network of interconnected islands, with empty channels in-between, is then formed (fig.4.2e, Section 4.5.4). Secondary nucleation now becomes possible in the channels, as areas that were previously occupied by islands (or their associated capture zones, Section 4.5.1) has been revealed due to the reduction in coverage resulting from coalescence of primary islands. Following this, a continuous thin film with no gaps will eventually be formed by coalescence of secondary nuclei, and their incorporation into the channel walls (fig.4.2f).

The above sequence of processes, and driving forces for them, are described in detail in Sections 4.4 and 4.5. Firstly (Section 4.4), the formation of stable nuclei will be described with reference to thermodynamic and atomistic models. Secondly (Section 4.5), the growth and coalescence of stable islands and the formation of a complete film will be described.

4.4 Nucleation of thin films

The formation of three dimensional nuclei on a surface is considered the starting point of Volmer-Weber thin film growth, the nuclei being small clusters of material condensed on the surface. The relative size and distribution of nuclei formed at this early stage will be influenced by factors such as the surface temperature and the deposition rate. This section outlines the thermodynamic and atomistic principles related to the formation of nuclei.

4.4.1 Condensation and the driving force for nucleation

In the case of CSS, nucleation takes place via a vapour – solid phase transition. The thermodynamic driving force behind this, and the subsequent occurrence of nucleation, is the change in the Gibbs free energy of the system ΔG (see for example Ekertova[2]), during this phase transition;

$$\Delta G = G_{Final} - G_{Initial} \qquad (4.1)$$

where G_{Final} and $G_{Initial}$ are the Gibbs free energies of the system in its final and initial states respectively. Nucleation occurs when $\Delta G<0$, i.e. when the free energy of the system is reduced by condensation from the vapour into the solid phase. A positive value for the change in free energy will mean nucleation is unfavourable and will therefore not occur under such conditions.

The capillarity, or droplet model of nucleation assumes that nuclei take the form of a spherical cap[19] (shown in fig.4.4) and whilst solidified nuclei may often have crystallographic forms, the spherical cap model provides a reasonable approximation with convenient geometries. If a droplet, of radius r, forms on the surface after condensing from the vapour phase, the associated change in Gibbs free energy is given by;

$$\Delta G = a_1 r^2 \gamma_{VC} + a_2 r^2 \gamma_{SC} - a_2 r^2 \gamma_{SV} + a_3 r^3 \Delta G_V \qquad (4.2)$$

where a_i terms are geometrical constants. $a_1 r^2$ is the surface area of the condensate in contact with the vapour and γ_{VC} is the free energy for the formation of the surface between the vapour and condensate. $a_2 r^2$ is the contact area between the condensate and substrate with γ_{SC} the free energy of the surface between the substrate and the condensate. The term $a_2 r^2 \gamma_{SV}$ accounts for the reduction in substrate area in contact with the vapour as a result of the condensate forming where γ_{SV} is the associated surface-vapour free energy term. $a_3 r^3$ is the volume of the condensate and ΔG_V is the change in free energy of condensation defined as;

$$\Delta G_V = -\frac{kT}{V} \ln \frac{p}{p_e} \qquad (4.3)$$

where k is Boltzmann's constant, V is the volume of an adatom of deposited material, T is the temperature, p is the vapour pressure and p_e is the equilibrium vapour pressure. The term (p/p_e) is known as the supersaturation ratio, S. In order for nucleation to occur ΔG_V must be <0. The supersaturation ratio must therefore be >1 with the vapour pressure greater than the equilibrium pressure and 'saturated' in order for nucleation to occur.

Equation 4.2 may be simplified if it is assumed that the aggregate has a spherical shape. In this case the equation 4.2 becomes:

$$\Delta G = 4\pi r^2 \gamma_{VC} + \tfrac{4}{3}\pi r^3 \Delta G_V \qquad (4.4)$$

The free energy of nucleation is plotted as a function of radius in fig. 4.3. It may be seen that there is a maximum value for the change in free energy at a particular radius, know as the critical radius, r^*.

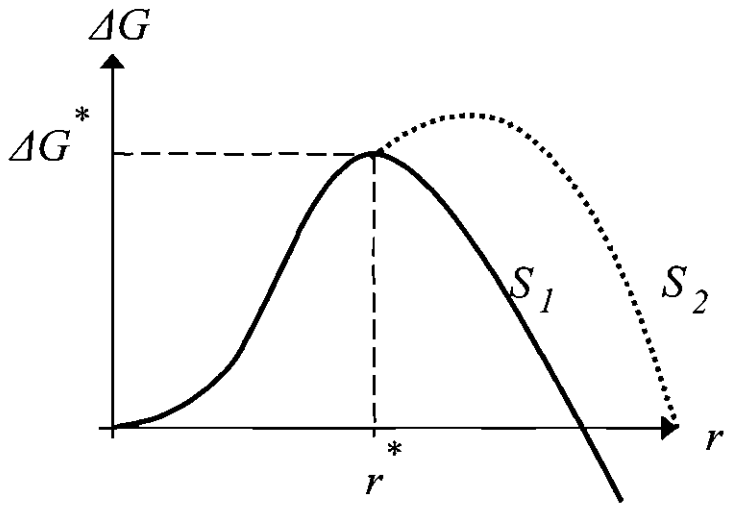

Figure 4.3: Free energy for formation of a nucleus as a function of radius r for different supersaturation values ($S_1 > S_2$).

This critical radius is the lower limit of size that a nucleus must attain to be stable. Small aggregates of a size $< r^*$ will experience an increase in their free energy as they grow. This means that as further material adds to the nucleus it remains susceptible to evaporation. For nuclei of radius $> r^*$ the free energy will decrease with growth and hence these nuclei may be considered as stable clusters. The value of r^* will be the value at which:

$$\frac{\partial(\Delta G)}{\partial r} = 0 \qquad (4.5)$$

Differentiating equation 4.4 and using the above condition gives:

$$\frac{\partial \Delta G}{dr} = 4\pi r^2 \Delta G_V + 8\pi r \gamma_{VC} = 0 \qquad (4.6)$$

Re-arranging equation 4.6 for r and substituting in equation 4.3 gives:

$$r^* = \frac{2\gamma_{VC} V}{kT \ln\left(\frac{p}{p_e}\right)} \qquad (4.7)$$

It may be seen from equation 4.7 that the critical radius is principally dependent upon the temperature and supersaturation ratio, as all other terms are constant for a given material. At constant temperature an increase in the supersaturation ratio (which will increase the deposition rate of material onto the surface) will reduce the size of the critical nucleus. The temperature dependence of r^* is not as simple to discern. From equation 4.7 it may at first appear that if temperature is increased that the value of r^* will decrease. However, the equilibrium vapour pressure, p_e, is dependent upon temperature and as a consequence the supersaturation ratio is also temperature dependent. The equilibrium vapour pressure of a liquid may be related to temperature via the Clausius-Clapeyron relation (see for example Sears *et al*[20]);

$$p_e = A \exp\left(\frac{-\Delta H_{vap}}{RT}\right) \qquad (4.8)$$

where ΔH_{vap} is the change in molar enthalpy for vaporisation, R is the universal gas constant and A is a constant. Equation 4.8 shows that the equilibrium vapour pressure increases exponentially with temperature, leading to an exponential decrease in the supersaturation ratio. The term, $\ln(p/p_e)$, in equation 4.7 therefore decreases at a greater rate than the associated increase in T and increasing the temperature therefore increases the size of the critical radius.

In the case of polycrystalline thin films, the grain structure in the completed film will be determined in part by the initial distribution of nuclei formed on the surface. Under conditions where each nucleus develops to form a single grain, achieving control of the nucleation density may be expected to give direct control of the grain

size. In conditions where the nucleation density is not constant throughout growth, the initial density will still play an important role in determining grain structure as it provides an initial template for growth. The concepts introduced in this section, the critical radius and its dependence on factors such as temperature and supersaturation ratio, may in part determine the nucleation density. In conditions that define a relatively large critical radius (e.g. high temperature), the probability of a stable nucleus forming is small and as a result the density of nuclei on the surface will be low. As the size of the critical radius is reduced, the formation of stable nuclei becomes increasingly likely and the nucleation density will thus be increased. Therefore, it is possible that control of grain size in the completed film may be achieved by manipulation of the critical radius. This concept is explored further in Chapters 7 and 8.

While the background for the above argument is presented for the case of homogenous nucleation in the vapour phase, analogous outcomes are expected for heterogeneous nucleation (see for example Venables[9]).

4.4.2 Contact wetting angle

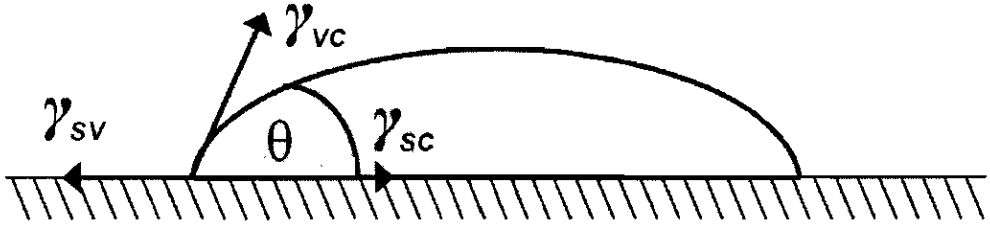

Figure 4.4: Equilibrium surface forces and contact wetting angle for a spherical cap.

In the previous section, the capillarity theory of nucleation was introduced, where nuclei take the form of a spherical cap. Nuclei will make a given angle with the surface, dependent on upon the surface forces acting upon it as illustrated in fig.4.4. This is known as the contact or wetting angle θ. In the instance of strong attraction between atoms of the deposited material, the contact angle will be high as atoms will bunch together and from 3-D nuclei. In the case of strong film-substrate attraction, the deposit will instead spread across the surface with a small contact angle. In the previous Section (4.4.1), γ_{VC}, γ_{SC}, and γ_{SV} were defined as the surface free energies between the surface, condensate and vapour for the purpose of free energy

calculations. These terms may also be considered as the respective interfacial tensions between the surface, condensate and vapour. These tensions determine the contact wetting angle by the relation:

$$Cos\theta = \frac{\gamma_{SV} - \gamma_{SC}}{\gamma_{VC}} \qquad (4.9)$$

In the case of 'layer-by-layer' growth the contact wetting angle is assumed to be zero and the nucleus will be a flattened disk. Here the deposit 'wets' the surface and the surface-vapour tension is balanced by the surface-condensate and vapour-condensate tensions as follows:

$$\gamma_{SV} = \gamma_{SC} + \gamma_{VC} \qquad (4.10)$$

For island growth the wetting angle will be finite ($\theta > 0$) and the surface-vapour tension will be less than the combination of the surface-condensate and vapour-condensate tensions:

$$\gamma_{SV} < \gamma_{SC} + \gamma_{VC} \qquad (4.11)$$

In Stranski-Krastanov growth the value of θ changes during growth. After initially being zero, with growth progressing by 'layer-by-layer', the angle will become finite after deposition of a number of monolayers. Island growth will then begin on top of a continuous layer.

4.4.3 Atomistic surface processes

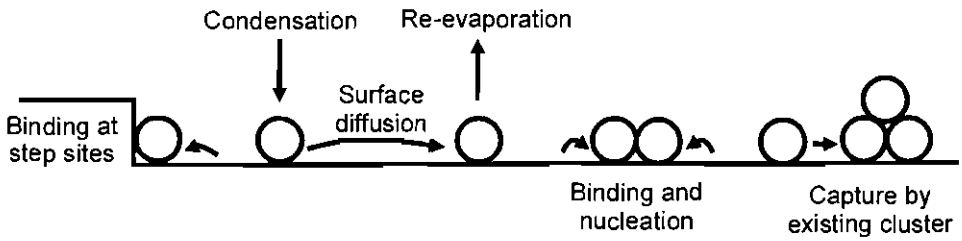

Figure 4.5: Surface processes in thin film formation.

In order to better understand the mechanics of thin film growth the various processes encountered by species on the surface are considered from an atomistic standpoint, as illustrated in fig.4.5 (the equations used in this section may be found in, for example, Ekertova[2]). When atoms or molecules condense onto the surface from the vapour phase they are termed adatoms, this being synonymous with 'adsorbed

monomers' or 'surface species'. Once on the surface, adatoms are assumed to migrate across it by surface diffusion. Following this an adatom may bind with other adatoms on the surface, bind at a kink or step site, undergo capture and be incorporated by an existing nucleus, or simply re-evaporate from the surface. The rate and frequency with which these interactions occur will be dependent not only upon the nature of the surface and deposited material, but also by the conditions under which material is deposited.

Nucleation from an atomistic viewpoint may be treated as a series of collisions, migrations and binding events between adatoms on the surface. From thermodynamic theory (Section 4.4.1) it is known that clusters need to attain the critical radius before being stable and no longer prone to re-evaporation. The formation of a stable nucleus will therefore require a certain number of adatom-adatom collisions to occur, with a larger critical radius increasing the number of collisions required. For example, higher substrate temperature will increase the size of the critical radius and will thus increase the number of adatom collisions required to form a stable nucleus. As the number of required adatom collisions increases the probability of a stable nucleus being formed is thereby reduced. However, once a nucleus of a super-critical size is achieved it is assumed to remain on the surface and will continue to grow into an island structure, principally by capture of further adatoms diffusing across the surface.

An important parameter to be considered during nucleation is the number of adatoms on the surface at a given time, $n_1(t)$[21]. For a surface assumed to have a fixed number, n_0, of sites available, this leads to a surface occupancy of (n_1/n_0)[22]. The probability of surface collisions occurring, hence leading to successful nucleation, will be increased by a greater number of species being present on the surface at any given time. Therefore by controlling the arrival and re-evaporation rates of adatoms on the surface, the nucleation dynamics of the growing film may be controlled. Lower adatom surface concentrations will reduce the number of nuclei formed, due to the decreased probability of collisions occurring. Nuclei formed at low surface concentrations may therefore be expected grow to larger island sizes than those formed at high concentrations, due to a greater fraction of adatoms resident on the surface being collected by each island. Assuming the number of surface sites available is constant for a given surface, the surface occupancy is determined by the population of adatoms on the surface. The value of n_1 will depend on the rate adatoms impinge onto the surface, and how long they remain adsorbed before re-evaporating

from it, or being incorporated into a cluster. If adatoms arrive at the surface at a constant rate, R, and leave the surface via re-evaporation at a given rate, we may therefore ascribe an average lifetime for an adatom on the surface, τ_s, during which time the adatom will diffuse across the surface and either collide with another monomer or re-evaporate. The number of adatoms on the surface may be related to the arrival rate and the average monomer lifetime by:

$$n_1 = R\tau_S \quad (4.12)$$

From equation 4.12 it can be seen that a lower arrival rate or shorter lifetime will reduce the species surface concentration. Conditions resulting in lowering either of these parameters may therefore be expected to lower the nucleation density while higher values will increase the probability of the formation of stable nuclei. The rate of arrival of adatoms onto a surface may be altered by numerous factors that are normally specific to the deposition system being employed (e.g. factors affecting the rate of species arrival in electro-deposition will not be applicable to vacuum evaporation). In the case of CSS (Section 5.1) the arrival rate may be affected by source-substrate geometry, source temperature and inert gas pressure in the reactor[23]. The impact of these on the growth of CdTe and CdS layers will be discussed in Chapters 7 and 8.

The average adatom lifetime for a given materials system is determined principally by the temperature of the substrate. While the manner of deposition may still change the adatom lifetime, substrate temperature is important in most growth systems and the impact of changing the adatom lifetime on growth is therefore more generally applicable. The average lifetime of an adatom on the surface before re-evaporation, τ_s, is given by[22]:

$$\tau_S = \frac{1}{\nu}\exp\left(\frac{E_a}{kT_{sub}}\right) \quad (4.13)$$

Where T_{sub} is the temperature of the substrate, E_a is the energy required for re-evaporation from the surface and ν is the vibrational frequency of an adatom on the surface. Variation of τ_s will also affect the diffusion of adatoms on the surface as adatoms that remain on the surface for a longer time will be able to diffuse a greater distance. However at higher substrate temperatures adatoms will have higher mobility

on the surface. The mean diffusion distance of an adatom, X, can be related to the lifetime via[2];

$$X = \sqrt{2D_S\tau_S} \qquad (4.14)$$

Where;

$$D_S = (1/2)a_0^2 \nu \exp\left(-\frac{E_d}{kT_{sub}}\right) \qquad (4.15)$$

D_S is the surface diffusion coefficient, a_0 is a constant, E_d is the activation energy for diffusion and therefore:

$$X = a_0 \exp\left(\frac{E_a - E_d}{2kT_{sub}}\right) \qquad (4.16)$$

As E_a, E_d and ν are properties of the surface and the deposited material it can be seen from equations 4.13 and 4.16 that the principal experimental control over the lifetime and diffusion of adatoms, for a given material system, comes from variation of the substrate temperature. Increasing the substrate temperature will decrease the average lifetime of an adatom on the substrate and decrease the surface occupancy (n_1/n_0). In this instance nucleation becomes less likely due to the reduction in probability of adatom collisions and the density of nuclei formed will be reduced.

On a perfect surface, nucleation will only occur due to adatom collisions. However, on a real surface nucleation may also occur at a kink or step sites on the surface (fig.4.5). These are defects in the surface and offer preferred binding sites since they provide a higher number of nearest neighbour bonds to an adatom than on a planar surface: an atom absorbed onto a flat surface will have a single neighbouring atom, whereas an adatom absorbed at a step site will have two. By this logic the absorption energy at the step site will be twice that of the planar surface, making binding far more probable at these locations. Under conditions where nucleation due to monomer collisions is unlikely, nucleation at step and kink sites becomes an important process and may be key in defining the structure (and growth rate) of the completed films.

4.5 Post-nucleation growth phase

This section describes in detail the individual processes of film development that follow nucleation according to the scheme outlined in Section 4.3. Other alternatives

are possible, but for the CdTe material system explored in this thesis, film growth by the island mechanism is the most relevant. The description is ordered according to the development of the film. First the growth of nuclei to form islands is discussed (Section 4.5.1), including the addition processes that take place on crystalline facets (Section 4.5.2). Next, the coalescence of islands is described, this taking place by a variety of possible mechanisms including Ostwald ripening, by the motion of islands and by a simple growth mechanism. Finally, the processes by which a film comprising of islands is developed into a film with complete surface coverage are described. At this point (Section 4.5.4) the conditions required for channel formation and secondary nucleation are considered.

4.5.1 Island growth and capture zone

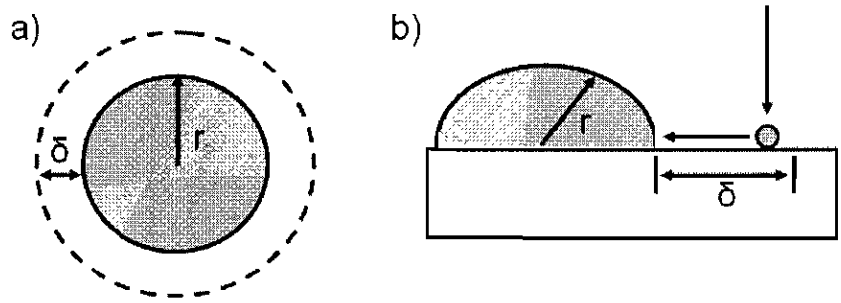

Figure 4.6: Island radius and adatom capture zone of width δ, a) plan view and b) side view

After nucleation, islands will increase in size by further addition of adatom species. This may occur by two means, i) by adatoms impinging directly onto islands from the vapour phase and ii) by surface diffusion of adsorbed species. In the case of total substrate coverage, growth must take place solely by direct impingement but, in the instance of small island size and low coverage, surface diffusion is likely to be the dominant process. Any adatom incident within a certain distance (δ) of an existing island is assumed to diffuse toward the island and be captured by it[2,24-26], the capture zone width, being illustrated in fig.4.6. The size of the capture zone is of the order of the average adatom diffusion distance, and will hence also depend on the surface diffusion and adatom lifetime via the relation[18];

$$\delta \approx \sqrt{D_S \tau_S} \qquad (4.17)$$

The capture zone width is therefore related to the mean adatom diffusion distance X (equation 4.14), by $\delta \approx \sqrt{2}X$ .The rate at which islands grow will be dependent on the

surface diffusion coefficient[2], as well as the impingent rate of new monomers onto the surface. As any adatom within this region is assumed to be captured, the region can also be considered as a nucleation exclusion zone (since the local surface occupancy is reduced, the probability of collisions generating nuclei $r > r^*$ is reduced). As island growth progresses, the surface area covered by islands and their associated exclusion zones will increase, reducing the probability of new nucleation. After a certain amount of growth no subsequent nucleation becomes possible, as all adatoms incident on the surface will be incorporated into existing islands. Nucleation then ceases and a secondary bout of nucleation may only occur at a later stage of growth after the dynamics of the island distribution have been altered by coalescence effects (Section 4.5.3).

4.5.2 Step flow processes and facet formation

Polycrystalline thin films often exhibit visible grain structure with smooth crystal facets being apparent[27]. Formation of these facets is indicative of uninterrupted step flow within the growing film. This section provides a brief explanation of the step flow process.

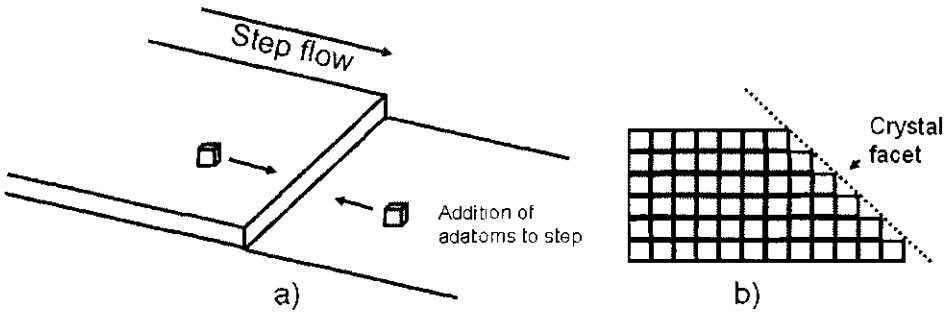

Figure 4.7: a) Addition, diffusion and binding of adatoms to a step producing the phenomenon of step flow, b) Formation of a smooth crystal facet by uninterrupted step flow.

At an atomic level a smooth surface is not truly flat but will rather take the form of an ordered series of terraces, as shown in fig.4.7b, giving the illusion of a smooth surface. In order for flat facets to be produced it is essential these steps form without inhibition. Fig.4.7a shows the addition of surface species to a terrace and binding at a step. By continued addition to this step, the step may be considered to propagate along the surface, a process known as 'step flow'.

Disruption of the step flow process will lead to rounding of the grains (or islands). Rounded grains are typically formed due to low mobility of surface species, usually

resulting from low deposition temperatures. However, polycrystalline films can also develop rounded grains as a result of the co-deposition of impurity species, especially oxygen on account of its reactivity. Impurities may gather at the steps disrupting the step flow, and consequently the formation of singular crystal facets is inhibited. A brief review of deposition of Al by evaporation in the presence of oxygen is given in Section 4.6, followed by a review of the influence of oxygen in vapour deposition of CdTe. The role of gas ambient (including oxygen) on CdTe and CdS growth constitutes a major part of this thesis and is described in Chapters 7 and 8.

Although the above description is presented as part of a narrative of nucleation events, it is the case that surface processes on the film material itself shall be important at all stages of thin film formation and not exclusively during nucleation.

4.5.3 Coalescence of growth islands

Coalescence is the processes by which two previously separate islands merge together, thus reducing the total surface area of islands and their coverage of the substrate. Coalescence may be divided into two forms: i) incomplete, where a grain boundary remains incorporated, or ii) complete, liquid-like coalescence where the merged islands re-order to form a single island. In the latter the two islands may behave as two liquid droplets merging together to form a single droplet before re-crystallising as a single island. While this seems strange behaviour for solid islands on a surface it has been demonstrated by various groups using in-situ techniques[6,21,24,28-30] and explained in terms of sintering and neck formation by Pashley et al[31]. The occurrence of liquid-like behaviour depends explicitly on the size of islands: there is a critical size for a given set of conditions, below which they may behave in a liquid-like manner. Above this size however, they will remain solid during coalescence and complete coalescence will not occur unless by another mechanism. This was demonstrated in work by Barna and Pocaza discussed in Section 4.6.1.

This section shall concentrate on the various modes by which coalescence may occur such as Ostwald ripening[32], coalescence by cluster mobility[33] and coalescence by growth[30].

a) Ostwald ripening

In Ostwald ripening larger islands are assumed to grow at the expense of nearby smaller islands, as they are favoured energetically and are more stable due to their

larger surface area. In the case of close-space sublimation or vacuum evaporation, Ostwald ripening occurs due to the difference in the vapour pressures of large and small islands, with smaller islands having a higher vapour pressure. The smaller islands are therefore more likely to dissolve and be absorbed by the larger islands than to continue to grow. However, in thin film growth Ostwald ripening is more important during post growth annealing rather than deposition[2] as it is a slow process in comparison to the typically rapid deposition of thin films.

b) Coalescence due to island motion

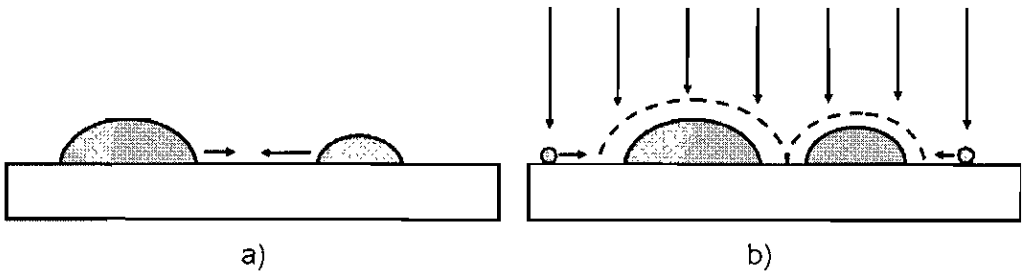

Figure 4.8: Coalescence mechanisms: a) coalescence by island motion, b) coalescence by growth.

Islands formed on a surface are not necessarily static, and due to high substrate temperatures clusters may be mobile. Their level of mobility will depend principally on the island size, with smaller islands being more mobile. Coalescence may occur by islands meeting due to migration across the surface as shown in fig.4.8a. This was first demonstrated by Skofronick and Philips[34] and by Phillips *et al*[35] by fitting the model for island mobility to observations made form SEM images of vacuum deposited gold films. More recent work by Anton directly showed the motion of palladium crystals[24] and gold particles[33] deposited on graphite using an in-situ heating stage in a TEM system with video imaging. Small crystallites were seen to move across the surface before colliding with other particles and engaging in liquid-like coalescence. Anton also showed that the process was not limited to small aggregates of a few atoms in size but that larger islands with distinct crystal facets were also mobile on the surface. This is however unlikely to be the dominant mode of coalescence in thin film formation, due to the relatively slow nature of the process compared with the time required to form a complete film.

c) Coalescence by growth

Assumed to be the dominant coalescence process in thin film formation[2], coalescence by growth (fig.4.8b) occurs when islands come into contact with one another as they increase in size. Islands may initially be well spaced due to capture zones surrounding the islands (Section 4.5.1), but as the growth progresses the islands will increase in size, the capture zones will overlap and the islands will eventually touch. Islands may then coalesce rapidly in an apparently liquid-like manner to form a single island as shown in fig.4.9.

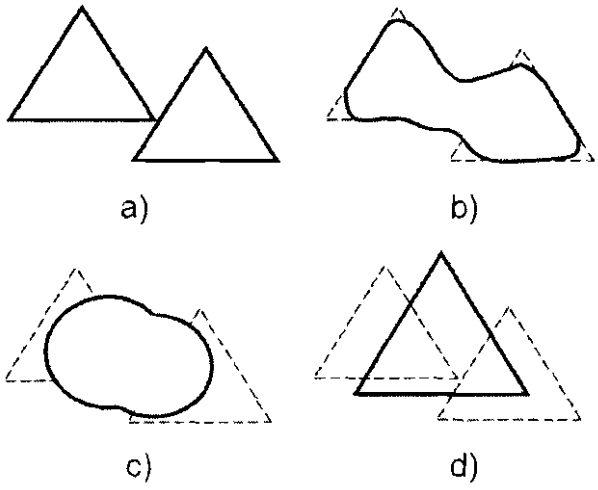

Figure 4.9: Liquid-like coalescence of islands, a) islands touch, b) neck formation, c) loss of orientation and d) re-crystallisation.

The principal driving force behind coalescence is the lowering of the surface energy by a reduction in the combined surface area of the constituent islands. If two islands with distinct orientations grow until they come into close proximity (fig.4.9a) a neck begins to form in the region between the two islands[31] (fig.4.9b).This neck formation process can be attributed to rapid surface self diffusion of material from the islands. The surface energy of the composite is quickly reduced during the initial stages of coalescence by rounding of the edges of the islands. Material from regions furthest from the neck is transferred to the neck, causing it to thicken at the join between the two islands. The islands may eventually lose their crystal habit planes as a result of this process (fig.4.9c). Finally, the surface energy is then minimised by reformation of a crystallographically shaped island from the composite (fig.4.9d). It is generally accepted that if islands of two different orientations coalesce, then the

resulting crystallographic orientation will be that of the larger of the two islands[2]. Coalescence in this manner reduces the density of islands on the surface.

The rate at which islands coalesce in this manner will be dependent on the size of islands, with smaller islands coalescing much more rapidly than larger ones - due to the faster rate of neck formation[6]. Eventually the rate of coalescence will become so slow for large islands so as to not fully complete before further addition of adatoms causes a significant increase in the size of the coalescing islands. Coalescence remains incomplete and leads to the process of channel formation (Section 4.5.4.1).

4.5.4 Formation of a complete film

A complete film is often not comprised solely of islands formed at the beginning of film deposition. Primary islands may coalesce and leave vacant channels, with the gaps being filled by secondary nucleation to produce a continuous film. The process of channel formation resulting from incomplete coalescence of primary islands and their subsequent filling by secondary nuclei will be discussed in this section.

4.5.4.1 Channel formation

Complete island coalescence will often not continue indefinitely up to the formation of a complete film, but will instead reach a limit as the composite islands reach a certain size. As island size increases, complete coalescence becomes improbable due to the relatively slow rate of the process at these sizes. Pashley *et al*[31] estimated the time required for neck formation between two spherical islands of various sizes. It was shown that the required time to produce a neck between two islands was proportional to the fourth power of the initial radius of the coalescing islands. Therefore for large island sizes the rate of addition to the composite island from species on the surface may be greater than the rate of material transfer between the coalescing islands[18]. The island's size therefore increase at a greater rate than coalescence progresses and the time required for coalescence increases as the process continues. Neck formation will not complete and the islands will take on an elongated shape leading to the definition of channels between the islands (fig.4.2e). The size at which islands will begin to behave in this manner is linked to the diffusion rate of species on the surface[6] and hence the substrate temperature. In the instance of high surface diffusion rates (high substrate temperature), complete coalescence will occur for relatively large island sizes as the rate of material transfer between islands is high.

An increased substrate temperature therefore also increases the rate at which coalescence progresses, due to this increase in the surface diffusion rate. Like the majority of surface processes involved in thin film formation, the occurrence of channel formation is dependent on the deposition conditions for film growth. In conditions where the rate of coalescence is low, channel formation may be expected to occur for significantly smaller island sizes than in other regimes where coalescence occurs at a more rapid rate.

4.5.4.2 Secondary nucleation and complete film formation

The channel formation stage leaves gaps in the material that are filled by secondary nucleation. This will eventually lead to the formation a continuous film[31]. The coalescence of islands reduces the combined surface area of the constituent islands and serves to reduce the overall coverage of the surface. During coalescence an area of the substrate previously occupied by islands (and their capture zones) will be revealed. This area therefore becomes available for nucleation and secondary nucleation of islands may occur in the channels formed by the coalescence of primary islands. Because these new islands are small, in comparison to the initial islands, they rapidly coalesce by the mechanism described above. They are then incorporated into the bulk of the material as they grow and come into contact with the sides of the channels. As growth continues the majority of channels are eliminated, leaving only a few small irregularly shaped holes[3]. Subsequent nucleation will then fill these holes and the resulting islands will become incorporated into the bulk .This leads to the formation of a continuous, hole free, film.

Although the proceeding is an account of secondary nucleation events encountered during channel filling, it is likely that secondary nucleation occurs throughout growth as a result of coalescence events. However, it is only at this stage that nuclei grow to super-critical sizes and are as such stable.

4.6 Selective review of thin film growth literature

The nucleation and the early growth phenomena of thin films have been studied in a wide range of materials systems. The vast nature of the associated literature makes a complete review impossible within these pages. As a result, this section will focus on work of particular relevance to the results presented within this thesis (Chapters 7 and 8) and is divided into two parts. Firstly, work on the effect of oxygen on the growth

and coalescence of aluminium and indium vacuum evaporated films is discussed. Secondly, reported work on CdTe thin film growth phenomena, for CdTe layers grown for solar cell devices and from the wider literature of epitaxial CdTe growth, is discussed. Numerous reviews have been published that provide a broader overview of the nucleation and thin film growth literature, and the reader is referred to these for further general information[22,36-40].

4.6.1 Thin film growth experiments – the role of oxygen

Oxygen is of particular importance to CSS-deposited CdTe solar cells. Many groups employ oxygen throughout the growth process as it is believed to be beneficial to device performance. However, the specific role oxygen plays in the early growth of CdTe films has not been examined thoroughly. Work on other material systems provides significant insight into the effect oxygen may have on grain development. Numerous papers have been published by a group at the Research Institute for Technical Physics of the Hungarian Academy of Sciences on this subject, as well as on the growth processes of thin films, particularly coalescence processes. Work was done principally on two different materials systems: i) indium and ii) aluminium deposited on amorphous carbon films. In both cases material was deposited under high purity conditions, and in the presence of various concentrations of oxygen. Films were monitored throughout growth via in-situ electron microscopy allowing clear recording of the growth processes occurring at different stages during growth. From these results, conclusions were drawn that were applicable to many thin film systems. Of particular interest is the insight gained into the role of oxygen in thin film deposition and the impact of islands size and the phase of islands (liquid or solid) at the point of coalescence.

From in-situ electron microscopy observations of growing indium films Pocaza *et al*[29,30] introduced the idea of a critical size for crystallisation of an island, d_{crit}. Islands were found to form on the surface by condensing as liquid droplets, these being identified as liquid by their rounded morphologies. As the size of droplets increased (by addition of adatoms or coalescence) they were found to change character at sizes above d_{crit} whereupon they assumed crystalline facets, and they were therefore presumed to be solid. This lead to a distribution of islands on the surface having two distinct phases termed liquid (L) and crystallite (C). The distribution of phases meant that three types of coalescence interactions were possible between two given islands:

L+L, L+C and C+C. It was inferred that the size and phases of coalescing islands would therefore determine whether coalescence of any two given islands went to completion or remained incomplete i.e. incorporating a grain boundary. In the case of L+L coalescence, the process was deemed to always complete, resulting in a single liquid island (L+L→L). Depending upon the size of the resulting island it would either remain in the liquid phase if the composite was smaller then d_{crit} or crystallise if larger than d_{crit}. In the L+C case, coalescence was also determined to complete via formation of a single liquid phase island which would subsequently crystallise, as the composite island was invariably larger than d_{crit}. For two crystallites coalescing (C+C), the size of the islands was found to determine whether coalescence completed. For islands below a certain size enough energy was released during coalescence due to size contraction so as to effect a temporary 'melting' of the crystallites. Coalescence in this instance may proceed in two ways. The first is as C+C→(L) →C, where (L) is the hypothetical liquid phase. This liquid phase was termed hypothetical by Pocaza due to the fact work by Pashley *et al*[31] showed by in-situ transmission electron microscopy (TEM) measurements that coalescing crystallites may display liquid character, but in fact remain solid throughout the process. Here coalescence completes and the two crystallites re-order to form a single crystallite with distinct facets and no incorporated grain boundary. For crystallites where the energy released during coalescence is not sufficient to melt the crystallites, coalescence proceeds in the second way i.e. C+C→C. In this case coalescence is incomplete and although they join, the crystallites do not re-order and a grain boundary remains incorporated in the composite crystallite. This observation for the failure of large crystallites to completely coalesce is the basis for the formation of channels in growing films, as described in section 4.5.4.1.

The value of d_{crit} was shown to increase with increased substrate temperature but was also found to be sensitive to the amount of oxygen present during growth. In-situ TEM work on indium films by Pocaza *et al*[29,30] determined that the addition of oxygen during growth reduced the size below which islands demonstrated liquid-like character, effectively increasing the melting temperature of crystallites. This meant that for samples grown in the presence of oxygen, complete coalescence was less likely than in a high purity ambient at the same temperature. The inclusion of oxygen was also found to alter the appearance of the grains, - they were found to be significantly smaller, due to the reduction in complete coalescence, and showed no

crystal faceting. The loss of faceting was explained by Barna[21,41] using the step flow model (Section 4.5.2) in which oxygen is considered as a co-deposited impurity species that interrupts step flow. In Barna's interpretation oxygen binds strongly to the step sites, hence disrupting the step flow of adatoms. This interrupts the formation of singular crystal habit planes and leads to the formation of an oxide phase coating the surface. It is this oxide phase that accounts for the increase in melting temperature of crystallites, since oxides typically having higher melting points than those of pure materials. Work by Barna *et al*[42-44] on aluminium deposits produced similar results to those reported by Pocaza but also determined an orientation dependence of the effect of impurities. Adsorbed oxygen was found to reside on the surface of (111) oriented faces, while on (100) faces oxygen became incorporated into the bulk during growth. As a result of this Barna was able to interpret the effect of surface oxides on coalescence of the grains. He discerned that crystallites meeting at oxide coated surfaces would not completely coalesce as a result of persistence of the solid phase to higher temperatures impeding liquid-like coalescence. This result showed directly the effect of oxidation as barrier to the coalescence of islands – coincidentally indicating a technological means of promoting the growth of small grains.

4.6.2 Studies of cadmium telluride thin film growth

The majority of fundamental materials work reported for the growth of CdTe has been for epitaxial layers. Work on the microstructure of CdTe thin films for solar cell applications is usually reported in terms of complete device structures, with little consideration being given to the growth processes involved in film formation. Fundamental studies of nucleation and growth rarely appear in solar cell literature, this omission being the motivation for the work presented in Chapter 7.

This section describes the work reported on the growth of CdTe thin films and is split into three parts, firstly (Section 4.6.2.1) some examples of fundamental work reported on epitaxial CdTe are discussed. Secondly (Section 4.6.2.2), the impact of deposition method, temperature and oxygen on the microstructure of polycrystalline CdTe thin films in solar cell devices is reviewed, with specific focus on CdTe layers deposited by close space sublimation. Finally (Section 4.6.2.3), the impact of post-growth annealing on the microstructure of CdTe thin films in solar cell structures is discussed, as significant changes in the grain structure may occur as a result of annealing.

4.6.2.1 Epitaxial growth of CdTe

Mercury cadmium telluride (HgCdTe) is widely used for the fabrication of infrared detectors. Growth is increasingly carried out on CdTe/Si or CdTe/GaAs hybrid substrates, as the lattice constant of CdTe is very close to that of HgCdTe, with one of the initial stages of fabrication being the growth of CdTe layers, of a suitable orientation, on Si or GaAs substrates. As a result the nucleation and growth of hetero-epitaxial CdTe has been studied in some detail. A complete review of the associated literature is therefore not possible here. Instead, work that is particular relevant to results within this thesis (Chapters 7 and 8) is briefly discussed.

Ebe and Nishijima[45] studied the impact of changing the deposition rate on the growth CdTe(111) epilayers on Si(111) substrates, grown by metalorganic chemical vapour phase epitaxy (MOVPE). Previous work by Ebe and Takigawa[46] identified that CdTe(111) epilayers deposited on Si(111) substrates had a rotated alignment, when the II -IV ratio of CdTe was low. Under analysis by X-ray diffraction, layers grown at a II-VI ratio of (1/30) were found to be rotated 30° about the epilayer's [111] axis. This effect was termed as a 'rotation-like' alignment by Ebe and Takigawa and was found to reduce the lattice mismatch between CdTe and silicon from 19.4% to 3.4%, significantly improving the crystallinity of the layers. Ebe and Nishijima[45] then studied the initial nucleation of CdTe layers grown in the same manner, and discerned that two types of nuclei formed, the first having a 30° rotation alignment and the second a twinning-like alignment. The formation of the 'rotation-like' nuclei was again attributed to a decrease in the II-VI ratio of the deposited material. By adjusting the concentrations of the growth precursors they were able to alter the growth rate of the layer and alter the abundance of each type of nuclei. In particular reducing II-IV ratio reduced the number of twinning nuclei and increased the proportion of 'rotation-like' nuclei observed. Using surface interfacial tensions, they were also able to deduce the relative probabilities for the nucleation of each type of nucleus, under a given vapour pressure. They concluded that a reduction in growth rate increased the likelihood of the 'rotation-like' nuclei forming, and thus of a layer having the 'rotation-like' alignment, this being desirable so as to produce layers of improved crytallinity.

Lalev et al[47] grew CdTe(111) layers on Si(111) and CdTe(100) on Si(100) substrates by hot wall epitaxy. They compared the nucleation in these two systems at

an early stage of growth using atomic force microscopy (AFM), and examined how the structure varied with growth time. CdTe(100) was found to nucleate as three dimensional domes. As growth progressed the height and diameter distributions of the domes were found to widen, while the average aspect ratio (height/diameter) of the domes increased. CdTe nuclei having the (111) orientation were found to adopt a more crystalline pyramidal structure, similar to those observed by other groups studying growth of CdTe films on Si(111) surfaces[47-49]. This work demonstrated that nuclei may take different forms depending on their individual orientations and is of particular relevance to results presented in Chapter 7.

4.6.2.2 Growth of CdTe thin films for solar cell applications

CdTe thin films for solar cell applications are deposited on CdS by a variety of techniques. The type of technique employed will principally determine the microstructure of the layer. Lower temperature techniques such as electrodeposition[48] tend to produce grains of sub-micron size. Sputtering[49] and metal organic chemical vapour deposition (MOCVD)[50] produce grains on the order of 1μm, while higher temperature techniques such as CSS produce significantly larger grains, 3μm and above, often with facets[51]. This section summarises work on grain structure of CdTe thin films deposited by CSS.

It is widely found that high substrate temperatures produce larger CdTe grains in CSS growth. This has been demonstrated by various groups[52,53] with large grains generally being accepted to be beneficial for device performance owing to the reduced contribution of grain boundaries. Ferekides *et al*[54] examined the impact of substrate temperature on CdTe grain structure. They deposited CdTe layers of 4-8μm thickness by CSS on chemical bath deposited CdS at substrate temperatures in the range of 500-600°C. For a substrate temperature of 600°C the films were found to have relatively large grains, 3-4μm in diameter, and were very dense with few voids in the material. Grains were found to be significantly smaller for a substrate temperature of 500°C, with grains typically being only 1μm in diameter. Films deposited at the lower temperature also had large amounts of voids which led to shunting in completed devices. X-ray diffraction analysis revealed that the orientation of films also depended on the substrate temperature. Films deposited at 600°C were found to be highly oriented along the (111) plane, whilst at 550°C films were randomly oriented and at 500°C the (200) plane began to dominate. The impact of substrate temperature on the

microstructure of CdTe layers was further expanded upon by Luchitz *et al*[55]. Using a CSS deposition system that incorporated moveable source and substrate heaters, they were able to vary the substrate temperature in the range 250-550°C while maintaining a constant source temperature of 590°C. CdTe layers grown at 255°C on CdS demonstrated columnar growth, with the columns being clustered in regions separated by large cracks. Under examination by high resolution SEM, the columns were found to be hexagonal, were approximately 200nm in diameter, and extended for the entire thickness of the film. At a higher substrate temperature (523°C) growth of grains of a type more commonly reported for CdTe thin films deposited by CSS was observed, with a relatively large size of up to 5μm in diameter.

Other groups have looked at the impact of applying a modified deposition temperature profile on the grain structure of CdTe thin films. In a standard CSS deposition constant source and substrate temperatures are maintained throughout growth. By altering either source or substrate temperatures for different periods of the growth, the microstructure of the film may be altered. Li *et al*[56] used a high temperature nucleation period, followed by a lower temperature for the remaining growth. This allowed nucleation at temperatures up to 645°C, without degrading the CdS and TCO layers and led to an increase in average grain size of CdTe films, as well as well defined crystal faceting. Devices produced using these layers showed significant improvements in V_{oc}, increasing from 0.774V to 0.827V, with an associated increase in device efficiency from 10.4% to 12.0%. A similar temperature profiling technique was used by Okamoto *et al*[57] for CSS deposition of thin film CdTe on CdS. They investigated the effect of ramping the source and substrate temperatures at different rates. By increasing the substrate temperature at a greater rate than the source temperature, they demonstrated that this effectively slowed the deposition rate of material. This produced an improvement in device performance compared to conventional depositions with device efficiency increasing from 13-14% to 15.3%; however no qualification of the impact of this regime on grain structure was made.

The use of oxygen in CSS CdTe deposition has been reported by many groups. It is believed to enhance the *p*-type characteristics of II-VI semiconductors[54] (Section 3.2.4.2) and to have a significant impact on the intermixing between the CdTe and CdS layers[58]. Oxygen has also been shown to affect the grain formation of CdTe thin films. Rose *et al*[59] found inclusion of oxygen in CSS growth of CdTe layers produced films with smaller, less faceted grains. Films were also found to have a reduced

number of pinholes. They attributed these observations to an increase in nucleation density and a subsequent improvement in the level of coverage. Similar results have been reported by other groups[52,54,60,61] who all cite a reduced grain size, improved coverage and reduced faceting as the impact of oxygen on CSS growth. Romeo *et al*[61] provided comparative grain size data for layers grown in both Ar and Ar/O_2 ambients. Grain sizes were found to reduce from 10μm in the Ar ambient, to 2-3μm as a result of oxygen inclusion in the processing ambient.

The effect of oxygen on the growth of CdS and CdTe films, and the subsequent impact on device performance, forms a large part of this work and is discussed further in Chapters 6, 7 and 8.

4.6.2.3 Post-growth annealing of CdTe thin films in solar cells

The microstructure of CdTe thin films may be significantly altered by post-growth annealing, and there are numerous reports of grain growth in CdTe films annealed in the presence of $CdCl_2$. Not all of these reports are systematic and are often presented in terms of reports on cell performance, rather than as materials studies. However, detailed work by Moutinho *et al*[62]has explained the principal phenomena using the framework of the development of metallurgical microstructure during annealing: Humphreys and Hatherly[63] provide a book length review including descriptions of metallurgical recovery, recrystallisation and grain growth following heavy cold working. Moutinho showed direct evidence for the recrystallisation of CdTe thin films deposited by physical vapour deposition (PVD). AFM analysis of as-deposited films was compared with that of films annealed in the presence of $CdCl_2$ at temperatures of 350°C and 400°C, the different temperatures being used to change the rate of recrystallisation. For annealing at 350°C, it was observed that new, smaller, grains had nucleated at the interstices of the original grains observed in the as-deposited material. For a 400°C anneal, significant grain growth had occurred after recrystallisation and the average grain size had increased from 0.26μm to 1.24μm. Subsequent XRD analysis of the films showed that as-grown films had a strong {111} texture, while the annealed films were randomly oriented. These results showed direct evidence for the phenomena of recrystallisation and grain growth in CdTe thin films. However, owing to the high deposition temperatures typically employed for CdTe thin films deposited by CSS, the impact of grain growth and recrystallisation on CdTe microstructure is expected to be small as follows: Further work by Moutinho *et al*[64],

looked at the impact of post-growth annealing on the microstructure of CdTe thin films deposited by CSS at different substrate temperatures and determined a temperature dependence for grain growth and recrystallisation effects in CSS deposited films. For a low substrate temperature (~420°C), grain sizes were found to be small (~0.36μm) in the as-deposited material and grain growth leading to significantly larger grains (~1.6μm), was observed after annealing at 400°C in the presence of $CdCl_2$. However, when using a higher substrate temperature (~620°C), grains were found to be large in the as-deposited material (~2.7μm) and subsequently no evidence of grain growth was observed as a result of annealing. Similar result were reported by Cousins[65], who determined grain size as a function of annealing time in the presence of $CdCl_2$ at 400°C, for CdTe layers deposited by CSS. Grain sizes were also measured at various depths throughout the layers (revealed using a chemical bevel method). For CdTe layers deposited at a substrate temperature of 500°C, grain size was found to increase with distance from the CdTe/CdS interface, however, no evidence of enhanced grain growth throughout the bulk of layers was found as a result of annealing in the presence of $CdCl_2$ at 400°C for times in the range 0-60mins. However it was demonstrated that the near interface grains did undergo some grain growth upon $CdCl_2$ treatment at 400°C[66]. Throughout this work substrate temperatures of ≥500°C have been used. As a result post growth annealing was anticipated to have little effect on the film microstructure. Nevertheless, where the grain structure is compared for layers subjected to any form of post-growth annealing, it is done so for the layers that have been annealed under the same conditions.

It has been demonstrated by various groups that control over the grain structure of CdTe thin films is attainable by the adjustment of temperature, growth rate or ambient gas during deposition. All studies discussed however give little consideration to the structure and development of films at early stages of growth - and any impact these processes may have on the completed film. By studying the rudimentary thin film formation process of CdTe a better understanding of the process may be achieved. This may then serve to allow layer growth to be carried out in a more informed manner with consequent benefits for device fabrication.

4.7 References for Chapter 4

1 K. L. Chopra, *Thin Film Phenomena*, McGraw-Hill Inc, New York, 1969.

2 L. Eckertova, *Physics of Thin Films*, Plenum Publishing Corporation, New York, 1986.

3 J. E. Greene, in *Handbook of Deposition Technologies for Films and Coatings*, edited by R. F. Bunshah (Noyes Publications, Park Ridge, 1994), 681-739.

4 B. Lewis and J. C. Anderson, *Nucleation and Growth of Thin Films,* Academic Press, London, 1978.

5 M. Ohring, *The Materials Science of Thin Films*, Academic Press Ltd, London, 1992.

6 D. W. Pashley, in *Materials Science and Technology: A Comprehensive Treatment*; *Vol. 15*, edited by R W Cahn, P Haasen, and E. J. Kramer (VCH Publishers Inc, Weinheim, 1991), 289-329.

7 A. Pimpinelli and J. Villain, *Physics of Crystal Growth*, Cambridge University Press, Cambridge, 1998.

8 H. Vehkamaki, *Classical Nucleation Theory in Multicomponent Systems*, Springer, Berlin, 2006.

9 J. A. Venables, *Introduction to Surface and Thin Film Processes*, Cambridge University Press, Cambridge, 2000.

10 Y. K. Kim, J. Y. Lee, H. S. Kim, J. H. Song, and S. H. Suh, Journal of Crystal Growth **192,** 109-116 (1998).

11 H. J. Lee, H. Ni, H. T. Wu, and A. G. Ramirez, Applied Physics Letters **87,** 102-114 (2005).

12 N. G. Semaltianos, J. L. Pastol, and P. Doppelt, Surface Science **562,** 157-169 (2004).

13 E. Sibert, F. Ozanam, F. Maroun, R. J. Behm, and O. M. Magnussen, Surface Science **572,** 115-125 (2004).

14 K. Morita, K. Soda, T. Katoh, and M. Hanebuchi, Journal of Electronic Materials **25,** 727-731 (1996).

15 C. S. Yang, Y. J. Lai, W. C. Chou, D. S. Chen, J. S. Wang, K. F. Chien, and Y. T. Shih, Journal of Crystal Growth **301,** 301-305 (2007).

[16] A. P. Belyaev, V. P. Rubets, M. Y. Nuzhdin, and I. P. Kalinkin, Semiconductors **37,** 617-619 (2003).

[17] M. Zinke-Allmang, L. C. Feldman, and W. van Saarloos, Physical Review Letters **68,** 2358-2361 (1992).

[18] C. A. Neugebauer, in *Handbook of Thin Film Technology*, edited by L. I. Maissel and R. Glang (McGraw-Hill Book Company, New York, 1970), 1-41.

[19] R. A. Sigsbee, Journal of Applied Physics **42,** 3904-3915 (1971).

[20] F. W. Sears and G. L. Salinger, *Thermodynamics, Kinetic Theory, and Statistical Thermodynamics*, Addison-Wesley Publishing Company, Reading, 1986.

[21] P. B. Barna, in *International Summer School of Diagnostics and Applications of Thin Films*, (Chhum u Trebone, Czechoslovakia, 1991), 295-310.

[22] J. A. Venables, G. D. T. Spiller, and M. Hanbucken, Reports on Progress in Physics **47,** 399 - 459 (1984).

[23] S. N. Alamri, Physica Status Solidi a-Applied Research **200,** 352-360 (2003).

[24] R. Anton, Physical Review B (Condensed Matter and Materials Physics) **70,** 1-7 (2004).

[25] C. V. Thompson, Journal of Materials Research **14,** 3164-3168 (1999).

[26] C. V. Thompson, Annual Review of Materials Science **30,** 159-190 (2000).

[27] I. V. Markov, *Crystal Growth for Beginners: Fundamentals of Nucleation, Crystal Growth and Epitaxy*, World Scientific Publishing Co., Singapore, 1995.

[28] P. B. Barna, M. Adamik, U. Kaiser, S. Laux, H. Bangert, M. Pulliainen, and K. A. Pischow, Surface & Coatings Technology **101,** 72-75 (1998).

[29] J. F. Pocza, A. Barna, and P. B. Barna, Journal of Vacuum Science & Technology **6,** 472-475 (1969).

[30] J. F. Pocza, A. Barna, P. B. Barna, I. Pozsgai, and G. Radnoczi, Japanese Journal of Applied Physics **6,** 525-532 (1974).

[31] D. W. Pashley, M. J. Stowell, M. H. Jacobs, and T. J. Law, Philosophical Magazine **10,** 127-158 (1964).

[32] M. Epifani, J. Arbiol, E. Pellicer, and J. R. Morante, Chemistry of Materials **19** 4919-4924 (2007).

[33] R. Anton and P. Kreutzer, Physical Review B **61,** 16077-16083 (2000).

[34] J. G. Skofronick and W. B. Phillips, Journal of Applied Physics **38,** 4791-4796 (1967).

[35] W. B. Phillips, E. A. Desloge, and J. G. Skofronick, Journal of Applied Physics **39,** 3210-3218 (1968).

[36] P. Jensen, Reviews of Modern Physics **71,** 1695-1735 (1999).

[37] D. W. Pashley, in *Advances in Physics; Vol. 14* (1965), 327-417.

[38] D. W. Pashley, in *Epitaxial Growth Part A*, edited by J. W. Matthews (Academic Press, New York, 1975), 29-88.

[39] H. Poppa, in *Epitaxial Growth Part A*, edited by J. W. Matthews (Academic Press, New York, 1975), 215-275.

[40] M. Zinke-Allmang, Thin Solid Films **346,** 1-68 (1999).

[41] P. B. Barna, in *Conference Record of the Ninth International Vacuum Congress and Fifth International Conference on Solid Surfaces* (Madrid, 1983), 382-396.

[42] A. Barna, Phys. Stat. Sol (a) **55,** 427-435 (1979).

[43] P. B. Barna, F. M. Reicha, G. Barcza, L. Gosztola, and F. Koltai, Vacuum **33,** 25-30 (1983).

[44] P. B. Barna and P. M. Reicha, in *Conference Record of the Eighth International Vacuum Congress* (Cannes, 1980), 165-168.

[45] H. Ebe and Y. Nishijima, Applied Physics Letters **67,** 3138-3140 (1995).

[46] H. Ebe and H. Takigawa, Materials Science and Engineering **B16,** 57-59 (1993).

[47] G. M. Lalev, J. Wang, J.-W. Lim, S. Abe, K. Masumoto, and M. Isshiki, Applied Surface Science **242,** 295-303 (2005).

[48] D. R. Johnson, Thin Solid Films **361,** 321-326 (2000).

[49] R. Wendt, A. Fisher, D. Gercu, and A. D. Compaan, Journal of Applied Physics **84,** 2920-2925 (1998).

[50] G. Zoppi, K. Durose, S. J. C. Irvine, and V. Barrioz, Semiconductor Science and Technology **21,** 763-770 (2006).

[51] R. W. Birkmire and E. Eser, Annual Review of Matterials Science **27,** 625-653 (1997).

[52] V. D. Falcao, W. A. Pinheiro, C. L. Ferreira, and L. R. Cruz, Materials Research **9,** 29-32 (2006).

[53] A. Seth, G. B. Lush, J. C. McClure, V. P. Singh, and D. Flood, Solar Energy Materials and Solar Cells **59,** 35-49 (1999).

[54] C. S. Ferekides, D. Marinsky, V. Viswanathan, B. Tetali, V. Palekis, P. Selvaraj, and D. L. Morel, Thin Solid Films **361-362,** 520-526 (2000).

[55] J. Luschitz, K. Lakus-Wollny, A. Klein, and W. Jaegermann, Thin Solid Films **515,** 5814-5818 (2007).

[56] X. Li, P. Sheldon, H. Moutinho, and R. Matson, in *Conference Record of the Twenty Fifth IEEE Photovoltaics Specialists Conference* (Washington D.C, 1996), 933-936.

[57] T. Okamoto, Y. Harada, A. Yamada, and M. Konagai, Solar Energy Materials and Solar Cells **67,** 187-194 (2001).

[58] D. S. Albin, Y. Yan, and M. M. Al-Jassim, Progress in Photovoltaics **10,** 309-322 (2002).

[59] D. H. Rose, D. H. Levi, R. J. Matson, D. S. Albin, R. G. Dhere, and P. Sheldon, in *Twenty Fifth IEEE Photovoltaics Specialists Conference* (Washington D.C, 1996), 777-780.

[60] M. E. Hernandez-Torres, R. Silva-Gonzalez, G. Casarrubias-Segura, and J. M. Garcia-Jimenez, Solar Energy Materials and Solar Cells **90,** 2241-2247 (2006).

[61] N. Romeo, A. Bosio, R. Tedeschi, and V. Canevari, Materials Chemistry and Physics **66,** 201-206 (2000).

[62] H. R. Moutinho, M. M. Al-Jassim, F. A. Abulfotuh, D. H. Levi, P. C. Dippo, R. G. Dhere, and L. L. Kazmerski, in *Conference Record of the Twenty Sixth IEEE Photovoltaic Specialists Conference* (Anaheim, 1997), 431-434.

[63] F. J. Humphreys and M. Hatherly, *Recrystallization and Related Annealing Phenomena*, Galliard Ltd, Great Yarmouth, 1995.

[64] H. Moutinho, R. G. Dhere, M. M. Al-Jassim, D. H. Levi, L. L. Kazmerski, and B. Mayo, in *National Center for Photovoltaics Program Review Meeting*, Denver, Colorado, 1-7 (1998).

[65] M. A. Cousins, PhD Thesis, University of Durham, 2001.

[66] K. Durose, M. A. Cousins, D. S. Boyle, J. Beier, and D. Bonnet, Thin solid films **403,** 396-404 (2002).

5 Experimental techniques

5.1 Introduction

A range of experimental techniques to both grow and characterise thin films and thin film devices, have been employed during this work. This chapter describes these techniques and is presented in three parts: Firstly, the thin film growth techniques used to produce both individual solar cell devices and complete semiconductor films are discussed. Secondly, physical thin film characterisation techniques, used to determine the structure and morphology of films, are described. Finally, electrical characterisation techniques used to determine CdTe/CdS device performance are discussed.

5.2 Thin film growth techniques and device processing

In this section the methods used in the growth and processing of CdTe/CdS solar cells are described generally and with reference to CdTe. Where apparatus has been built for this project, it is described. Specific details of the growth and processing conditions are described wherever possible. However, where particular ranges of processing conditions were used, then they are given in the appropriate results chapter.

5.2.1 Close space sublimation

Close space sublimation (CSS) is a specialised form of physical vapour deposition (PVD) used for the deposition of materials with high melting points (typically >1000°C)[1]. Rather than being evaporated these materials may sublime, producing a density of vapour suitable for deposition at temperatures far below the materials melting point. CSS is therefore a suitable technique for the deposition of both CdTe and CdS, which have melting points of 1365K and 1750K respectively[2]. However, owing to the relatively low vapour density resulting from sublimation (in comparison to thermal evaporation) the substrate for growth must be in close proximity to the sublimation source. The source material must therefore also cover a suitably large area to allow this, with the area of the source tray typically being larger than the substrate in order to ensure good film uniformity.

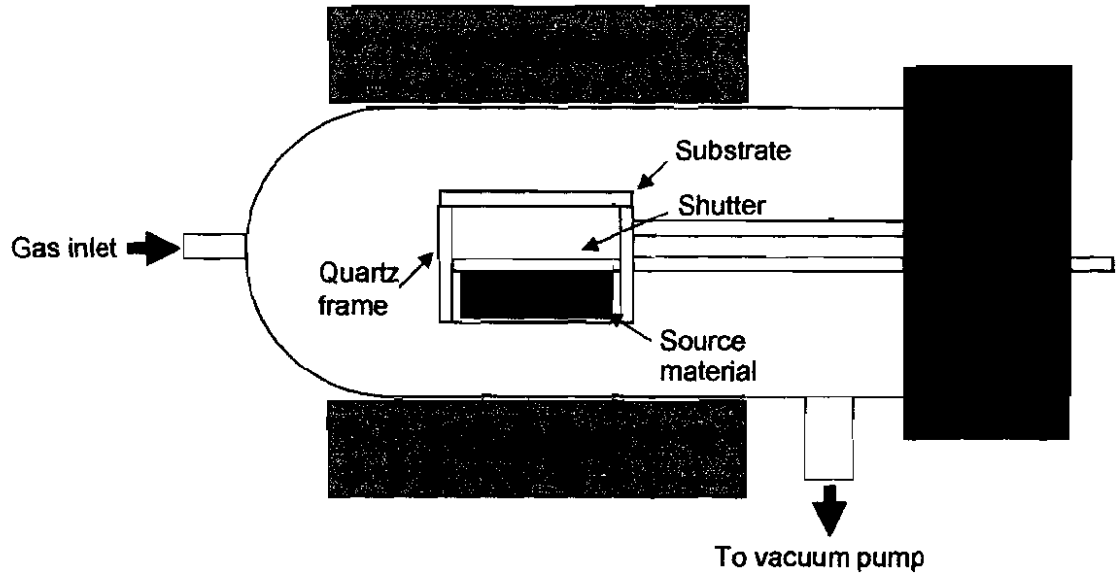

Figure 5.1: Schematic diagram of the close space sublimation (CSS) system.

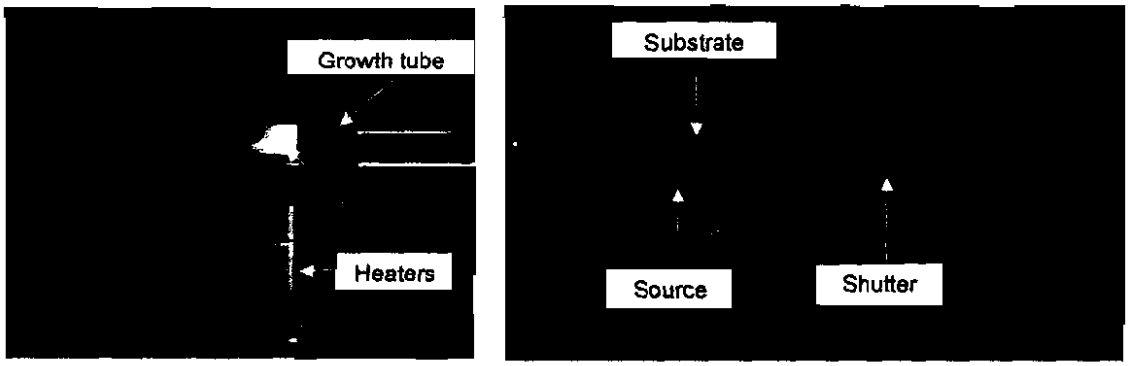

Figure 5.2: The close space sublimation (CSS) system used in this work. Left: system during growth, right: the substrate, frame and source arrangement.

a) System design

The CSS system used for work presented in this thesis was custom built by Electro-Gas systems Ltd and was designed to provide a high purity deposition environment. It is common for CSS systems to incorporate metallic components, heater elements or graphite that may introduce impurities. However, the CSS system used here was constructed almost entirely of high purity quartz glass, the only non-quartz material present in the deposition chamber being high purity silicon used as a heat spreader and two thermocouples. Graphite was not used so as to allow experiments with oxygen

present. A schematic diagram of the system is shown in fig.5.1, whilst images of the system in operation and of the source-substrate arrangement are shown in fig.5.2. The substrate (5x5cm) is held in a quartz frame with the TCO face down, at a distance of 15mm from the source material. A retractable quartz shutter was aligned between the source material and substrate, with the shutter being used to control deposition onto the substrate. Thermocouples were placed on the back of the substrate and inside the source tray to monitor the substrate and source temperatures respectively.

b) Heating

Heating to the source material is provided by a tungsten coil heater, whilst the substrate is heated by an infrared ceramic heater. Although both heaters are able to be individually controlled, due to the close proximity of source and substrate there is some coupling of the heating. For example, at a source temperature of 500°C the substrate reached a temperature of approximately 350°C, without the substrate heater being active. This means there is a limit to the temperature difference that can be achieved between the source and substrate in this system.

c) Gas ambient

The system is capable of utilising a range of gas ambients during growth, with constant flows (up to 100mls/min) of nitrogen, oxygen and hydrogen able to be added to the chamber. Gas mixtures of nitrogen/oxygen and nitrogen/hydrogen were able to be used, but the system contains an interlock system to stop oxygen/hydrogen mixtures being used. The system also incorporates an automated pressure control to allow a constant deposition pressure to be set, with the pressure in the range 0-700Torr being achievable.

d) Source material

Two separate CSS chambers were set up for CdTe and CdS deposition, with both sources being provided by powdered material of 5N purity bought from Alfa Aesar. The deposition of both CdTe and CdS films by CSS occurs via the reversible dissociation of the material at an elevated temperature, as shown in equations 5.1 and 5.2:

$$2CdTe(s) \leftrightarrow 2Cd(g) + Te_2(g)^3 \quad (5.1)$$

$$2CdS(s) \leftrightarrow 2Cd(g) + S_2(g) \quad (5.2)$$

The source materials dissociates into the component elemental vapours before recombining on the surface to form a thin film. The rate at which this process occurs is principally controlled by the source and substrate temperatures, but is also dependent upon the CSS chamber pressure (Section 4.4).

Throughout this work CSS has been used for both a) fundamental growth studies, mainly for CdTe and with some work on CdS, and b) the fabrication of complete CdTe/CdS devices. Precise details of the growth times, pressures, temperatures etc used are given in the relevant results chapters. Some layers and devices were grown by chemical bath deposition and metal organic chemical vapour deposition which are described in the next sections.

5.2.2 Chemical bath deposition

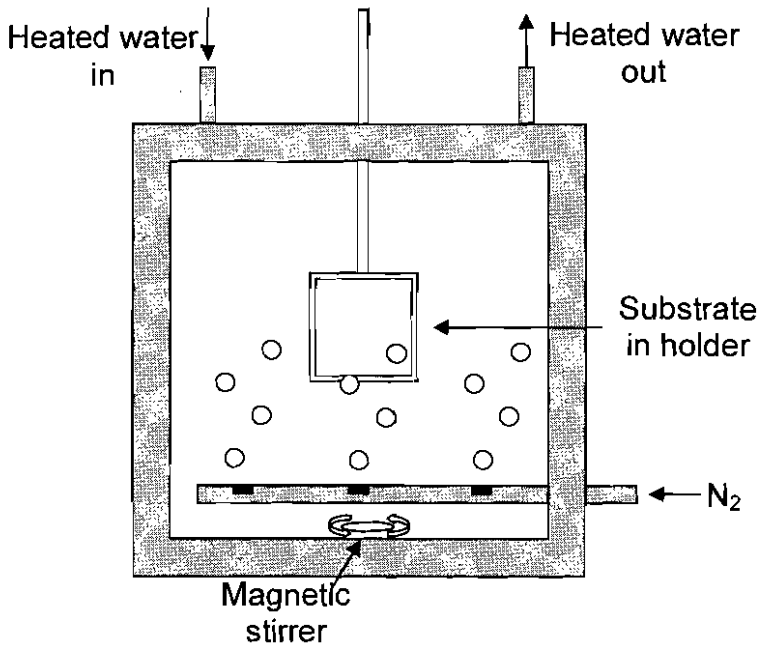

Figure 5.3: Chemical bath deposition apparatus system schematic.

Chemical bath deposition (CBD) allows thin films to be formed by the precipitation from solution onto a substrate. The bath constituents are combined in aqueous solution and stirred in a heated bath, along with a substrate. In the case of CdS, this may be achieved

by the controlled thermal decomposition of thiourea in the presence of Cd^{2+}(aq) ions. Experimentally it has been demonstrated that by carefully monitoring the pH and temperature of the bath solution, the rate of deposition may be adjusted and very fine control over the layer thickness can be achieved. CBD is a low temperature technique as deposition is usually performed at temperatures <100°C, which leads to a small grain size and high levels of substrate coverage[4], making it an ideal technology for the deposition of thin (<100nm) CdS layers for solar cells. The CBD growth of CdS films in this work was performed using a novel growth system[5,6] (shown in fig.5.3), with the heating of the substrate and the bath constituents being achieved by passing temperature controlled water between pairs of glass plates, situated at the front and back of the bath. This allowed heating to be in the same plane as the substrate, leading to more uniform heat distribution across the substrate. The system also incorporated a nitrogen "bubbler", which was designed to displace any static gas bubbles that may form on the substrate surface during CBD deposition. Bubbles resident on the surface during deposition may lead to the formation of pinholes in the film, as the bubbles block the reactants from reaching the substrate.

Bath constituent	Molar concentration	Volume
Cadmium Acetate ($CdAc_2$)	0.033M	8ml
Ammonium Acetate (NH_4Ac)	1.0M	4.7ml
Ammonium (NH_4OH)	14.76M	15ml
Thiourea	0.067M	8ml
De-ionized Water	-	550ml

Table 5.1: Bath constituents for CdS chemical bath deposition used in this work.

There are numerous CBD recipes reported for the deposition of CdS[6-8], using various deposition temperatures and chemicals. The recipe found to produce layers of a quality most suited for CdTe/CdS devices, is generally considered to be the "standard" recipe[9]. However, difficulties were initially encountered in achieving good quality films using this recipe, due to the CdS forming principally as solid precipitates rather than condensing on the substrate. However, by slight adjustments to the bath temperature and

by careful monitoring of the bath pH, to ensure it remained in the 9.5-10.0 range, good quality, highly uniform films (typically <10nm variation across 5cm sample width) were produced. The bath constituents for CdS deposition used in this work are listed in table 5.1, along with the volumes of each used and their respective molar concentrations. The growth methodology for CBD CdS film deposition was as follows:

- The DI water, ammonium, ammonium acetate and cadmium acetate were added to the bath and the mixture was stirred by a magnetic stirrer.
- The substrates were cleaned and then added to the bath in a quartz glass holder, with up to four 5x5cm plates being immersed simultaneously.
- The nitrogen bubbler was started and the bath heater turned on and set to 90°C. Once this temperature had been reached the bath and constituents were left for a period of 15mins to reach thermal equilibrium.
- A quarter of the thiourea (2ml) was then added to start the reaction. The remaining thiourea was added in 2ml portions at ten minute intervals.
- Growth was carried out for a total time of 90mins (measured from the point at which the initial portion of thiourea was added), leading to a CdS film of 80-100nm thickness being formed.

5.2.3 Metal organic chemical vapour deposition

Metal organic chemical vapour deposition (MOCVD) and metal organic vapour phase epitaxy[10] (MOVPE) are specific embodiments of chemical vapour deposition (CVD) processes[11]. Material is deposited onto a heated substrate from a vapour, due to a chemical reaction occurring close to the substrate surface. Reactants containing the desired species are admitted to the deposition chamber, and for CdTe deposition these are the organometallics dimethylcadmium (DMCd) and di-isopropyltelluride (DIPTe), present as vapours in a hydrogen carrier gas[12]. For the work presented in this thesis, CdTe layers produced by MOCVD were grown at Bangor University and incorporated high concentrations of arsenic during growth, but which are nevertheless subject to $CdCl_2$ processing. This is a non-standard technique that has been developed to enhance the *p*-type doping of the CdTe layers and the reader is referred to the papers by Barrioz *et al*[13,14] for further information.

5.2.4 Transparent conducting oxides and deposition substrates

For the devices reported in this work TCO coated glass substrates were bought from commercial suppliers. Four different TCOs were used, with the material, supplier and sheet resistivity for each listed in table 3.1.

Manufacturer	Glass type	TCO structure	Sheet resistance
Merck Display Technologies Ltd	Soda-lime	Glass/ITO (100nm)	15 Ω/□
Visiontek Systems Ltd.	Soda-lime	Glass/SiO_2/ITO (150nm)	12 Ω/□
Delta Technologies Ltd.	Aluminosilicate	Glass/ ITO (150nm-200nm)	4-8 Ω/□
Pilkington	Soda-lime	Glass/TO (25nm)/ SiO_2(25nm)/FTO(600nm)	8 Ω/□

Table 5.2: Types of TCO/substrate used in this work.

5.2.5 Post growth treatment of CdTe/CdS devices with $CdCl_2$

In this work $CdCl_2$ films were deposited onto the CdTe back surface by vacuum evaporation, with $CdCl_2$ layers typically being 200nm thick. Samples were then annealed in a tube furnace in air. A range of annealing temperatures (380-500°C) and times (5-50min) were used, however it was found to be vital for good device performance to optimise these treatment parameters for each device. After annealing the samples were allowed to cool, before any excess $CdCl_2$ was rinsed from the back surface of the device using de-ionized water. The specific annealing temperatures and times used for the various devices produced during this work may be found in the relevant results chapters.

5.2.6 Contacting procedure

In this work back contacts were formed using pure Au deposited by vacuum evaporation, with contacts being a series of ~25 2mm diameter dots. The dot contacts were formed by vacuum evaporation using an evaporation mask between the gold

evaporation source and the sample. This contacting geometry was used instead of a large single back contact as it allowed the uniformity of device performance across cells to be evaluated. Prior to the application of the back contact the CdTe back surface was subjected to a nitric-phosphoric (NP) acid etch in order to produce a suitable Te-rich surface (see Section 3.2.7). The etching solution consisted of 1% nitric acid, 70% phosphoric acid and 29% de-ionized water. Samples were immersed in the solution for a period of 10s, before being rinsed with de-ionized water and dried using nitrogen.

5.3 Physical characterisation of devices and layers

5.3.1 Atomic force microscopy

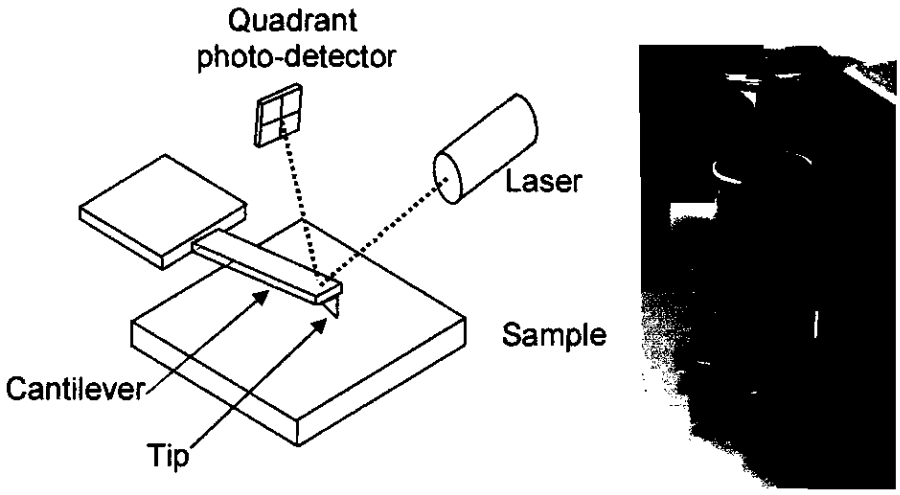

Figure 5.4: AFM apparatus and schematic diagram.

Atomic force microscopy (AFM) provides high resolution measurement of the surface topography. Invented by Binning, Quate and Gerber[15], the AFM operates in a similar manner to most scanning probe microscopy techniques[16], measuring the repulsive or attractive force between the surface being examined and an atomically sharp tip mounted on a cantilever. As the force between tip and surface changes due to variations in the height of the surface, the cantilever bends accordingly. By measuring the deflection of the cantilever as the tip is rastered across the surface, the topography of the surface may be determined. The deflection of the cantilever tip is usually measured by a

laser beam being reflected from the back of the cantilever, onto a quadrant photo-detector. The photo-detector generates an induced current that is proportional to the cantilever's position, and the surface topography can be deduced from this current signal.

In this work a Tompometrix explorer AFM was used which had a maximum x-y scan range of 150μm and a z-axis range of 12μm. The tips used for measurement were non-conductive silicon nitride tips, bought from Veeco Instruments.

5.3.2 Film thickness measurement

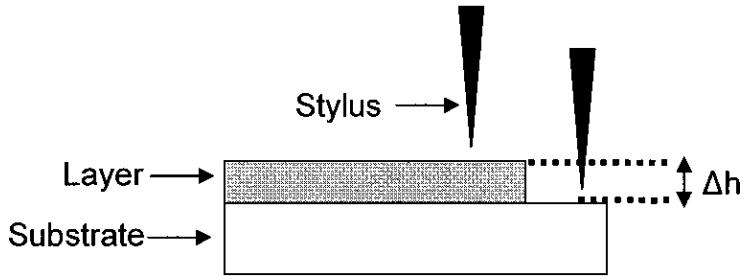

Figure 5.5: Surface profiler measurement of layer thickness.

The thickness of deposited films was determined using a Tencor Alpha-Step 200 surface profiler. A small section of material was removed from the substrate (simply using a scalpel in the case of CdTe, or swabbing with hydrochloric acid in the case of CdS) and the profiler stylus was scanned from the exposed substrate to the layer (shown in fig.5.5). The thickness of the layer was then determined from the change in height of the stylus.

5.3.3 Scanning electron microscopy secondary electron imaging

The scanning electron microscope (SEM) is a powerful characterisation tool, that while primarily used to image surface morphology at high levels of magnification (up to 300,000x), may also be used for other forms of characterisation such as energy dispersive X-ray analysis (Section 5.3.4) or electron beam induced current (Section 5.3.3)[17]. It interrogates the sample using a highly focused beam of electrons. Typical beam interactions with the sample are shown in fig.5.6. Most of the work reported in this thesis used the topographically sensitive secondary electron mode.

In this work SEM measurements were made using FEI XL30 - SFEG (Schottky Field Emission Gun) and Hitachi SU-70 microscopes.

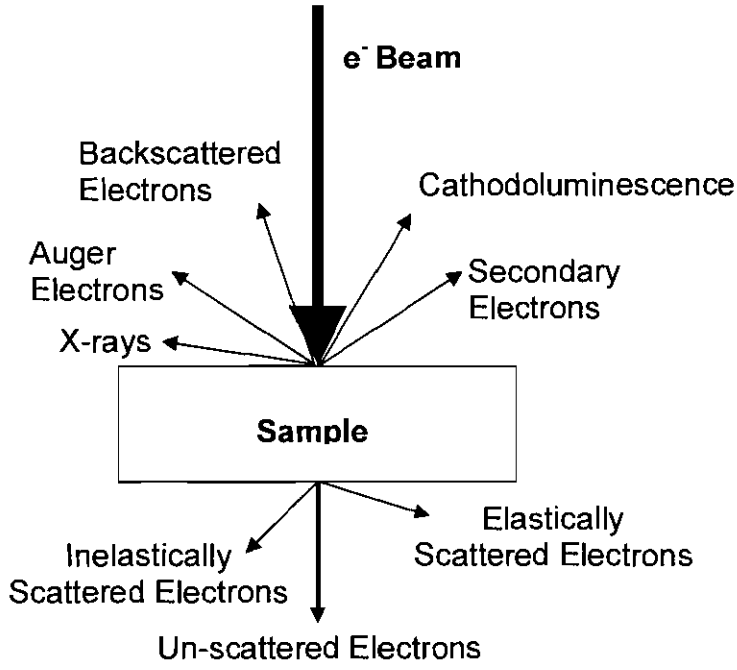

Figure 5.6: Electron beam interactions with a solid sample relevant to scanning electron microscopy.

5.3.4 Energy dispersive X-ray analysis

In energy dispersive X-ray (EDX) analysis the SEM electron beam interacts with the sample, producing characteristic X-rays (fig.5.6) and allowing elemental analysis of samples to be performed. The processes are as follows: A high energy electron beam (typically 10-20 KeV) is incident upon the sample, causing electrons within the inner shell of atoms to be ejected and the atom ionized[18]. The resulting electron vacancy is subsequently filled by an electron from an outer shell dropping down, with the excess energy being emitted in the form of an X-ray (or alternatively an Auger electron). The energy of this X-ray is defined by the energy difference between the inner and outer shells involved in the ionization event, and as such is characteristic of the element that has been ionized. The composition of the sample may therefore be determined by analysis of the energy spectrum of the emitted X-rays.

5.3.5 X-ray diffraction

a) Basic operation

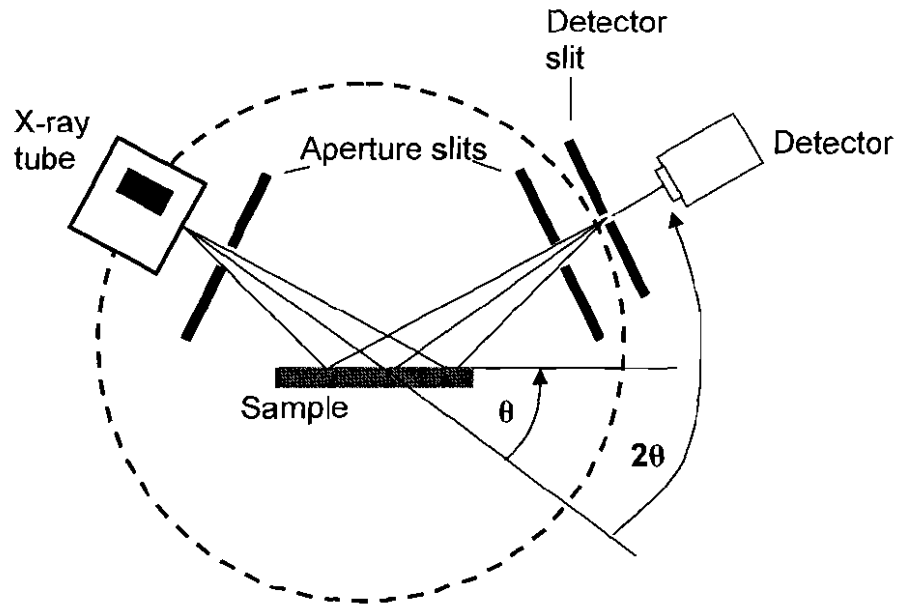

Figure 5.7: Schematic of an X-ray diffractometer in the Bragg-Brentano geometry.

X-ray diffraction (XRD) allows the crystal structure of materials to be probed and information such as the lattice spacing, grain size, strain and texture to be determined as X-rays incident upon a crystal lattice are diffracted by the lattice spacing.

For this work the powder diffraction technique was used to analyse the preferred orientation of deposited CdTe layers. This technique analyses polycrystalline samples using a monochromatic X-ray beam, in the Bragg-Brentano (or θ-2θ) mode[19] shown in fig.5.7. The diffracted X-ray intensity is recorded as a function of θ, with peaks being observed for angles at which the Bragg condition (equation 5.3) is satisfied and the beam is successfully reflected by the *hkl* planes:

$$n\lambda = 2d_{hkl}\sin\theta \tag{5.3}$$

Here λ is the wavelength of the incident X-rays, θ is the angle between the beam and the surface, n is the diffraction order (assumed to be 1) and d_{hkl} is the lattice spacing. In the Bragg-Brentano geometry, the detector and sample are linked such that as the detector rotates 2θ, the sample rotates through θ. Hence for any given angle θ, those planes

oriented parallel to the substrate are oriented for diffraction thus allowing the preferred orientation to be determined.

In this work a Siemens D5000 diffractometer was used, with emission at the Cu Kα (1.5406Å) line. Scans were taken from 20° to 80° with a step of 0.02° and an integration time of 2 seconds for each step. X-ray tube settings of 40kV and 40mA were used for all samples.

b) Determination of orientation and texture coefficient

Powder diffraction allows the intensity of individual *hkl* peaks to be determined. For samples that show a measure of preferred orientation, also known as texture, the corresponding diffraction peak will be strong. A measure of this preferred orientation for a given *hkl* plane is the texture coefficient, C_{hkl}[20] ,which is defined using the Harris method[20] as:

$$C_{hkl} = \frac{\frac{I_{hkl}}{I_{r,hkl}}}{\frac{1}{n}\sum_{n=1}^{n}\frac{I_{hkl}}{I_{r,hkl}}} \qquad (5.4)$$

where I_{hkl} is the measured intensity for diffraction from a given *hkl* plane, with $I_{r,hkl}$ being the intensity of reflection from the same plane but for a randomly oriented sample and n is the number of reflections being considered. For work presented in this thesis $I_{r,hkl}$ values for CdTe were obtained from the ASTM index (set 15, card 770).

The standard deviation (σ) of the texture coefficient values (C_{hkl}) provides a measure of their spread and hence of the overall preferred orientation of the film. σ may be determined using the equation:

$$\sigma = \sqrt{\sum 1/n (C_{hkl} - 1)^2} \qquad (5.5)$$

Comparison of σ values for different samples allows the level of preferred orientation to be evaluated, with a higher value indicating an increase in the degree of preferred orientation.

5.4 Electrical/optical characterisation of CdTe/CdS devices

5.4.1 Current density-Voltage measurement

Current density-Voltage (J-V) analysis of solar cells is a standard characterisation technique used to determine the principal device performance parameters (η, FF, J_{sc} and V_{oc}). Devices are placed under simulated AM1.5 illumination, with the current generated by the device being measured as a function of applied bias. The standard device parameters may then be extracted from the resultant curve via the method outlined in Section 2.3. Further analysis of the curves may also yield the equivalent circuit parameters R_s, R_{sh} and A (see Section 2.3).

In this work an Oriel 81160 solar simulator was used to provide AM1.5 illumination, with a total intensity of 100mW/cm^2 being calibrated at the sample position. Current measurement and cell biasing were performed by a Keithley 2400 source meter, with computer control being performed by GPIB interface and dedicated software written in Labview[5]. All measurements were performed at room temperature, for either 101 or 201 points, in a bias range or -1V to +1V.

5.4.2 External quantum efficiency

External quantum efficiency (EQE) measurements (sometimes known as spectral response) are made by recording the photo-generated current from a device under monochromatic illumination, as a function of wavelength. By reference to a calibrated source the quantum efficiency of the device may be calculated for each wavelength. The system used was developed as part of this work and therefore a full description is deferred until Chapter 6.

5.4.3 Electron beam induced current

Electron beam induced current (EBIC) is a SEM based semiconductor characterisation technique, that measures the electrical current induced by an electron beam incident upon a sample[17]. There are different geometries of EBIC for the analysis of p-n junction devices, such as cross section and plan view modes as shown in fig.5.8. In cross section mode the electron beam is scanned across the p-n interface and by this manner may reveal the position of the junction. It is also possible to estimate the minority

diffusion length from the EBIC signal in this mode, however this is often difficult in thin films as the beam size is comparable with the diffusion length[21]. In plan view mode, the incident electron beam direction is normal to the assumed line of the junction. The resultant EBIC image will therefore reveal any localised variations in performance and highlight recombination centers, such as grain boundaries[21].

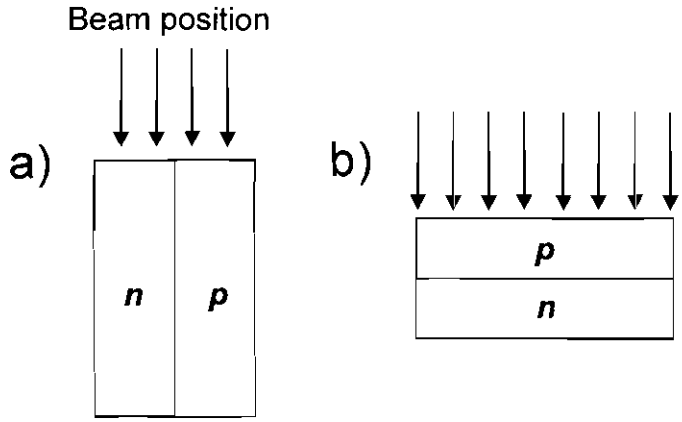

Figure 5.8: EBIC analysis of a *p-n* junction in a) cross section and b) plan view.

All EBIC analysis presented in this thesis was performed with the sample in the cross section arrangement and using a Hitachi SU-70 SEM.

5.4.4 Optical beam induced current

Optical beam induced current (OBIC) probes the spatial uniformity of device performance by measuring the device current under illumination from a small light spot. As part of this work, a high resolution OBIC apparatus was designed, constructed, tested and used in evaluating PV devices. A review of the use of OBIC in evaluating CdTe/CdS devices is therefore deferred until Chapter 6 where it is presented alongside a description of the instrument and its capabilities.

5.5 References for Chapter 5

1 R. F. Bunshah, in *Handbook of Deposition Technologies for Films and Coatings*, edited by R. F. Bunshah (Noyes Publications, New Jersey, 1994), 131-248.

2 L. I. Berger and B. R. Pamplin, in *CRC Handbook of Chemistry and Physics*, edited by D. R. Lide (CRC Press, New York, 1997), 12-93.

3 D. Albin, D. Rose, A. Swartzlander, H. Moutinho, F. Hasoon, S. Asher, R. Matson, and P. Sheldon, in *Covalent Ceramics III - Science and Technology of Non-Oxides; Vol. 410*, edited by A. F. Hepp, P. N. Kumta, J. J. Sullivan, G. S. Fischman, and A. E. Kaloyeros (Materials Research Soceity,1996), 45-50.

4 H. R. Moutinho, D. Albin, Y. Yan, R. G. Dhere, X. Li, C. Perkins, C. S. Jiang, B. To, and M. M. Al-Jassim, Thin Solid Films **436,** 175-180 (2003).

5 M. D. Archbold, PhD Thesis, Durham University, 2007.

6 M. D. Archbold, D. P. Halliday, K. Durose, T. P. A. Hase, D. S. Boyle, S. Mazzamuto, N. Romeo, and A. Bosio, Thin Solid Films **515,** 2954-2957 (2007).

7 D. S. Boyle, A. Bayer, M. R. Heinrich, O. Robbe, and P. O'Brien, Thin Solid Films **361,** 150-154 (2000).

8 H. R. Moutinho, R. G. Dhere, K. Ramanathan, P. Sheldon, and L. L. Kazmerski, in *Conference Record of the Twenty Fifth IEEE Photovoltaic Specialists Conference* (Washington D.C, 1996), 945-948.

9 J. Lee, Applied Surface Science **252,** 1398-1403 (2005).

10 S. J. C. Irvine, in *Narrow-gap II-VI Compounds for Optoelectronic and Electromagnetic Applications*, edited by P. Capper (Chapman & Hall, London, 1997), 71-96.

11 J. Carlsson, in *Handbook of Deposition Technologies for Films and Coatings*, edited by R. F. Bunshah (Noyes Publications, New Jersey, 1994), p. 374-433.

12 G. Zoppi, K. Durose, S. J. C. Irvine, and V. Barrioz, Semiconductor Science and Technology **21,** 763-770 (2006).

13 V. Barrioz, Y. Y. Proskuryakov, E. W. Jones, J. D. Major, S. J. C. Irvine, K. Durose, and D. A. Lamb, Materials Research Society Symposium Proceedings **1012,** 367-372 (2007).

[14] V. Barrioz, R. L. Rowlands, E. W. Jones, S. J. C. Irvine, G. Zoppi, and K. Durose, in *Thin-Film Compound Semiconductor Photovoltaics*; *Vol. 865*, edited by W. Shafarman, T. Gessert, S. Niki, and S. Siebentritt (2005), 67-72.

[15] G. Binnig, C. F. Quate, and C. Gerber, Physical Review Letters **56,** 930-933 (1986).

[16] R. Wiesendanger, *Scanning Probe Microscopy and Spectroscopy,* Cambridge University Press, Cambridge, 1994.

[17] D. B. Holt and D. C. Joy, *SEM Microcharacterization of Semiconductors,* Academic Press, San Diego, 1989.

[18] D. C. Joy, in *SEM Microcharacterization of Semiconductors*, edited by D. B. Holt and D. C. Joy (Academic Press, San Diego, 1989), 119-152.

[19] R. L. Snyder, in *X-ray Characterization of Materials*, edited by E. Lifshin (Wiley-VCH, Weinheim, 1999), 1-104.

[20] C. S. Barret and T. B. Massalski, *Structure of Metals*, McGraw-Hill, U.S.A, 1966.

[21] P. R. Edwards, S. A. Galloway, and K. Durose, Thin Solid Films **372,** 284-291 (2000).

6 OBIC and EQE measurements of CdTe/CdS devices

6.1 Introduction

Determination of the uniformity of photovoltaic response in CdTe/CdS solar cells may offer insight into the defects and non-uniformities that limit device performance. Characterisation using the optical beam induced current (OBIC) method, sometimes referred to as light/laser beam induced current (LBIC), probes the response of a cell under localised excitation. By scanning a focussed light spot over the surface, defects may be revealed by changes occurring in the generated photocurrent. Whilst not offering as fine resolution as NSOM[1] (near-field scanning optical microscopy) or EBIC[2] (electron beam induced current) techniques, OBIC does offer the advantage of probing the device in its standard operating geometry.

The majority of high resolution OBIC systems reported utilise a laser as a light source. However, the use of a monochromated white light source, whilst not offering as fine resolution as that of a laser source, does provide spectral as well as spatial resolution when evaluating device performance. Defects may then be characterised by localised external quantum efficiency (EQE) measurements, as well as by quantifying the device uniformity determined as a function of wavelength. Throughout this chapter a distinction is made between a *value* of the external quantum efficiency, henceforth referred to as *EQE*, and an external quantum efficiency *measurement* (*EQE* as a function of wavelength), which will be referred to as EQE.

This Chapter describes the construction and testing of a combined OBIC and EQE system, and its use for the evaluation of the performance of CdTe/CdS solar cells.

6.2 Review of OBIC/spatially resolved EQE

The first reported use of a system that may be termed as OBIC was in 1951 by Goucher *et al*[3]. By scanning a small light spot across a germanium p-n junction the minority carrier lifetime was able to be determined from variations in the photocurrent.

Since the development of computer data capture, modern OBIC systems typically scan in two dimensions, producing maps of either photocurrent response or *EQE*. Numerous system geometries have been developed and applied to a wide range of solar cell materials. This section provides a brief review of OBIC and EQE measurements and is split into three parts: Firstly, the various OBIC systems reported in the literature shall be discussed in terms of their capabilities. Secondly, the interpretation of EQE measurements for CdTe/CdS devices is discussed as a function of incident wavelength. Finally, a review of OBIC techniques as applied to thin film solar cells will be made, with particular emphasis on CdTe/CdS solar cells.

6.2.1 OBIC systems

The majority of OBIC systems are based around a laser source, as lasers provide a beam with small divergence, allowing reasonably high resolutions to be easily obtained. As a result, OBIC assessment utilising a laser source has been widely used as a quality control measure for solar cell fabrication[4-6]. OBIC systems that utilise a monochromated white light source are less widely reported, presumably as they afford much lower levels of resolution. However, they do have the added advantage of being able to provide spectral as well as spatial resolution and some groups have developed systems that allow lower resolution (typically >100μm) OBIC mapping allied to localised EQE measurements[7,8].

The first report of a high resolution OBIC system applied to a thin film solar cell was by Galloway *et al*[8]. Numerous high resolution OBIC systems followed that offer sub-micron resolutions, an example of this being the system reported by De Vittorrio *et al* who developed what they termed as a μ-OBIC system[9]. By using an argon laser source, focussed to its diffraction limit, they were able to achieve resolutions in the order of 0.4μm. Because of the high resolution of the system they were able identify sub-micron size defects and directly compare results with EBIC measurements. A high resolution system incorporating a laser source has also been reported by a group at Colorado State University. However, while the system was still capable of resolutions of 1μm[10] it was a far more general characterisation tool than that reported by De Vittori *et al*. By using different laser diodes as light sources, allied with some wavelength tuning techniques[11],

they were able to record high resolution maps at different wavelengths. The system was also capable of measurement at numerous spot sizes[12] (100μm, 10μm, 1μm), for a range of light intensities[13] (1-300suns) and at various cell bias allowing localised resistivity as well as photocurrent measurement[14]. This allowed for a wide range cell characterisation techniques and, by analysing the effect of bias and light intensity on defect sites, they were able to separately identify optical and electrical defects. Other novel systems have been developed to expand upon the standard OBIC technique and thus afford extra characterisation possibilities. Kaminski *et al*[15,16] report the use of an OBIC system in conjunction with infrared thermography measurements, to evaluate the performance of shunts within multicrystalline silicon solar cells. These two measurements were found to be complementary to one another, with shunts appearing as hot spots in thermography images and as dark regions in OBIC maps. The CELLO system(Carstensen *et al*[17]) uses the OBIC method as a basis for in-depth equivalent circuit analysis of solar cells at localised points. The system is capable of mapping generated current for different bias voltages, and also mapping potential for various applied currents. This meant localised *J-V* curves could be constructed for each point of the solar cell examined, allowing the extraction of localised shunt and series resistance values.

6.2.2 Key features of EQE as a function of wavelength

For solar cells the observed OBIC response shows significant variation for different excitation wavelengths: Careful selection of the wavelength therefore makes it possible to reveal details about particular aspects of the device structure. This is explained in the remainder of this section with reference to the EQE spectrum shown in fig.6.1. Features of the EQE spectra - related to the influence of the CdS layer, level of intermixing and the absorber – are all described. Exploitation of these EQE features in OBIC mapping and local EQE measurement to reveal information about cells follows in Section 6.4.

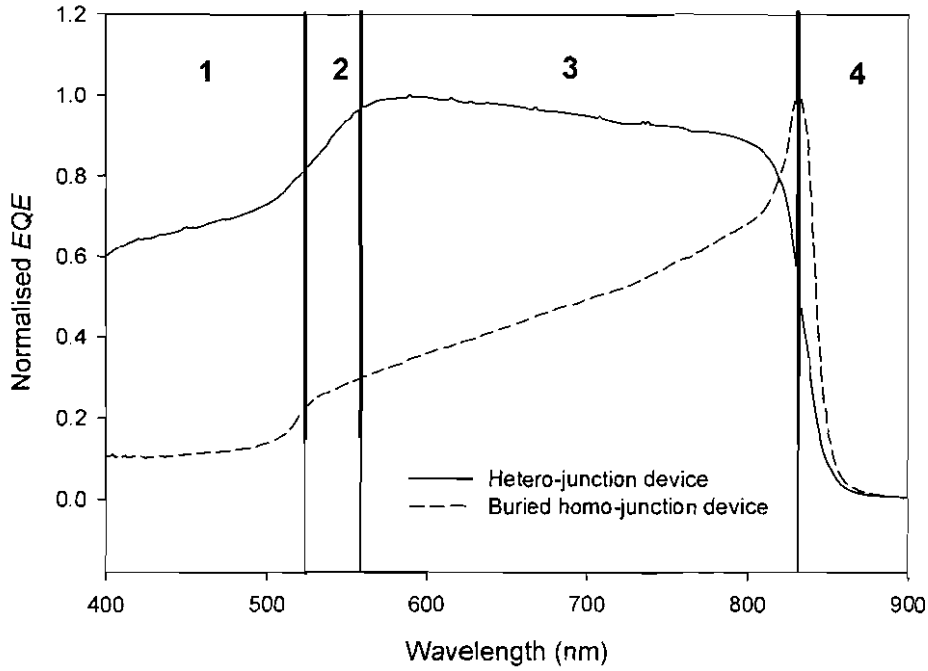

Figure 6.1: Schematic EQE response for a CdTe/CdS solar cell showing a normal hetero-junction response and the response for a buried homo-junction device (these curves were from cells grown as part of this work).

Region 1 (400 - 520nm): CdS region

For incident light at wavelengths below the CdS bandgap (~520nm, 2.4eV), light is absorbed within the CdS layer. The fraction of incident light absorbed within this region is dependent upon the CdS thickness, with thick CdS (>250nm) allowing no light transmission (resulting in no current generation) in the 400-520nm range. Thinner CdS layers allow a portion of this incident light to reach the CdTe layer, with CdS thicknesses of <100nm being routinely used to allow partial light transmission and thus current generation at these wavelengths. The hetero-junction device shown in fig.6.1 has a thin CdS layer (~80nm) and as such the EQE curve shows an *EQE* response in the 0.6-0.7 range. For thick CdS devices the *EQE* would be zero within this region.

The variation of response within this region as a function of CdS thickness has been reported by numerous authors[18,19], with an improved J_{sc} for thinner CdS typically being achieved due to the increased current generation for wavelengths within this region. For OBIC measurement using wavelengths of light in this range, variations in the CdS

thickness will be revealed by non-uniform response, due to the inconsistent attenuation provided by the changing CdS thickness.

Region 2 (520 - 550nm): CdS intermixing region

The level of intermixing between the CdTe and CdS layers plays an important role in determining the overall shape of the EQE response curve, with the effect of intermixing being apparent in regions 2 and 4. In a device where no intermixing occurs the device will show a sharp cut-off at the CdS bandgap (assuming the CdS is sufficiently thick), due to photons being absorbed by the CdS layer. In devices where there is intermixing with the CdTe layer, a CdS-rich ternary $CdS_{1-y}Te_y$ alloyed layer is formed at the CdTe/CdS interface and a more gradual cut-off is observed. The diffusion of Te into the CdS layer reduces the CdS bandgap[20], leading to enhanced absorption in the 520-550nm range by the intermixed layer[21-23]. Higher levels of intermixing will therefore reduce the response within this region and any localised fluctuations in the level of intermixing will be revealed by non-uniform response, under OBIC examination at these wavelengths. The EQE plot shown in fig.6.1 displays some evidence of intermixing, due to the slope observed in region 2 (diffusion of CdS into the CdTe is described in 'Region 4').

Region 3 (550nm - 835nm): Bulk response region

For high efficiency devices the EQE response observed in this region should be relatively constant, as all light within this range is transmitted, without absorption, through the CdS layer and then absorbed by the CdTe layer. However, the average penetration depth of photons within this range is increased for longer wavelengths (lower energy), as individual photons have a lower probability of absorption by the CdTe layer as their energy decreases. A decrease in the *EQE* response may therefore be observed for longer wavelengths in the case of: a)devices with very thin CdTe layers[24], where not all incident photons are absorbed, or b) for devices with low minority carrier lifetime[25], where photons maybe absorbed but recombination may occur before charges reach the depletion region. This can be seen for the hetero-junction response in fig.6.1, with there being a slope towards longer wavelengths in region 3. However, this is not expected to

have major bearing on the OBIC device response, unless there is significant variation in CdTe thickness across the examined area.

In the case of a device containing a buried homo-junction (fig.6.1), the *EQE* curve is significantly altered within this wavelength range. Because the junction is located away from the front surface (Section 3.2.4) the *EQE* will instead increase for longer wavelengths[26], as deeper penetrating photons excite carriers closer to the junction. As the wavelength approaches the CdTe bandgap (~840nm, 1.5eV) in a hetero-junction containing device the *EQE* decreases rapidly. However, for a homo-junction response the *EQE* rises to a peak around the CdTe bandgap, as this represents the maximum penetration depth for photons within the CdTe layer. For homo-junction devices significant variation in OBIC response may be seen for wavelengths across this range, due to the enhanced collection at longer wavelengths.

Region 4 (835 - 900nm): CdTe intermixing region

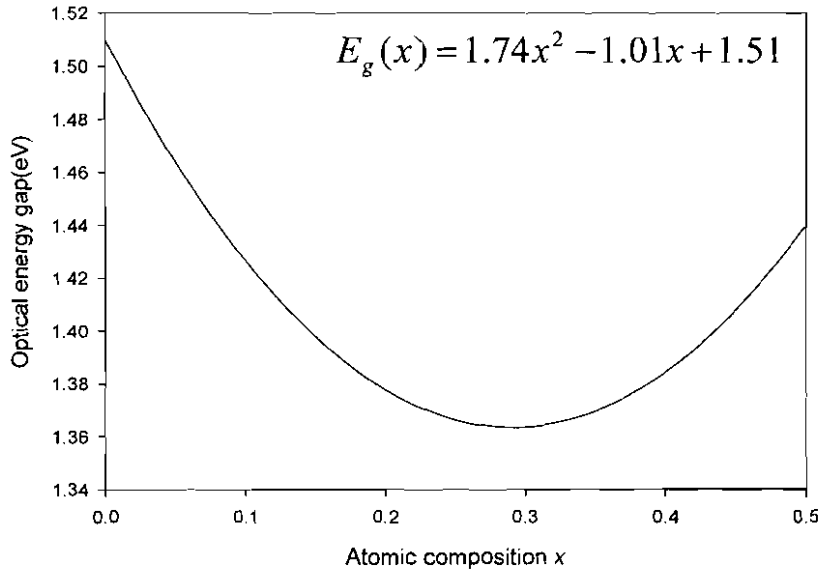

Figure 6.2: The bandgap bowing equation for the CdS_xTe_{1-x} alloy[27].

As well as the response being modified by Te diffusion into the CdS layer, the EQE curve is also modified by S diffusion into the CdTe layer, leading to the formation of a CdTe-rich CdS_xTe_{1-x} layer[27]. This leads to the band bowing effect (fig.6.2), whereby the

bandgap of the intermixed layer is less than that of the pure CdTe layer and thus absorbs light of longer wavelengths. This means that the observed long-wavelength cut-off at the CdTe bandgap is shifted towards longer wavelength, due to the presence of this alloyed layer at the CdTe/CdS interface. As can be seen from fig.6.2, the bandgap of the intermixed layer changes with the level of intermixing, meaning the position of the long wavelength cut-off will depend on the level of intermixing. It is in fact possible to deduce the effective bandgap from the position of the cut-off, and from this to infer the level of intermixing within a device (a method to do this has been reported by Rakhshani[28]). For OBIC measurement using wavelengths close to and above the CdTe bandgap, localised variations in the level of intermixing will produce significant non-uniformity. Regions with high levels of intermixing will have greatly increased absorption for wavelengths above the CdTe bandgap.

6.2.3 OBIC studies of thin film solar cells

The use of OBIC as a means of thin film solar cell characterisation has been widely reported for different solar cell materials. For example, in GaAs based devices OBIC has been used to evaluate the impact of the substrate on device defects[29] and determine the junction position and minority carrier diffusion length[30].

The study of CdTe/CdS devices using OBIC has been principally reported by three different groups, all utilising slightly different approaches. Significant work has been carried out at Durham University in comparing OBIC and EBIC data for CdTe devices[2,8,31,32]. The principal focus of the work was looking at the impact of post growth treatments (i.e. heat and $CdCl_2$ treatment) on the uniformity of the device response[8,31,32]. Untreated devices were found to display a large degree of non-uniformity, with variations in performance on a scale far greater than that of the grain size of the material. The uniformity was improved by heat treatment in air, with the majority of remaining performance variation found to result from the films grain structure. $CdCl_2$ treatment provided a far greater improvement in the level of uniformity, with grain structure no longer impacting on the observed response. Use of localised EQE measurements revealed the untreated cell to contain a buried homo-junction; whilst the heat and $CdCl_2$ treated cells displayed the expected hetero-junction response. Comparative plan-view EBIC

measurements (in this case by e^- beam excitation through the opaque or 'back' contact) were made but were noted to be difficult to interpret, as the technique probes both the CdTe/CdS junction and the CdTe layer at regions away from the junction. As such, this was evidence for the comparative ease of use of OBIC as a simple characterisation tool.

As noted in the previous Section, a group at Colorado State University have developed a sophisticated laser based OBIC system that achieves both high spatial resolution, as well as spectral resolution via the use of different laser diode sources. They have reported various studies on CdTe/CdS solar cells utilising this system. Because the system incorporated a sample holder that allowed samples to be measured, subjected to accelerated aging and then replaced to within +/- 1μm of their original position[11], they were able to evaluate the effect of such stress on specific areas of a device[10,12,33]. Stress was applied to devices by keeping the cells at an elevated temperature (e.g. 100°C for 8 days) under illumination, at either short circuit or biased conditions. Cells were found to degrade non-uniformly with specific defect sites appearing as a result of the applied stress, rather than there being a general decrease in performance. In Davies *et al*[18], the effect of CdS thickness on the performance of CdTe/CdS devices was examined by OBIC measurements. Devices with CdS layers thinner than ~100nm were found to have lower efficiency, as a result of a decrease in the device V_{oc}. OBIC maps revealed a significant increase in the non-uniformity of the device response, with this non-uniformity being attributed to fluctuations in the local CdS thickness, leading to a subsequent variation in the junction quality. The system has also been used to determine localised resistivity values by measurement at different levels of bias and light intensity[14], the uniformity of this was then compared for different thin film devices[11].

A slightly different approach to OBIC characterisation of CdTe/CdS solar cells has been reported by Agostinelli *et al*[7,34]. OBIC maps were recorded at different levels of bias and at different wavelengths in order to identify spatial inhomogeneities. Such defects were then further analysed by localised EQE measurements at different levels of bias (apparent quantum efficiency - AQE). They also considered the phase of the photocurrent for the AQE curves (determined with reference to a chopped light beam), and found that at large applied forward bias the photocurrent recorded from defect points exhibited a large phase change (~140°) in comparison to an unbiased measurement. They interpreted

this as a reversal of the direction of photocurrent with defect point being found to behave differently to uniform portions of analysed devices. Such phase reversal of the photocurrent is discussed by Durose *et al*[35]. It is usually attributed to currents flowing at high forward bias and under the influence of the back contact field. Hence Agostinelli's results indicate localised buried junction behaviour.

6.3 OBIC/EQE apparatus: System design and testing

This section outlines the design and testing of the combined OBIC/EQE system constructed during this work. In the first part of this section (6.3.1), the design and construction of the various system components are discussed. In Section 6.3.2, the testing of the system to calibrate EQE measurements and determine the spot size of the light beam is discussed.

6.3.1 System design

The general discussion of the apparatus that follows has been divided into sections, firstly the basic design of the system is described, before the sub-systems of the device are each described in turn.

6.3.1.1 General considerations

An OBIC system records the photocurrent generated in a solar cell due to a small light spot that is sequentially moved across the surface, leading to the formation of a 2-D "map" of photocurrent or *EQE*. The motion of the light spot across the surface is typically produced in one of two ways: i) the light spot remains stationary and the sample is moved beneath it with translation stages[36]or, ii) the light spot is moved across the sample surface by using a series of beam steering mirrors[37]. Of these two methods the first is by far the simpler to implement as by moving the sample underneath the beam, the path length of light from the lens to the sample remains constant. When using beam steering mirrors this path length, and as a result the light intensity, may vary for different positions across the sample. The system detailed in this chapter generates OBIC maps by using stepper motors to adjust the position of the sample beneath a stationary beam. EQE plots are generated by determining the photocurrent as a function of incident wavelength for a fixed sample position. The basic operation of the system may be described as

follows: a monochromated white light source is chopped and then focussed through a series of lenses onto the sample. The photocurrent generated by the sample is then detected via a lock-in amplifier and recorded by specially written software. A schematic diagram of the system is shown in fig.6.3. The apparatus comprises three interlinked systems: electronics and focussing optics, sample/lens positioning equipment and computer control. Each of these sub-systems will now be discussed in turn.

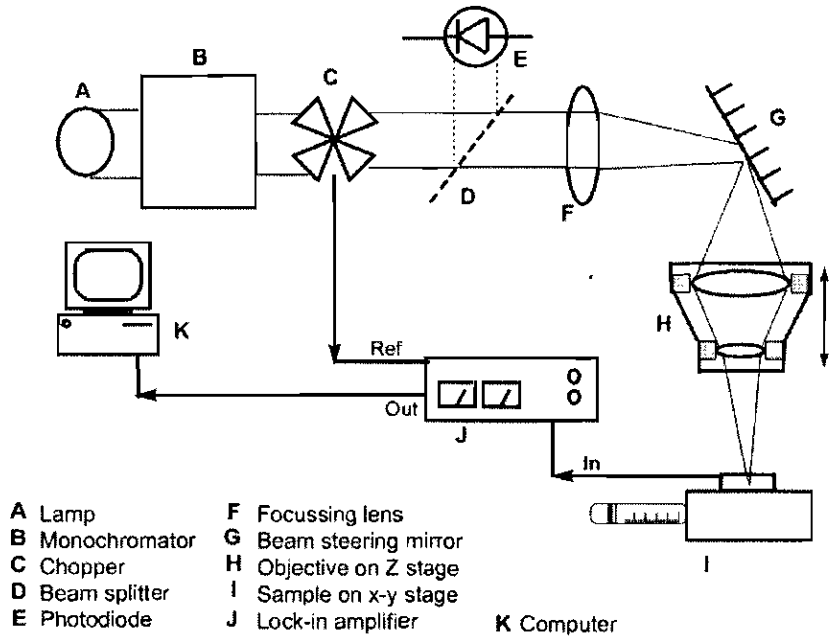

Figure 6.3: OBIC/EQE schematic diagram of the system.

6.3.1.2 Focussing optics

The system uses a 100W quartz halogen lamp as a white light source which is passed through a Bentham M300 monochromator fitted with a grating having high reflectivity in the wavelength range ~300-1700nm. Light outputted from the monochromator is passed through a chopper with a frequency of 120Hz (as frequencies above 100Hz were found to produce the most reliable signals), allowing lock-in detection to be used. The light is then passed through a beam splitter which sends a fraction of the incident light to a calibrated photodiode, used as a reference to determine the *EQE* from the device photocurrent (Section 6.3.2.2). The remaining light not sent to the photodiode passes through a condensing lens, before being reflected by a beam steering mirror into a microscope

objective. The microscope objective used was an Olympus 1-UB377 LU C Plan Fluoride 40x/0.6 N.A, which is equipped with a correction collar allowing focussing through up to 2.5mm of glass. This lens was mounted on a computer controlled Z-axis stage, so as to allow fine focussing of the light onto the sample.

The system also incorporates a retractable mirror (positioned after the beam splitter) that delivers the light onto a separate sample holder with a much larger spot size (~ 3cm diameter). This was used to generate EQE measurements for a complete cell, rather than for a localised point using a small spot size.

6.3.1.3 Sample and lens positioning

Three computer controlled stepper motors are incorporated in the system. Two provide motion of the sample beneath the beam on an X-Y stage, while the objective lens is mounted on the third at 90° to the sample in order to provide Z-axis motion. The stages have a maximum range of 25mm and a resolution of 1.25μm. The stepper motors were capable of individual or simultaneous movement.

6.3.1.4 Electronics and computer control

Due to the small levels of current generated, as a result of illumination by a small light spot, it is necessary to use a lock-in amplifier during OBIC/localised EQE measurements. Chopping was achieved by a mechanical chopper, this being used a reference for lock-in detection by a Signal Recovery 7225 DSP lock-in amplifier. The lock-in amplifier was capable of resolving currents <50pA and was able to resolve OBIC photocurrents with a good signal to noise ratio. The lock-in amplifier was also capable of determining the phase of the photocurrent with respect to the chopped light waveform (typically set to 0°), however no significant phase sensitivity was observed with there being only a small variation (+/- 5°) across a measured region. Phase information is thus not reported.

Various features of the OBIC/EQE system are subject to computer control: i) control of the monochromator output wavelength, ii) control of the stepper motor motion, iii) control of the lock-in amplifier and recording of photocurrent values. A schematic diagram of the computer control of the system is given in fig.6.4.

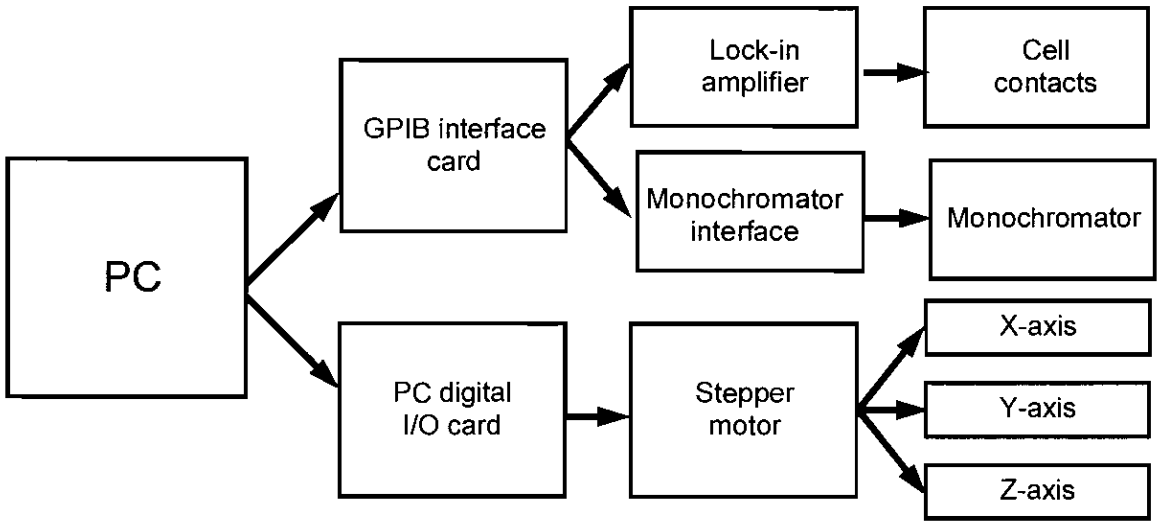

Figure 6.4: Computer control of OBIC/EQE apparatus

Two separate software applications were written to provide control for OBIC mapping measurements and EQE measurements in Visual C++ and Visual Basic respectively. Fig.6.5a shows the control panels for the OBIC mapping software. For OBIC measurements the scan area is divided into a grid, typically of 50x50 points. The software then adjusts the stepper motors, moving the sample systematically through the grid, recording the photocurrent at each pixel. The system is capable of recording a 50x50 point map in ~5mins for a given wavelength, and is also capable of repeating the mapping process for a series of wavelengths. The software also incorporates individual controls for each stepper motor, allowing the beam to be positioned at any point on the sample. Fine control of the Z-axis stepper motor allows the diameter of the beam to be altered by adjusting the position of the objective lens (Section 6.3.2).

Fig.6.5.b shows the software control for recording EQE spectra. This software scans the output wavelength of the monochromator through the range 400-900nm in 1.5nm intervals, recording the photocurrent generated each time via the lock-in amplifier. Combined use of these two software programs allows features to be identified by OBIC mapping and then subsequently examined using localised EQE measurement.

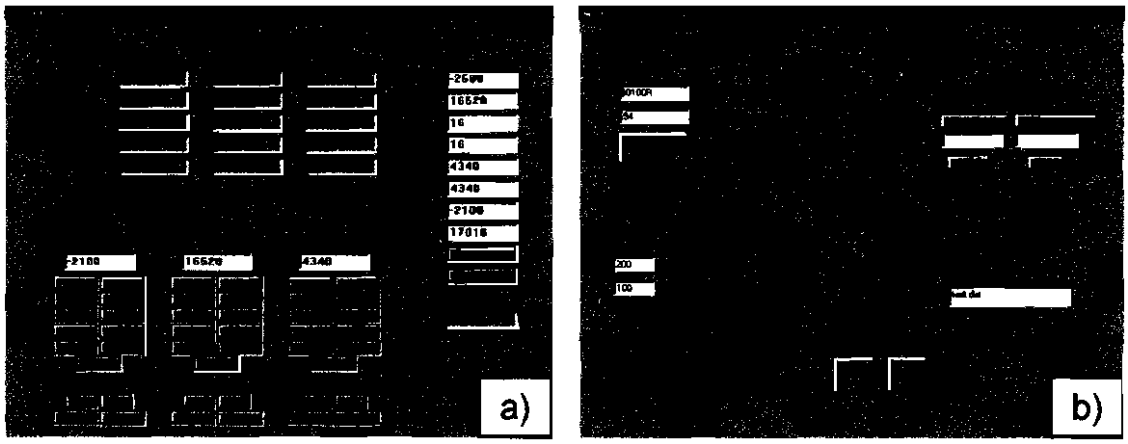

Figure 6.5: Control panels for, a) OBIC mapping and b) EQE software

6.3.2 Testing/calibration

This section describes the determination of the spot size used for OBIC measurements, and the subsequent optimisation to minimise this spot size. This section also describes the determination of *EQE* by the measurement of photocurrent values and with the aid of a calibrated photodiode.

6.3.2.1 Determination of spot size for OBIC measurements

In order to produce meaningful OBIC maps it is vital to first know the size of the light spot being projected onto the sample, as the size of this spot defines the maximum resolution of the system. The OBIC response of a cell may be treated as a convolution (see for example Kreyzig[38]) of the overlap between two functions, the beam profile function and the cell response function. Therefore, in order to determine the beam profile a de-convolution method is used when the beam is scanned over a cell with a known response function. The simplest way to generate a known cell response is to produce a step function, i.e. creating a region of the device where no current is generated upon illumination by the beam. A step response may be created in a number of ways, for example some groups have achieved this by fixing a razor blade to the glass surface of the device[11]. In order to accurately determine the beam profile a microscopically smooth step is required, otherwise the extracted beam profile may be distorted. Whilst a number of different methods were tested during this work in order to achieve a good quality step response the most reliable and repeatable method was found to be removal of the

CdTe/CdS layers from an area close to the back contact, as shown in fig.6.6. For the purposes of calculations it is assumed that the device has a uniform response where the beam was incident on the CdTe layer, and that no current is generated when the beam is not incident on the CdTe layer.

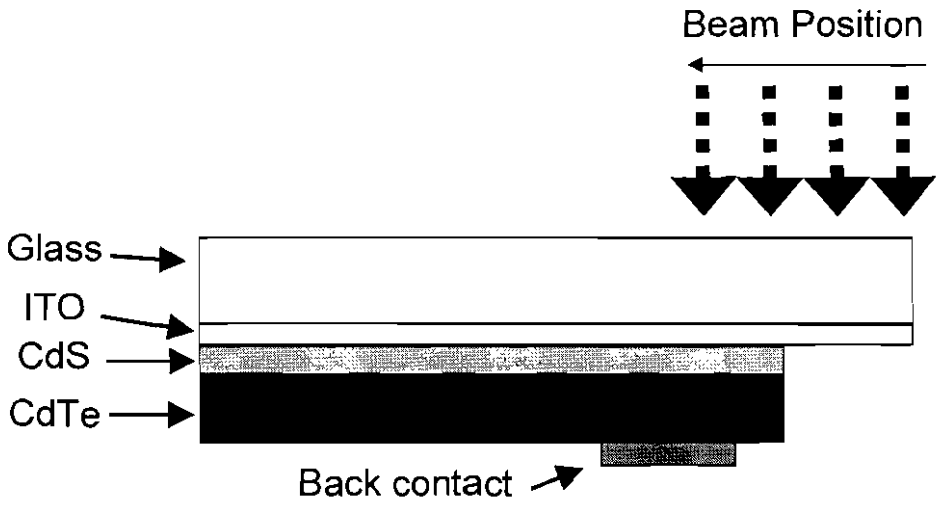

Figure 6.6: CdTe/CdS cell with removed section to allow focussing for OBIC measurements.

The convolution of two functions is given by;

$$Y(t) = \int_{v=0}^{v=t} H(v)X(t - v)dv \quad (6.1)$$

where $X(t\text{-}v)$ is the beam profile , $H(v)$ is the sample response step function, $Y(t)$ is the induced OBIC current profile and t and v are the spatial distances. Re-arranging this equation into the de-convolution equation for the beam profile gives;

$$X(t - v) = [dY(t)/dv]/H(v) \quad (6.2)$$

For positions where the beam is not incident on the cell, $H(v) = 0$ and no OBIC response is generated. As the device is assumed to respond uniformly for all position where the beam is incident on the CdTe surface, $H(v)$ is therefore presumed to be a constant. Equation 6.2 may therefore be approximated as;

$$X(t - v) \approx C[dY(t)/dv] \quad (6.3)$$

where C is a constant. Using equation 6.3 the beam profile, $X(t\text{-}v)$, may be determined by differentiation of the OBIC response resulting from scanning the beam over a step response. An example of the generated photocurrent as the beam is scanned over the step is shown in fig.6.7a, while the determined beam profile obtained by differentiating the current signal is shown in fig.6.7b.

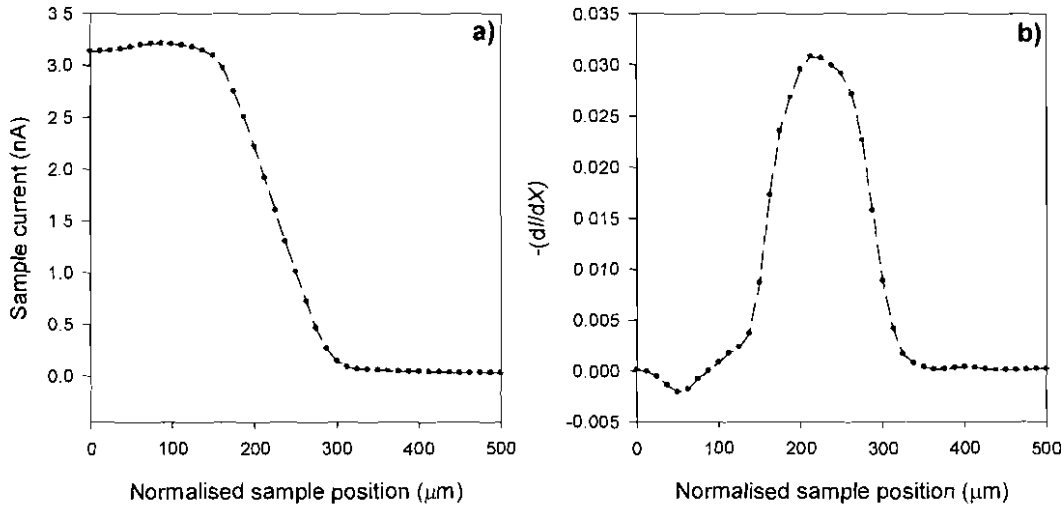

Figure 6.7: Determination of the OBIC beam profile, a) photocurrent generated by cell and b) differentiated photocurrent giving beam profile. The beam profile shown indicates a $1/e^2$ spot radius of 55μm (see fig.6.8). The smallest spot size obtained in this work was 12.5μm.

A similar de-convolution technique to determine beam size has been applied to LBIC measurement for CdTe devices by Hiltner[11], and also for junction EBIC (J-EBIC) measurements on CIS devices by Rechid *et al*[39]. When a good quality step junction (i.e. one that is microscopically smooth) had been produced, a beam profile with a good fit to a Gaussian distribution generally resulted. Poor quality step scribing often led to profiles showing multiple peaks, these being rejected since they did not provide an accurate representation of the beam profile.

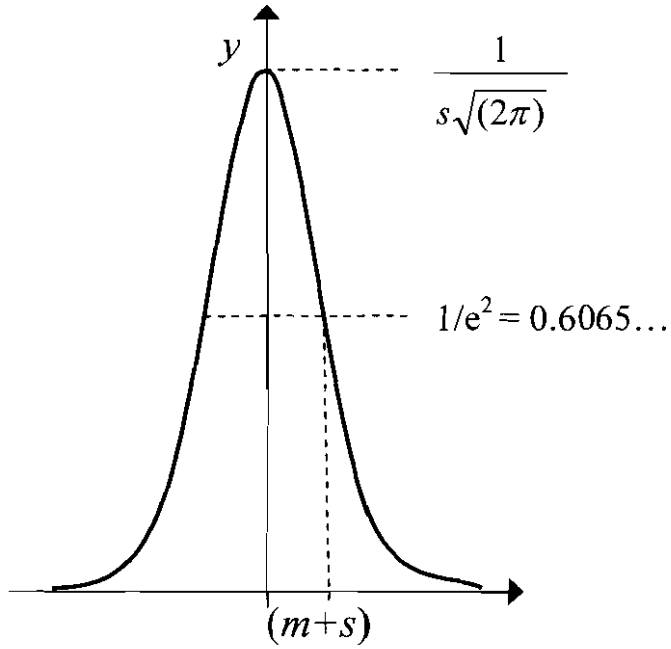

Figure 6.8: Model of the Gaussian beam profile, showing the $1/e^2$ width. Where *s* is the standard deviation of the distribution and *m* is the median value

Once the beam profile has been determined, the resolution of the system may be determined from the $1/e^2$ diameter of the profile[13], as shown graphically in fig.6.8 and used by Tang *et al*[29]. The $1/e^2$ diameter encompasses approximately 87% of the total light intensity incident on the surface. However, other groups have noted that a more accurate representation of the system resolution is the *radius* of the beam at this point[13,40] i.e. $1/2e^2$. Indeed comparison of the beam profile with images of small features recorded in this work support the later definition. As a result the system resolution (or beam size) is defined as the $1/2e^2$ *radius* hereon. In order to determine the resolution of the OBIC system, the de-convoluted beam profiles were then fitted to the Gaussian distribution given by;

$$y = \frac{1}{s\sqrt{2\pi}} e^{-[\frac{1}{2}(\frac{x-m}{s})^2]} \quad (6.4)$$

where *s* is the standard deviation, *m* is the mean of the distribution, *y* is the light intensity and *x* is the width. The resolution of the instrument was then determined from the standard deviation of the fitted Gaussian model, as this equates to the radius at an intensity of $1/e^2$.

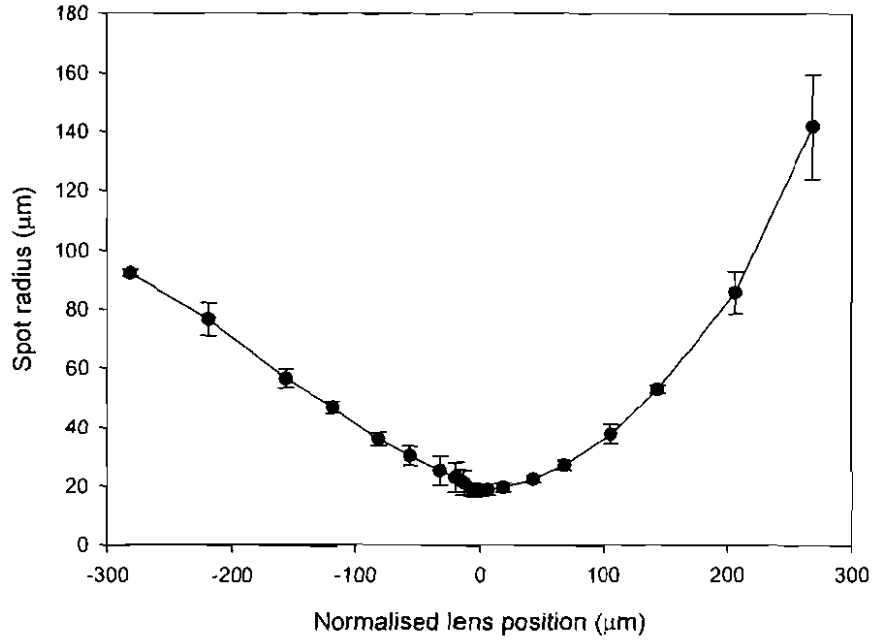

Figure 6.9: OBIC beam radius as a function of objective lens position determined for a wavelength of 600nm.

The resolution of the system was able to be altered by adjusting the distance between the sample and the objective lens using the Z-axis stepper motor, which allowed fine focussing control. By plotting the spot radius as a function of the lens position, the maximum resolution of the system was determined from the minimum point of the curve, as shown in fig.6.9. In this instance the maximum attainable resolution of the system is 20μm, with the corresponding lens position being normalised to zero. Through careful adjustment of the focussing optics and use of the lens correction collar, a minimum resolution for the system of 12.5μm was achieved.

6.3.2.2 Calibration for EQE determination

The quantum efficiency (*QE*) for a solar cell is defined as the ratio of the number of light photons incident on the cell, to the number of generated electrons collected by the internal field. The *EQE* differs from the internal quantum efficiency (*IQE*) in that in the former no correction is made for absorption/reflection by the glass superstrate and TCO layer. The *EQE* is therefore a measure of the efficiency of the entire device structure,

whereas *IQE* is solely a measure of generation and the p-n junction collection efficiency. In order to determine the *EQE* of a cell, a device of known response is required as a reference for calibration of the light source. This reference was provided by a calibrated Hamamatsu silicon photodiode, which had a known photo-sensitivity in the wavelength range 200-1200nm. The photo-sensitivity of the photodiode, S_{diode}, is given by;

$$S_{diode} = \frac{I_{diode}}{P_{photon}} \quad (6.5)$$

where P_{photon} is the power of photons incident on the cell and I_{diode} is the resultant current generated in the diode. The photon power P can be calculated by:

$$P_{photon} = N\frac{h\upsilon}{\Delta t} = \frac{h\upsilon}{e} \times \frac{Ne}{\Delta t} \quad (6.6)$$

where N is the number of incident photons, h is Planck's constant, υ is the frequency of incident photons, t is time and e is the charge of an electron. For the calculation of the *EQE* it is conventional to determine the photon current , I_{photon}, this being defined as the maximum photogenerated current that can result from the incident photons (i.e. equating to 100% *EQE*). It should be noted however that I_{photon} is not a real current term, but rather the theoretical limit for the photocurrent that may be generated by a device under illumination from the source. I_{photon} is determined from the photon power via the equation;

$$I_{photon} = \frac{Ne}{\Delta t} = P_{photon}\frac{e}{h\upsilon} \quad (6.7)$$

By re-arrangement and substitution into equation 6.5, the photon current can then be determined from the diode current by;

$$I_{photon} = \frac{I_{diode}}{S_{diode}} \times \frac{e}{h\upsilon} \quad (6.8)$$

Once the photon current has been determined, the *EQE* can be calculated from the current generated in the device, I_{device}, by;

$$EQE = \frac{I_{device}}{I_{photon}} = \frac{h\upsilon}{e}\frac{I_{device}S_{diode}}{I_{diode}} \quad (6.9)$$

The procedure for measurement was that a calibrated silicon photodiode was placed at the sample position and the current flowing from it (I_{diode}) was recorded as a function of the incident wavelength. Values for I_{photon} arriving at the sample position were then determined (as a function of wavelength) from this measurement using equation 6.8. Using this data the *EQE* for a given cell was determined from the induced sample current using equation 6.9.

This method gives calibrated *EQE* values at all wavelengths, independent of the intensity profile of the lamp/monochromator combination. Note however that this measurement was not done using white light bias, and so is not sensitive to probing any device effects arising from such broad spectrum illumination.

6.4 Analysis of CdTe/CdS solar cells using OBIC and EQE measurements

This section reports investigations into CdTe/CdS solar cell performance utilising the OBIC system described in the preceding sections. The results are ordered as follows: i) in depth analysis of a single cell is presented, with focus being placed on the cell's performance as a function of incident wavelength, ii) OBIC evaluation of the impact of etching on the device back contact, iii) the uniformity of four different CdTe/CdS devices is compared using OBIC, and iv) the effect of the CdTe layer thickness on device performance is investigated. These results showcase the capabilities of the system and demonstrate its abilities as a characterisation tool for solar cells.

6.4.1 Spatial uniformity of PV response at different wavelengths

The efficiency and uniformity of a CdTe/CdS solar cell may vary significantly dependent upon the wavelength of light incident upon the cell[11]. Non-uniformities relating to defect sites may only be apparent at selected wavelengths, whilst performing normally at others. The determination of uniformity as a function of wavelength may therefore offer useful information into the nature of observed defects.

This section details investigations into the variation of cell performance as a function of wavelength, analysed by OBIC and EQE measurements.

6.4.1.1 Device fabrication

OBIC measurements were performed on a typical CdTe/CdS device fabricated at Durham University, the cell was produced as follows: A 150nm thick CdS layer was deposited by chemical bath deposition (CBD), at 90°C on an ITO coated substrate bought from Vision Tech (the CBD deposition process is described in Section 5.2.2). The CdS layer was then annealed under 2Torr of hydrogen at 400°C for 2 min, prior to CdTe deposition to remove any oxide phases formed on the surface. The CdTe layer was deposited by CSS at source and substrate temperatures of 600°C and 500°C respectively, in a 2Torr pressure of oxygen. The growth time was 3 min, which yielded a 6μm thick film. A 50nm layer of $CdCl_2$ was evaporated onto the CdTe back surface before the structure was annealed for 10 min at 400°C in air. After annealing the back surface was subjected to a 10s NP etch, before a series of 25 2mm diameter gold back contacts were applied to the CdTe back surface.

6.4.1.2 J-V analysis

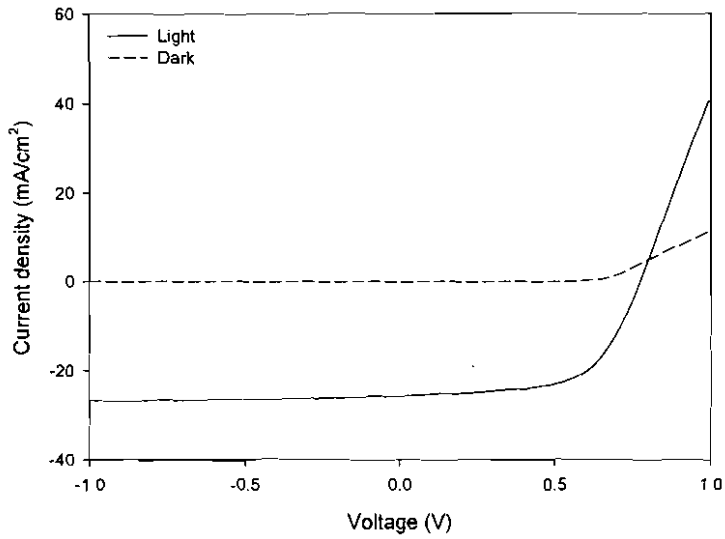

Figure 6.10: Light and dark J-V measurements of the CdTe/CdS cell to be evaluated by OBIC

J-V measurements were performed on all contact dots in order to determine one suitable for OBIC analysis. The contacts were found to have a wide range of performance, with efficiencies in the range 6.7-13.6% depending upon the position of the

contact. Contacts towards the centre of the device were generally found to perform better. This variation itself indicates substantial long range non-uniformity in the PV response that was then further investigated using OBIC. A contact was selected for OBIC evaluation that had efficiency (η) of 12.81%, an open circuit voltage (V_{oc}) of 0.77V, a short circuit current density (J_{sc}) of 26.88mA and a fill factor (FF) of 61.89%. The measured J-V data for this contact, recorded at both AM1.5 illumination and in the dark, is shown in fig.6.10.

6.4.1.3 Uniformity of PV response

a) Screening using a spot size of ~100μm

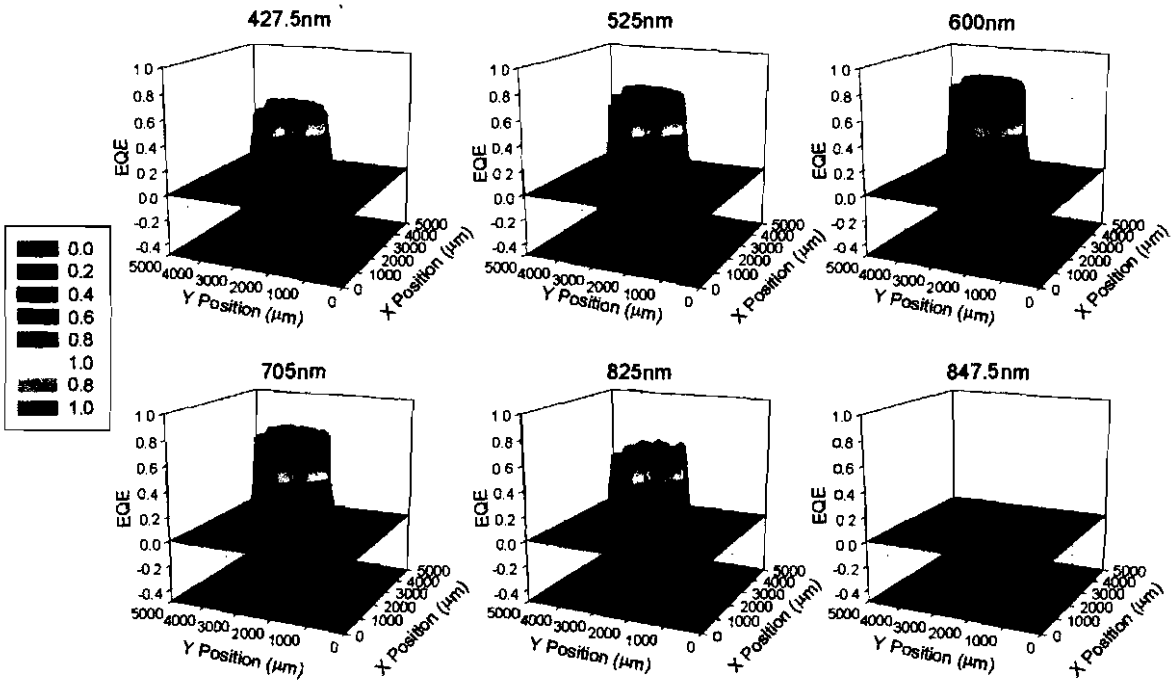

Figure 6.11: Low resolution (100μm) OBIC maps recorded at 6 wavelengths: 427.5nm, 525nm, 600nm, 705nm, 825nm and 847.5nm.

Using a large optical spot size it was possible to evaluate quickly the entire area of a dot contact on a device, with a series of six 50x50 point maps being recorded in ~30 min. OBIC measurements examining a 5x5mm area were performed at a low resolution, using a spot size of 100μm. A series of 6 wavelengths was used that covered the range of response for the cell, 427.5nm, 525nm, 600nm, 705nm, 825nm and 847.5nm. These

wavelengths were selected as they provide incident photon energies above and below the expected CdS bandgap (~2.5eV, 427.5nm and 525nm), approaching the expected CdTe bandgap (~1.5eV, 825nm and 847.5nm) and in the range between the two bandgaps (600nm and 705nm). The resultant maps are shown in fig.6.11.

These low resolution maps showed the cell to be reasonably uniform across the contacted region, apart from a small defect in a central position (~X=1500, Y=2000), observed for all wavelengths applied. Because of the poor performance of this defect across the entire wavelength range it is likely to have been caused by either a pinhole in the material, or a small optical blockage. However, as the surrounding area shows relatively high performance it seems unlikely this defect is due to a pinhole, as the a defect resulting from shunting will typically limit performance over a much wider area[12]. The cell displays high *EQE* values for most wavelengths, with a peak value of 0.87 obtained at a wavelength of 600nm. The device displays good uniformity at 427.5nm, which corresponds to a photon energy greater than the CdS bandgap and is therefore expected to be influenced by absorption from the CdS. However, as there is only an approximate *EQE* decrease of 0.2 from the response measured at 600nm, this implies that light transmission through the CdS is high, and that the CdS is relatively uniform: Fluctuations in CdS thickness may be expected to increase the level of non-uniformity observed at this wavelength (Section 6.2.2). For the wavelength range 525-705nm there is very little variation in the level of device response (i.e. the map recorded at 525nm shows only a slight reduction in the *EQE* compared to that recorded at 705nm). For long wavelengths approaching the CdTe bandgap (825nm and 847.5nm) the overall *EQE* value decreases, and for the map recorded at 847.5nm the response is very low. The latter is due to deep penetration of photons having energy greater than the CdTe (absorber's) bandgap.

After low resolution maps were recorded, the resolution of the system was able to be adjusted (without loss of X-Y positioning) and a selected area investigated at a higher resolution.

b) High resolution (~12.5μm) imaging

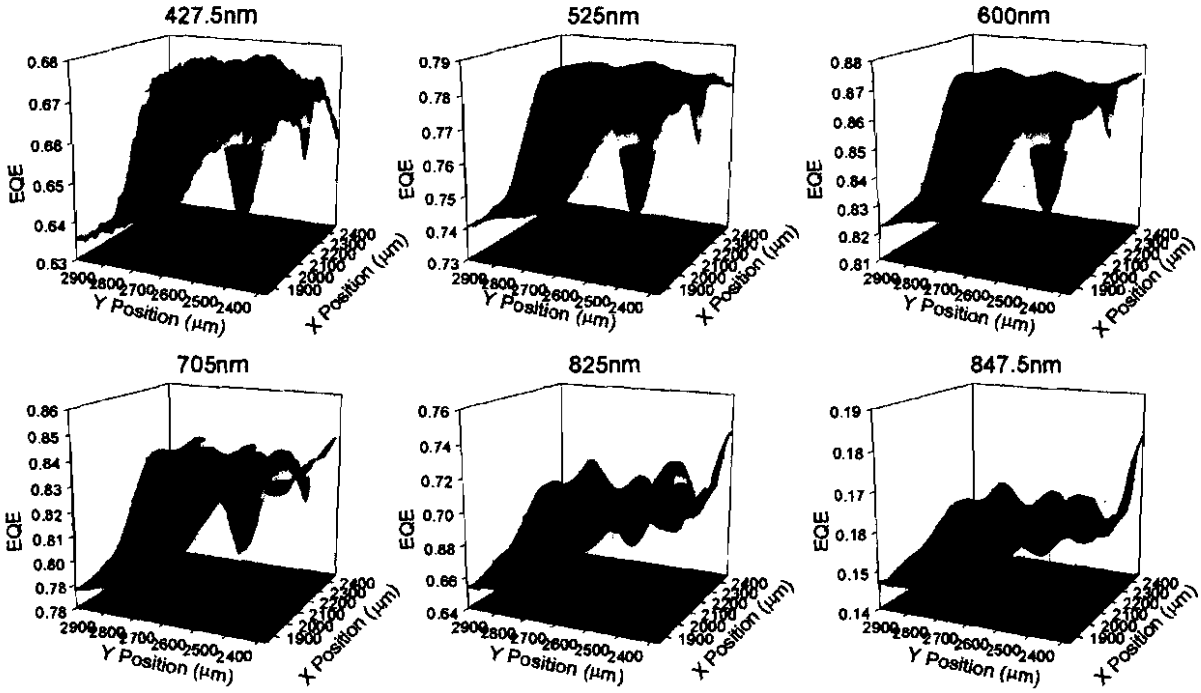

Figure 6.12: High resolution (12.5μm) OBIC maps at 6 wavelengths: 427.5nm, 525nm, 600nm, 705nm, 825nm and 847.5nm. The Z-axis has been scaled to show the maximum range of *EQE* for each wavelength employed, with a separate colour scheme reflecting this range in each case.

Whilst low resolution OBIC maps covering the entire cell area offer a simple evaluation of device performance, high resolution maps may reveal more subtle information about the photovoltaic response of a cell, for a selected area. The performance of a small selected area (0.5x0.5mm), identified from maps shown in fig.6.11, was examined using a spot size of 12.5μm. The same wavelengths were employed, with the resulting maps being shown in fig.6.12. Due to the scaling of these plots it may at first appear that the examined areas have a very non-uniform PV response. However, the maximum *EQE* variation observed across the region is only ~0.08, for all wavelengths utilised. A simple way to compare the uniformity of response from a region examined by OBIC at different wavelengths, is by the maximal variation in *EQE*[11]. By scaling this value using the average *EQE* for each wavelength, the values are normalised and as such are directly comparable. Fig.6.13 shows this *EQE* defined by, (Max *EQE* – Min *EQE*)/Average *EQE*, plotted as a function of the photon energy (the corresponding

light wavelength utilised for each point has been marked for reference). The inset plot shows a comparison between this device and a similar, lower efficiency device. The device being discussed here shows an increase in the variation for photons with energy close to the CdTe bandgap (825 and 847.5nm) and the smallest variation in response at an incident energy close to the CdS bandgap (525nm). The variation decreases slightly for a photon energy below the CdS bandgap (427.5nm) due to some non-uniformities introduced as a result of absorption by the CdS layer. Comparison with the lower efficiency device shows that for lower photon energies there is only a small difference in the level of variation of the cell performance. However, as the incident energy is increased, the lower efficiency device becomes more and more non-uniform by comparison.

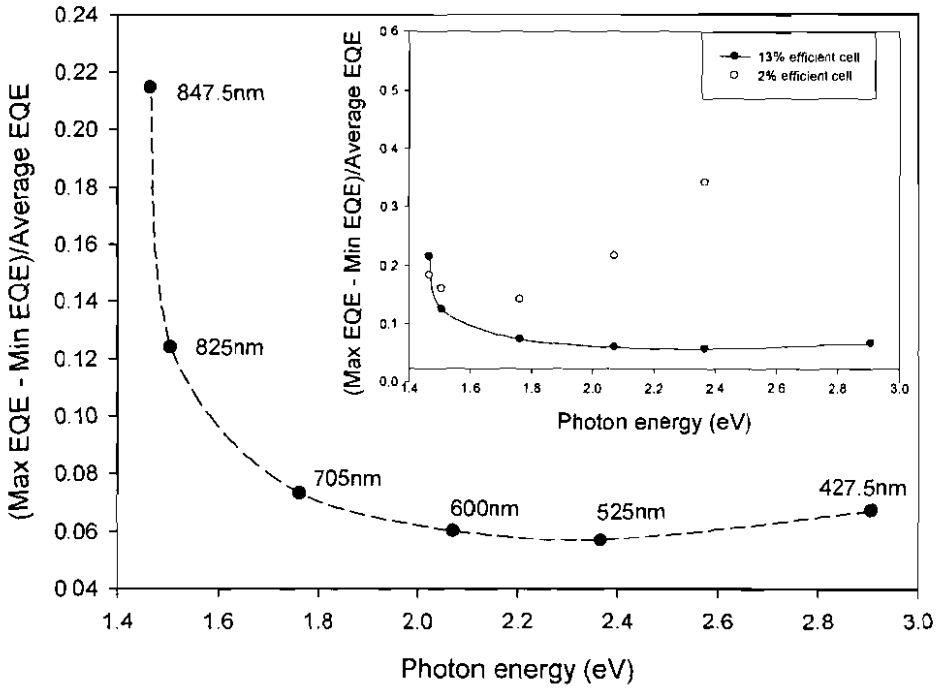

Figure 6.13: *EQE* variation - (Max *EQE* – Min *EQE*)/Ave *EQE*, as a function of photon energy, inset: comparison between high and low efficiency devices

The maps presented in fig.6.12, reveal small localised variations in the device performance. At positions towards the front of the plots ($X \approx 1800\mu m$) there are two regions that display lower performance than the majority of the region. A small defect is

visible in the range, $Y = 2400$-$2500\mu m$, and a much larger one in the range $Y = 2700$-$2950\mu m$. These two regions maintain their poor performance across all wavelengths, but only display a small decrease in EQE (~0.05) in comparison to the rest of the cell. Because of the relatively minor variation in performance, and the persistence of the variations across all wavelengths, they are most likely due to optical rather than electrical defects (e.g. inclusions/damage to glass superstrate or dirt on glass surface). Electrical defects, such as shunts or variations in junction quality, may be expected to hinder performance over a much wider area[12] (in the case of shunting) or show some variation with wavelength (in the case of junction based defects). Maps obtained using longer wavelengths (825nm and 847.5nm) show the development of a number of small localised peaks in the PV response. The peaks are most likely caused by localised variations in the bandgap of the CdTe layer as a result of intermixing between the CdTe and CdS layers (see Sections 3.2.6 and 6.2.2).

c) Detailed multi-wavelength investigation of the absorber band edge region

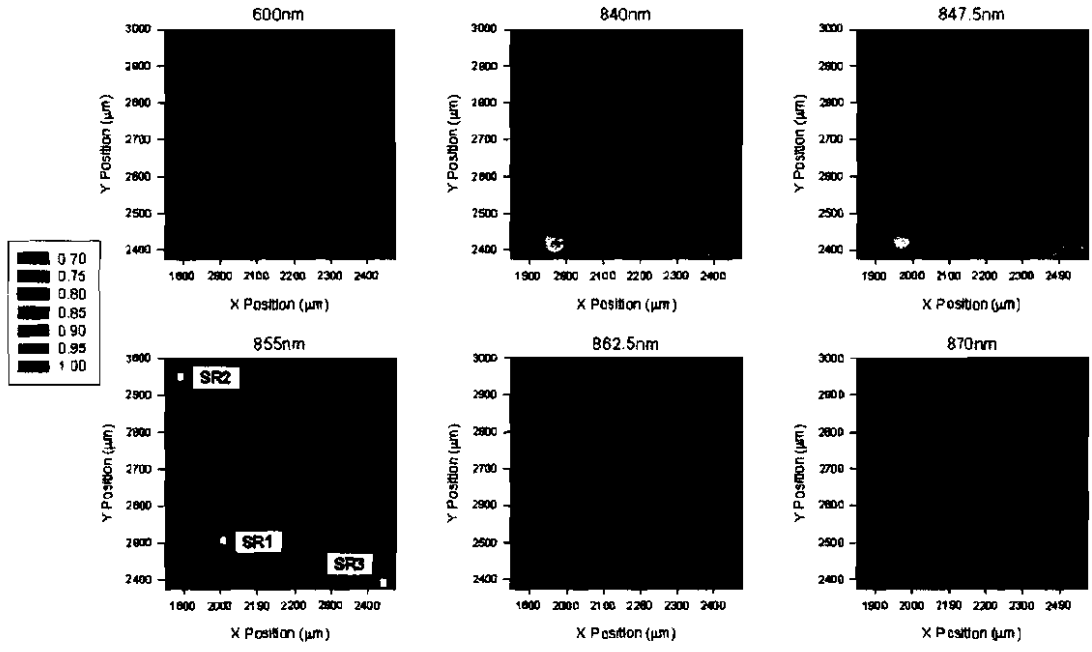

Figure 6.14: Normalised OBIC maps showing non-uniformity development around the CdTe bandgap. Three positions selected for EQE analysis are marked as SR1-3 in the 855nm map. The resulting EQE curves are shown in fig.6.15.

The observed variation for wavelengths around the absorber band edge was more thoroughly examined by recording a series of 5 OBIC maps, taken in the range 840-870nm. The resultant plots are shown in fig.6.14, along with a map taken at 600nm for comparison. The *EQE* has been normalised to 1.0 for each wavelength so as to better show the development of non-uniformities.

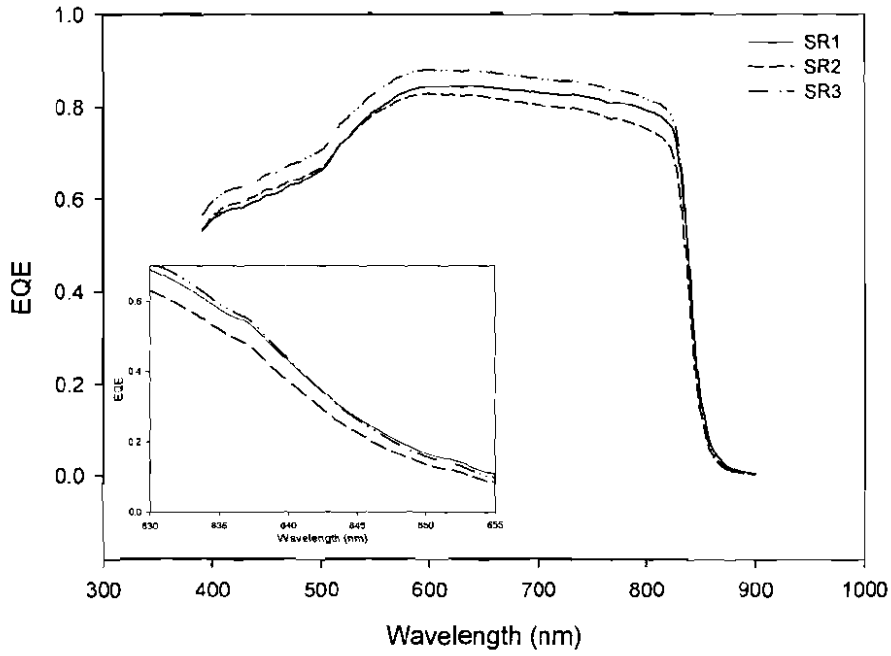

Figure 6.15: Localised EQE measurements from small area OBIC map at: SR1 (X = 150μm, Y = 125μm), SR2 (X = 50μm, Y = 587.5μm) and SR3 (X = 612.5μm, Y = 12.5μm).

Whilst all response is within the 0.95-1.0 range for the map recorded at 600nm, the range of response at wavelengths close to the bandgap is much greater (0.70-1.0). Small areas are seen to develop (X = 150μm, Y = 125μm and X = 612.5μm, Y = 12.5μm) that perform significantly better at longer wavelengths than the majority of the examined area. Two of these areas are marked in fig.6.14 as SR1 and SR3, and localised EQE measurements were taken from these positions. A third measurement was recorded from a position that performs poorly at all wavelengths (SR2). The resulting plots are given in fig.6.15. The EQE curves from the marked positions all show the same basic shape, with a strong response in the 520-825nm range. Position SR3 shows the best response across the majority of the examined wavelength range, however, at longer wavelengths

(approaching the CdTe bandgap) there is a crossover between the curves for positions SR1 and SR3. This can be seen in the OBIC maps in fig.6.14, where position SR1 develops as a "hotspot" as the wavelength increases. This implies the presence of CdTe with a slightly reduced bandgap at position SR1 in comparison to position SR3. This may result due to a localised variation in the amount of intermixing altering the bandgap at this point, leading to poorer performance at the majority of wavelengths but superior performance for wavelengths above the CdTe bandgap. Position SR2 has an improved response in comparison to SR1 at short wavelengths (400-520nm) but shows a significant drop-off in the 520-825nm range. A drop-off over this range is typically ascribed to photons penetrating too deeply for complete collection[21,41] (Section 6.2.2) and will typically be greater for devices with small depletion widths.

6.4.1.4 Discussion

An OBIC system was constructed and shown to be capable of in-depth analysis of CdTe/CdS devices over the entire wavelength range of their response. Measurements made on a single cell demonstrate how the PV uniformity varies as a function of wavelength for both low (100μm) and high (12.5μm) resolutions. By comparison of maps recorded at different wavelengths, it is possible to identify defect sites that may be hidden to OBIC analysis utilising a single wavelength. Non-uniformities may only be apparent within a certain wavelength range, for example, localised variations in the CdTe bandgap were shown to introduce a degree of non-uniformity to OBIC measurements, with certain regions showing enhanced response at longer wavelengths. The system has also been shown to be capable of performing localised EQE measurements at specific areas identified by OBIC analysis, as well as performing EQE analysis for the whole cell area.

6.4.2 Impact of etching on the back contact

Due to the high work function of CdTe, it is necessary to chemically etch the CdTe back surface of CdTe/CdS devices in order to produce a tellurium-rich layer and allow formation of a back contact having a low barrier height (Section 3.2.7). Numerous etching solutions are used to achieve a good surface for contacting, one of the most commonly used being the nitric-phosphoric (NP) acid etch. Whilst this is considered a necessary step for the production of efficiency devices, it may nevertheless be expected

to impact upon the uniformity of device response. This section describes an OBIC investigation into the performance of CdTe/CdS devices having undergone NP etching for times between 0 and 600s.

6.4.2.1 J-V and OBIC analysis

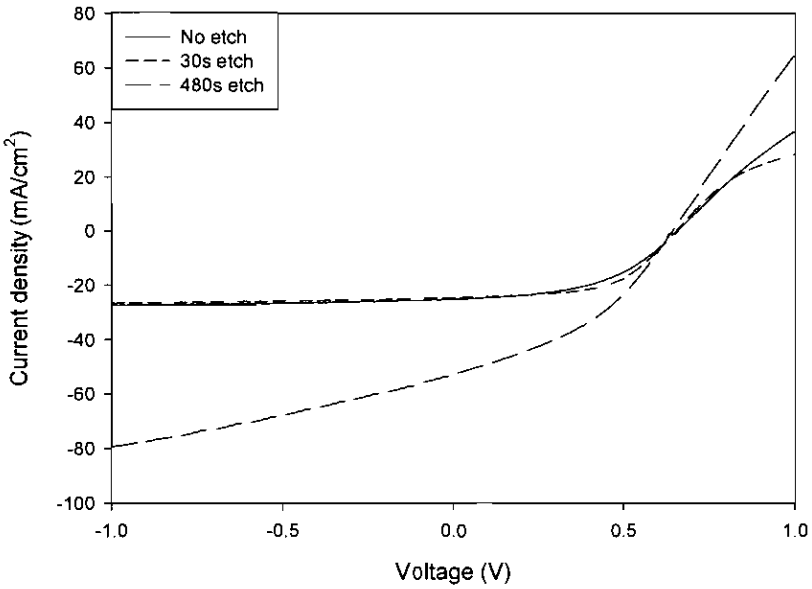

Figure 6.16: *J-V* curves recorded for ANTEC cells contacted with 2mm diameter Au dots after NP etching for 0, 30 and 480s.

In the production of laboratory scale test cells it is useful to apply a matrix of small back contacts, rather than a single large back contact. This is done in order to test the uniformity of the material and processes. However, as the short circuit current density, J_{sc}, value is dependent on the area of the back contact, the contact area must be accurately known in order for the device efficiency to be correctly determined. It was noted, during *J-V* testing of cells fabricated at Durham University, that test cells with small back contacts (2mm diameter) often had J_{sc} values of greater than 30mA/cm^2. As the CdTe/CdS cell with the highest recorded efficiency[42] (16.5%) only generated 25.88mA/cm^2, this was strong indication of some kind of systematic error. Initial investigations revealed that cells that had undergone a very short (1-5s) or no etch, did not display these inflated J_{sc} values, with values typically being in the range 20-25mA/cm^2. In order to investigate this anomaly a series of eight 1cm^2 samples were cut

from a single large commercial CdTe/CdS solar cell obtained from ANTEC. A series of NP etch times in the range 0-600 seconds were used, with the time being measured from the point the cell was submerged in the etching solution. Each cell was then contacted with four, 2mm diameter, circular back contacts. *J-V* curves were recorded for the four contacts from each sample (generating a total of 32 *J-V* curves). Typical *J-V* curves recorded from three of these samples are shown in fig.6.16, while the average values for η, *FF*, V_{oc} and J_{sc}, determined for each sample are plotted as a function of etch time in fig.6.17.

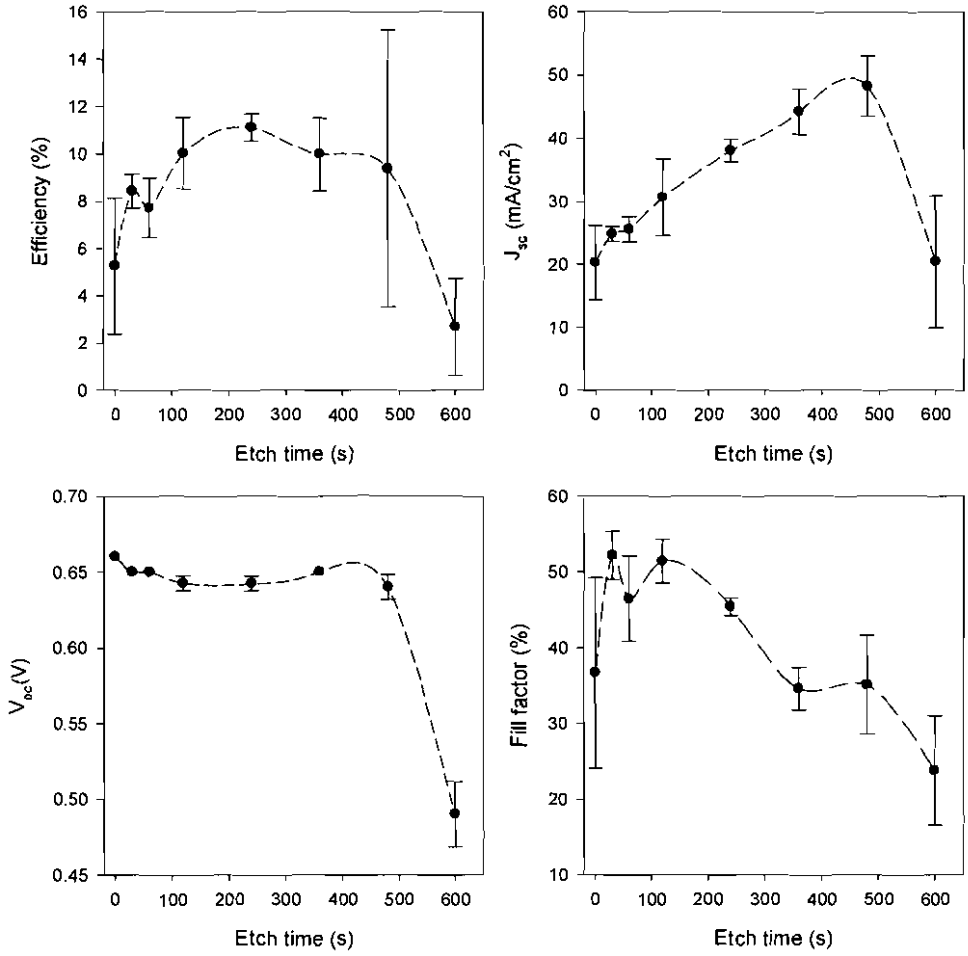

Figure 6.17: Average performance parameters extracted from the *J-V* curves of ANTEC cells (contacted with Au dots) as a function of the NP etching time applied to the CdTe surface. The anomalously high J_{sc} values are discussed in the text. Error bars are +/- 1 standard deviation.

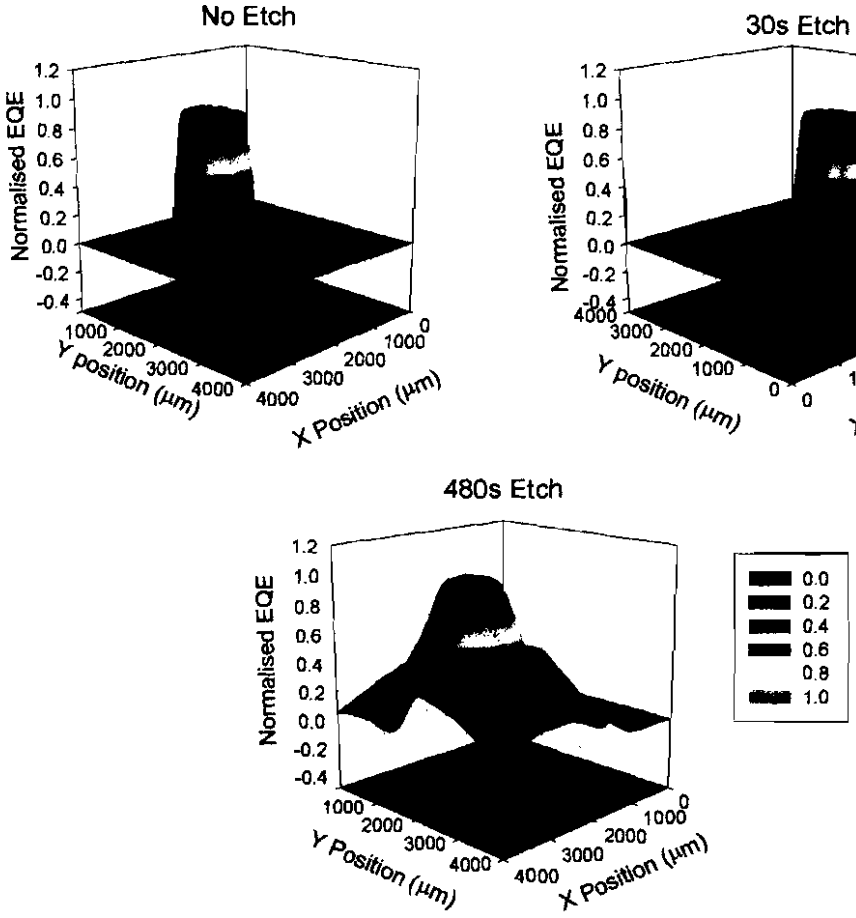

Figure 6.18: 600 nm OBIC maps of cells treated with different NP etch times.

It can be seen from fig.6.17 that there is an increase in the average efficiency of devices with increased etching time, with peak being reached at 240s etch time. However, while the average efficiency decreased for etch times above this, the efficiency of individual contacts was found to further increase. The peak efficiency obtained for a contact from the cell with a 30s etch time was 9.1%, while for the cell etched for 480s that figure increased to 13.3%. This increase seems far too dramatic to be as a simple result of improvement in the back contact performance, that results from etching. The plot of J_{sc} as a function of etch time shows a large increase in the determined values with increased etching time. For an un-etched sample the maximum J_{sc} value obtained was 25mA/cm^2, while for an etch time of 480s this value had more than doubled to 53mA/cm^2, far exceeding the theoretical limit for a CdTe/CdS solar cell. The plots in

fig.6.17 also show that while the J_{sc} values increased with etch time, the V_{oc} and FF values showed an overall decrease, implying the quality of the junction is reduced by prolonged periods of etching. OBIC measurements were performed on the contacts with the highest performance for three cells: i) un-etched, ii) 30s etch and iii) 400s etch. OBIC maps were recorded over a 4mm x 4mm area, using a 100μm spot at a series of six wavelengths (427.5nm, 525nm, 600nm, 705nm, 825nm and 847.5nm). The resulting maps for scans recorded at 600nm are plotted in fig.6.18. For each map the response was normalised such that the peak of response was equated to an EQE of 1.0, with all other values determined as a fraction of this peak value. The effective area of the contact was determined from the OBIC response by calculating the area that displayed a normalised response > 0.3. The contact diameter was then determined from this value by assuming the contact to be a circle of equivalent area. This value (EQE>0.3) was selected as for the un-etched sample examined, it yielded a contact diameter equivalent to that determined by manual measurement (~2.1mm). This "effective contact diameter" for the three cells is plotted as a function of wavelength in fig.6.19.

It can be seen in fig.6.19 that whilst there is little variation in the effective contact diameter as a function of wavelength for each device, there is a significant change in the diameter as a function of the etching time. A small increase is observed in the average diameter for the sample having undergone a 30s etch, in comparison to the un-etched sample (2.1mm to 2.5mm), although little difference can be seen in the OBIC maps shown in fig.6.18. For the sample etched for 480s, it can be seen directly from the OBIC maps that there has been a large increase in the area of the cell contributing to the current generation. The results in fig.6.19 confirm this and show that the effective back contact diameter has more than doubled to an average of 5.1mm. This suggests that the conduction of the back surface has been altered by the prolonged etching process. The increase in efficiency associated with longer etching therefore appears to be as a result of the effective back contact being increased by the action of etching using the NP solution. If the efficiency value for the cell with the 480s etch is recalculated, using the effective contact area of 5.1mm diameter determined by OBIC measurement (instead of the assumed 2mm), the efficiency is estimated to decrease to 6.8%. It is clear therefore that NP etching is capable of introducing a significant error into efficiency measurements.

The increase in effective contact size may be attributable to lateral conduction, since NP etching is known to enrich the surface of CdTe with tellurium, with the thickness of the Te rich layer being found to increase with etch time[43]. It may therefore be expected that this may impact upon the conduction of the back surface, leading to the increase in effective contact diameter and thus J_{sc} observed.

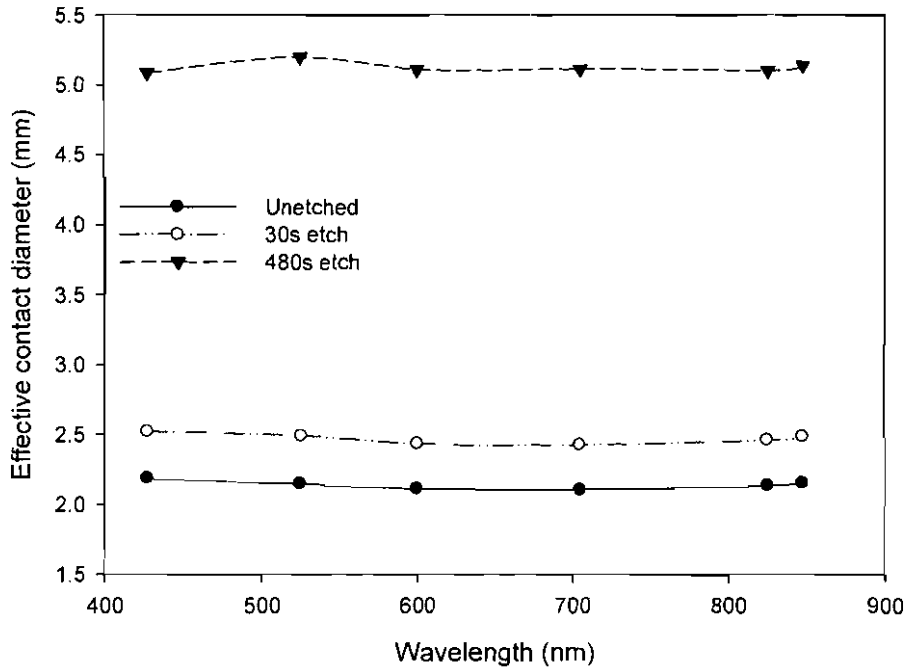

Figure 6.19: Variation of effective contact diameter as a function of wavelength for samples having undergone: i) no etch, ii) 30s etch and iii) 480s etch

The degradation of both the V_{oc} and FF observed was believed to be attributable to the formation of shunts within the device, as prolonged periods of etching are known to reduce the CdTe layer thickness. Under SEM examination large fissures in the CdTe surface were found to have been produced as a result of prolonged etching, which may have acted as shunting pathways. In order to access the impact of these, the shunt resistance of each device was calculated from the reverse bias region of the J-V curves (see Section 2.4.2.3), for the highest performing contact from each device. The shunt resistance is plotted as a function of etching time in fig.6.20. It can be clearly be seen for these results that the NP etching process has significantly reduced the device shunt resistance, further highlighting the negative impact the etching process had on the performance of devices.

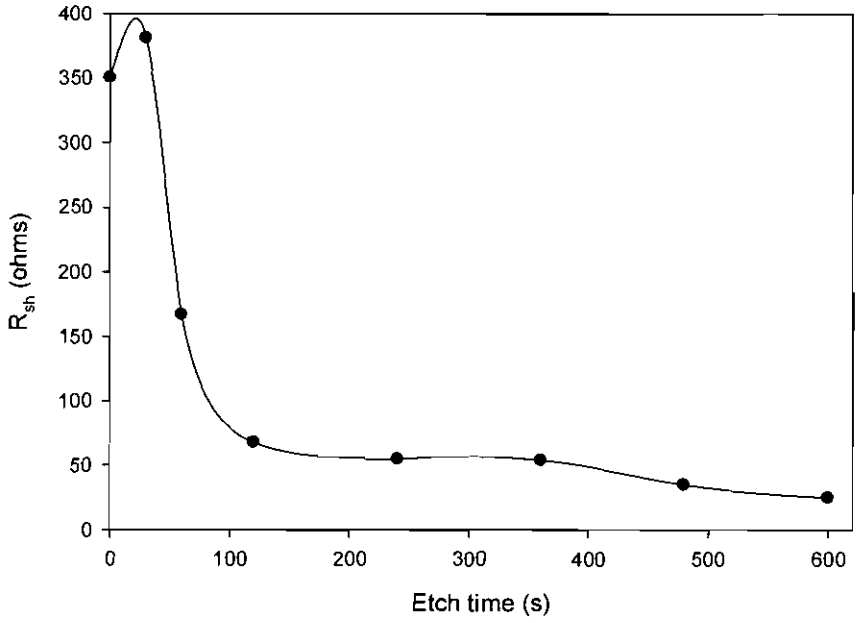

Figure 6.20: Variation of device R_{sh} as a function of NP etch time. The shunt resistance is estimated from the slope of the *J-V* curves under reverse bias (this method is discussed in Section 2.4.2.3).

6.4.2.2 Discussion

The OBIC measurement of devices subjected to NP etching for various times revealed evidence of a systematic error in the device current measurement. Whilst it may be expected that current collection would only occur from within the bounds of the back contact, OBIC measurements revealed this region may be extended after prolonged etching. It is widely accepted that NP etching preferentially etches the grain boundaries in polycrystalline materials (see for example Batzner *et al*[44]), leading to a tellurium rich layer coating the inside of the boundaries. These boundaries may then have the potential to act as conduction pathways thus leading to lateral conduction, and producing the increase in the effective contact area observed. This "spreading" of the back contact was found to lead to an error in the J_{sc} determination, providing the erroneous result that device efficiency was enhanced by long etching periods. Data determined from *J-V* analysis (which assumed the contact size remained constant) suggested that the efficiency increased from a maximum of 9.31%, for a cell with a 30s etch, to 13.31%, for a cell with a 480s etch. Correcting the current density values using the effective contact areas determined by OBIC measurement, meant the efficiency for the cell etched for 480s is in

fact estimated to be 6.8%, representing a significant decrease. Whilst the contacts used in this study may be relatively small (2mm diameter), and as such the introduced error is magnified, there is still the potential for significant miscalculation for larger contact sizes. It was demonstrated here that a contact with a diameter of 3mm may display collection from a region with a 5mm diameter, as a result of NP etching. For a contact with a diameter of 3cm, a similar extension would introduce a 20% increase in the effective area of the contact, leading to a 20% increase in the current density determined and a similarly inaccurate device efficiency calculation. Batzner *et al*[45] reported that CdTe/CdS device efficiency increased with NP etching time, showing an increase with time from an average of ~8.2% to ~10.5% for one NP solution. However, as no qualification was made as to the impact of etching time of the J_{sc} of these devices, it is difficult to ascertain the validity of the observed increase in efficiency for that particular study.

6.4.3 Comparison of PV response from CdTe/CdS devices fabricated by different techniques

The method by which layers within a device are fabricated may be expected to have significant bearing on the uniformity of the device's PV response. This section reports an investigation into the uniformity of CdTe/CdS devices, with various layers deposited using a range of techniques (CBD, CSS and MOCVD), evaluated by OBIC and EQE.

6.4.3.1 OBIC analysis

A series of four devices produced using various techniques have been assessed using OBIC and EQE measurement. The deposition method for each layer in the four samples is given in table 6.1. In each case the devices were subjected to a10s NP-etch, prior to the addition of a matrix of 2mm diameter gold dot contacts. For each cell a suitable representative contact for OBIC and EQE analysis was identified by *J-V* measurement. Normalised OBIC maps recorded at 600nm are shown in fig.6.21 (the data was normalised by scaling with a single coefficient such that the maximum *EQE* value was 1.0), with each map consisting of a 50x50 point grid, recorded using a spot size of 12.5μm and covering a 0.6x0.6mm area. Histograms of the *EQE* values for each sample recorded are shown in fig.6.22.

Sample	Description	CdTe layer	CdS layer	TCO layer	Notes
A	CdS layer deposited by CBD with CdTe layer by CSS – Grown in Durham	CSS	CBD	ITO – Delta technology	Good performance ~11.5%
B	All-CSS device – Grown in Durham	CSS	CSS	ITO - Delta technology	Poor performing cell ~1%
C	All MOCVD device – Grown at Bangor University	MOCVD	MOCVD	ITO - Delta technology	Good performance ~8.5%
D	All-CSS cell from ANTEC	CSS	CSS	(SnO_2/ITO) - ANTEC	Good performance ~9%

Table 6.1: Deposition methods of the four devices evaluated by OBIC and EQE.

A) CSS CdTe/CBD CdS cell

In sample A (fig.6.21A) the majority of the examined area performs at a level close to the peak quantum efficiency value, with the majority *EQE* values determined falling within the 0.95-1.0 range. However, the device displays a few regions that perform below the majority of the examined area (~0.90), seen as green areas in fig.6.21A. The associated uniformity histogram for this map (fig.6.22A) shows a relatively narrow distribution, with a peak close to the maximal *EQE* value, highlighting the good uniformity of this device.

B) All-CSS cell

The OBIC map recorded for sample B (fig.6.21B) is noticeably different and significantly less uniform than that of sample A. Rather than there being a high baseline level of performance, with a few isolated defect areas, the majority of the cell performs well below the peak level, with a few high performance areas. This can be seen by the

double peaked distribution of the histogram in fig.6.22B, where the majority of performance is within the 0.8-0.9 *EQE* range, but there is a smaller peak located at a higher *EQE* value of ~0.97. This suggests that the device is not performing in the expected manner: It may for example have a buried homo-junction. Evaluation of the EQE spectrum (see next section) reveals this to be the case.

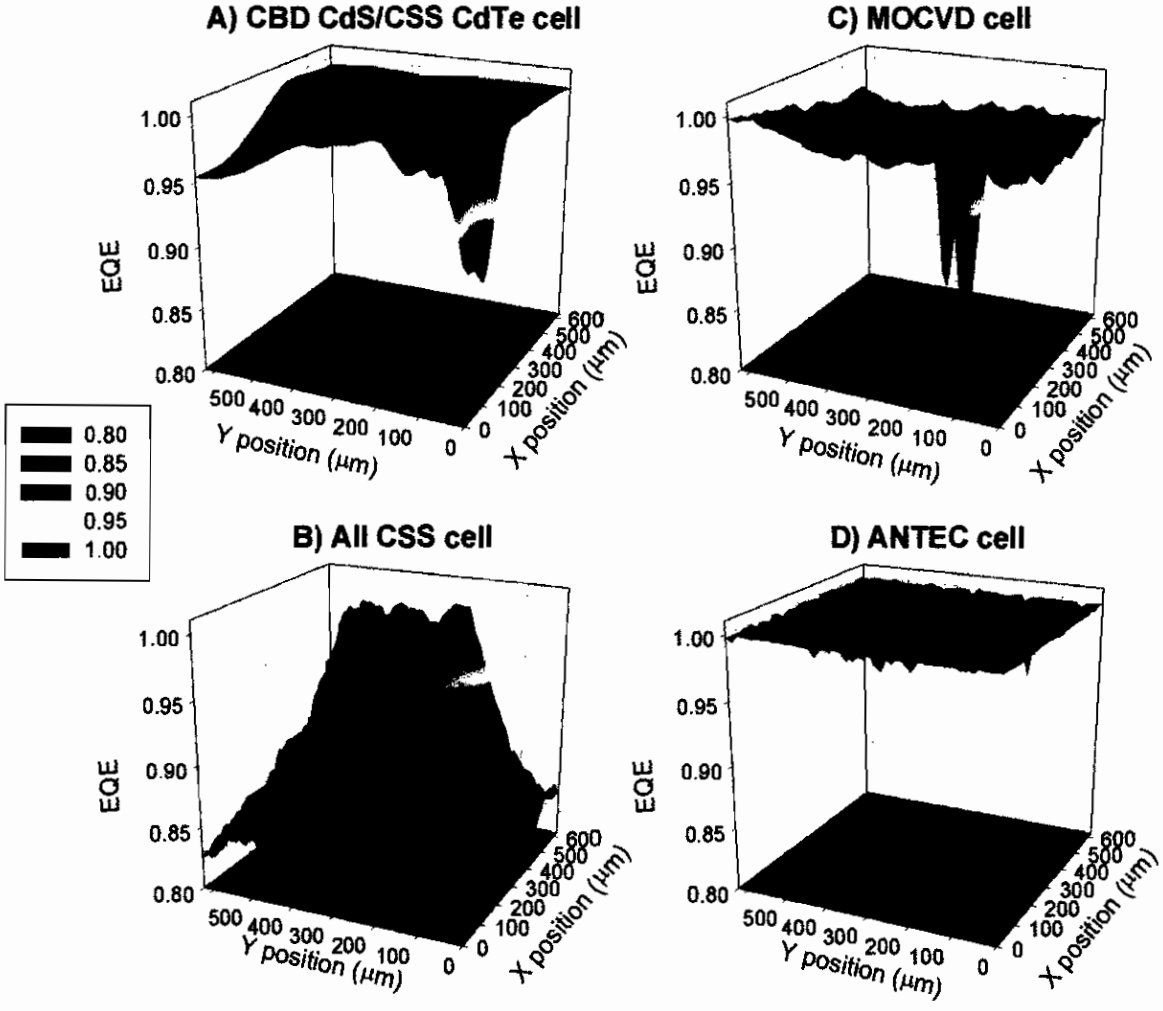

Figure 6.21: OBIC maps (600nm) of CdTe devices fabricated by different methods; A) CBD CdS on ITO with CdTe deposited by CSS, B) all-CSS deposited cell, C) all-MOCVD cell and D) commercial ANTEC cell. For details of the cells see table 6.1.

C) All-MOCVD cell

Under OBIC examination sample C (fig.6.21C) shows a slight decrease in the level of uniformity in comparison to sample A, but is significantly better than sample B. The OBIC map shows that while the majority of the response is close to the peak of performance, similar to sample A, there is a slight variation across the width of the examined area. As a result the uniformity histogram (fig.6.22C) shows a wider distribution in comparison to sample A. There are also some isolated areas of poor performance ($EQE \sim 0.80$-0.85) that are most likely attributable to optical blockages, or possibly to pinholes within the CdTe and CdS layers. In fact visual inspection of MOCVD-grown CdS layers often reveals visible circular blemishes.

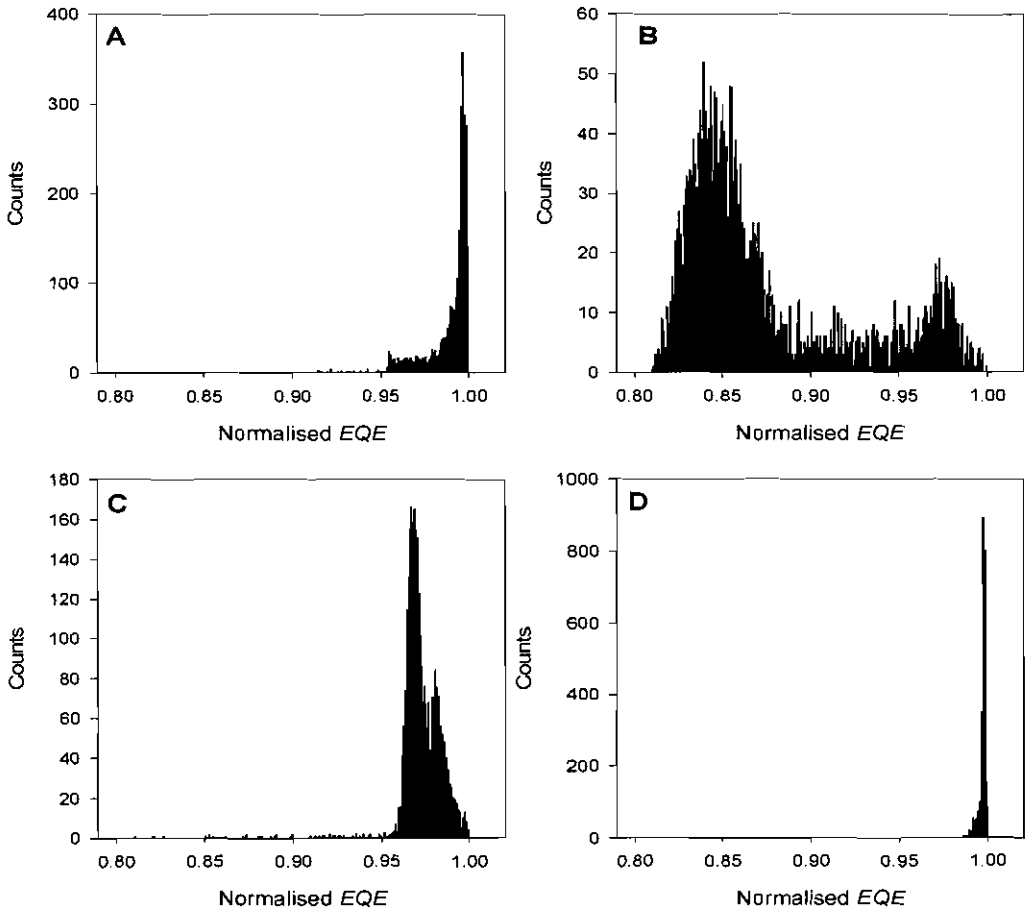

Figure 6.22: Normalised histograms for small area OBIC maps recorded for various types of CdTe solar cell; A) CBD CdS on ITO with CdTe deposited by CSS, B) all-CSS deposited cell, C) all-MOCVD cell and D) commercial ANTEC cell. The data was extracted from the OBIC maps in fig.6.21.

D) ANTEC cell

Sample D shows the most uniform OBIC response (fig.6.21D) of the four devices examined, with the entire examined area showing an *EQE* response in the 0.97-1.00 range. There are only a few minor defect sites, which are very small in size and induce only a small reduction in the *EQE* below the baseline level of performance. As a result the response histogram has a very narrow distribution, revealing this cell to have the highest degree of uniformity for the four devices examined.

6.4.3.2 EQE analysis

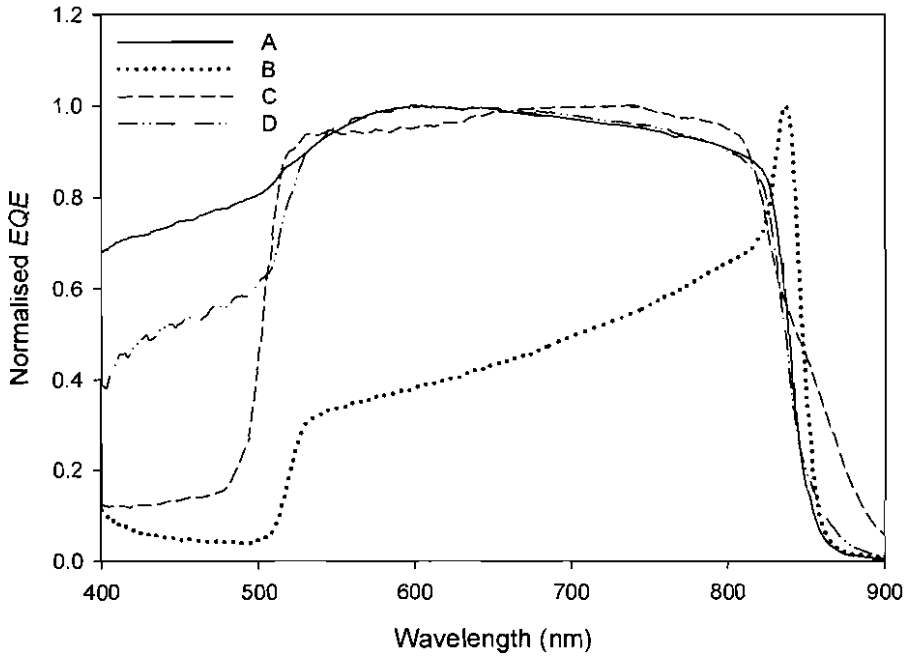

Figure 6.23: Normalised EQE curves for various cell types; A) CBD CdS on ITO with CdTe deposited by CSS, B) all-CSS deposited cell, C) all-MOCVD cell and D) commercial ANTEC cell.

EQE measurements for all of the cells examined by OBIC above were made using a light spot that covered the entire contacted area for each device. The resulting curves have been normalised (by scaling each curve such that the maximum *EQE* value is 1.0) and are shown in fig.6.23.

The devices that displayed the most uniform OBIC response (samples A and D) have similar EQE curves. Both display what may be described as a "typical" shape, with a

relatively uniform response in the 520-840nm range and cut-offs associated with the CdS and CdTe bandgaps at ~520nm and ~840nm respectively. There are some subtle differences between the curves with the CBD CdS based device (sample A) showing improved performance at wavelengths <520nm (for photon energies below the CdS bandgap), suggesting this device contained a thinner CdS layer.

The EQE curve for sample B shows a significantly different response, with a shape characteristic of a cell containing a buried homo-junction (*n*-CdTe/*p*-CdTe, see Sections 3.2.4.3 and 6.2.2). As a result the junction is further toward the back contact than for a hetero-junction and the performance of the device is therefore limited for high photon energies, as these are more likely to be absorbed towards the front of the cell and excitation thus occurs away from the depletion region. The peak in performance occurs for photons with energies close to the CdTe bandgap, as these penetrate deeper into the CdTe layer and are more likely to excite electrons within the depletion region. This leads to the peak observed at ~850nm in fig.6.23. The presence of this buried homo-junction explains the poor performance of sample B, as devices containing buried homo-junctions were generally found to be of lower efficiency. Localised EQE measurements were also performed on sample B to determine the cause of the non-uniformity observed using OBIC analysis (fig.6.21B). These measurements revealed that for the better performing positions the EQE curves showed a more typical hetero-junction type response (i.e. similar to curves A and D) in comparison to lower performance areas which showed buried homo-junction behaviour. This implied that for the good performing region the junction was located closer to the device front surface and for poor performing areas the homo-junction was more deeply buried. This local variation in the junction position in this device therefore appears to be the principle cause of the high non-uniformity observed.

The cell deposited by MOCVD (sample C) displayed a distinctive EQE response. Whilst there is low response below ~500nm indicating thick CdS, of more interest is the extended response in the long wavelength region compared to the sublimation grown cells. The CdTe layer in this device was fabricated by an MOCVD technique that incorporated in-situ arsenic doping to improve the device performance (full details of this method may be found in Barrioz *et al*[46]). It appears from the EQE results presented here

that the incorporation of arsenic during growth has served to affect a reduction in the CdTe bandgap from the typical 1.5eV: This is discussed at the end of the next section.

6.4.3.3 Discussion

OBIC and EQE measurements of different CdTe/CdS device types revealed varying levels of uniformity and distinct differences in the shape of the EQE curves. The most uniform device responses were observed for a device fabricated using CBD CdS and for a commercial (ANTEC) cell. The all-MOCVD cell had a reasonably uniform PV response, albeit with a slight variation in the baseline level of the response. The device did display two strong defect points, these may be due to pinholes in the CdS (which are common), or possibly optical defects (e.g. dust, inclusions in the glass) rather than as a result of the device fabrication, however the cause cannot be identified without further physical investigation.

EQE measurements of these devices revealed significant information about the nature of the junction and CdTe layer of these devices. It was noted that both the ANTEC cell (sample D) and CBD CdS based cell (sample A) displayed what may be described as typical EQE curves for CdTe/CdS hetero-junction devices, whilst the all-CSS (sample B) and all-MOCVD (sample C) displayed atypical responses. Sample B clearly displayed a buried homo-junction response, which provided an explanation for the poor performance of the device. Comparison of the fabrication process of this device with that of sample A, allows insight to be drawn as to the underlying cause of the buried homo-junction formation. Samples A and B were both grown using the same substrate (Delta technology ITO coated glass) and CdTe deposition process, with the only difference in their growth being the CdS deposition process. It therefore appears at first sight that CBD CdS favours a normal junction whereas CSS CdS encourages a buried homo-junction. Additional evidence of the mechanism is provided by the good performance of the all-CSS ANTEC cell (D). It differs from the poor-performing sample B only in that the TCO is capped by a tin oxide layer. The following explanation of the results for samples A, B and D is postulated: Out diffusion of In from ITO into the CdTe is known to cause n-type doping which would act to shift the junction deeper into the CdTe[47]. Such out-diffusion is blocked by the SnO_2 capping layer in sample D. In sample A, the low temperature CBD

deposition of CdS does not cause out-diffusion of In and moreover any subsequent diffusion (during CdTe growth and processing) is contained by the CdS. Hence both A and D do not suffer from buried junction formation. However, in the case of sample B, the high temperature CSS deposition of CdS causes significant out-diffusion which is deleterious to the completed devices.

The differences observed in the EQE measurement for sample C in comparison to the others examined was particularly noteworthy, as the device displayed extended performance at wavelengths >845nm. This provides evidence that the bandgap of the CdTe layer in the MOCVD sample is reduced in comparison to the other samples. The key difference between the MOCVD material and the other samples is that the former includes concentrations of As[46] up to 1.5×10^{19} atoms/cm^3, as described in Section 5.2.3. Hence it may be speculated that the extended performance at wavelengths >845nm results from the incorporation of As during CdTe growth, perhaps as a compound of As or by introducing a significant impurity band tail.

6.4.4 Effect of varying the CdTe thickness grown by CSS

The thickness of the CdTe layer in CdTe/CdS solar cells may directly impact upon the conversion efficiency of devices. Layers that are too thin may have voids in the material and lead to shunting, devices with thick CdTe layers may have higher series resistance, thus reducing device performance. Therefore, the uniformity of PV response may be expected to vary as a function of CdTe layer thickness. This section reports an investigation into the performance of the devices of varying CdTe thickness, evaluated by *J-V*, EQE and OBIC analysis.

6.4.4.1 Device fabrication

A series of CdTe/CdS cells were produce with CdTe thickness in the range 2-6μm. Devices were fabricated using TEC8 fluorine doped tin oxide (FTO) coated glass substrates (5 x 5 cm), purchased from Pilkington. CdS layers were deposited at a thickness of 350nm by CSS under 1Torr of nitrogen. Source and substrate temperatures of 650°C and 540°C respectively were used, with the growth time being 3 minutes. Prior to CdTe deposition, the CdS layers were subjected to a 2 minute anneal under 3Torr of hydrogen at 400°C. This was performed in the CdTe deposition chamber and was done in

order to remove any oxides phases that may have formed on the CdS surface. Three different thicknesses of CdTe (2,4, and 6μm) were deposited onto the CdS layers, with the deposition being carried out under 2Torr of oxygen and using source and substrate temperatures of 600°C and 520°C respectively. The completed CdTe/CdS structures were treated with a 200nm layer of $CdCl_2$ before each sample was split into 2.5x2.5cm quarters, these then being subjected to a range of annealing times (20-50mins) at 400°C. This was done so as to ensure that the $CdCl_2$ treatment was optimised for each CdTe thickness used. The CdTe back surface was prepared for contacting by a 10s NP etch, before a series of 2mm diameter gold back contacts were applied by vacuum evaporation. Each 2.5x2.5cm sample had approximately 25 gold back contacts applied to it.

6.4.4.2 *J-V* analysis

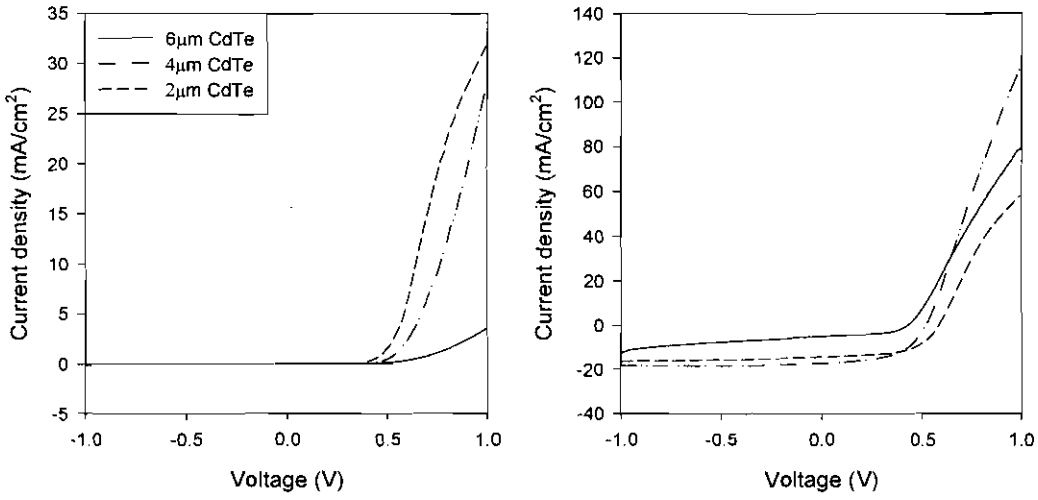

Figure 6.24: *J-V* curves for devices with different CdTe thickness measure in the dark (left) and under AM1.5 illumination (right).

The performance of each device was evaluated by recording *J-V* curves from each contact dot, with ~300 *J-V* curves being recorded in total. Representative *J-V* data curves taken in both the light and the dark for each CdTe thickness, are shown in fig.6.24. The curves shown were all recorded from contacts located in a central position, from the quarters that had undergone a 20min $CdCl_2$ anneal. The measurements made in the light reveal a reduction in the amount of power generated in the cell from the thickest (6μm) to the thinnest CdTe layer (2μm). The curves recorded in the dark show a decrease in the

gradient of the curve in forward bias with increased CdTe thickness, implying an increase in the series resistance of the devices.

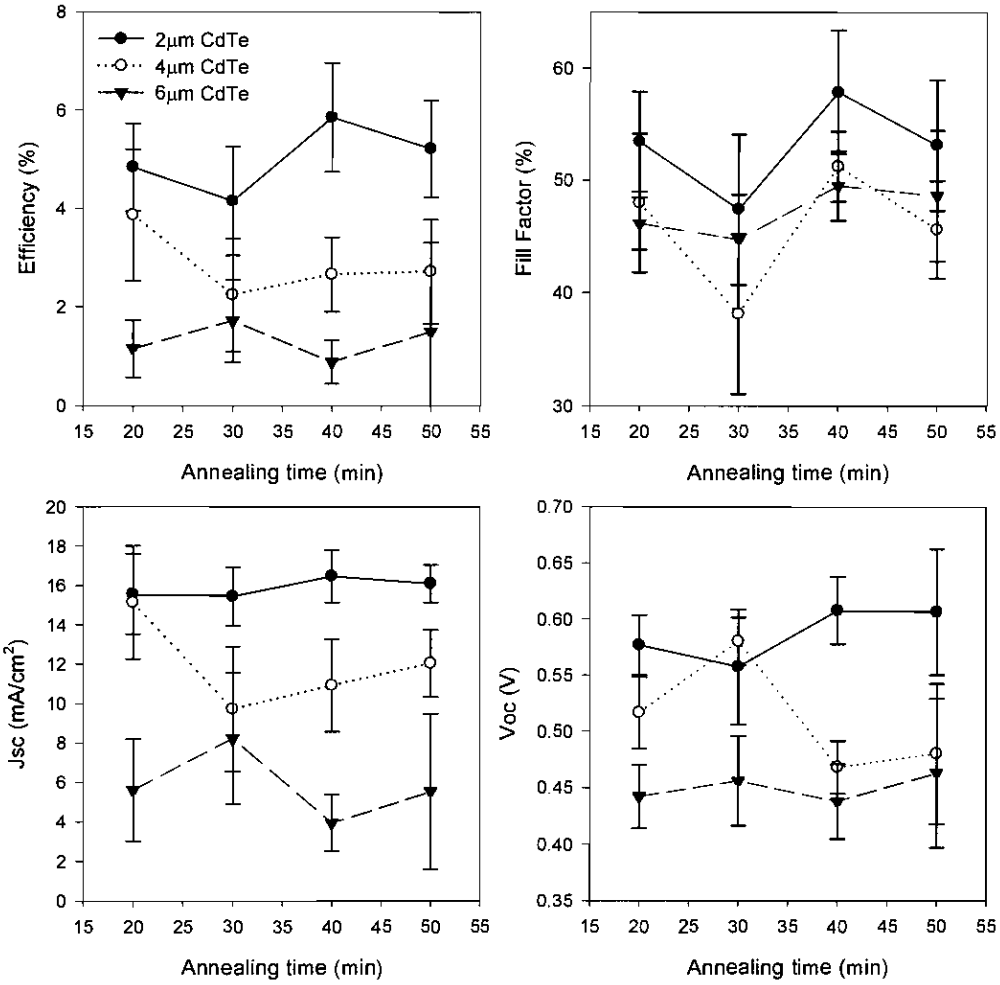

Figure 6.25: Variation of device performance parameters with annealing time for devices with different CdTe layer thickness (each point represents an average of 25 *J-V* measurements).

For each contact the values for the efficiency, fill factor, short circuit current density and open circuit voltage were extracted from the *J-V* curves. An average value (taken from approximately 25 contact positions) for each parameter was determined for every 2.5x2.5cm sample. The resulting values are plotted as a function of $CdCl_2$ annealing time, for each CdTe layer thickness, in fig.6.25. The cell with the thinnest absorber layer thickness (2μm) was found to have the highest efficiency for all treatment times, with η=5.85%, FF=57.86%, J_{sc}=16.47mA/cm^2 and V_{oc}=0.61V being the peak of performance

(achieved after an anneal time of 40min). The devices with thicker CdTe layers showed a reduction in performance and did not display significant improvement with an increased anneal time. The device with the thickest CdTe layer (6μm) was the poorest performing cell, with particular reduction observed in the J_{sc} values. The peak J_{sc} values determined for this device was 8.22mA/cm^2, less than half that of the cell with the thinnest absorber layer. The determined V_{oc} values showed a similar trend, with the cell with the thinnest absorber layer providing the highest V_{oc} values (although for an anneal time of 30min the V_{oc} was higher for the 4μm cell). The variation in fill factor is less systematic, with an overlap in the determined values for cells with 4μm and 6μm CdTe layers. However, the 2μm CdTe device again provides the highest values.

6.4.4.3 OBIC and localised EQE analysis

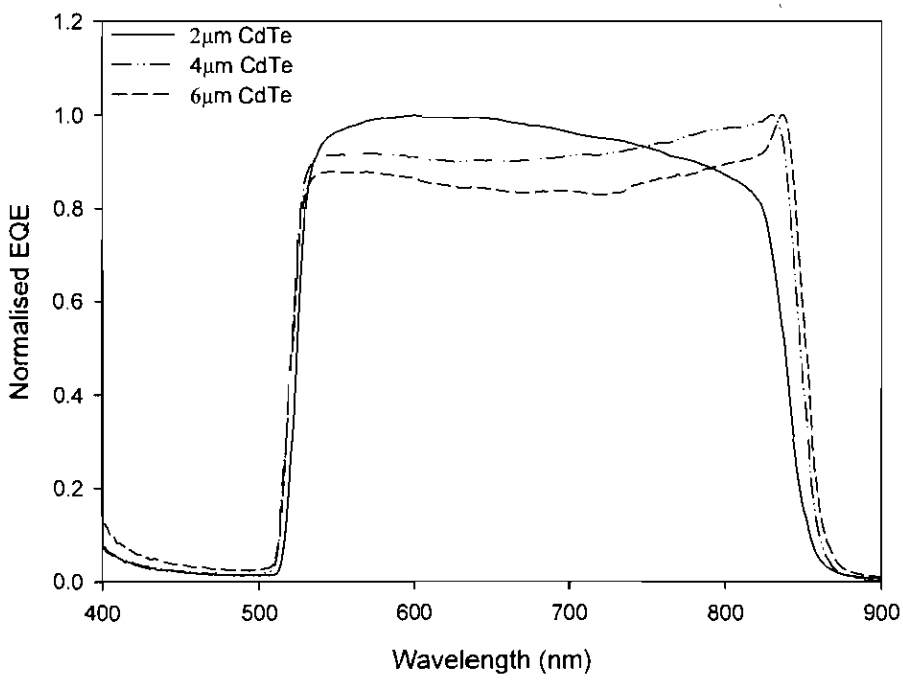

Figure 6.26: Normalised spectral response curves for cells with different CdTe thickness (2, 4 and 6μm) and subjected to identical $CdCl_2$ annealing at 400°C for 40mins.

For each CdTe device thickness interrogated (2, 4 and 6μm) the samples annealed at 40mins in $CdCl_2$ were selected for further investigation. For each sample, a dot contact having good performance was selected. These contacts were then examined by EQE

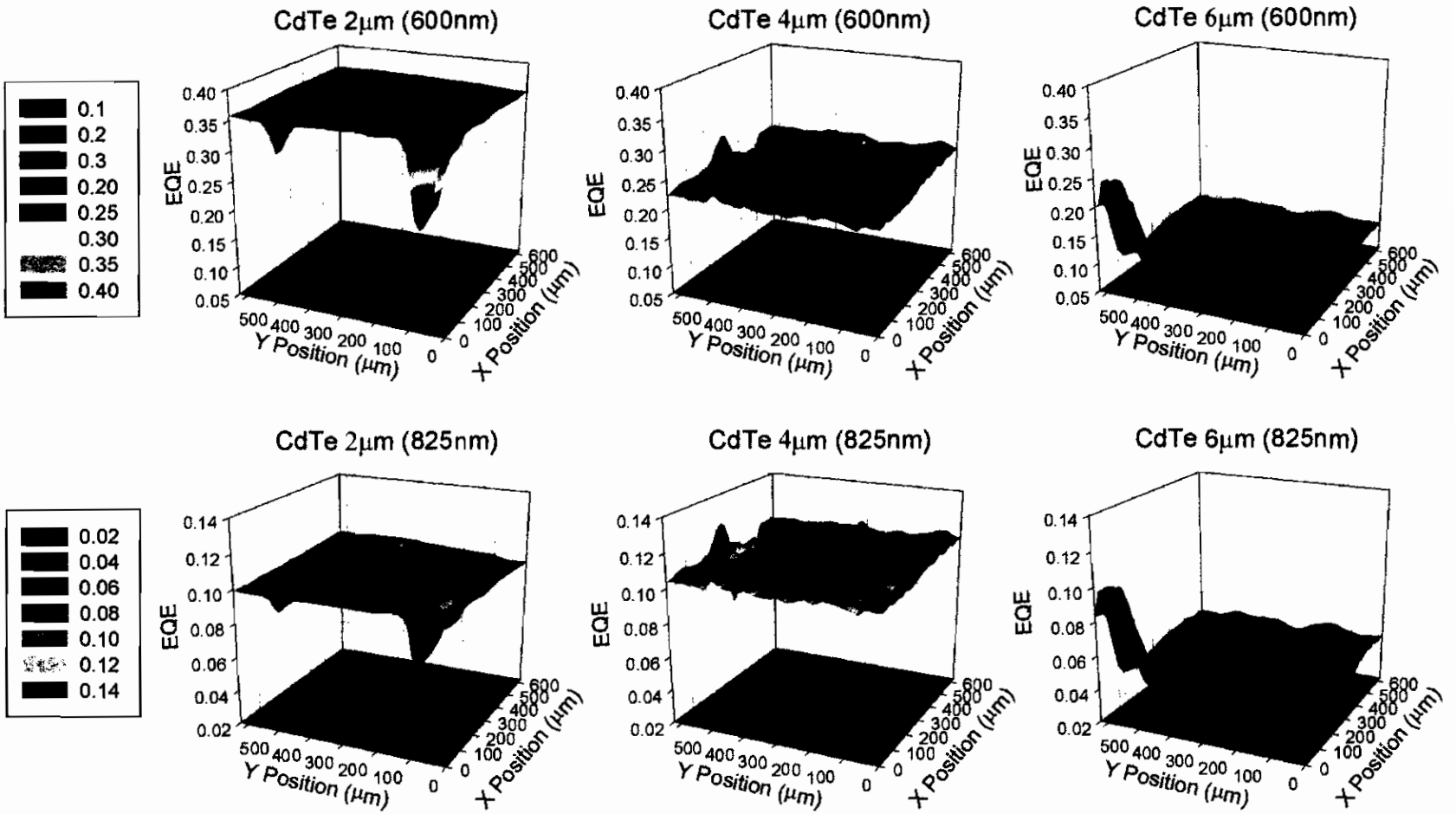

Figure 6.27: OBIC maps of cells with different CdTe layer thickness measured at 600nm and 825nm. All maps recorded at 600nm have the same *EQE* axis scaling, as do all those recorded at 825nm.

measurement, using a light spot that illuminated the entire contact, and by OBIC analysis to determine the uniformity of the response.

Fig.6.26 shows the normalised EQE curves determined for each device. Whilst the device with a 2μm thick CdTe layer displays a normal device response, the devices with thicker CdTe layers show an altered response. For these devices (4μm and 6μm CdTe layers) the response curves had a maximum *EQE* value at ~845nm, typical of a buried homo-junction (Section 6.2.2). The buried-junction response is more pronounced for the 6μm device than in the 4μm device, suggesting that the junction is moving further from the front wall of the cell with increasing CdTe thickness. OBIC maps of the same three devices were recorded at a series of six wavelengths (427.5nm, 525nm, 600nm, 705nm, 825nm and 847.5nm) for a 0.6 x 0.6mm area using a 12.5μm optical spot size. The resulting maps for incident wavelengths of 600nm and 825nm are plotted in fig.6.27. As has been discussed previously, a simple measure of the *EQE* variation over an area examined by OBIC may be obtained by calculating the value: (Max *EQE* – Min *EQE*)/Average *EQE*. This value is plotted as a function of wavelength in fig.6.28 for the three samples examined.

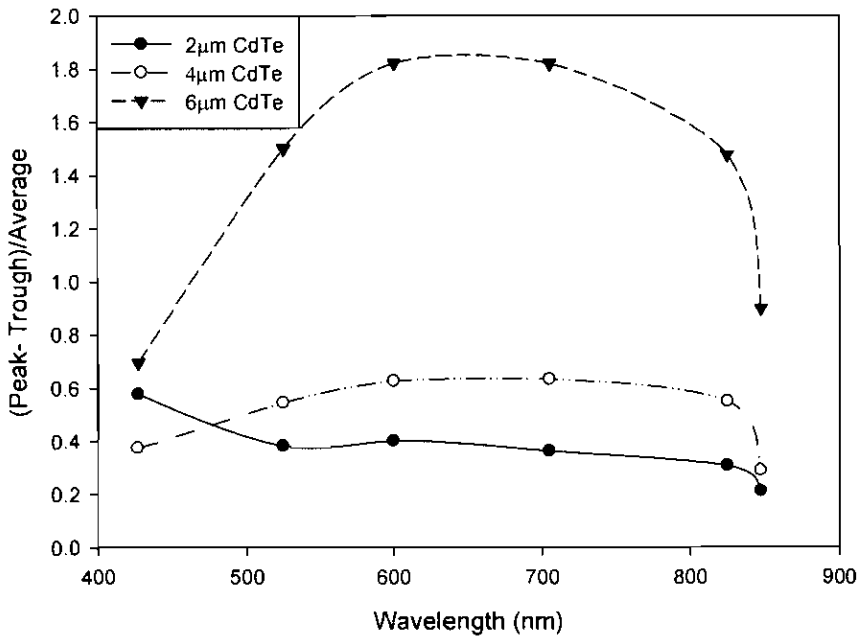

Figure 6.28: Variation of *EQE* as a function of wavelength, for devices with different CdTe thickness (2, 4 and 6μm).

For the maps recorded using a 600nm wavelength, the average *EQE* of the examined areas is increased as the CdTe layer thickness decreases (0.10 for 6μm, 0.23 for 4μm and 0.36 for 2μm). The OBIC maps of the cell with a 2μm CdTe layer show that the majority of the examined area performs at levels close to the cell's peak performance, seen as red or orange areas on the plots in fig.6.27. Only a few small areas show performance lower than that of the bulk response. By contrast the majority of the area of each cell with a thicker absorber layers is below that of the peak performance observed within a given region. The relative uniformity of the device can be better understood by comparison of the curves in fig.6.28, which show the overall variation of response is greatly reduce for the thinnest absorber layer cell. It is interesting to note that all curves reveal an improvement in the uniformity of PV response at 847.5nm (a photon energy close CdTe bandgap value) in comparison to scans performed at shorter wavelengths. This result is in opposition to that for devices fabricated on CBD deposited CdS reported in this thesis (discussed in Section 6.4.1) and that in work reported by Hiltner[11], which both showed a decrease in uniformity at longer wavelengths.

6.4.4.4 Discussion

It is shown in Section 6.4.4 that device performance was improved by a reduction in the CdTe layer thickness, with PV uniformity determined by OBIC being increased as a result. Devices with thick CdTe layers (4μm and 6μm) clearly displayed buried homo-junction characteristics under EQE examination, whilst the thinnest CdTe layer device (2μm) displayed a typical hetero-junction response. However, it is unclear from these results whether a hetero-junction had in fact been formed, or whether the homo-junction has simply been brought towards the front surface by virtue of the reduced CdTe thickness. In instances where a homo-junction is formed close to the front surface there is no way to distinguish it from a hetero-junction using the methods reported here (these junction types may however be distinguished using cross sectional EBIC analysis). This may explain the significant increase in device performance seen for the thinner device, a result which would not typically be expected as devices with thinner CdTe layers are more prone to performance losses due to shunting as a result of pinholes within the layer.

The fact that homo-junctions were observed at all is in itself an unexpected result. In Section 6.4.3 the formation of buried a homo-junction was attributed to In diffusion from the ITO layer, leading to strong *n*-type doping of the CdTe layer. However, as work carried out in this section was performed solely on FTO, In diffusion is clearly not the cause of the homo-junction formation. The exact cause is unclear from these results, but it seems probable that it is as a direct result of the CdS layer, as devices fabricated on CBD CdS were not found to display buried homo-junctions. In Chapter 8 the formation of buried homo-junctions in CSS CdS based devices fabricated using FTO substrates is again discussed. Various methods to correct this problem are reported and the reader is referred there for further information.

6.5 Summary and conclusion

A system has been developed that is capable of evaluating the PV response of devices with complete spectral resolution. The system has a maximum resolution of 12.5μm and is capable of performing localised EQE measurements on positions of interest that have been identified by OBIC analysis. It has been shown that the system is capable of identifying defect positions in CdTe solar cells, as well as showing the variation in uniformity of response as a function of wavelength (Section 6.4.1). Investigation into the effect of the NP etching process on the device back contact, revealed etching to potentially introduce a significant error into device current density calculations due to lateral conduction (Section 6.4.2). Comparison between devices fabricated by different methods revealed significant variation in the uniformity determined by OBIC and also the EQE response (Section 6.4.3). Formation of buried homo-junctions in CSS CdS devices is ascribed to In diffusion from ITO substrates, leading to *n*-type doping of the CdTe layer. The extension of EQE response observed in MOCVD based devices is attributed to the inclusion of in-situ arsenic doping. Buried homo-junction structures were again observed for devices fabricated using FTO substrates (Section 6.4.4), but significant improvement in PV uniformity and device efficiency, were observed by reduction of the CdTe layer thickness.

The results in this chapter demonstrate that spectrally resolved OBIC analysis and associated EQE measurements may provide significant information into the nature and performance of CdTe/CdS devices.

6.6 References for Chapter 6

1 S. Smith, P. Zhang, T. Gessert, and A. Mascarenhas, Applied Physics Letters **85,** 3854-3856 (2004).

2 S. A. Galloway, P. R. Edwards, and K. Durose, Solar Energy Materials and Solar Cells **57,** 61-74 (1999).

3 F. S. Goucher, G. L. Pearson, M. Sparks, G. K. Teal, and W. Shockley, Physical Review **81,** 637-638 (1951).

4 M. Acciarri, S. Binetti, A. Racz, S. Pizzini, and G. Agostinelli, Solar Energy Materials and Solar Cells **72,** 417-424 (2002).

5 S. Damaskinos, Solar Cells **26,** 151-158 (1989).

6 R. J. Matson, K. A. Emery, I. L. Eisgruber, and L. L. Kazmerski, in *Conference Record of the Twelfth European Photovoltaic Solar Energy Conference* (Amsterdam, The Netherlands, 1994), 1222.

7 G. Agostinelli and E. D. Dunlop, Thin Solid Films **431,** 448-452 (2003).

8 S. A. Galloway, A. J. Holland, P. R. Wilshaw, A. W. Brinkman, and K. Durose, in *Conference Record of the Thirteenth European Photovoltaic Solar Energy Conference* (Nice, France, 1995), 2072-2075.

9 M. De Vittorio, R. Cingolani, M. Mazzer, and D. B. Holt, Review of Scientific Instruments **70,** 3429-3431 (1999).

10 J. F. Hiltner and J. R. Sites, Materials Research Society Symposium Proceedings **668,** H9.8 (2001).

11 J. F. Hiltner, PhD Thesis, Colorado State University, 2001.

12 J. R. Sites and T. J. Nagle, in *Conference Record of the Thirty-First IEEE Photovoltaics Specialists Conference* (Lake Buena Vista, Florida, 2005), 199-204.

13 J. F. Hiltner and J. R. Sites, in *Conference Record of the Sixteenth European Photovoltaic Solar Energy Conference* (Glasgow, 2000), 1-4.

14 J. F. Hiltner and J. R. Sites, in *Conference Record of the Twenty-Eighth IEEE Photovoltaic Specialists Conference* (Anchorage, Alaska, 2000), 543-546.

[15] J. P. Boyeaux, A. Kaminski, N. Ferrer, S. Berger, and A. Laugier, in *Conference Record of the Twenty-Eighth IEEE Photovoltaic Specialists Conference* (Anchorage, Alaska, 2000), 319-322.

[16] A. Kaminski, O. Breitenstein, J. P. Boyeaux, P. Rakotoniaina, and A. Laugier, Journal of Physics:Condensed Matter **16,** S9-S18 (2004).

[17] J. Carstensen, G. Popkirov, J. Bahr, and H. Foll, in *Photovoltaic and Photoactive Materials - Properties, Technology and Applications; Vol. 80*, edited by J. M. Marshall and D. DimovaMalinovska (2002), 321-324.

[18] A. R. Davies, J. R. Sites, R. A. Enzenroth, W. S. Sampath, and K. L. Barth, Materials Research Society Symposium Proceedings **1012,** 157-162 (2007).

[19] B. E. McCandless and S. S. Hegedus, in *Conference Record of the Twenty-Second IEEE Photovoltaic Specialists Conference* (Las Vegas, 1991), 967-972.

[20] J. P. Enriquez, E. G. Barojas, R. S. Gonzalez, and U. Pal, Solar Energy Materials and Solar Cells **91,** 1392-1397 (2007).

[21] S. H. Demtsu and J. R. Sites, in *Conference Record of the Thirty-First IEEE Photovoltaic Specialists Conference* (Lake Buena Vista, Florida, 2005), 347-350.

[22] C. S. Ferekides, K. Dugan, V. Ceekala, J. Killian, D. Oman, R. Swaminathan, and D. L. Morel, in *Conference Record of the IEEE First World Conference on Photovoltaic Energy Conversion/Conference Record of the Twenty-Fourth IEEE Photovoltaic Specialists Conference* (Waikoloa, Hawaii, 1994), 99-102.

[23] C. S. Ferekides, D. Marinskiy, S. Marinskaya, B. Tetali, D. Oman, and D. L. Morel, in *Conference Record of the Twenty-Fifth IEEE Photovoltaic Specialists Conference* (Washington D.C, 1996), 751-756.

[24] N. Amin, T. Isaka, T. Okamoto, A. Yamada, and M. Konagai, Japanese Journal of Applied Physics Part 1-Regular Papers Short Notes & Review Papers **38,** 4666-4672 (1999).

[25] K. Mitchell, A. L. Fahrenbruch, and R. H. Bube, Journal of Applied Physics **48,** 829-830 (1977).

[26] Y. S. Tyan, F. Vazan, and S. Barge, in *Conference Record of the Seventeenth IEEE Photovoltaic Specialists Conference* (Kissimmee, Florida, 1984), 840-845.

[27] K. Ohata, J. Saraie, and T. Tanaka, Japanese Journal of Applied Physics **12,** 1641-1642 (1973).

[28] A. E. Rakhshani, Journal of Applied Physics **90,** 4265-4271 (2001).

[29] X. Tang, P. J. M. Boots, and L. J. Giling, in *Conference Record of the Twenty-First IEEE Photovoltaics Specialists Conference* (Kissimmee, Florida, 1990), 348-352.

[30] A. Camanzi, A. Parretta, M. Garozzo, and M. Vittori, Solar Energy Materials **17,** 457-469 (1988).

[31] S. A. Galloway, A. W. Brinkman, K. Durose, P. R. Wilshaw, and A. J. Holland, Applied Physics Letters **68,** 3725-3727 (1996).

[32] S. A. Galloway, A. J. Holland, and K. Durose, Journal of Crystal Growth **159,** 925-929 (1996).

[33] A. O. Pudov, M. Gloeckler, S. H. Demtsu, J. R. Sites, K. L. Barth, R. A. Enzenroth, and W. S. Sampath, in *Conference Record of the Twenty-Ninth IEEE Photovoltaic Specialists Conference* (New Orleans, Louisiana, 2002), 760-763.

[34] G. Agostinelli, E. D. Dunlop, P. N. Gibson, and F. Dos Santos, in *Conference Record of the Seventeenth European Photovoltaic Solar Energy Conference* (Munich, Germany, 2001), 1251-1253.

[35] K. Durose, D. Boyle, A. Abken, C. J. Ottley, P. Nollet, S. Degrave, M. Burgelman, R. Wendt, J. Beier, and D. Bonnet, Physica Status Solidi B-Basic Research **229,** 1055-1064 (2002).

[36] W. D. Sawyer, Journal of Applied Physics **59,** 2361-2363 (1986).

[37] S. Damaskinos, Solar Cells **26,** 151-158 (1989).

[38] E. Kreyzig, *Advanced Engineering Mathematics* John Wiley & Sons Inc., Singapore, 1999.

[39] J Rechid, Thin Solid Films **361-362,** 198-202 (2000).

[40] A. C. Ribes, S. Damaskinos, H. F. Tiedge, A. E. Dixon, and D. E. Brodie, Solar Energy Materials and Solar Cells **44,** 439-450 (1996).

[41] J. R. Sites, Solar Energy Materials and Solar Cells **75,** 243-251 (2003).

[42] X. Wu, Solar Energy **77,** 803-814 (2004).

[43] J. Sarlund, M. Ritala, M. Leskela, E. Siponmaa, and R. Zilliacus, Solar Energy Materials and Solar Cells **44,** 177-190 (1996).

[44] D. L. Batzner, A. Romeo, H. Zogg, R. Wendt, and A. N. Tiwari, Thin Solid Films **387,** 151-154 (2001).

[45] D. L. Batzner, R. Wendt, A. Romeo, H. Zogg, and A. N. Tiwari, Thin Solid Films **361,** 463-467 (2000).

[46] V. Barrioz, R. L. Rowlands, E. W. Jones, S. J. C. Irvine, G. Zoppi, and K. Durose, in *Thin-Film Compound Semiconductor Photovoltaics*; *Vol. 865*, edited by W. Shafarman, T. Gessert, S. Niki, and S. Siebentritt (2005), 67-72.

[47] D. Bonnet, Thin Solid Films **361,** 547-552 (2000).

7 Nucleation and the early stages of growth of CdTe thin films

7.1 Introduction

Physical thin film crystal growth processes including nucleation and grain size development may be expected to have a profound effect on film continuity and microstructure. With reference to solar cell devices, both pinholes[1] and grain size/grain boundary effects[2] are known to have a direct impact on the conversion efficiency. Various techniques have been used to control the grain structure. Inclusion of oxygen in the processing ambient[3] leads to more uniform coverage but smaller grains, while higher substrate temperatures lead to the growth of larger grains[4,5].

This chapter reports investigations into the early stages of CdTe thin film growth deposited by close space sublimation. Attempts are made to understand the processes by which the films are formed, and the impact of different growth conditions on these processes is examined.

7.2 Methodology

In order to study the formation process of CdTe thin films, their microstructural development as a function of time was examined. The most accurate and informative way to perform this would be analysis via in-situ electron microscopy during growth, as has been demonstrated for other systems such as those outlined in Section 4.6. However, CSS growth is not a suitable technology for in-situ techniques, and so post-growth analysis of films offers the best alternative. By growing CdTe thin films for a range of growth times under identical conditions, it was possible to analyse the film development using ex-situ AFM and SEM analysis.

The principal focus of this work was to examine the early stages of growth before the formation of a complete layer: it is this period of growth, encompassing nucleation and coalescence of island structures, which determines the progression of the later stages of

growth and hence the overall microstructure of the final film. As CSS is a rapid deposition process, with films of a few μm thickness typically deposited in a matter of minutes[3], island formation takes only seconds. In order to reliably determine film development as a function of time by post-growth analysis, it is imperative that any uncertainty in the growth time is minimised. For such short growth times, control of the growth period by the use of a manual shutter to start and stop growth would introduce a significant error. By reducing the deposition rate of material and thus increasing the deposition time, this timing error may be minimised. The source sublimation rate within a CSS chamber, and hence the deposition rate, is inversely proportional to the gas pressure used[6]. By increasing the pressure above the standard range of pressures used, typically 0-10Torr, the deposition rate of material may be significantly reduced. Nitrogen pressures of 100-200Torr were therefore used to slow the growth rate of CdTe thin films and allow accurate monitoring of film development as a function of time. Throughout this Chapter pressures of 50Torr and above, used during CSS deposition will be referred to as 'high pressure' growth runs.

From the thin film nucleation and growth theory presented in Chapter 4, it was anticipated that the relatively high pressure employed here for deposition may affect the nucleation and growth processes. However, it was not expected that the principal manner of growth would be fundamentally altered i.e. growth by the formation of islands. The impact of high pressure growth on CdTe grain structure is discussed in Section 7.4, and the subsequent impact on device performance is detailed in Section 8.4.

Analysis of samples discussed within this chapter was performed using AFM and SEM, with quantative data being extracted using "UTHSCSA Image Tool" and "SPIP". AFM analysis was carried out using a Topometrix Explorer instrument while SEM measurements were made using FEI XL30 - SFEG (Schottky Field Emission Gun) and Hitachi SU-70 microscopes.

7.3 Early stage growth of CdTe thin films on ITO

Initial studies of thin film CdTe growth were performed using commercially bought ITO substrates, as these provided a convenient and reproducible surface. This section details analysis of CdTe/ITO structures grown using a 200Torr pressure for a range of gas

ambients (N_2, 99% N_2 + 1% O_2 and 99% N_2 + 1% H_2) and a range of growth times (1-60min). Full results for film development as a function of time for growth in N_2 and 99% N_2 + 1% H_2 ambients are presented. Comparisons between growth in the two different ambients are made using AFM images and the quantative data extracted from them. AFM analysis of samples grown in a 99% N_2 + 1% O_2 ambient is compared with that for samples grown in an N_2 ambient, with the impact of oxygen on grain size and morphology being discussed. SEM analysis of samples grown in ambients containing high partial pressures of hydrogen is also presented.

7.3.1 Sample fabrication

Thin CdTe films were grown by CSS on ITO/glass substrates from Merck Display Technologies Ltd. Details of the CSS apparatus may be found in Section 5.2.1, while details of the substrates may be found in Section 5.2.4. Substrates (2.5x2.5cm) were cleaned by ultrasonication in a 2% solution of Decon 90 detergent in DI water, followed by ultrasonication in DI water, acetone and finally isopropanol. CdTe deposition was carried out at constant source and substrate temperatures of 600°C and 500°C respectively, the temperatures being maintained using both source and substrate heaters. Once the deposition temperature had been reached, the temperatures were allowed to stabilise for 5mins. Using automated pressure control, a chamber pressure of 200Torr was established and maintained throughout growth. For the initial examination of film formation processes growth was carried out in a pure nitrogen ambient (100% N_2), this being considered inert. In order to determine the effect of including oxygen or hydrogen into the processing ambient, a 2Torr pressure of either gas was included in the 200Torr total pressure (i.e. 99% N_2 + 1% O_2 or 99% N_2 + 1% H_2). Growth was controlled by the use of a manual shutter situated between source and substrate. The shutter was retracted to start growth and replaced to stop it. For nitrogen and hydrogen ambients a series of 5 samples were grown for a range of times (1, 5, 10, 30 and 60mins), with the time being measured from the point at which the shutter was removed. At the end of the growth period the system was flushed with nitrogen for 10min, in order to rapidly cool the system. Samples were grown out of sequence to minimise any systematic error.

7.3.2 AFM characterisation of CdTe thin films deposited on ITO in a nitrogen ambient

This section described the AFM analysis of CdTe thin films deposited on an ITO surface in a 200Torr pressure of nitrogen. Inspection of the layers by the eye showed visible light transmission through the layer. Examination under an optical microscope showed the substrates to be sparsely populated by island structures, indicative of the Volmer-Weber growth mode. Fig.7.1 shows AFM images of the CdTe layers grown for 1, 5, 10, 30 and 60mins whilst fig.7.2 shows quantative data for the average island area, nucleation density, coverage and roughness extracted from AFM scans, plotted as a function of growth time.

It can be seen from fig.7.1 that the layers are at a very early stage of growth, due to the high pressure employed slowing the rate of deposition on the surface. The images clearly demonstrate that island growth takes place, with a large number of small islands being distributed across the surface. Initially (fig.7.1a) the island density is high, $0.228\mu m^{-2}$, while the average area is only $0.26\mu m^2$. Islands are not uniform in size, with there being some significantly larger islands, although at this stage they show no evidence of crystallographic orientation or faceting. After 5 minutes growth (fig.7.1b) the density of islands on the surface has decreased, while island size has increased significantly. This rapid reduction in island density is attributable to the complete coalescence of some of the islands, a process which is expected to occur rapidly for small islands. An example of island coalescence is shown in the AFM image in fig.7.3a. In this process, two previously separate islands come into contact as a result of their growth, coalesce, and re-order to form a single island, thus reducing island density. At this stage the larger, more developed, islands have begun to demonstrate evidence of faceting. By t = 10min, island density has further decreased, due to the continuation of coalescence, while the islands have continued to increase in size. The average island area is now $1.29\mu m^2$ and most islands have begun to exhibit smooth crystal facets. At t = 30min, there has been a significant increase in the island area, due to large islands observed in fig.7.1c having substantially coalesced and re-ordered to form single islands. The islands have also continued to grow by addition of species diffusing across the surface during

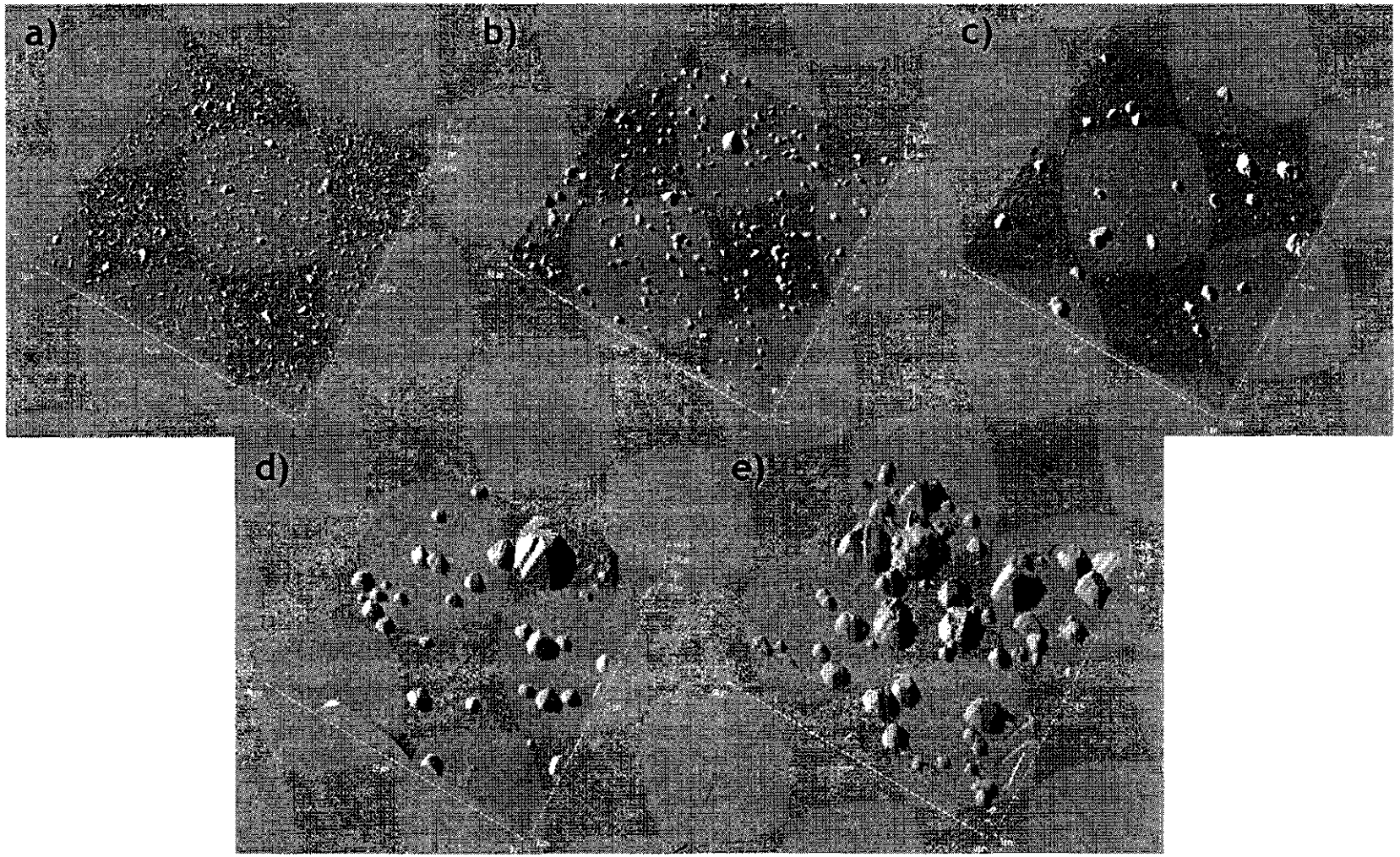

Figure 7.1: AFM images of CdTe thin films deposited on ITO under 200Torr of nitrogen for growth times of: a) *t*=1min, b) *t*=5min, c) *t*=10 min, d) *t*=30min and e) *t*=60min. The range of each axis is as follows; X = 0 – 50μm, Y = 0 – 50μm and Z = 0 – 3.5μm.

this period. By the end of the studied growth period t = 60min, a distribution of large islands has been established. The population now has an increased average area of 23.10μm^2, a reduced island density of 0.01μm^{-2}, and the majority of islands display well defined crystal facets. No evidence of channel formation or nucleation of secondary islands is apparent. Due to the absence of such latter stage growth effects, and the relatively low coverage (23%) of the substrate, film development at the end of the examined growth period is still assumed to be at an early stage. Formation of a complete layer under these conditions may therefore be expected to take a number of hours. Nevertheless, secondary nucleation and channel filling effects, although not observed here, might be expected to occur and lead to the formation of a complete film. Fig.7.2d shows the root mean square (rms) surface roughness of the samples measured by AFM. As may be expected from the images presented in fig.7.1 the roughness increases throughout the growth period (roughness data for the ITO substrate may be found in Appendix A).

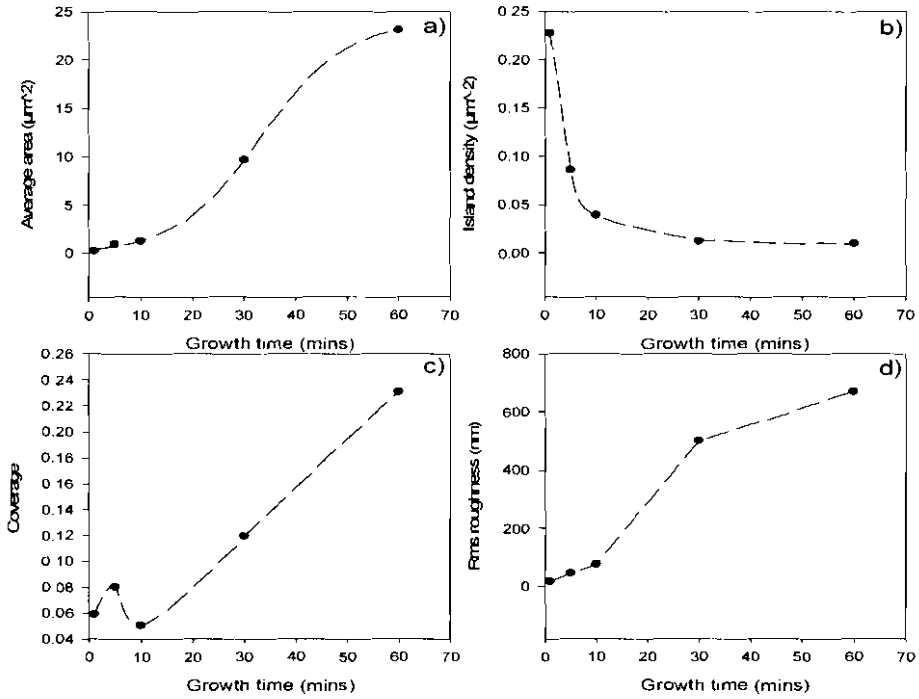

Figure 7.2: Data extracted from the AFM images of CdTe growth on ITO under 200Torr of N_2 (fig.7.1): a) average island area, b) island density, c) substrate coverage as a fraction of total area and d) rms roughness. Errors estimated from the standard deviations were as follows: a) average area +/- 9% of measured value, b) island density +/- 5% of measured value, c) coverage +/- 9% of measured value, d) roughness +/- 4% of measured value

From fig.7.2c it can be seen that the coverage does not continually increase throughout growth, with the coverage decreasing in the 5–10min period. This may be attributed to a large amount of island coalescence during this period. As discussed in Section 4.5.3, coalescence reduces the combined surface area of islands, and in instances where it is prevalent this may lead to a reduction in the substrate coverage fraction.

In order to ensure the consistency of the data, a repeat of the sample grown for 30mins was produced and analysed. All values determined for grain size, island density, coverage and surface roughness showed a variation of less than 6% from the original values determined.

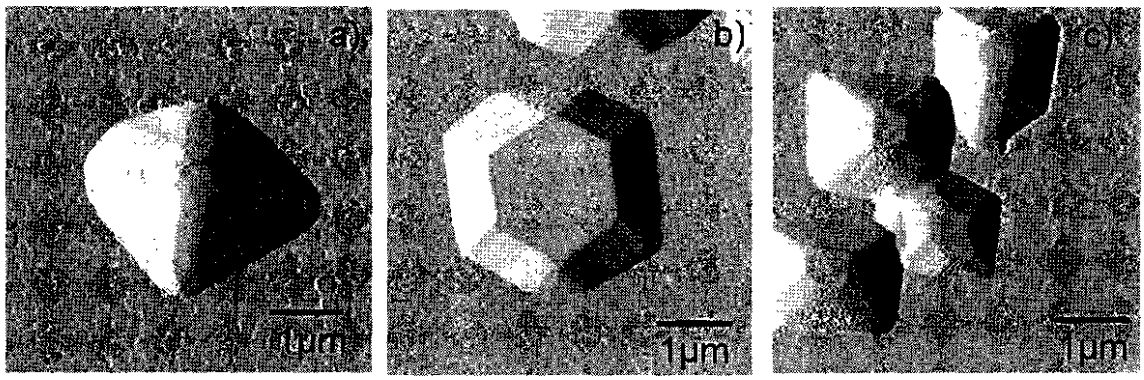

Figure 7.3: Example AFM images of common island structures for CdTe growth on ITO under 200Torr N_2: a) "Pyramidal" island shape, b) hexagonal" island shape and c) islands coalescing.

A variety of island sizes and shapes were observed by AFM analysis of the films. Examination of island morphology may reveal significant information about the growth processes in their formation, as outlined in Section 4.5.2. Islands at later stages of growth (10-60min) clearly display smooth crystal facets, evidence that they are crystalline and that they grow by uninterrupted addition of condensed species to steps on flat growth surfaces[7] (Section 4.5.2). The presence of impurities, in either the source (99.999%) or the process gas, has therefore not significantly impeded the growth processes. Various habits are displayed by the islands, with two common structures "pyramidal", fig.7.3a, and "hexagonal", fig.7.3b, repeatedly observed. Of these two variants the "pyramidal" structure was more frequently observed, as demonstrated in fig.7.3c which shows four islands of this type coalescing. By comparison of these island shapes with the singular

surface polyhedron of the sphalerite structure[8], one may attempt to infer the orientation corresponding to each observed island shape. Generally it has been seen for vapour-growth of CdTe that the growth facets[9-11] are dominated by the formation of habit planes[9]. In this instance, the square based 'pyramidal' form of islands resembles part of the surface polyhedron, comprising planes with the normal to the substrate being <001>. The interpretation of the 'hexagonal' shape was less clear: Although the islands conformed to a regular and reproducible shape, there is no clear match to a simple set of low index planes. An attempt was made to probe the orientations of the islands using EBSD, but was frustrated by two factors: i) it was difficult to distinguish between island types at the high tilt angle (70°) used for EBSD and ii) although patterns were recorded, they were not easily reconciled by the auto identification software using a cubic lattice type. However, extensive reaction with the substrate was ruled out since analysis of the islands using SEM/EDX revealed them to be CdTe. Perhaps further, more exhaustive, EBSD study would resolve the question of the identity of the island orientations.

7.3.3 Growth on ITO in an oxygen ambient

In order to study the effect of inclusion of oxygen into the CSS possessing ambient, samples were grown in a 200Torr total pressure, with a 1% partial pressure of oxygen (99% N_2 + 1% O_2). A series of three samples was produced, with growth times of 1min, 5min and 10min. Samples were grown out of sequence, with the 5min growth being the first deposition performed and the 10min growth the last. Examination of theses samples under an optical microscope revealed that a thin CdTe layer had been formed on the substrate during the 5min growth, but there was no observable growth for sample with the 10min deposition period. This indicated that there was a systematic error within the deposition process, as the film grown for 10min should have been the thicker of the two. Inspection of the CdTe source showed it had been altered by the use of oxygen, with visible oxide phases (assumed to be CdO) being present which had changed the character of the material. Prior to the first deposition, the source was noted to be free running, black and powder-like in nature. After deposition runs had been performed with oxygen present, the source had noticeably hardened and discoloured, taking on a brown colour. It was found that use of oxygen under these conditions drastically reduced the sublimation

rate from the source for subsequent runs, as a result of this source oxidation. This reduction in growth rate has been confirmed by others[3]. In principle, the change could be compensated for by changing the growth time. However, for a reliable study of the early stages of thin film growth, the rate of deposition is required to be constant with no run-to-run variation. Therefore, it was not possible to study fully the deposition of CdTe in the presence of oxygen, as a function of time. However, qualitative comparisons were still able to be made between the sample with 5min deposition time and the equivalent nitrogen sample, as no oxidation of the source had occurred prior to deposition of this sample. Fig.7.4 shows two AFM scans of the sample grown for 5min in a 99%N_2+1%O_2 ambient, which should be compared to a similar but oxygen-free sample as shown in fig.7.1b. In the film grown in the presence of oxygen, the density of CdTe islands is significantly higher and the coverage of the substrate by the film is complete, even at this short deposition time. Less than 10% coverage was observed for an equivalent growth time in the pure nitrogen ambient. The island size was greatly reduced in comparison to the nitrogen case. Full statistical analysis was not possible, as the analysis software used was unable to distinguish individual islands in the instance of high coverage. However, the islands were estimated to have a typical major-axis diameter of 200-300nm for growth in an oxygen containing ambient, compared to approximately 1μm for a nitrogen ambient. The islands grown in an oxygen containing ambient also showed no evidence for the formation of crystal facets, but instead had rounded shapes.

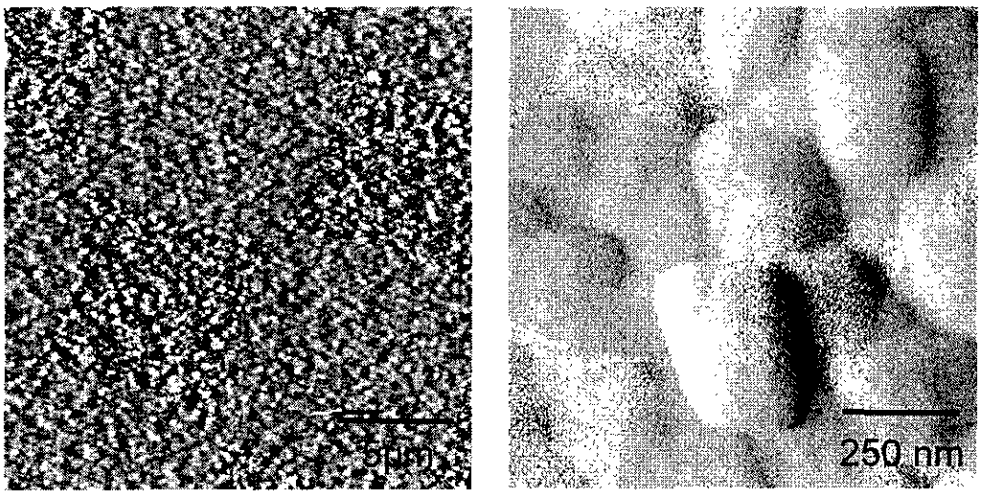

Figure 7.4: AFM images of CdTe thin film grown for 5 min on ITO in a 200Torr ambient containing a 1% partial pressure of oxygen (99% N_2 + 1% O_2).

Due to the problems encountered with source oxidation, and the requirement for a constant sublimation rate between runs, further work utilising an oxygen containing ambient was not undertaken.

7.3.4 Growth on ITO in a hydrogen containing ambient

While the inclusion of oxygen in the processing ambient for CSS deposition of CdTe thin films is widely reported, little work has been reported on the impact of hydrogen. This section examines the effect of growth ambients containing hydrogen on CdTe deposition on ITO, with the impact of hydrogen being assessed by comparisons with CdTe thin film growth carried out in a pure nitrogen ambient. Results in this section shall be divided into two parts. Firstly, a time dependent study, directly comparable to that in Section 7.2.2, will be presented. Secondly, SEM results demonstrating the impact of hydrogen on the morphology and composition of deposits for CdTe/ITO structures will be presented.

7.3.4.1 Growth in a hydrogen containing ambient as a function of time

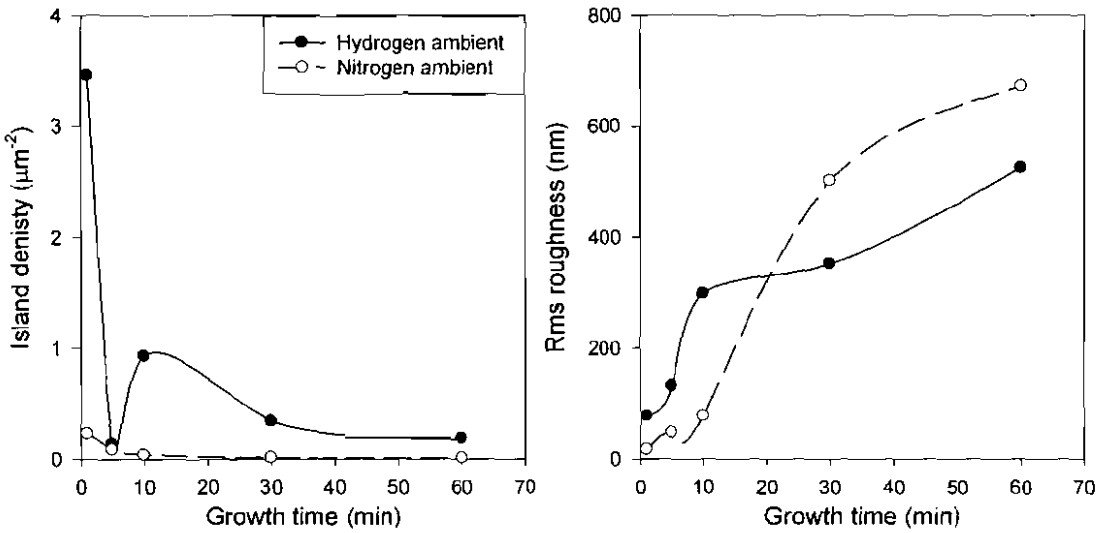

Figure 7.5: CdTe Island density and rms roughness as a function of growth time for deposition on ITO under a) N_2 and b) 99% N_2 + 1% H_2 ambients.

A series of six samples was fabricated using growth times in the range 1-60 min, with times selected so as to allow direct comparison with deposition in a pure nitrogen

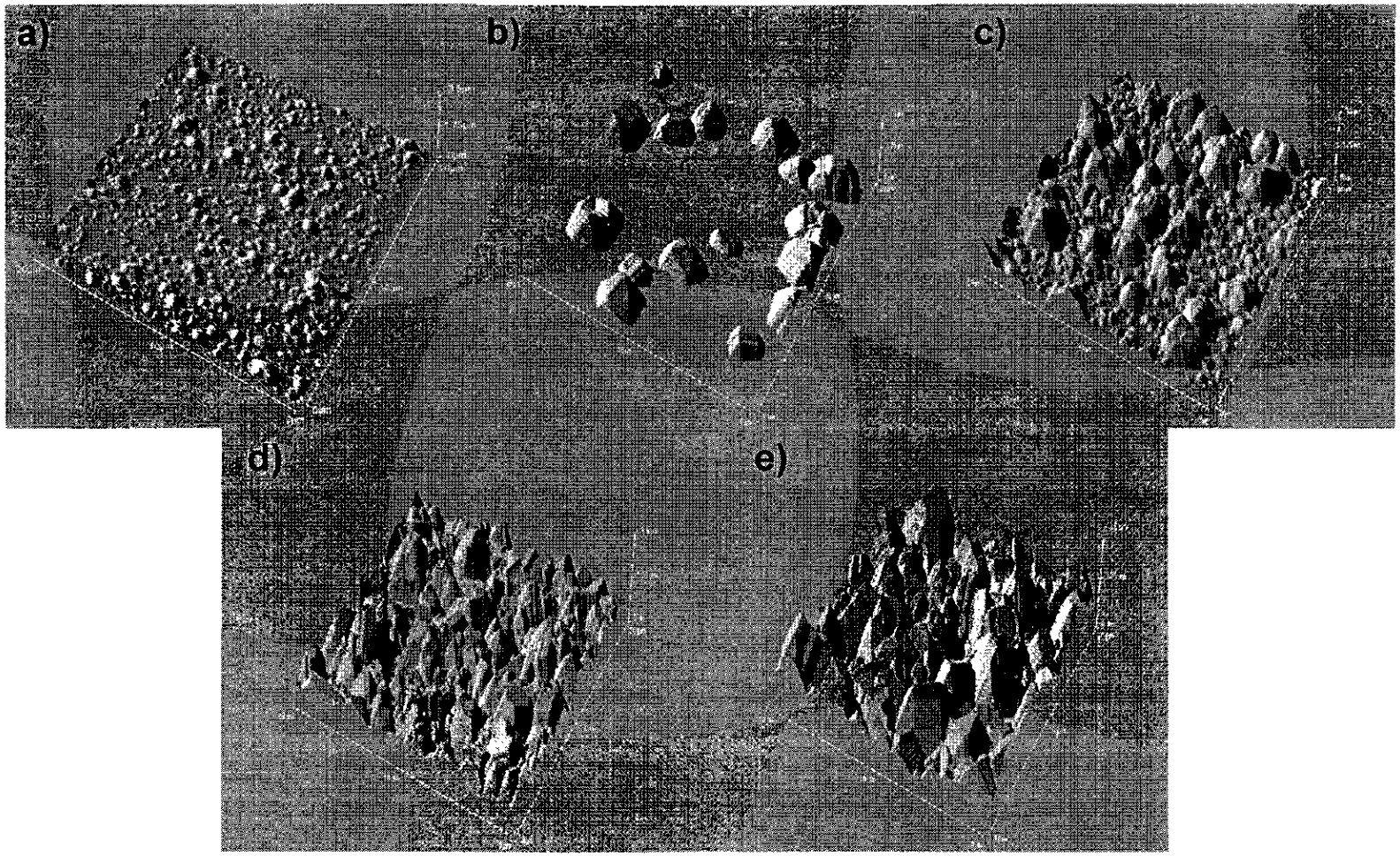

Figure 7.6: AFM images of CdTe islands grown on ITO under 200Torr pressure (99% N_2 + 1% H_2) for growth times of: a) *t*=1min, b) *t*=5min, c) *t*=10 min, d) *t*=30min, e) *t*=60min. The range of each axis is as follows; X = 0 – 20μm, Y = 0 – 20μm and Z = 0 – 3.5μm.

ambient (Section 7.3.2). A 1% partial pressure of hydrogen (99% N_2 +1 % H_2) was included in the processing ambient, but all other deposition parameters were the same as for the samples discussed in Section 7.3.2. Fig.7.6 shows the AFM images of the resultant films, and fig.7.5 shows the rms roughness values and island densities, plotted as a function of the growth time. Comparative data from AFM analysis of samples grown in a nitrogen ambient is plotted on the same figure. Fig.7.6a shows the film structure after 1 min growth and it may be seen that the initial island density is very high ($3.46\mu m^{-2}$) in comparison to the nitrogen case ($0.23\mu m^{-2}$). Fig.7.5a shows that by t=5min, the island density for the film grown in a hydrogen containing ambient has dropped rapidly and has become close to the value observed under pure nitrogen. The rate of coalescence of islands in the hydrogen containing ambient, up to this stage, is therefore significantly higher. At t=10min the island density increases sharply, with the corresponding AFM image (fig.7.6c) showing that primary islands have now formed a network, with secondary nucleation occurring in the channels, accounting for the increase in island density. Fig.7.5 shows that, prior to the onset of secondary nucleation, the surface roughness had been developing at a high rate but, after secondary nucleation begins (t>10min), this rate slows. As secondary islands develop, ($10\text{min} \leq t \leq 60\text{min}$) they fill the gaps left by the primary islands and the rate of roughness development is lessened. By t=30min (fig.7.6d), the secondary islands have begun to coalesce and become incorporated into the channels, leading to a further reduction in the island density. At this stage of growth, coverage is high, with few gaps in the material remaining. By t=60min, this process has completed and a continuous film had been formed. The island (or now rather '*grain*') density has been further reduced by continued coalescence, but is still slightly greater than that for deposition in a nitrogen ambient. At the end of the growth period measured, the level of substrate coverage by the film grown in a hydrogen containing ambient, is significantly higher than that of the film grown in a nitrogen ambient.

Full statistical measurement of island area as a function of time was not possible for all films grown in a hydrogen containing ambient, as analysis software used was not able to discriminate between islands at high coverage. However, manual measurements from

the images indicated that islands formed in the presence of hydrogen, were significantly smaller than for islands grown under equivalent conditions in a nitrogen ambient.

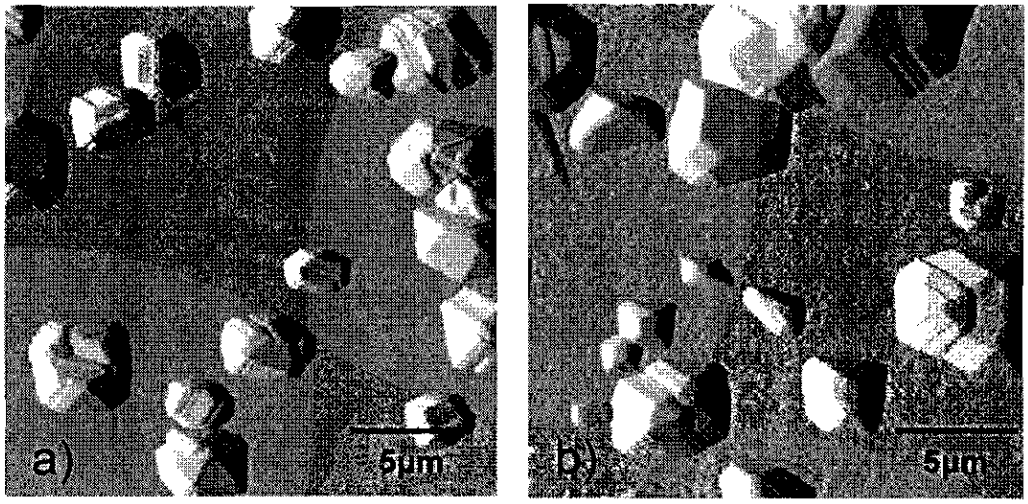

Figure 7.7: AFM images of CdTe island structures deposited on ITO at 200Torr for a) 5min in a hydrogen (99%N_2 + 1% H_2) ambient, b) 60min in a pure nitrogen ambient.

AFM images show that islands deposited under a hydrogen containing ambient (fig.7.7a) still demonstrate smooth crystal facets, as had been observed for growth in pure nitrogen (fig.7.7b). However, there were differences in the morphologies between the two growth ambients. Inclusion of hydrogen was found to increase the prevalence of 'hexagonal' islands and moreover it also increased the incidence of islands that displayed twin related phenomena. This indicated that hydrogen may have altered the substrate, and possibly increase the incidence of growth accidents yielding twins. This raised questions about the suitability of ITO as a deposition surface under these conditions, so to ascertain the stability of the substrate to hydrogen at high temperatures, the effect of using higher partial pressures of hydrogen during CdTe deposition was also investigated.

7.3.4.2 SEM and EDX analysis of CdTe films grown in high partial pressures of hydrogen

For samples discussed in the previous section, the growth was carried out under a constant flow of processing gas having the required composition. However, due to the limits of the CSS system being used, the maximum attainable partial pressure of

hydrogen was 5% in a total chamber pressure of 200Torr. In order to fabricate samples using higher partial pressures of hydrogen a slightly different growth methodology was therefore required. The chamber was filled with the constituent gasses required for deposition at room temperature, and then isolated before growth began. A range of 0-100% partial pressures of hydrogen were used, with 0% representing 200Torr of standing nitrogen at room temperature and 100% representing 200Torr of standing hydrogen. Due to the pressure being established at room temperature, the pressure at the deposition temperature was significantly higher (~300Torr). Results presented in this section are therefore not directly comparable to those presented earlier in this chapter, due to the increased deposition pressure. All samples had a growth time of 10min.

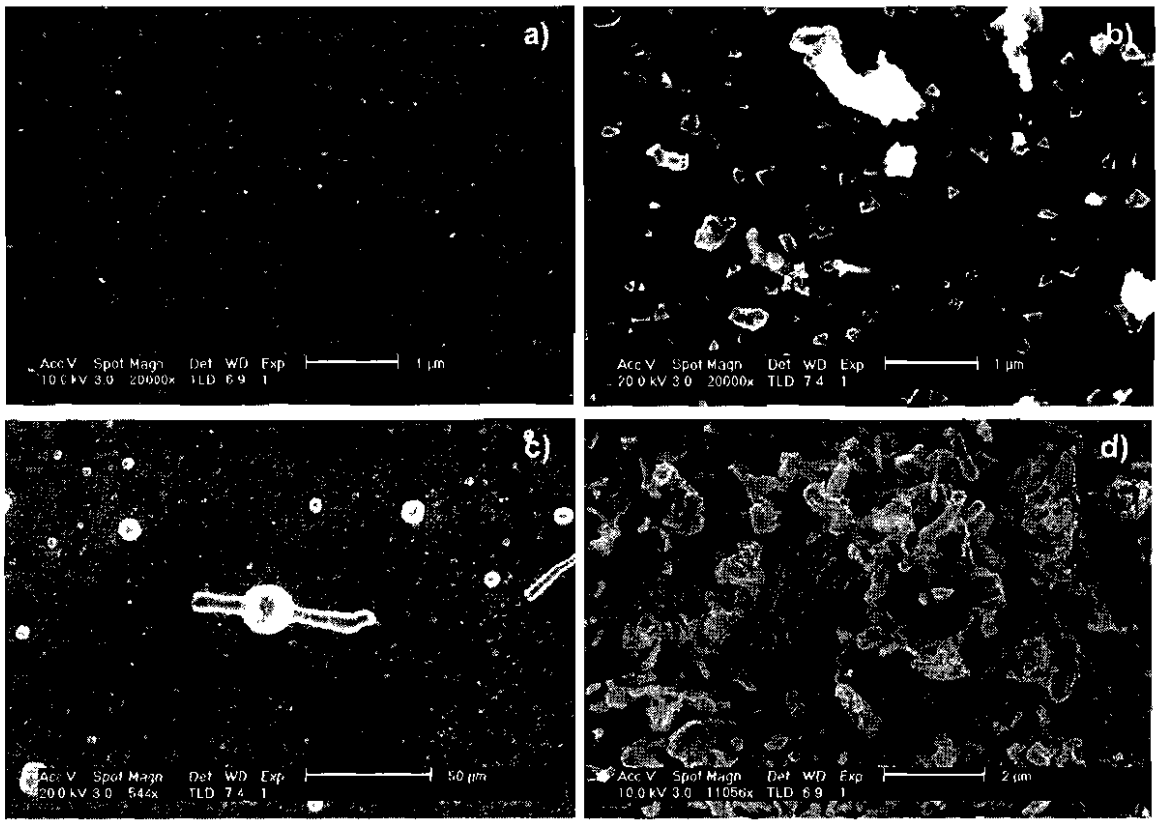

Figure 7.8: SEM images of CdTe films grown on ITO in 200Torr of nitrogen/ hydrogen of composition, $(100\%\text{-}X)N_2 + XH_2$, where X = a) 0%, b) 10%, c) 40% and d) 100%. Under pure nitrogen (a) a low density of small islands is visible with light contrast against the background morphology of ITO. In (b) the effect of hydrogen is to increase the size of the islands. At higher fractions of hydrogen new microstructural features emerge, indicating that reactions have taken place with the substrate.

Fig.7.8 shows SEM images of samples grown in various hydrogen partial pressures. For growth under pure nitrogen, fig.7.8a, very little island growth is observed, with only small well spaced islands formed on the surface, at a low number density. Addition of a 10% partial pressure of hydrogen to the ambient (fig.7.8b) increases the size and density of islands formed on the surface, with the majority of islands having a distinct triangular shape and displaying well defined crystal facets. At high hydrogen partial pressures of 40% and above, the observed growth changes significantly and the effect on the surface becomes apparent. Fig.7.8c shows a sample grown in a 60% N_2 + 40% H_2 ambient. The surface is populated by large rounded islands, often with "tails" leading off from them. The islands are significantly larger than those shown in fig.7.8b and display no crystal facets. Areas of the substrate around these islands show signs of damage, which appear as black spots in the SEM images. Closer inspection revealed these regions to be holes in the ITO layer. Very little "normal" CdTe island growth, similar to that observed previously, occurs under these conditions. In a 100% H_2 ambient (fig.7.8d), the nature of the growth has again changed and the ITO surface bears little resemblance to that shown in fig.7.8a. The surface is populated by two apparently different phases, distinguishable by their different contrast on SEM images, as shown in fig.7.8d. One phase forms large islands consisting of stacked plates of material, while the second phase forms small cluster which decorates the outside of these larger structures. Inspection under an optical microscope, showed that samples grown in hydrogen partial pressures of $\geq$40%, had regions that appeared distinctly metallic. This was believed to result from of reduction of the ITO surface, leading to possible indium and/or tin phases on the surface. EDX analysis was therefore performed in order to determine the composition of the islands observed on the surface.

Fig.7.9 shows the morphological features and the EDX spectra recorded from a sample grown under a 40% partial pressure of hydrogen (fig7.8c). Locations 1 and 2 indicate the sites from which the X-ray spectra were recorded, whilst quantative data for the relative weight of the elements detected is given in table 7.1. Spectrum 1 shows the bulbous part of the feature to be mainly comprised of indium and tellurium, with very little cadmium being detected. This indicates that is was not a CdTe island and implies that the island was likely to be indium telluride. There are numerous commonly occurring

stoichiometries of indium telluride[10] (some common stoichiometries are given in table 7.1) but, since a the 1:1 ratio of indium to tellurium by weight was detected, it seems probable that the island comprises InTe. Spectrum 2 was recorded from the "tail" region of the same deposit and shows distinct differences to that recorded for the bulk of the deposit. Here, the spectrum indicated that the primary constituent was indium (68%) in combination with tellurium (10%) and tin (21%). Due to the relatively small fraction of tellurium it seems reasonable to assume that there is only a small amount of either indium telluride or possibly tin telluride in this region. The bulk of this "tail" is therefore likely to consist of a mixture of indium and tin.

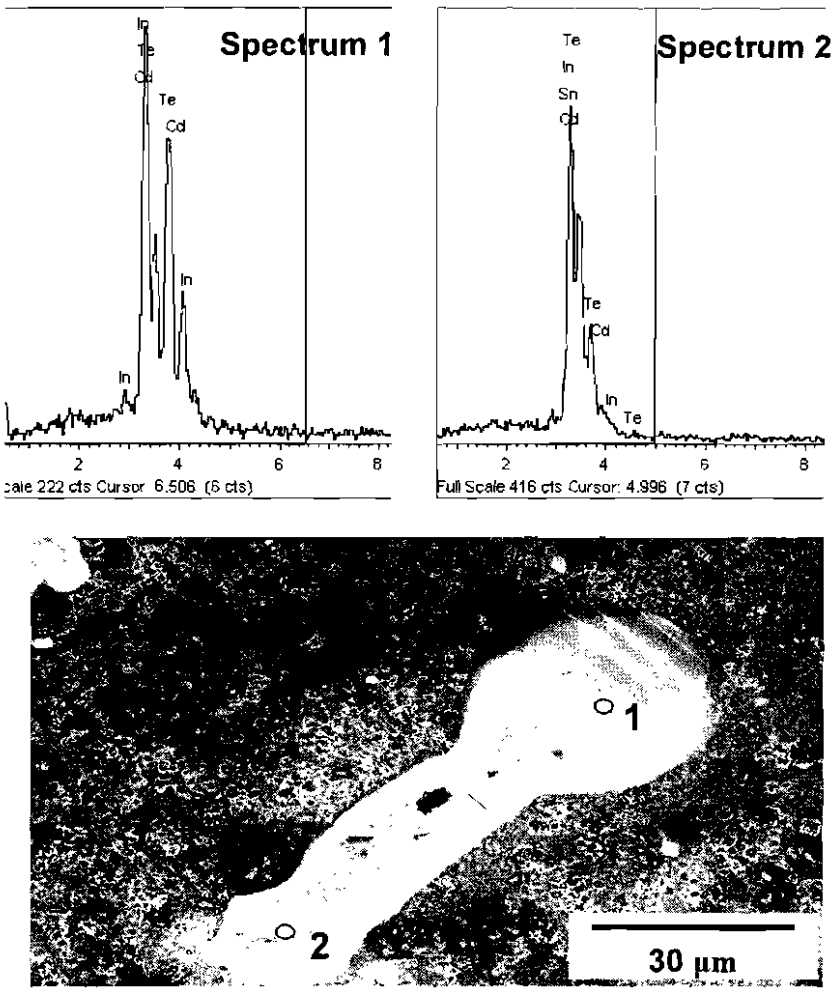

Figure 7.9: SEM image and associated EDX spectra for sample grown in 40% hydrogen ambient

Results in this section demonstrate that ITO is not a suitable stable substrate for growth of CdTe thin films in the presence of hydrogen, at high temperatures. Formation

of indium and tin phases revealed the substrate was reduced under these conditions and that reaction with the forming film had taken place.

Element	Spectrum 1 weight (%)	Spectrum 2 weight (%)	InTe	In_2Te_3	SnTe	$SnTe_2$
Cd	1.52 +/- 2.04	0	0	0	0	0
Te	49.71 +/- 2.33	10.20 +/- 2.02	52.6%	62.5%	48.2%	68.3%
In	48.77 +/- 2.32	68.40 +/- 2.99	47.4%	37.5%	0	0
Sn	0	21.40 +/- 2.02	0	0	51.8%	31.7%

Table 7.1: Quantative data obtained from spectra in figure 7.9 with expected weight compositions of commonly occurring indium telluride and tin telluride compounds.

7.3.5 Discussion

The AFM and SEM analysis presented in Section 7.3 provides direct evidence that CdTe thin films, deposited by CSS on ITO, grow via the Volmer-Weber or 'island' mode. As such, this is evidence that the bonds between atoms within the deposited film are stronger than film-substrate bonds. No evidence of growth via the 'layer-by-layer' or 'layer-plus-island' modes was observed in any of the samples analysed during this work. The study of CdTe thin film deposition in a high pressure nitrogen ambient (Section 7.3.2), allowed some of the growth processes involved in the film formation to be evaluated. Processes outlined in Chapter 4, such as, nucleation of islands, island growth and coalescence are clearly apparent: Growth begins by the nucleation of a high density of small islands, which display no crystallographic orientation or evidence of crystal facets. As growth progresses the typical island size increases rapidly and the density of islands on the surface is reduced as islands undergo coalescence and re-order to form single islands. At later stages of growth, islands began to display oriented crystal facets, with the faceting being convincingly crystallographic in origin, even though confirmation and indexing by EBSD was not possible. Under the conditions and time frame used for this study, growth failed to progress to a completed CdTe thin film. However, formation of a complete film is still anticipated, albeit for significantly longer growth times than those used here. Similar CdTe depositions performed using ITO substrates, but utilising

lower chamber pressures, did yield complete films. The failure to form a complete film is therefore not as a result of the ITO substrate limiting the density at which CdTe islands form.

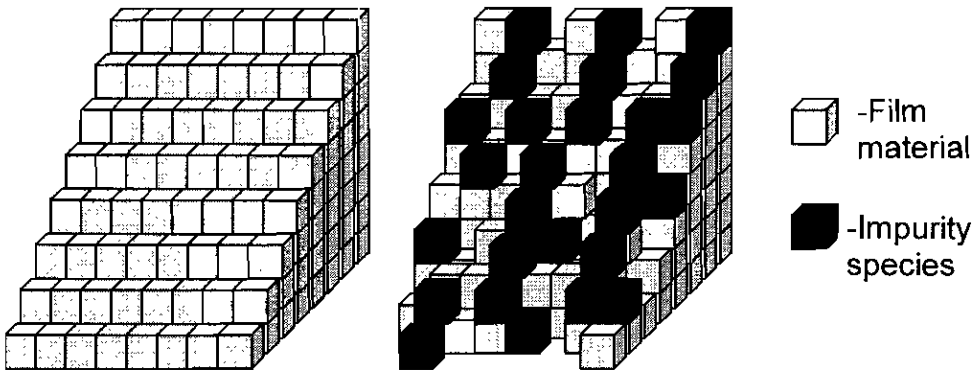

Figure 7.10: Schematic model of crystal growth showing the development of crystallographic facets (left), and interference from co-deposited oxygen as an impurity (right).

The inclusion of a 1% partial pressure of oxygen in the growth ambient was found to reduce grain size, impede the formation of crystal facets and increase the level of substrate coverage by the forming layer. A possible explanation for the rounded appearance of islands is suggested by considering oxygen as a co-deposited impurity species by Barna *et al*[9,11,12] (see Section 4.6.1). If the step flow of the forming film (Section 4.5.2) is interrupted by oxygen species binding at the terraces, then facets will form in a disordered, rounded manner. Fig.7.10 illustrates this model for the cases of deposition in which: a) the ambient is inert (left hand model) and b) the ambient contains oxygen, an impurity that binds to the film material (right hand model). In the case of the inert ambient, the deposited species add to the steps, step flow progresses unimpeded and a smooth crystal facet is formed. In the instance of deposition in an oxygen containing ambient, the step site acts as a preferential capture site for both the deposited impurity species and layer adatoms. Oxygen adatoms that are absorbed at step sites disrupt the step flow process and crystal facets do not form. Islands instead take on a rounded morphology, due to the disordered nature of the steps. Barna's work also highlighted the effect of oxygen uptake on the coalescence of islands. He observed that islands meeting at surfaces coated with an oxide phase did not completely coalesce. He ascribed this to the increased melting temperature associated with the oxide phase in comparison to that

of the pure material. In the model proposed here, the facing edges of the islands are effectively coated with an oxide phase which will impede the complete coalescence of islands. This coating may also serve to stabilise islands as follows: Islands of a small size that may have been prone to re-evaporation, will experience an increase in their melting point as a result of the formation of a coating oxide phase. This will allow such islands to remain on the surface as stable islands. This is consistent with the reduced island size and increase in substrate coverage observed for CdTe thin films deposited in an oxygen containing ambient. The step flow process is interrupted by impurities during island formation leading to an oxide phase forming on the outside of islands. This stabilises the nascent nuclei, increasing the nucleation density on the surface. Addition of material to the growing islands is limited by the presence of impurity species and the oxide phase coating the islands inhibits coalescence. This maintains the high island density, leading to complete coverage of the surface and small grains observed.

Oxidation of the CSS source material was found lead to a variation in the sublimation rate between growth runs. This meant it was not possible to study the impact of oxygen on CdTe growth phenomena in the same depth as had been done for nitrogen and hydrogen containing ambients. Nevertheless a study on the impact of an oxygen containing ambient on CdTe thin film microstructure and device performance in complete CdTe/CdS devices is reported in Section 8.3.

Inclusion of hydrogen in the growth ambient was found to distinctly alter the early growth of CdTe layers on ITO. Comparisons between depositions performed in N_2 and 99%N_2 + 1%H_2 ambients, showed the latter to increase the nucleation density and the rate of film formation. There are two possible explanations for this; either a) the rate of sublimation from the source was altered, or b) the sticking processes were enhanced by hydrogen. These two possibilities are now explored in turn:

a) Influence of sublimation rate

The fact that it is known that source oxidation reduces growth rate makes it logical to suggest that a reducing ambient may remove native oxide phases from the source, thus increasing the sublimation rate. In turn this would increase the adatom arrival rate at the surface and, from atomistic theory presented in Section 4.4, may increase the nucleation

density by changing the probability of a stable nucleus being formed: An increase in adatom arrival rate, and as a result an increased adatom surface occupancy, makes the occurrence of adatom-adatom surface collision more probable. This increases the chances of the formation of nuclei of a super-critical size. An increase in sublimation rate would therefore explain the higher nucleation density observed in comparison to growth in a pure nitrogen ambient. However, as the source had been replenished with fresh CdTe powder prior to commencing work using a hydrogen ambient, any source oxidation should therefore have been minimal. Any increase in the deposition rate is unlikely to have occurred as a result of reduction in the amount of CSS source oxidation.

b) Influence of hydrogen on the surface processes

A number of morphological changes were observed for films deposited in hydrogen such as enhanced twinning and a large increase in the number of "hexagonal" shaped islands. It was believed these changes may have resulted from the substrate being altered by the use of hydrogen. SEM analysis of samples grown under high partial pressures of hydrogen confirmed this, revealing that ITO is not an inert substrate in the presence of hydrogen. This change in the nature of the substrate may also offer an explanation for the change in nucleation density and island growth noted in Section 7.3.4.1. The substrate plays a vital role in thin film nucleation, any change to the deposition surface will drastically alter the way the film forms (results showing the effect of different substrates on CdTe deposition are given in Section 7.4.3). In the instance of low adatom surface occupancy, such as has been utilised here, the effect of the substrate may be heightened. Binding and subsequent nucleation at defect sites (e.g. surface steps) is more likely to occur, than binding and nucleation as a result of adatom-adatom surface collisions (Section 4.4.3). Reduction of the surface by hydrogen may provide more defect sites available for binding and nucleation, increasing the island density as a result, but may also lead to the creation of metal islands on the surface.

Whilst each of the above ideas may individually offer a partial explanation for the change in thin film growth observed, it was deemed more likely that a combination of effects was a more probable cause. It is believed that the increase in sublimation rate may

lead to the increased island density and reduced island size observed, whilst modification of the deposition surface by hydrogen may account for the island shape change observed. In an attempt to separate the impact of the substrate surface from adatom-adatom effects, a separate study was carried out whereby hydrogen was introduced to the CSS chamber at different stages of growth (Section 7.4.5).

EDX analysis of CdTe thin films deposited in low partial pressures of hydrogen (Section 7.3.4.1), revealed no evidence of reduction of the ITO surface. The island structures observed in such depositions were determined to be CdTe structures, with no evidence of indium or tin phases. However, growth carried out using ambients containing high partial pressures of hydrogen was found to cause reduction of the substrate, leading to indium and tin phases being formed on the surface, and damage to the ITO layer. This raised concerns about the general stability of ITO as a substrate for use in high temperature CSS deposition. However, depositions that did not include hydrogen in the processing ambient, no evidence of reduction of the substrate was found.

Due to the results presented in Section 7.3.4.2, it was decided that ITO was an unsuitable substrate for any further work under these conditions. Subsequent work was therefore performed on CdS coated ITO substrates.

7.4 Growth of CdTe thin films on CdS

CdTe thin films, deposited on CdS/ITO/glass, constitute the superstrate device configuration regularly employed in CdTe/CdS solar cells. Study of the formation process of CdTe thin films deposited upon CdS is therefore of direct relevance to solar cell device fabrication. In this section, the growth events for CdTe on CdS/ITO/glass structures as a function of time were examined via post-growth AFM and SEM analysis. The impact of a hydrogen containing ambient on the growth was investigated by comparison to films grown in a nitrogen ambient. Investigations on CdTe films where a hydrogen containing ambient was introduced at different points during growth, are also described.

7.4.1 Sample fabrication

CdS thin films were deposited by CSS onto ITO/glass substrates bought from Vision Tech Ltd. Substrates were cleaned prior to CdS deposition by ultrasonication in Decon 90, water, acetone then isopropanol. CdS films were deposited in vacuum at constant source and substrate temperatures of 650°C and 540°C respectively. The growth time was 2 min, which produced CdS layers of ~300nm thickness. The substrates were 5x5cm in size but were broken in 2.5x2.5cm quarters after CdS deposition. This was done to reduce the number of CdS growth runs required, and to minimise any systematic error due to variation in the growth of the CdS layers. CdTe films were deposited on top of the CdS layer at constant source and substrate temperatures of 600°C and 500°C respectively. A chamber pressure of 100Torr was used, as preliminary measurements indicated that for deposition at 200Torr (as previously used) the growth rate was too slow.

7.4.2 Growth in a nitrogen ambient

A series of CdTe thin films were grown for various times in the range 5-360min in a nitrogen ambient, at a pressure of 100Torr. Samples were grown out of sequence to avoid any systematic error. Figs.7.11 and 7.12 show SEM and AFM images of the series. Data extracted from AFM measurements for average island area, coverage, density and surface roughness are plotted as a function of time in fig.7.13. The development of CdTe island structures can be clearly seen from the SEM and AFM images of the samples and as with CdTe deposition onto ITO substrates (Section 7.3) film formation occurs via the Volmer-Weber mode of growth.

At the earliest stage of growth examined, t=5min (Fig.7.11a, 7.12a), nucleation has occurred by the formation of a number of small well spaced islands at a density of $0.08\mu m^{-2}$ and with an average area of $0.78nm^2$. By t=10min (Fig.7.11b, 7.12b), the island density has increased dramatically (Fig.7.13c) indicating that nucleation has continued in the preceding period. Individual islands grow continually throughout this period by further addition of species diffusing across the surface. Despite this however, the average island area has decreased slightly over this period (Fig.7.13a), due to the formation of a large number of new, smaller, islands which act to reduce the average size. Substrate coverage more than doubles during this period (Fig7.13b), increasing from 6% to 14%.

At t = 10min, the island density is at a peak for the period studied, while the average area is at a minimum. This point may therefore be considered as the end of the initial nucleation period (as discernable from the growth times chosen for this experiment). At this point a network of stable islands has been established on the substrate and these islands proceed to grow by further addition of species at the expense of any further nucleation occurring. No further nucleation is observed to occur during this period, by either SEM or AFM analysis. Hence, for the period of growth succeeding this, 10min$< t \leq$ 120min (Fig.7.11c-f, 7.12c-f), the island density continually decreases while the average island area increases. Due to their increase in size, islands come into contact and undergo complete coalescence (re-ordering as a single island) and this reduces the island density. By the end of this period, t = 120min (Fig7.11f, 7.12f), island density has significantly reduced. Islands are now relatively large as a result of coalescence and continued growth, while some have begun to take on an elongated shape as a result of coalescence. This is an indication that islands have reached a large enough size so as to make complete coalescence improbable due to the long times required for neck formation to progress (Section 4.5.3). This is the beginning of the channel formation stage (Section 4.5.4). At t = 240min (Fig7.11g, 7.12g), the formation of channels can be seen more clearly. Primary islands have formed a coalesced network, leaving vacant channels between. Secondary nucleation of islands begins to occur in these channels, leading to an increase in the island density. Whilst islands do continue to grow by further addition of adatoms, the increase in average area (shown in fig.7.13a) is relatively small. This believed to result from the onset of secondary nucleation introducing a number of smaller islands (thus reducing the average), rather than any change in island growth rate. For the final growth monitoring time, t = 360min (Fig.7.11h, 7.12h), the size of the networked primary islands has increased while secondary nucleation has continued in the channels. The island density has increased but the average area has reduced, due to the occurrence of these secondary islands. At this final monitoring stage, coverage is reasonably high (~70%) and the formation of a complete film is expected to be achieved at growth times longer than were employed here. The manner of film completion is expected to be by the continued growth of the secondary islands, their incorporation into the network of primary islands and a final bout of nucleation to fill any remaining gaps.

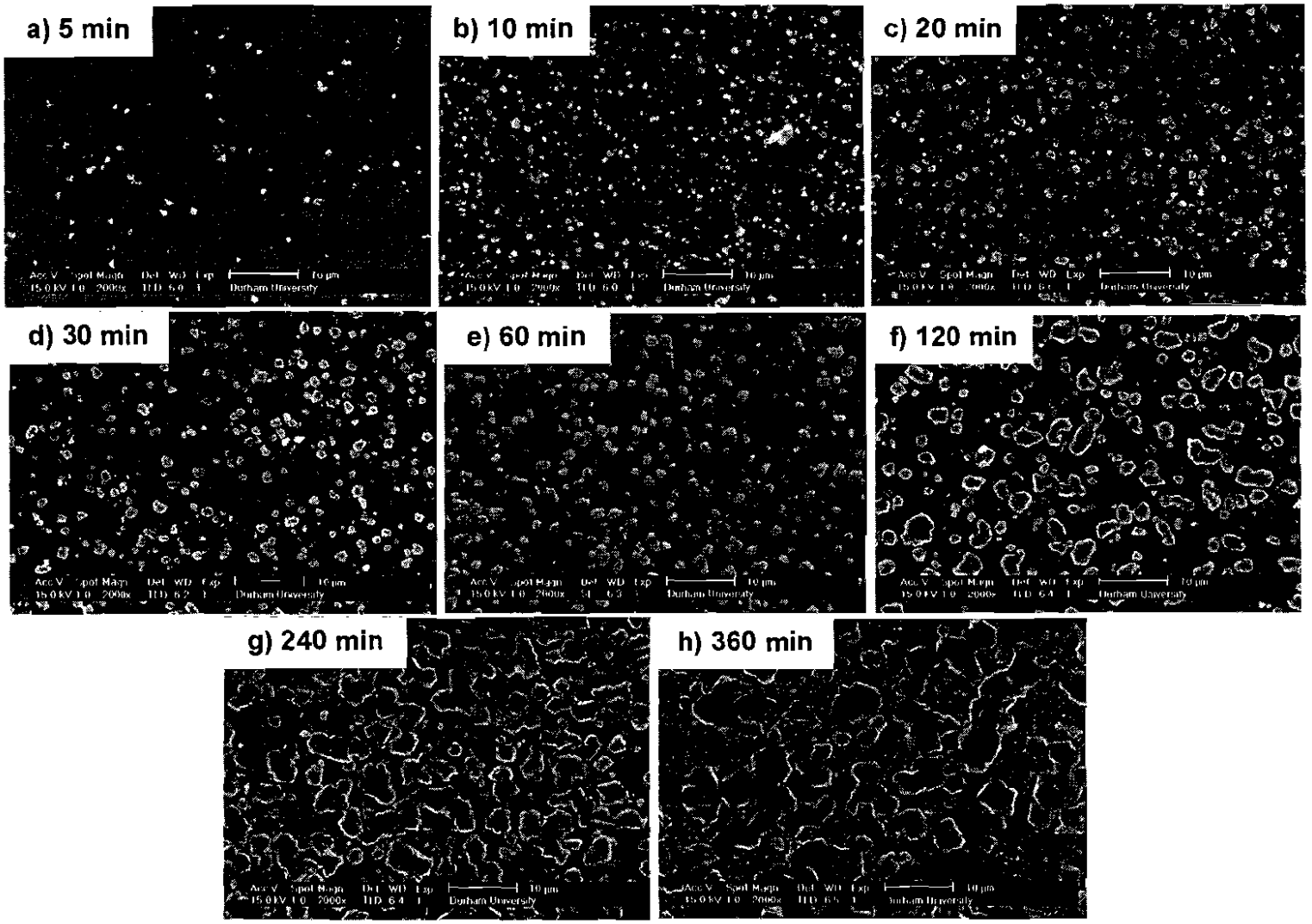

Figure 7.11: SEM images of CdTe thin films deposited on CdS under 200Torr of nitrogen, growth times are in the range 5-360mins.

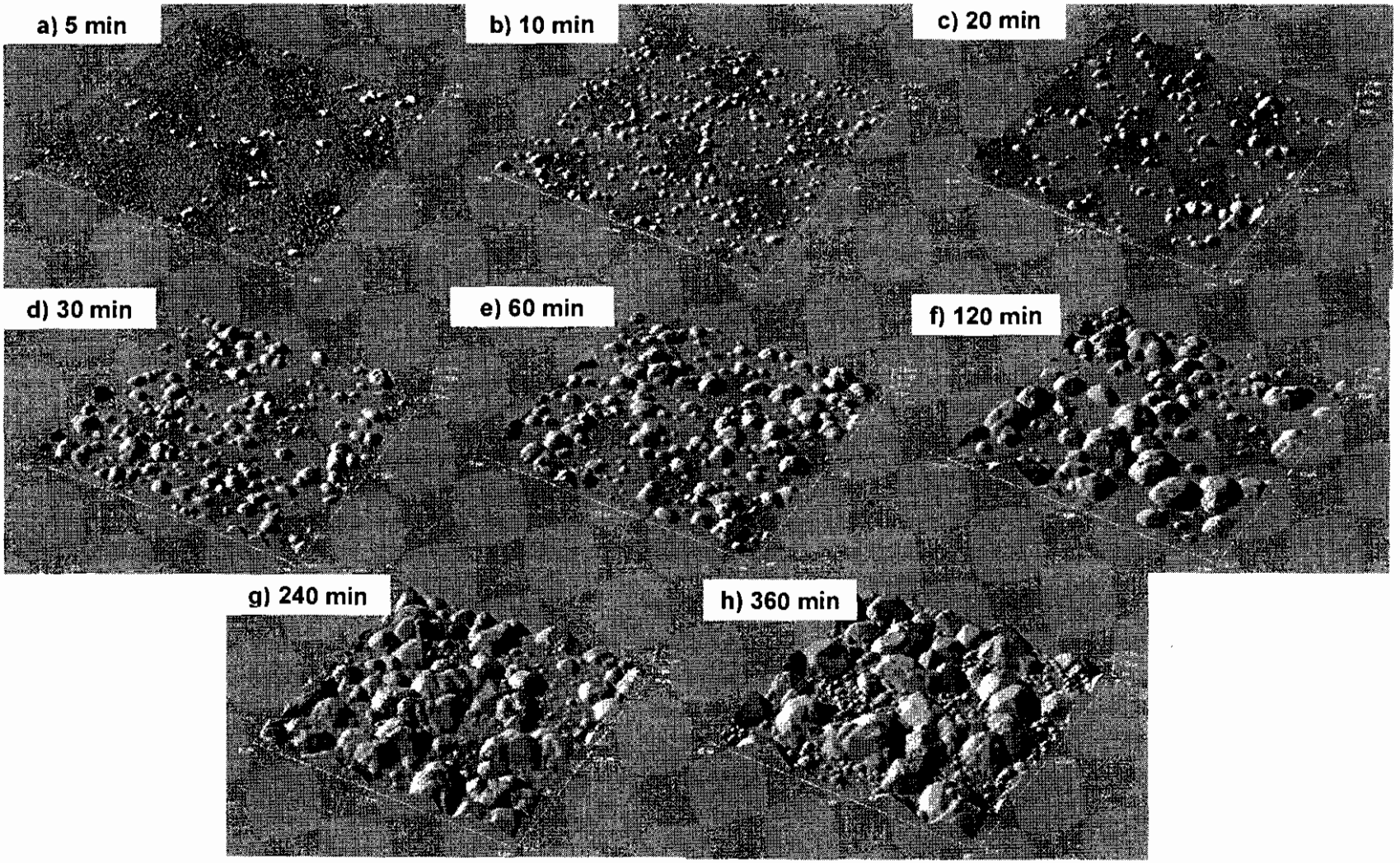

Figure 7.12: AFM images of CdTe thin films deposited on CdS under 200Torr of nitrogen for growth times between 5 and 360min. The range of each axis is as follows; X = 0 – 35μm, Y = 0 – 35μm and Z = 0 – 2.5μm.

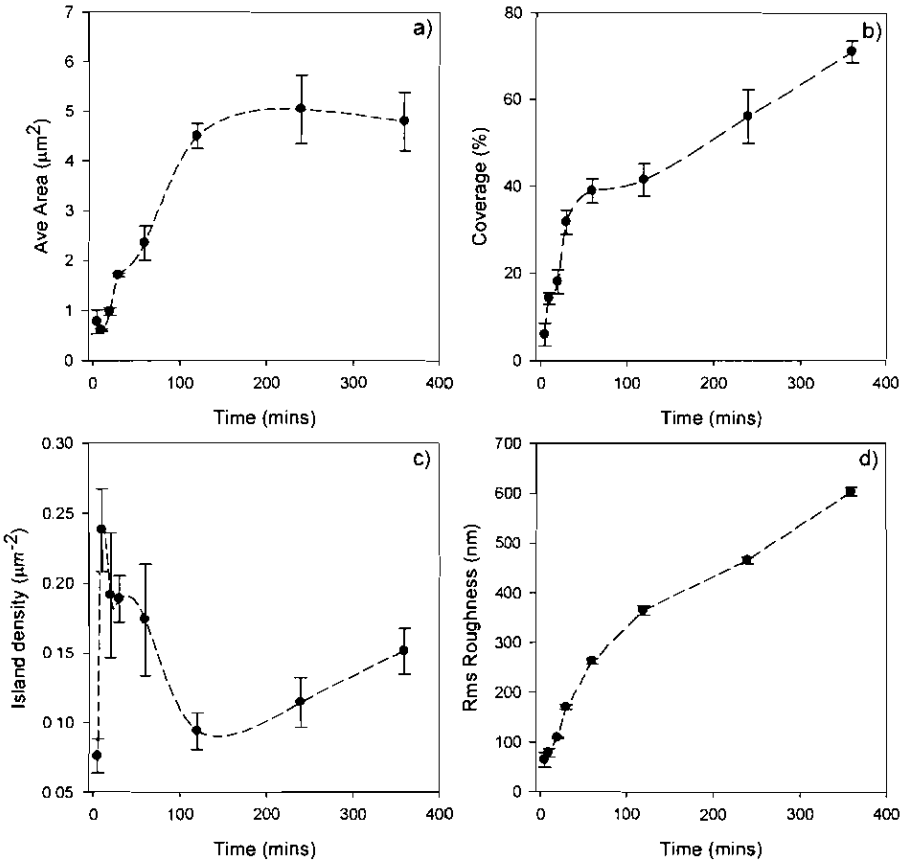

Figure 7.13: Data extracted from AFM scans of CdTe films grown on CdS/ITO for various times a) Average area, b) Coverage, c) Island density and d) rms surface roughness (plotted lines are guides for the eye).

Data for average island aspect ratio (width/height) and average layer thickness is plotted in fig.7.14 as a function of the growth time. The mean layer height was determined directly from averaging the AFM measurements, while aspect ratio values were determined by subsequent computer analysis of the AFM data. While layer thickness increases throughout growth (fig.7.14) there is little variation in the aspect ratio, implying that growth in the horizontal and vertical directions is balanced. Therefore, islands maintain their initial dimensions during growth and coalescence, and the island contact angle remains relatively constant throughout growth.

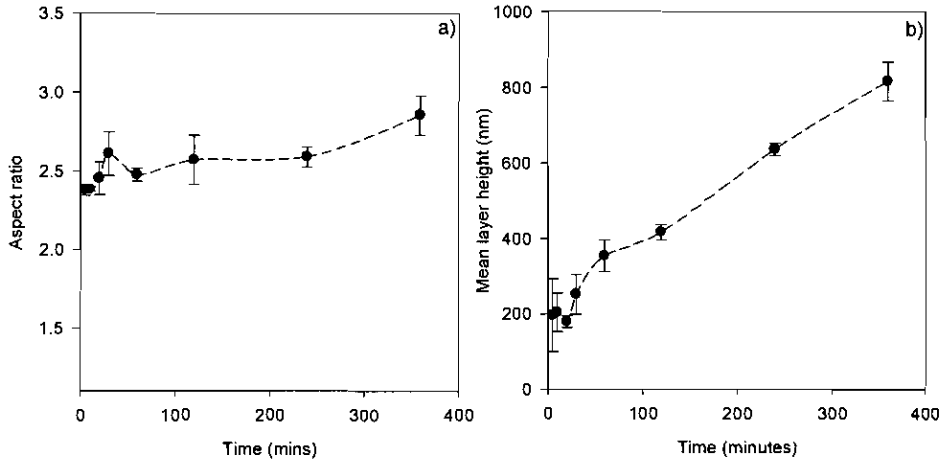

Figure 7.14: Island height data extracted from AFM scans a) Average island aspect ratio (width/height) b) Mean height of films

As well as the average values for island size, significant information may be extracted from the distribution of island sizes[13] and its progression with time. Fig.7.15 shows the normalised island diameter distribution plotted as a function of growth time. Diameters were determined from AFM images of films shown in fig.7.12. Data from the t = 5min sample is not included, due to the small number of observed islands. Diameter values were calculated from an equivalent circle based on the island area using the equation;

$$D = 2\sqrt{\frac{A}{\pi}} \qquad (7.1)$$

where D is the diameter of the equivalent circle and A is the island area, this being determined from AFM analysis. Due to the various processes involved in thin film growth that may alter the size distribution of islands (e.g. coalescence, secondary nucleation), successful fitting to a Gaussian distribution is unlikely[14] (the possible exceptions to this are at very early stages of growth, before coalescence effects begin to occur, and after the film has formed a complete layer). Instead, Rayleigh distributions have been successfully fitted to grain size distributions in complete CdTe thin films[15]. For the early stages of growth examined in this work (10min$\leq t \leq$ 20min), the histograms are approximated by a Gaussian distribution. As the growth progresses and coalescence processes begin to dominate, this Gaussian character is lost and secondary peaks at larger island diameters begin to appear.

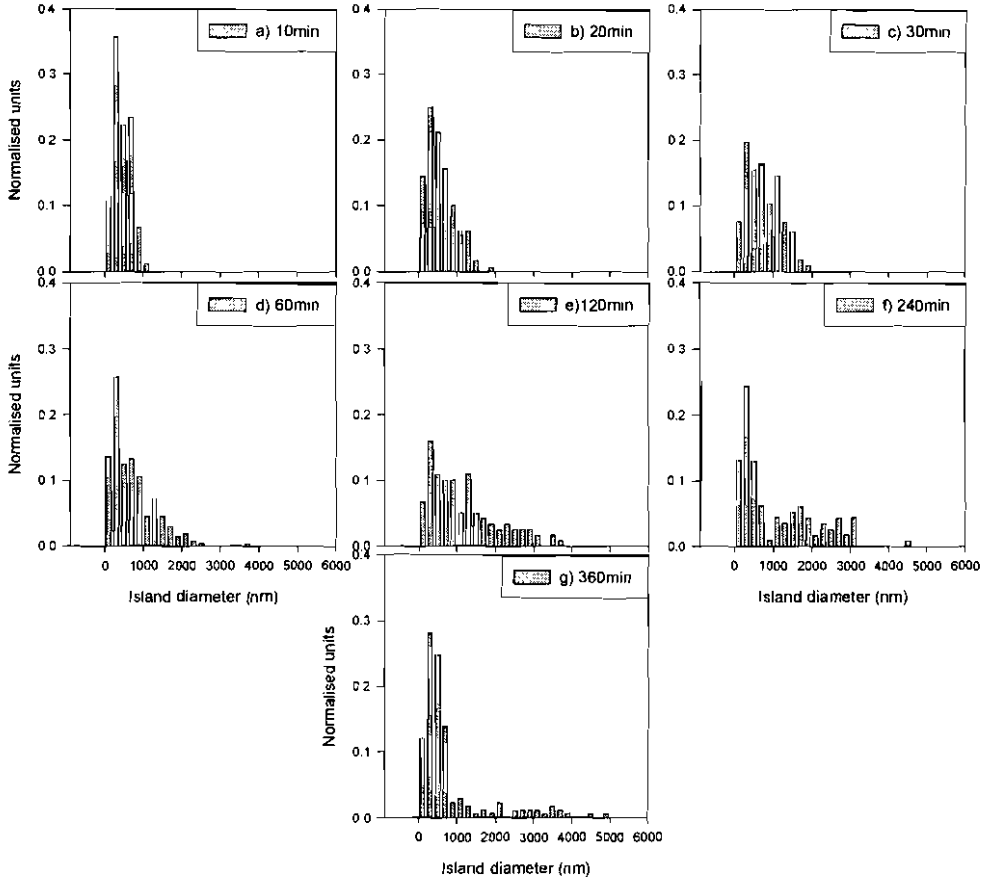

Figure 7.15: Island width histograms for various growth times.

This can be most clearly seen at t = 240min, where the histogram has a well defined minimum for an island diameter of ~900nm. The appearance of this double peaked distribution provides an indication of the mode of coalescence prevalent during growth. Venables *et al*[13] stated that the dominant coalescence mechanism will influence the size distributions of stable islands. Fig.7.16 shows the schematic histograms for the cases of: a) coalescence via island mobility and b) coalescence by island growth (these processes are discussed in Section 4.5.3). Venables generated these forms via rate equation calculations, but the underlying processes may be understood relatively simply as follows: The island size distributions are assumed to be Gaussian prior to the onset of any coalescence effects. In the instance of coalescence by island mobility, smaller islands are more mobile on the surface than larger islands and are therefore more likely to be involved in coalescence interactions. This produces a shift in the whole distribution

towards the larger cluster diameters and results in the distribution seen in fig.7.16a. For coalescence by growth it is the larger islands that are more likely to undergo coalescence, as they are more likely to come into contact with neighbouring islands due to their increased size. The distribution therefore splits into a double peak, as the large islands in the initial distribution coalesce and then re-order to form yet larger islands than those present in the initial distribution. The island distributions observed here for CdTe thin film formation indicate that coalescence occurs by island growth (yielding double peaked distributions), with no evidence for coalescence by island mobility being observed.

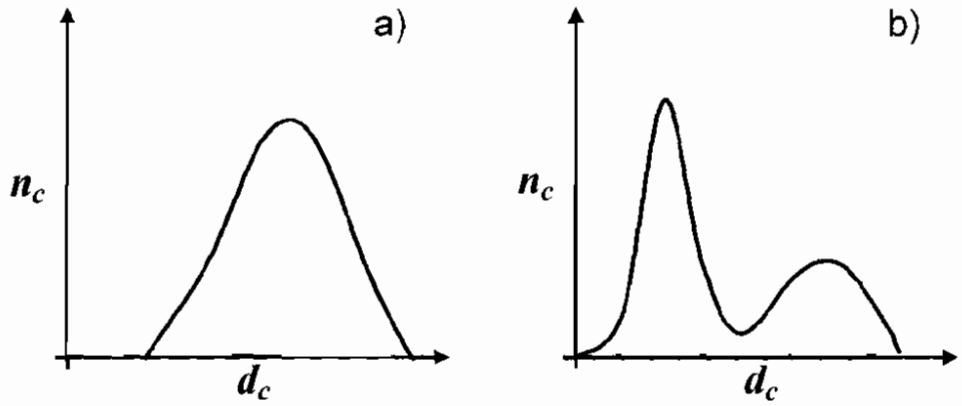

Figure 7.16: Schematic island size distributions for: a) coalescence by island mobility, b) coalescence by island growth.

7.4.3 *Effect of the substrate type on CdTe growth in a nitrogen ambient*

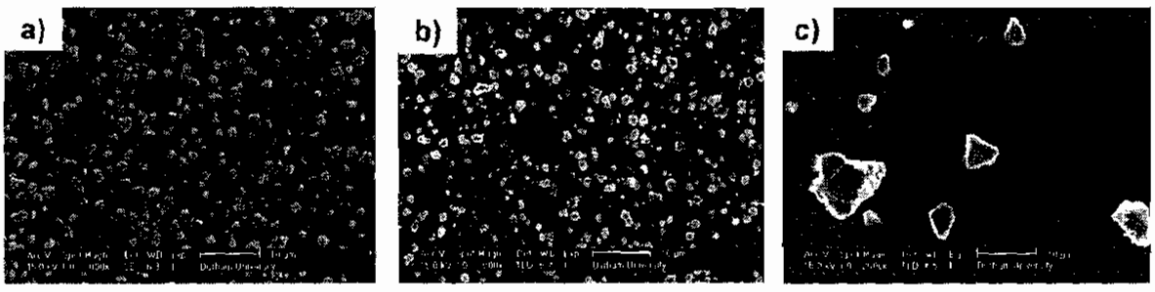

Figure 7.17: SEM images of CdTe deposited on different surfaces a) CSS CdS, b) CBD CdS, c) ITO. All images were recorded at the same magnification.

The observations of CdTe surface morphology in Sections 7.3.2 and 7.4.2 indicate that the type of substrate has a profound effect on the layers. In order to investigate this

systematically, a set of CdTe films were deposited under identical conditions but on different surfaces, these being a) 300nm of CdS deposited by CSS on ITO, b) 300nm of CdS deposited by chemical bath deposition (CBD) on ITO and c) ITO. In all cases identical ITO from Vision Tech was used and the samples were grown under 100Torr of nitrogen for 60min. Fig.7.17 shows SEM images of the resulting films. Very little variation in island size or density is observed between depositions carried out on the two varieties of CdS (fig.7.17a, b). Islands form with a relatively high density in both cases and the average island diameters were approximately 1μm for CdTe islands on both surfaces. However, in the case of deposition onto an ITO surface (fig.7.17c), the average island diameter is significantly larger (~ 4μm), while the average island density is reduced by a factor of ~14.

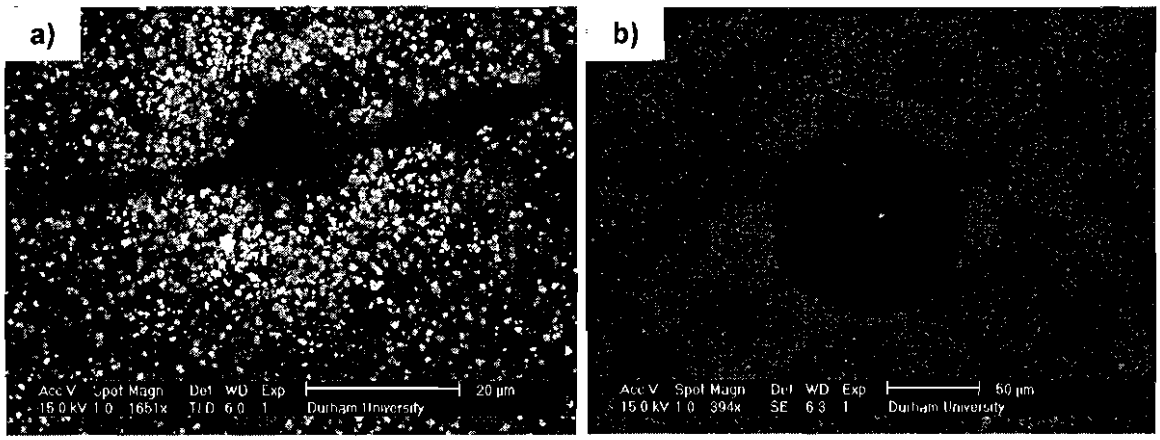

Figure 7.18: SEM images of CdTe island formation at CdS surface defects. CdS was deposited by CSS onto ITO.

CdS surface defects were found to significantly retard or increase CdTe island formation under these conditions, producing significant morphological defects. Fig.7.18 shows SEM images of two examples. In fig.7.18a, a scratch running across the surface acts as an exclusion zone to island formation, whilst in fig.7.18b an area of apparent high surface mobility has occurred around a central island, leading to an increased island density around this region. Defects such as these were commonly observed in CdTe films deposited on CdS under these conditions with the defects being maintained up to high

coverage, effectively forming pinholes in the completed layers. No such defects were observed for deposition on ITO surfaces.

7.4.4 Growth in a hydrogen containing ambient

Growth of CdTe thin films using ambients containing hydrogen has been shown to increase the island density and level of substrate coverage for deposition onto ITO in Section 7.3.4. Here similar experiments are conducted using CdS/ITO substrates, since this has direct relevance to full working PV device structures. CdS was grown on ITO (Vision Tech) using CSS as described in section 7.4.2. For the CdTe growth a 2% partial pressure of hydrogen was included in the growth ambient (98% N_2 + 2% H_2), while a total chamber pressure of 100Torr was maintained throughout growth. Growth times in the range 5-60min were used (with growth times of 90min and above producing completed films that are not considered here). AFM images of the films are shown in fig.7.19, with data extracted from AFM measurements for average island area, coverage, density and surface roughness is plotted as a function of growth time in fig.7.20. Data from samples grown in a nitrogen ambient are plotted in the same figure for comparison.

Results show that the inclusion of hydrogen in the processing ambient to has a similar impact on CdTe film formation on CdS to that observed for deposition on ITO. Island density is significantly increased in comparison to growth in a pure nitrogen ambient with complete substrate coverage being achieved after a much shorter growth time – this being 90min for growth in a hydrogen containing ambient, while coverage was only 70% after 360min growth in a pure nitrogen ambient. Secondary nucleation occurs at a much earlier time, and more extensively than in the case of a pure nitrogen ambient. This is shown by a peak in the island density curve, at t = 30min, for growth under hydrogen. For growth in a nitrogen ambient, secondary nucleation occurs much later, at t >120min, implying that inclusion of hydrogen produces an increased film formation rate. After secondary nucleation the island density falls rapidly, due to fast coalescence of the secondary islands and their subsequent inclusion into the distribution of primary islands. This rapid coalescence leads to a sharp increase in island area, seen at t = 60min, to the extent that the average island area becomes higher than for the equivalent time for growth in a nitrogen ambient. It should be noted however that for t > 60min, when growth under

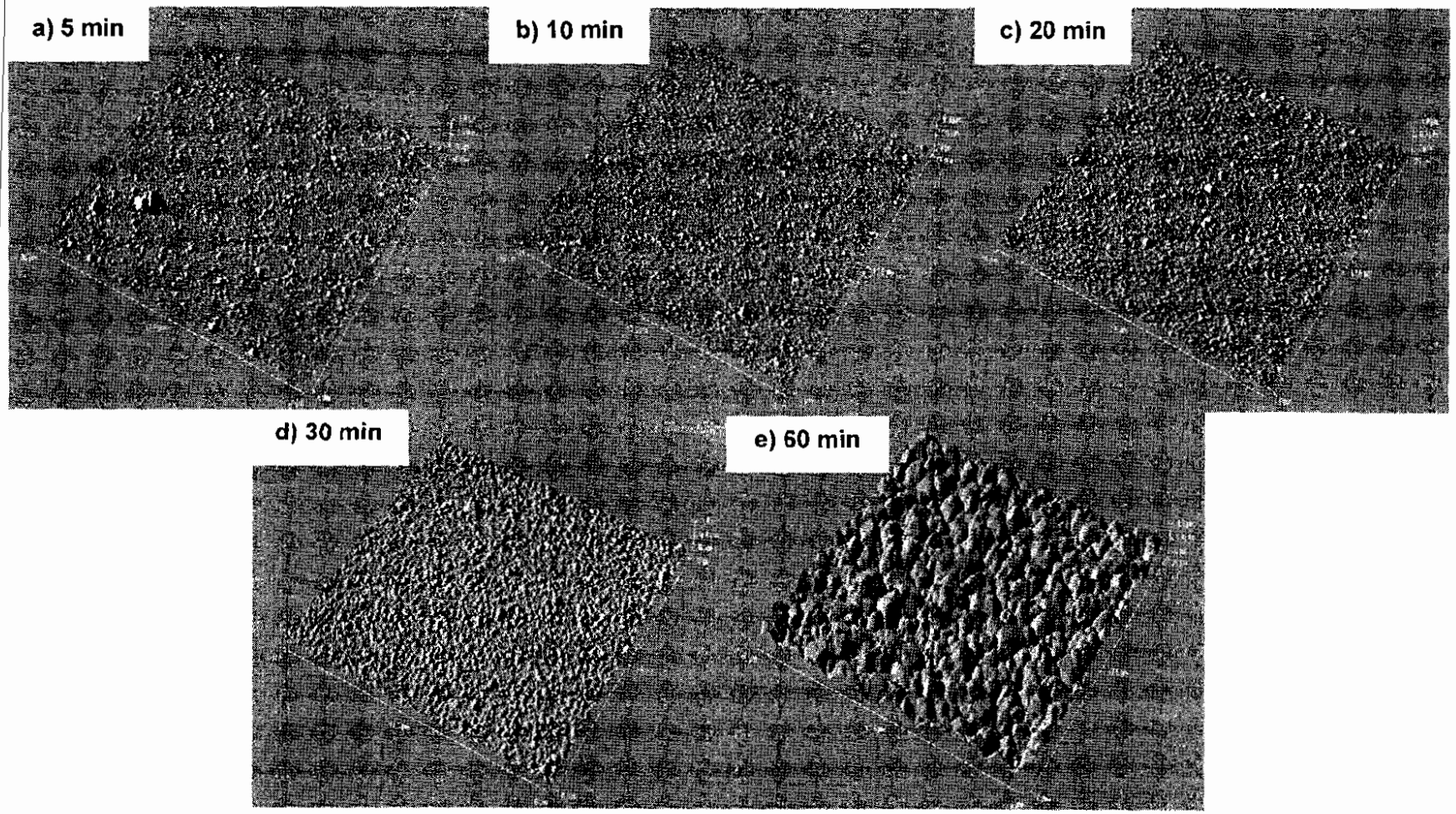

Figure7.19: AFM scans of CdTe thin films deposited in a hydrogen containing ambient on CdS, for times between 5 and 60min. The range of each axis is as follows; X = 0 – 35μm, Y = 0 – 35μm and Z = 0 – 1.8μm.

hydrogen was complete, the grain size was significantly smaller (2.32μm^2) than that of the islands observed at t = 360min in a nitrogen ambient (4.86μm^2), fig.7.13. It is therefore expected that for layers grown of equal thickness, samples grown in a nitrogen ambient would have a larger average grain size than those grown with hydrogen.

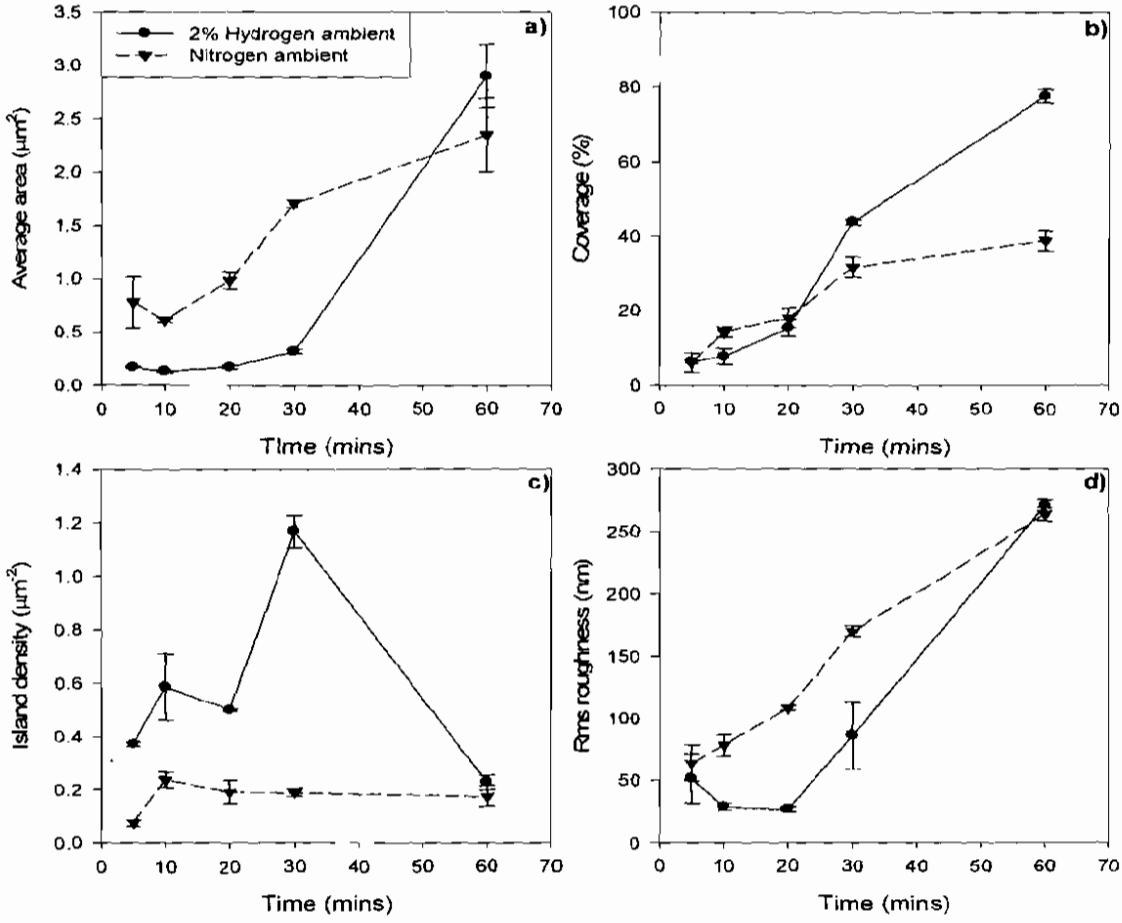

Figure 7.20: Comparative data for CdTe films grown in nitrogen and 2% hydrogen ambients a) Average area, b) Coverage, c) Island density, d) Surface roughness

7.4.5 Effect of changing the ambient during growth

The effect of including hydrogen into the CSS deposition ambient during the growth of CdTe thin films may be seen by comparing growth with and without hydrogen as presented in Section 7.4.4. However, as discussed in Section 7.3.5, the observations made from these results may be explained in two ways: The changes in growth seen may be attributable to the sublimation or deposition rate being altered by the presence of

hydrogen (i.e. the transfer rate is responsible). Alternatively, the hydrogen may be modifying the surface prior to, and during, CdTe island formation (i.e. the surface processes are responsible). Work described in this section attempts to separate the two effects by defining two stages of deposition in which the growth ambient may be different.

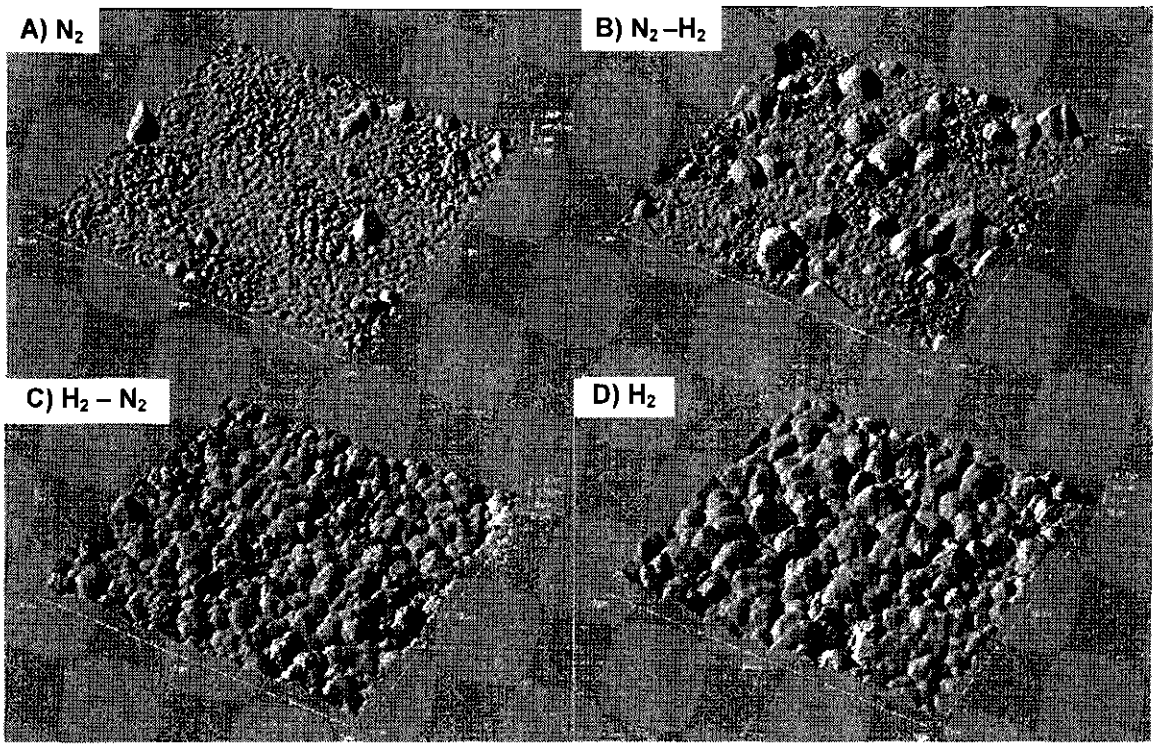

Figure 7.21: AFM images of CdTe layers deposited on CdS using various combinations of ambients: a) 30min in 100% N_2, b)15min in 100% N_2, 15min in 98% N_2 +2% H_2, c) 15min in 98% N_2 +2% H_2, 15min in 100% N_2 and d) 30min in 98% N_2 +2% H_2. For all images the field of view is 20x20μm. The vertical full scale deflection is a) 0.8μm, b) 1.3μm, c) 1.5μm and d) 1.2μm.

Sample	Ambient 1 (time)	Ambient 2 (time)
A	100% N_2 (30min)	-
B	100% N_2 (15min)	98% N_2 + 2% H_2 (15min)
C	98% N_2 + 2% H_2 (15min)	100% N_2 (15min)
D	98% N_2 + 2% H_2 (30min)	-

Table 7.2: Growth conditions used for CdTe deposition on CdS/ITO in which both one and two ambients were used. In all experiments the total pressure was 100Torr.

A series of four samples was produced. Growth was for a period of 30min, using a total deposition pressure of 100Torr but with two possible gas ambients, 100% N_2 and 98% N_2 + 2% H_2. Growth was divided into two periods, an initial period ($0 \leq t < 15$min) and a final period ($15 \leq t < 30$min). The combinations of ambients used for deposition of each sample are listed in table 7.2, while AFM images of the resultant films are shown in fig.7.21.

All four samples analysed show distinct differences as a result of the various combinations of growth ambients used. Fig.7.21a and 7.21d, are the two samples grown in a single ambient regime of, 100% N_2 and 98% N_2 + 2% H_2 respectively. As such, they demonstrate similar results to those presented in Section 7.4.4, namely an increase in island density and substrate coverage as a result of hydrogen inclusion in the growth ambient. Comparison between fig.7.21a and 7.21b shows that the inclusion of hydrogen at a later stage of growth has changed the island distribution. The deposit in sample B appears similar to that of sample A, but resembles that for a later stage of growth, with larger island sizes and increased coverage. This provides strong indication that the material transfer rate is increased by the presence of hydrogen. A similar result is found by comparison of fig.7.21c and 7.21d in which growth always starts under hydrogen. Here, while complete coverage of the surface has been achieved for both samples, sample D appears to have a larger island size. This may again be interpreted as a result of increased transfer rate to the substrate, owing to the inclusion of hydrogen in the processing ambient. By this means, sample D is at a more advanced stage of growth than sample A.

The most distinctive difference in growth occurs between samples B and C. Fig.7.21 shows that for sample B, islands have achieved a relatively large size, but at a low coverage. In contrast, islands in sample C have formed so as to completely cover the substrate, but with a much reduced island size. As both samples underwent a 15min growth period in the presence of hydrogen, this result cannot be attributed to a difference in the total amount of transport. This result demonstrates that the initial period of growth, encompassing nucleation, principally defines the film growth. In sample B, where the nucleation has occurred in the presence of nitrogen, the film has retained characteristics (e.g. large grain size, low coverage) previously observed for growth performed solely in

nitrogen. Similarly, the film nucleated in a hydrogen containing ambient retains the characteristics of a sample grown in hydrogen (e.g. reduced grain size, high coverage) despite the changing ambient.

7.4.6 Effect of the deposition pressure on CdTe thin film formation

As discussed in Section 7.2, changing the pressure within the CSS chamber, and thus the deposition rate, may alter the nucleation and growth of thin films. This may be attributed to the change in the supersaturation ratio (Section 4.4.1) and thus the adatom surface occupancy (Section 4.4.3). This effect was examined by comparison of three films deposited under 0.5Torr (the base pressure of the deposition system), 50Torr and 100Torr pressures of nitrogen. Growth times were varied to account for the associated change in deposition rate and films were grown for 2 seconds, 10min and 360min respectively. AFM images of the resultant films are shown in fig.7.22.

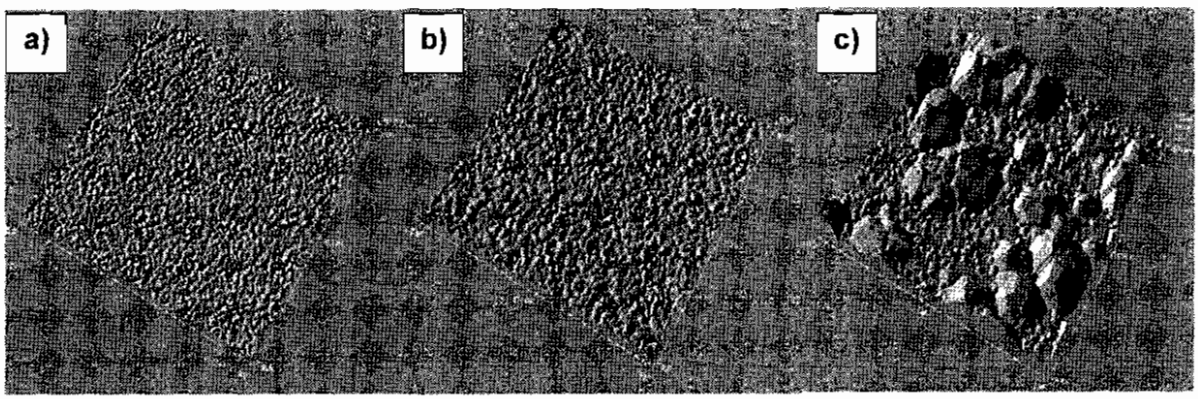

Figure 7.22: CdTe layers deposited on CdS at different chamber pressures, a) 0.5Torr (system base pressure) - a complete film has been deposited with small grain size, b) 50Torr - a complete film has been deposited but with an increase in grain size and c) 100Torr – an incomplete film with a distribution of large islands has been deposited. For all images the axis are as follows; X = 0 – 20μm, Y= 0 – 20μm. For figure a) Z = 0 – 0.3μm, b) Z = 0 – 0.9μm and c) Z = 0 – 2.6μm.

The images reveal significant differences in the microstructure of the films as a function of pressure. For the films grown at 0.5Torr and at 50Torr (fig.7.22a and b), the coverage is complete but that that the film grown at the higher pressure has larger grains (~0.7μm compared to ~1.5μm). Since surface profiler measurements of the film thickness indicated that both of these films were of comparable thickness, it may be stated that the grain size enhancement is as a result of pressure only (an example of the development of

grain size with thickness is given in Zoppi *et al*[16]). The most dramatic influence was seen upon increasing the pressure from 50 to 100Torr (fig.7.22b and c). For deposition at 100Torr the film development has been arrested before the formation of a complete film. The primary nuclei have developed to form even larger islands (~5μm diameter) and with a much reduced density than at lower pressure. Also there is clear evidence of secondary nucleation, there being channel filling by new islands (~1.5μm diameter). In making a comparison between these films it is emphasised that the growth runs were designed so as to ensure that the films were of comparable thickness, rather than being developed to a comparable stage of growth. It is clear however that the use of high pressure has the capacity to increase the maximum grain size achievable. The effect of CSS chamber pressure on deposition of CdTe thin films for solar cell devices is again discussed in Section 8.4. Further comparisons of grain size as a function of pressure are made, but are done so in terms of completed cell structures. The impact of grain size on device performance is also examined.

7.4.7 Discussion

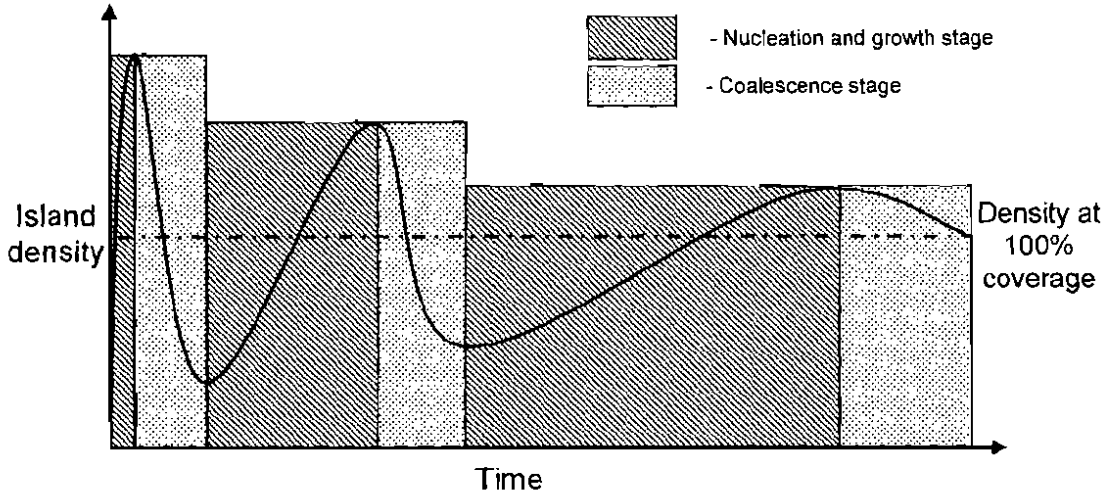

Figure 7.23: Schematic representation of the evolution of CdTe island density with growth up to the point of coverage. This model is derived from the empirical observations and qualitative predictions of the latter stages of growth. See text for further details.

Results in Section 7.4.2 show the development of CdTe films, deposited on CdS, as a function of time. As with CdTe deposition onto ITO, growth occurred via the Volmer-

Weber mode, this being an indication that bonding between atoms within the deposited film is stronger than the film-substrate bonding. CdTe films are seen to develop via the mechanism outlined in Chapter 4 and which is reported by other authors for a range of materials systems[16-20] i.e. nucleation, growth of islands, coalescence, channel formation and secondary nucleation. The results provide a basic understanding for the development of thin film CdTe microstructure when deposited on CdS, and the observed progression of growth (within the above scheme) may be summarised as follows: CdTe films form via the nucleation of a large number of small islands. As growth progresses, islands increase in size by the addition of species from the surface and by direct impingement of adatoms from the vapour flux. As a result of their growth, CdTe islands come into contact with one another and undergo complete coalescence i.e. re-ordering as single islands. This coalescence during growth reduces the island density on the surface. When the islands reach a certain size, complete coalescence takes a prohibitive amount of time to complete and islands form a coalesced network rather than re-ordering as single islands. The empty channels left by this network are filled by the formation of secondary nuclei which, along with the primary networked islands, grow by further addition of adatom species. At the end of the examined growth period a complete film had not yet been formed. However, it is assumed that if growth were allowed to continue in the same manner, a complete film would eventually be formed after a longer period of growth. Secondary islands would continue to grow and become incorporated into the primary island network, leaving holes in the material. These remaining holes would most likely be filled by a further, tertiary, bout of nucleation and the islands formed would become incorporated into the existing grain structure hence forming a complete film. The plot of island density vs growth time (fig.7.13c), provides the most direct indicator of the progression of growth as it is most directly influenced by the film development. A schematic representation of its development is given in fig.7.23. The observed results have been extended to include predictions for island density development up to the point of complete coverage. The growth period may be arbitrarily split into sections, in which either island formation or coalescence dominates. Peaks in the curve are assigned as the end point of the nucleation and island formation stage and the onset of coalescence, troughs are assigned as the start of nucleation and the end of coalescence. In reality these

processes are unlikely to be so discrete, with coalescence occurring at very early stages of growth. However, it is only when coalescence or island formation processes begin to dominate that we see the effect of these processes via an increase or decrease in the island density values. This model offers a simple representation of the microstructural evolution of CdTe thin films as a function of time, up to the point of formation of a complete layer.

Results presented in Section 7.4.3 show how the nature of CdTe thin film formation is to an extent dependent upon the nature of the deposition surface. The observed changes may be due to the high pressures utilised during nucleation of films in this chapter. As has been mentioned previously, under conditions of low adatom surface occupancy the nucleation of islands may depend on surface defect sites. It is possible that CdS layers have more of these sites available for nucleation than an ITO surface. However, material constants for deposition such as the vibrational frequency of an adatom on the surface, v, as well as the activation energies for adsorption and diffusion, E_a and E_d (Section 4.4.3), will be altered by changing the deposition surface. From equation 4.13 it may be seen that, this will change the lifetime of an adatom on the surface and in turn will alter the nucleation and island development as a result. The increased island density and reduced island size observed in deposition on CdS implies the CdTe-CdS system has higher E_a and E_d (hence a large τ and small D) values than the CdTe-ITO system. This seems the most probable cause for the change in film microstructure observed. Similar results have been reported by other authors for deposition on alternative substrates, in different materials systems (see for example Lee and Maa[17]). The impact of the substrate on film microstructure, demonstrates the importance of controlling the surface being used for deposition. It is possible that significant control over the grain structure in completed CdTe thin films may be achieved by manipulating the deposition surface in order to achieve the desired nucleation characteristics.

CdTe deposition on CdS performed in the presence of hydrogen (Section 7.4.4) yielded similar results to those reported for CdTe deposition onto ITO (Section 7.3.4) i.e. the island density and level of substrate coverage was increased, while the average island area was reduced. Results of the two stage growth experiments presented in Section 7.4.5 offer an insight into the manner by which hydrogen affects this change in growth. The

results highlight the importance of the initial nucleation stage of growth, showing that the initial distribution of islands in effect acts as a 'template' for subsequent growth. Once a distribution of stable islands and their associated capture zones (Section 4.5.1) is established, any change in deposition conditions should not overtly affect the progression of growth. Established islands will continue to grow with the same distribution at the expense of further nucleation occurring and changing the growth conditions (by alteration of the gas ambient) will simply alter the rate at which established islands develop. However, it is anticipated that altering the deposition conditions may change the growth at later stages. Secondary nucleation occurring under alternative conditions from that of the initial nucleation may be significantly different in character, though this will not have as pronounced effect on film formation as changing the initial nucleation conditions. Deposited CdTe films were shown to maintain their initial island distribution, determined during nucleation, despite the deposition ambient being changed at the midpoint of growth (fig.7.21b,c). Hydrogen was shown to produce increased island density and substrate coverage during the formation of CdTe thin films only when present at the start of the growth process. However, the exact mechanism by which hydrogen affects this change is still unclear. It is possible that the hydrogen modifies the CdS surface prior to CdTe deposition. This seems plausible as hydrogen may remove oxides phases that have formed on the surface, or alternatively may affect the surface materials constants (e.g. E_a, E_d). As for comparisons between depositions performed on CdS and on ITO surfaces, use of hydrogen in the processing ambient may increase the E_a and E_d values of the CdS surface. This would explain the increase in island density and reduction in island size observed. Results presented in Chapter 8 also show that the morphology of CdTe films deposited on CdS is altered by deposition in the presence of hydrogen. This implies that, as in the case of deposition on ITO, the CdS surface may be modified by high temperature hydrogen treatment. However, it was also established, in Section 7.4.5, that the inclusion of hydrogen produced an increase in the deposition rate of the material. Results in section 7.4.6 demonstrated that changing the deposition rate of material onto the surface may also drastically alter the growth. It follows from these results that, if hydrogen increases the arrival rate of adatoms at the surface (equivalent to lowering the deposition pressure) then an increased initial nucleation density may be expected. It

seems likely however that the change in island formation, resulting from the presence of hydrogen, is caused by a combination of modification of the substrate and a change in the deposition rate of CdTe.

Results in Section 7.4.6 show a dramatic change in the CdTe island size for growth under different pressures of nitrogen. These results may be explained in terms of the nucleation and growth theories outlined in Chapter 4. As discussed in Section 4.4.1, increasing the gas pressure within the CSS growth chamber will reduce the rate of sublimation from the source material. From the capillarity model for nucleation (Section 4.4.1), lowering the sublimation rate will reduce the supersaturation ratio of the system, as the system vapour pressure is reduced. From equation 4.7 it may be seen, this leads to an increase in the size of the critical radius and hence fewer stable nuclei will typically form in a given area. As the average area of islands will be proportional to the inverse of island density, the average island size will be greater as a result. An alternative explanation may be achieved by considering the atomistic surface processes involved in nucleation (Section 4.4.3). For higher pressures, the arrival rate of adatoms at the surface and thus the adatom surface occupancy at a given time, is reduced. This decreases the likelihood of successful collisions leading to the formation of stable nuclei. This in turn reduces the probability of nucleation occurring and leads to a lower density of initial islands formed on the surface. As a result, average island size should be increased. Both these mechanisms offer a valid explanation for the observed results, but they are by no means mutually exclusive.

7.5 Conclusions

The nucleation and early growth of CdTe thin films was studied by ex-situ AFM and SEM analysis. Films were grown at high pressures of nitrogen (with or without a 2% partial pressure of either hydrogen or oxygen) to slow the growth rate and allow accurate study of the film development as a function of time. The mode of growth by which CdTe thin films form was established for deposition on both ITO and CdS surfaces. In both cases, films formed via the Volmer-Weber growth mode and growth progressed in a similar manner to that reported for other materials systems (that grow via the Volmer-Weber mode). Film formation was found to differ significantly between depositions

carried out on the two surfaces with a large increase in the island density and a reduction in the size of islands being observed for deposition on CdS, in comparison to growth on ITO. This change was attributed to a difference in the surface activation energies (the energy required for re-evaporation from the surface, E_a, and the activation energy for diffusion, E_d) for the two substrates. However, to the author's knowledge these values have not been determined for the thin film CdTe/CdS interface.

Various techniques for manipulating the early growth of CdTe thin films were demonstrated. For deposition on an ITO surface, oxygen was shown to greatly reduce the island size, increase the island density and increase substrate coverage. These observations were explained via the step flow model, and by treating oxygen as a co-deposited impurity species, as suggested by Barna. Whilst not investigated here, a similar result is expected for CdTe deposition on a CdS surface in the presence of oxygen.

The effect of introducing hydrogen into the CSS ambient, for CdTe deposition, was evaluated for growth on both CdS and ITO surfaces. In both cases, the presence of hydrogen was found to increase the island density and also improve coverage of the substrate. Two possible explanations are offered for the manner by which this change occurs: i) hydrogen modifies the CdS/ ITO surfaces and alters the surface activation energies, thus changing the nucleation and ii) hydrogen produces a increased adatom arrival rate at the surface (by increasing the rate of sublimation from the source material), and thus changes the nucleation and film development. Hydrogen was shown to offer a route to improving substrate coverage, without the need for oxygen in the processing ambient.

A significant increase in the island size of CdTe thin films was achieved by using higher than standard CSS chamber pressures during deposition. The high pressures used were deemed to slow the adatom arrival rate and thereby reduce the surface occupancy. This lowered the probability of nucleation occurring, reduced the island density and lead to a larger island size. This is of particular interest for fabrication of CdTe solar cells, as it demonstrated a potential method for increasing the grain size in CdTe films without the need for higher temperatures.

Results in this chapter demonstrate the manner by which CdTe thin films form on CdS and ITO surfaces. Various techniques for controlling the early stages of film formation, such as selection of the deposition ambient and pressure, have been demonstrated and explained in terms of nucleation and growth theory. These techniques, and the general understanding of the CdTe formation process achieved as a result of this work, may be beneficial for the fabrication of CdTe/CdS solar cells. The application of these techniques to solar cell devices, and their subsequent impact on CdTe microstructure and device performance, is reported in Chapter 8.

7.6 References for Chapter 7

1 B. E. McCandless and K. D. Dobson, Solar Energy **77,** 839-856 (2004).

2 C. S. Ferekides, D. Marinskiy, V. Viswanathan, B. Tetali, V. Palekis, P. Selvaraj, and D. L. Morel, Thin Solid Films **361,** 520-526 (2000).

3 D. H. Rose, D. H. Levi, R. J. Matson, D. S. Albin, R. G. Dhere, and P. Sheldon, in *Conference Record of the Twenty Fifth IEEE Photovoltaic Specialists Conference*, Washington D.C., 1996, 777-780.

4 C. S. Ferekides, D. Marinsky, V. Viswanathan, B. Tetali, V. Palekis, P. Selvaraj, and D. L. Morel, Thin Solid Films **361-362,** 520-526 (2000).

5 J. Luschitz, K. Lakus-Wollny, A. Klein, and W. Jaegermann, Thin Solid Films **515,** 5814-5818 (2007).

6 S. N. Alamri, Physica Status Solidi a-Applied Research **200,** 352-360 (2003).

7 P. B. Barna, in *International Summer School of Diagnostics and Applications of Thin Films*, (Chhum u Trebone, Czechoslovakia, 1991), 295-310.

8 D. B. Holt, Journal of Materials Science **23,** 1131 - 1136 (1988).

9 P. B. Barna, F. M. Reicha, G. Barcza, L. Gosztola, and F. Koltai, Vacuum **33,** 25-30 (1983).

10 P. Peranantham, Y. L. Jeyachandran, C. Viswanathan, N. N. Praveena, P. C. Chitra, D. Mangalaraj, and S. K. Narayandass, Materials Characterization **58,** 756-764 (2007).

11 P. B. Barna, M. Adamik, J. Labar, L. Kover, J. Toth, A. Devenyi, and R. Manaila, Surface and Coatings Technology **125,** 147-150 (2000).

12 P. B. Barna, G. Radnoczi, and F. M. Reicha, Vacuum **38,** 527-532 (1988).

13 J. A. Venables, G. D. T. Spiller, and M. Hanbucken, Reports on Progress in Physics **47,** 399 - 459 (1984).

14 L. Eckertova, *Physics of Thin Films*, Plenum Publishing Corporation, New York, 1986.

15 M. A. Cousins, PhD Thesis, University of Durham, 2001.

16 G. Zoppi, K. Durose, S. J. C. Irvine, and V. Barrioz, Semiconductor Science and Technology **21,** 763-770 (2006).

17 Y. L. Lee and J. R. Maa, Journal of Materials Science **26,** 6068-6072 (1991).

[18] D. W. Pashley, in *Advances in Physics*; *Vol. 14* (1965), 327-417.

[19] J. F. Pocza, A. Barna, P. B. Barna, I. Pozsgai, and G. Radnoczi, Japanese Journal of Applied Physics **2,** 525-532 (1974).

[20] H. Poppa, in *Epitaxial Growth Part A*, edited by J. W. Matthews (Academic Press, New York, 1975), 215-275.

8 Nucleation led device fabrication of CSS deposited CdTe/CdS devices

8.1 Introduction

In Chapter 7 studies of the growth of early stages of CdTe thin films, deposited by CSS, provided significant insight into the film formation process, as well as demonstrating various methods by which the nucleation and development of CdTe films may be manipulated. The use of a higher nitrogen pressure during CdTe deposition (Section 7.4) was shown to increase the grain or island size, whilst the use of different ambient gasses (Section 7.3) was shown to alter the level of substrate coverage and morphology. The application of these techniques to solar cell production may be expected to benefit device performance.

This chapter centers on investigations into controlling the growth of CdTe and CdS films deposited by CSS, using the understanding and principles gained from fundamental work discussed in Chapter 7. In Section 8.2 controlling the CdS deposition is explored, in particular the thickness of the layer, the use of a growth shutter and the use of oxygen during growth. In Section 8.3 a study of the influence of the gas ambient used for CdTe deposition (i.e. N_2, O_2 or H_2) upon device performance is presented. This is followed by a detailed study of the effect on devices of increasing the CdTe grain size by controlling the N_2 gas pressure.

8.2 Influence of CdS deposition on device performance

The nature of the CdS layer has a significant impact on the performance of CdTe/CdS devices. In this chapter all CdS deposition has been carried out using CSS. This section is in three parts with device performance being compared for; i) devices with various CdS thickness, ii) devices with CdS layers deposited with and without use of a shutter to control growth and iii) devices with CdS layers deposited with various concentrations of oxygen present in the process gas.

8.2.1 Reduction in CdS thickness

Most high efficiency CdTe/CdS devices are fabricated using thin CdS layers (<100nm), as this increases the current generated from wavelengths of light below the CdS bandgap (~2.4eV), as described in Chapter 6. This section presents an investigation into the impact of a reduction in CdS thickness upon the performance of CdTe/CdS devices.

8.2.1.1 Device fabrication

Devices were fabricated using FTO Tec8 substrates (2.5 x 2.5cm) bought from Pilkington. CdS films were deposited by CSS under 0.9Torr of nitrogen at source and substrate temperatures of 650°C and 520°C respectively. The growth time was controlled using a shutter and a series of four devices with CdS thickness in the range 150-400nm were produced (layer thicknesses were determined post growth by surface profilometer measurement). Prior to CdTe deposition the CdS films were annealed under 3Torr of hydrogen at a temperature of 400°C, for a period of 2mins, in the CdTe deposition chamber. CdTe films were then deposited by CSS under 2Torr of oxygen at source and substrate temperatures of 600°C and 460°C respectively. The deposition time was 2min for all cells, leading to a layer thickness of ~6μm. A 200nm $CdCl_2$ layer was then deposited on the CdTe back surface by vacuum evaporation before the structures were annealed in air at 400°C for 40min. The cells were then subjected to a 10s NP etch, before a series (~25) of 2mm diameter circular gold back contacts were applied by vacuum evaporation.

8.2.1.2 J-V and EQE analysis

For each device around 25 contacts were evaluated by *J-V* analysis. The average values for η, FF, J_{sc} and V_{oc} determined from *J-V* curves, are plotted as a function of the CdS thickness in fig.8.1.

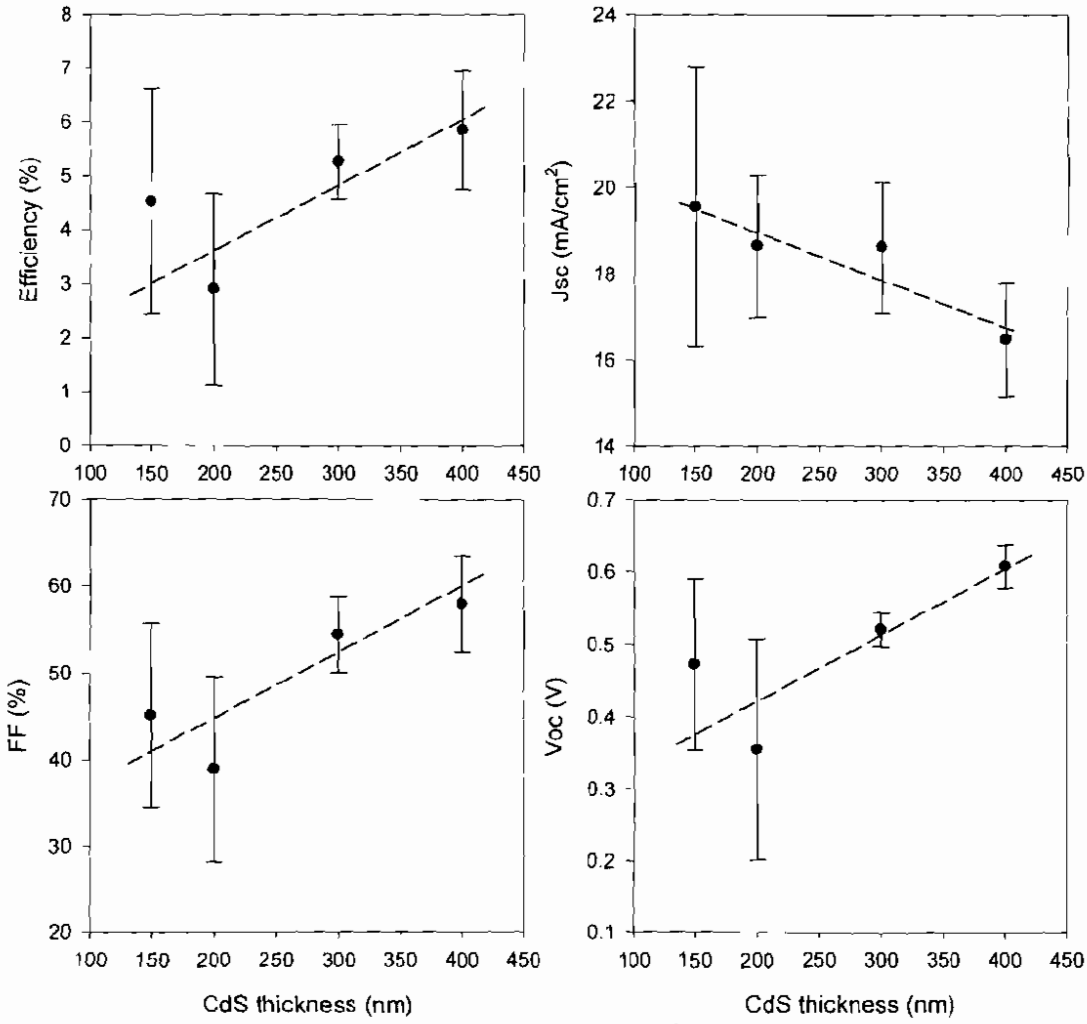

Figure 8.1: Device performance parameters determined from J-V measurements as a function of CdS thickness. Each point shows the average for ~25 dot contacts, with the error bars being +/- 1 S.D. The lines are added as a guide for the eye.

It may be seen from fig.8.1 that as expected the J_{sc} increases with a reduction in the CdS thickness, with an average value of 19.5mA/cm^2 at 150nm and 16.5mA/cm^2 at 400nm. Examination of the EQE curves in fig.8.2 shows there is extra collection by the junction in the 400-520nm range, due an increased fraction of the incident light in this range reaching the CdTe layer. However, despite the increase in average J_{sc} observed, the *variation* in J_{sc} values determined for individual contacts is greatly increased, as demonstrated by the large error bars for a thickness of 150nm. The overall performance of the device decreases with reduced CdS thickness with the average efficiency being reduced from 5.9% to 4.5%, this occurring due to reduction in V_{oc} (0.61V to 0.47V) and

FF (57.9% to 45.1%). This decrease in the V_{oc} and *FF* is most probably caused by the formation of pinholes resulting from the decrease in CdS thickness. This leads to the formation of a CdTe/FTO diode in regions of the device, lowering the V_{oc} and *FF*[1] as the CdTe/FTO junctions are inferior to the CdTe/CdS junctions[2].

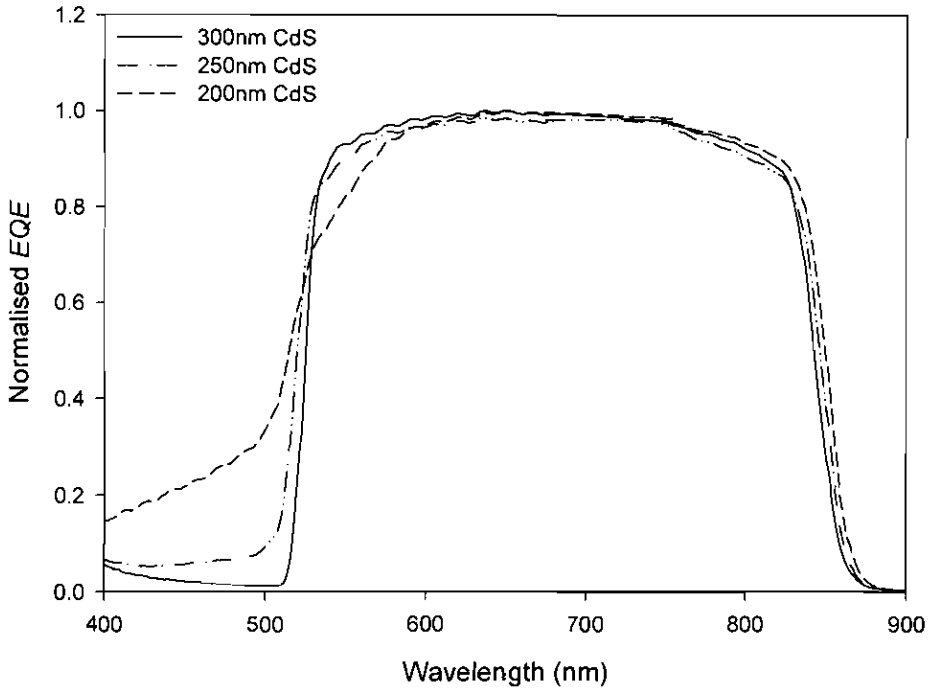

Figure 8.2: EQE measurement of devices fabricated with CdS having different thickness (200, 250 and 300nm). Plots have been normalised to allow direct comparison. The main qualitative difference is that for thinner CdS, the higher transmission of above-gap light contributes to the *EQE* (λ < 520nm). The periodic oscillations observed in the 520 – 600nm range may possibly result from optical interference fringes.

Fig.8.2 also shows a slight change in the shape of the EQE response as a function of CdS thickness for wavelengths above the CdS bandgap. In the short wavelength "shoulder" region (~520-600nm), the observed cutoff has a more gradual slope toward the CdS bandgap value for the thinner CdS based devices. This suggests a region of increased absorption has been formed near to the CdTe/CdS interface[3], which contributes a lower level of current generation. The CdTe bandgap cutoff (~840-870nm) is also shifted toward longer wavelength with reduced CdS thickness, implying a reduction of the CdTe bandgap. These findings are both consistent with the formation of the $CdS_{1-y}Te_y$ and CdS_xTe_{1-x} alloys[4], with there being an apparent increase in the level of intermixing

between CdS and CdTe layers with a reduction in the CdS thickness (the reader is referred to Chapter 6 for a more complete discussion on the effects of intermixing). Other work[5] has attributed this change in the level of intermixing to a change in grain size with film thickness, as smaller grains may enhance the formation of the alloyed layers.

8.2.1.3 Discussion

The overall decrease in device efficiency observed as a result of CdS thickness being reduced in the range 400-150nm was seen as an indication that CdS deposited in this manner was not ideally suited for device fabrication. Because of the high deposition temperatures used, CSS-grown CdS films typically have a large grain size in comparison to films deposited by lower temperature techniques such as CBD or sputtering[5,6]. Thickness reduction in large-grained films is more likely to lead to the formation of pinholes and thus lead to a decrease in the device performance. As a result CBD films of thickness <100nm have been reported without significant loss in device performance[7]. Indeed, thin, high quality CdS is seen as an advantage in the production of high efficiency CdTe/CdS devices. However, the CSS-grown devices reported here displayed significant performance loss as the thickness was reduced below 400nm. This is caused by the degradation of V_{oc} and FF, which more than offset the increase in J_{sc}. Sections 8.2.2 and 8.2.3 report attempts to improve the suitability of CdS layers for device fabrication by adapting the growth conditions.

8.2.2 CdS deposition without CSS shutter

This section reports a study on the influence of a shutter to control the nucleation of CdS layers. The impact of this on the photovoltaic performance of both CdTe/CdS cells grown with and without this shutter is evaluated and discussed.

8.2.2.1 Methodology

In order to improve the performance of devices and to allow thinner CdS layers to be used, without loss of efficiency, the CdS growth methodology was altered in an attempt to promote the formation of smaller grains and higher levels of substrate coverage. It has been reported that lower temperature deposition of CdS reduces the grain size and may

increase the coverage of the substrate by the film[5]. By considering the nucleation theory outlined in Chapter 4 this may be explained briefly as follows: A reduced substrate temperature (at the point of nucleation) will reduce the size of the critical nucleus (Section 4.4.1) and increase the lifetime of adatoms on the surface (Section 4.4.3), leading to a increased probability of stable nuclei forming. A greater number of nuclei will therefore form on average, resulting in a smaller grain size in the completed film. Due to the constraints of the CSS method (i.e. high source temperature, small source-substrate distance), the substrate temperature for CdS deposition is invariably high (>400°C), and grain size is typically large 300-400nm[6] in comparison to grains in, for example, solution-grown films. CdS films discussed in the previous section were deposited using a shutter positioned between the source and substrate, with the shutter being retracted once the source temperature (650°C) had been reached. This led to the CdS films being nucleated at a temperature of ~520°C, upon removal of the shutter. By neglecting to use the shutter it is possible to reduce the nucleation temperature to ~450°C and in theory reduce the grain size and increase the level of coverage.

In order to evaluate the impact of nucleating CdS films at a lower temperature two devices were fabricated with CdS layers deposited for a period of 2mins, with the time being measured from the point at which the source temperature reached 650°C. In one instance the shutter was not used and in the second device the shutter was removed once the source temperature had reached 650°C. It is therefore believed that the film grown without the shutter will have had a slightly longer effective growth time (increased by ~10-20s). However, both films were determined to be ~300nm thick by profilometer measurement. All other deposition and processing conditions used were the same as outlined in Section 8.2.1.1.

8.2.2.2 J-V and EQE analysis

J-V curves were recorded under AM1.5 illumination for all 25 contacts from each sample, with typical curves being shown in fig.8.3. The average values determined for η, FF, V_{oc} and FF from each device are given in table 8.1.

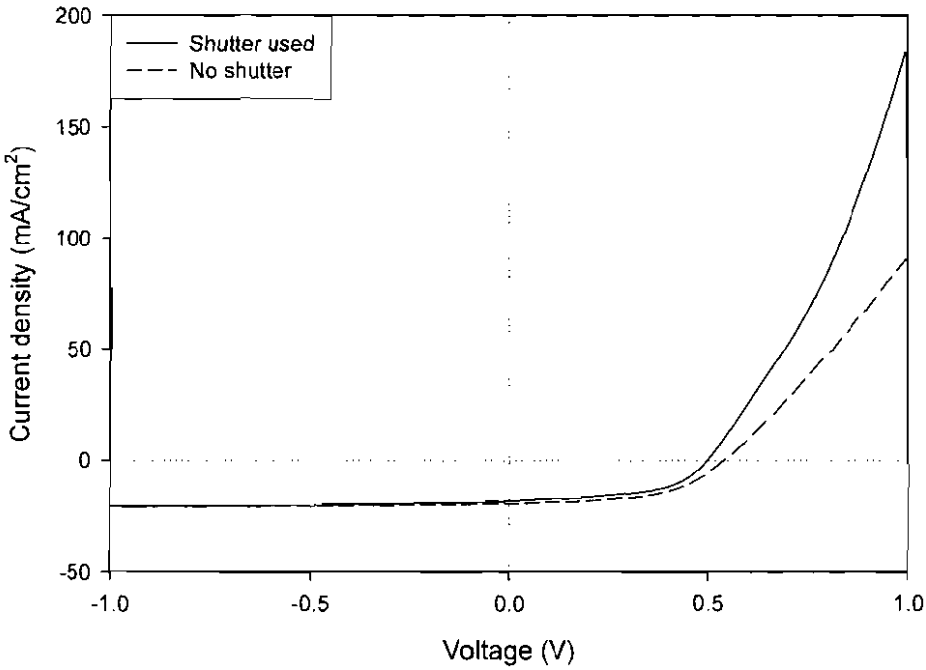

Figure 8.3: *J-V* curves recorded under AM1.5 illumination for devices with CdS layers deposited by CSS with and without use of a shutter.

It can be seen from the example *J-V* curves that whilst there is little difference between the curves in reverse bias, in forward bias the device with the CdS layer fabricated without the shutter displays improved performance. This is reflected in the average values determined for each device, whilst there is a small increase in the average J_{sc} (5.6% increase) for the device fabricated without the shutter, the increase in FF (8.3% increase) and in particular V_{oc} is greater (11.8% increase). As a result of this improvement the average device efficiency is seen to increase by 1.14%.

	η	FF	J_{sc}	V_{oc}
Shutter used	4.73%	50.82%	17.94mA/cm^2	0.51V
No shutter	5.87%	54.24%	18.95mA/cm^2	0.57V

Table 8.1: Average cell parameters extracted from *J-V* curves for cells fabricated using CdS layers deposited with and without a growth shutter. All other growth and processing parameters were identical.

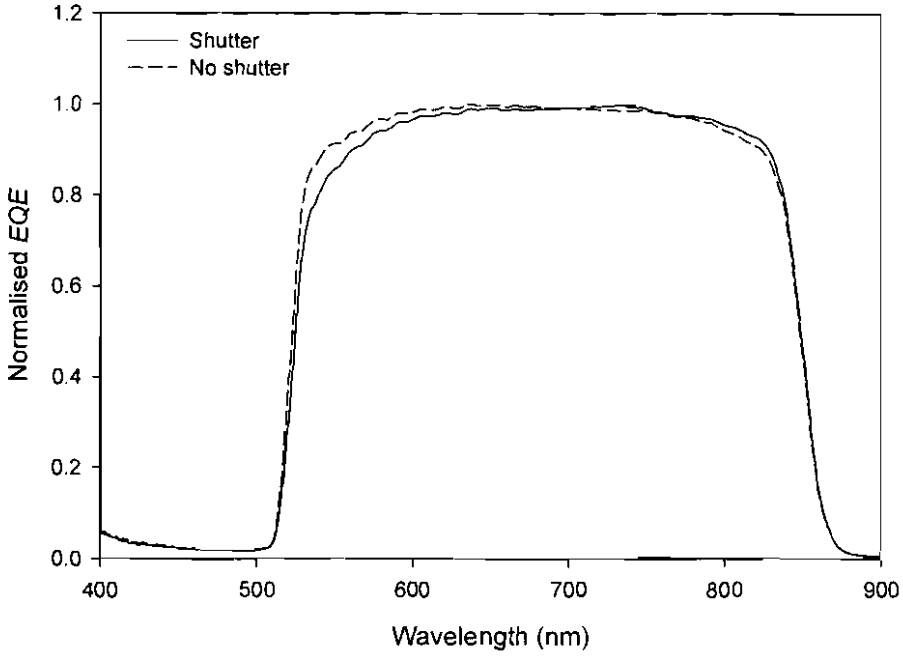

Figure 8.4: Normalised EQE curves for cells with CdS layers grown with and without a shutter to control growth. The periodic oscillations observed in the 520 – 600nm range may possibly result from optical interference fringes.

EQE curves of the two devices are shown in fig.8.4, with the curves having been normalised to allow direct comparison. The curves are qualitatively similar, with no evidence of current generation for wavelengths below the CdS bandgap in either case. There is a slight difference in the 520-600nm range, with the sample grown using a shutter displaying a slight decrease in *EQE*. This may imply that the sample grown with the shutter in place has a slightly higher level of intermixing. However, as there is no discernable shift in the long wavelength cutoff it is difficult to say with any degree of certainty and any change in intermixing is apparently small. The improvement in the device performance observed is therefore believed to result from an improvement in the quality of the CdS layer itself, rather than from an improvement in the transparency of the CdS or from any improvement in junction quality arising from intermixing.

8.2.2.3 Discussion

By lowering the temperature at which the CdS layer nucleates an improvement has been demonstrated in the cell efficiency, principally through gains in V_{oc} (and a small

increase in *FF*). This implies that reduce leakage of the junction diode resulted from the lower temperature (shutter-less) nucleation. While physical searches for pinholes have not been conducted in this work, it may be inferred that enhanced coverage has reduced the incidence of leakage paths (including shunts and direct CdTe/ITO contacts). It is expected that further reducing the CdS nucleation temperature would yield extra gains in the V_{oc} and would also allow the CdS thickness to be reduced, without loss of V_{oc}. However, due to the high source temperatures for the sublimation of CdS (>625°C), the lower limit of substrate temperature achievable is still relatively high. In order to achieve further improvements in V_{oc} it is therefore necessary to use alternative methods to increase substrate coverage and thereby reduce the CdS grain size.

8.2.3 CdS deposition using oxygen

In Chapter 7 the inclusion of oxygen in the CSS processing ambient was shown to improve coverage and reduce grain size in CdTe thin films (Section 7.2.3), this being explained by reference to a step flow model of crystal growth (Section 4.5.2). However, the impact of inclusion of oxygen during CSS growth is not limited to CdTe, with the same principles also being applicable to CdS deposition. A number of groups have cited the inclusion of oxygen in the CSS CdS deposition ambient to be advantageous for high device performance[5,8,9], owing to a significant reduction in the CdS grain size[9].

This section reports an investigation into the effect of including oxygen into the CSS CdS processing ambient upon device performance.

8.2.3.1 Methodology

A series of four samples were fabricated with CdS layers deposited under various pressures of oxygen (0, 0.5, 2 and 4Torr), with all films being deposited without the use of a shutter. All other deposition and processing conditions used were as outlined in Section 8.2.1.1.

It was shown in Section 7.3.3 that use of oxygen during CdTe deposition retarded the growth rate of films. This was also found to be an issue in the deposition of CdS films and it has also been noted by other authors that the inclusion of oxygen in the CdS processing ambient may retard the film growth rate[5]. As a result of this it was difficult to

fabricate comparable CdS layer thicknesses for different oxygen pressures and for the film deposited under the highest oxygen pressure (4Torr) the CdS layer was found to be significantly thinner (~200nm) than the other films (~400nm).

8.2.3.2 J-V and OBIC analysis

J-V curves were recorded for each of 25 back contacts from each sample under AM1.5 illumination. The device performance parameters extracted from these curves are plotted in fig.8.5 as a function of oxygen pressure.

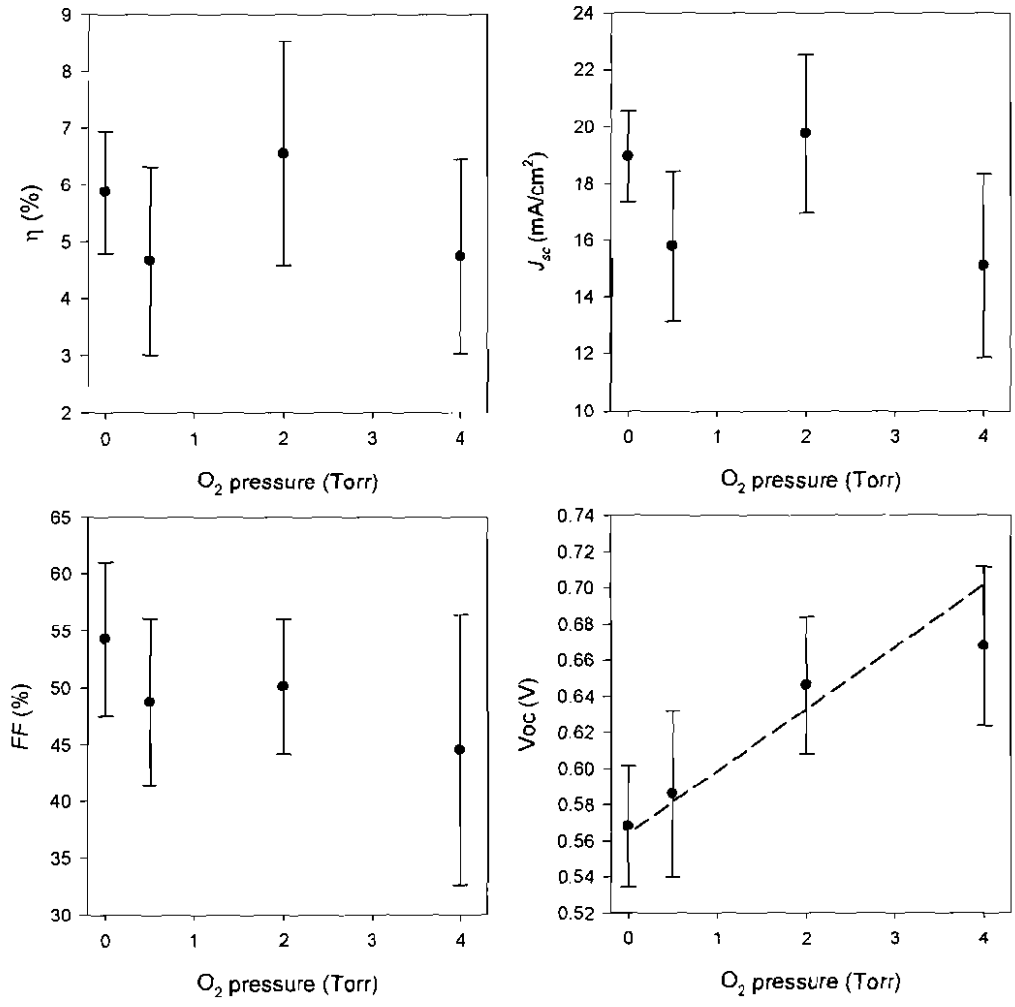

Figure 8.5: Device performance parameters determined from *J-V* measurements as a function of oxygen pressure used during CdS deposition. Each point shows the average for ~25 dot contacts, with the error bars being +/- 1 S.D. The line is added as a guide for the eye.

There was little evidence of a direct relationship between the oxygen pressure used during CdS deposition and the device efficiency. Whilst higher efficiencies were achieved for individual contacts from devices with CdS deposited under oxygen (peak efficiency achieved was increased from 7.35% at 0Torr to 9.84% at 2Torr), the average device efficiencies showed no discernable trend. However, a significant improvement in the V_{oc} was observed with increased oxygen pressure, with the average being 0.67V at 4Torr compared to 0.57V without oxygen (peak values increased from 0.64V without oxygen to 0.68V at 4Torr). This increase in V_{oc} did not however lead to an overall increase in efficiency, due to the decrease in the FF as a function of oxygen pressure.

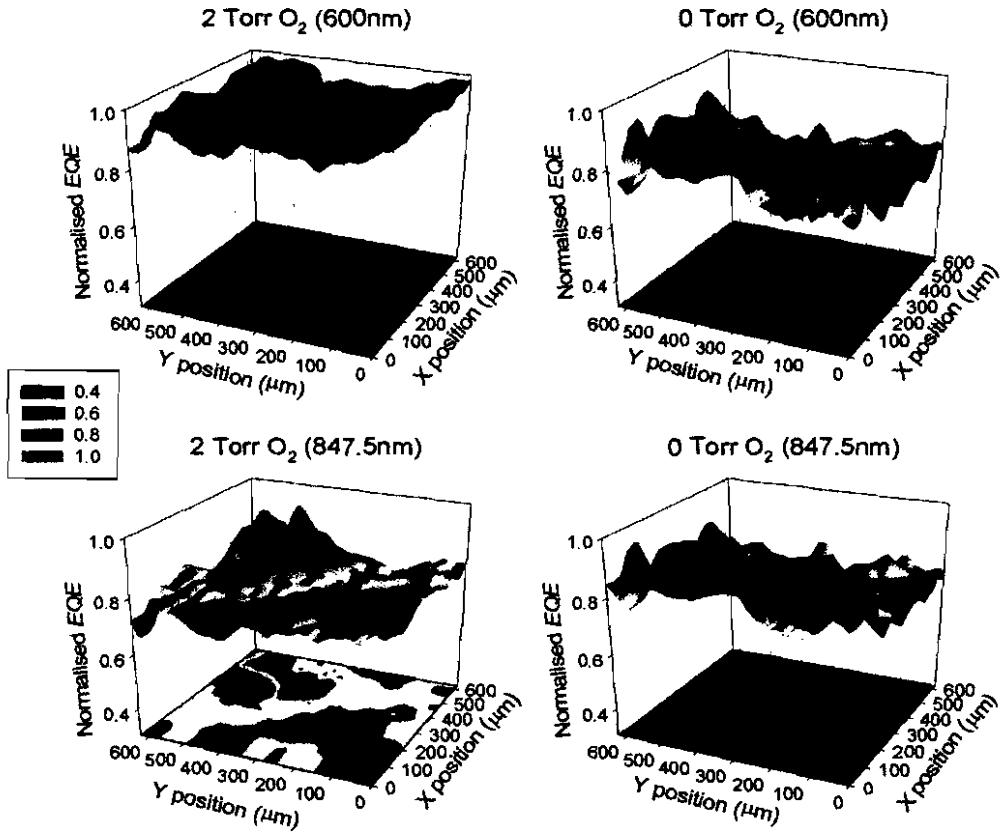

Figure 8.6: High resolution (12.5μm) OBIC maps (600nm and 847.5nm) of devices with CdS layers deposited in different pressures of oxygen (0 and 2Torr). *EQE* has been normalised (by scaling to give a maximum of 1.0) to allow direct comparison.

Fig.8.6 shows OBIC maps for the devices with CdS layers deposited with no oxygen present and under 2Torr of oxygen. Maps were recorded from contacts located in a central position of each device, that displayed an efficiency close to the average for that device. Measurements were made at a series of 6 wavelengths (425nm, 527.5nm, 600nm, 705nm, 825nm and 847.5nm), with the normalised maps for wavelengths of 600nm (2.07eV) and 847.5nm (2.91eV) being shown in fig.8.6. The spread of device response, (Max *EQE* – Min *EQE*)/Ave *EQE*, is plotted as a function of incident photon energy in fig.8.7.

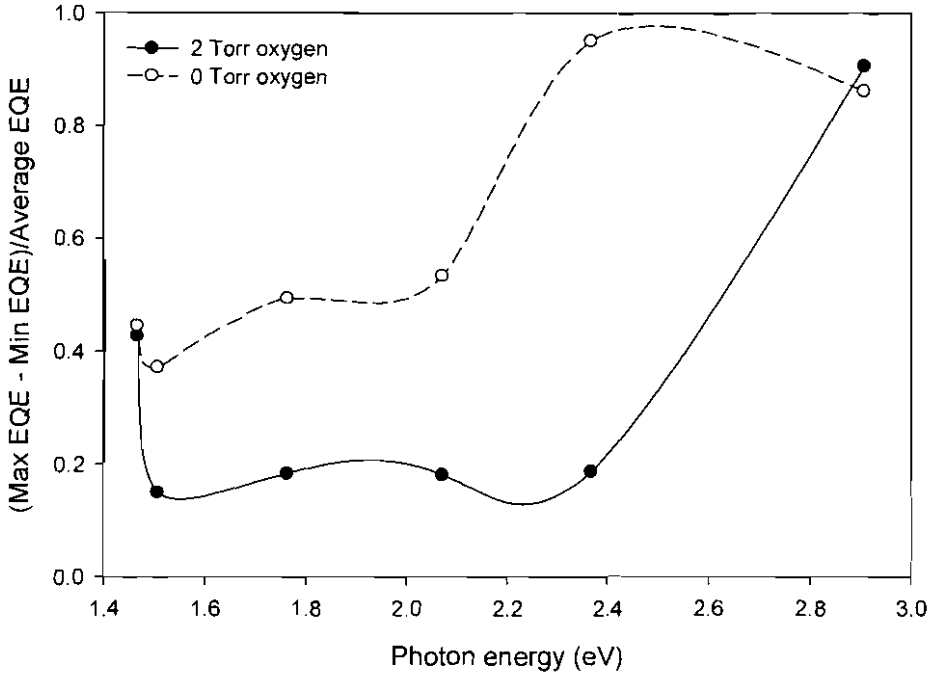

Figure 8.7: OBIC uniformity – The spread of *EQE* values i.e. (Max *EQE* – Min *EQE*)/Ave *EQE* , is plotted as a function of photon energy, for devices with CdS layers deposited under different oxygen pressures. The lines are added as a guide to the eye.

For the OBIC measurements taken at 600nm, the cell with the CdS layer grown in oxygen can be seen to perform at a much more consistent level. This is confirmed by the plot in fig.8.7, which shows the device with CdS deposited in oxygen has a more uniform PV response (i.e. lower value) for the majority of the energy range examined. However, the uniformity of the two devices coincides much more closely for photon energies close to the CdS and CdTe bandgaps. This can also be seen in fig.8.6 where the cell with CdS

fabricated in oxygen has shown a marked decrease in response spread at 847.5nm, whilst the other devices response has remained reasonably constant.

8.2.3.3 Discussion

The inclusion of oxygen in the CdS CSS deposition ambient has been shown to have a beneficial effect on device V_{oc}. Whilst little trend in the device efficiency was observed as a function of the oxygen pressure in the range 0-2Torr, the observed increase in V_{oc} may still be considered a more significant result. Numerous devices had been fabricated in this work, prior to those discussed here, that were based on CSS CdS layers deposited in the absence of oxygen. Many of these devices were found to display J_{sc} values equivalent to the peak observed here for oxygen deposited CdS layers (~20-25mA/cm^2), but they invariably had lower V_{oc} values. For devices based upon CdS grown without oxygen in the deposition ambient the open circuit voltage was never greater than 0.6V. For device with CdS deposited under 4Torr of oxygen this value was increased to a peak V_{oc} of 0.68V, a significant improvement. This improvement is attributed to a reduction in the pinhole density of the CdS films due to a reduced grain size, leading to a reduction in the formation of CdTe/FTO junction regions.

Despite deposition under 4Torr of oxygen generating the highest V_{oc}, if not the highest efficiency, CdS deposition under this pressure of oxygen was deemed unsuitable for cell fabrication. Substantial oxidation of the CdS source material was found to occur as a result of the CdS growth, rendering the source unusable for subsequent deposition runs. The oxygen was also found to slow the CdS deposition rate to such an extent, that it was not possible to deposit thick CdS layers before sublimation from the source was entirely stopped as a result of oxidation. Whilst some source oxidation problems did occur for lower oxygen pressures (0.5 and 2Torr), the effect was far less severe and these conditions were deemed as being suitable for CdS growth.

8.2.4 Summary of the study on the influence of CdS deposition on performance

The work presented in Section 8.2.1 demonstrated that CSS is not ideally suited for the deposition of good quality CdS films for CdTe/CdS devices. Owing to the high

deposition temperature films have a large grain size and the reduction of film thickness was found to lead to loss of device performance by shunting. Techniques were sought that may reduce the CdS grain size and improve device performance, using understanding gained from nucleation and early growth work on CdTe films (Chapter 7).By the use of a reduced nucleation temperature (Section 8.2.2) and including various pressures of oxygen during the deposition of CdS (Section 8.2.3), device efficiency was improved from an average of 4.73% to 6.54%. The principal cause of this increase was deemed to be due to an improvement in the V_{oc} of devices, from an average of 0.51V to 0.65V.

8.3 Influence of CdTe deposition ambient on device performance

Whilst numerous groups have looked at the impact of oxygen on CdTe/CdS device performance and microstructure[8,10-12], no work has been reported on the impact of hydrogen upon CdTe thin film formation. Results presented in Chapter 7 evaluated the impact of including oxygen or hydrogen into the CSS processing ambient, upon the microstructure of CdTe thin films at the early stages of growth. This section contains a further investigation of the impact of these gases upon the CdTe microstructure, but does so in terms of completed cell structures and also evaluates the associated effect on device performance.

8.3.1 Device fabrication

A series of three devices was fabricated using commercial FTO Tec8 substrates (5 x 5cm) bought from Pilkington. 300nm thick CdS films were deposited by CSS under 0.9Torr of nitrogen (as this work was performed prior to that presented in Section 8.2) at source and substrate temperatures of 650°C and 520°C respectively. Prior to CdTe deposition the CdS films were annealed under 3Torr of hydrogen at a temperature of 400°C for a period of 2mins, in the CdTe deposition chamber. The CdTe films were then deposited on the CdS layers by CSS under a 2Torr pressure of either nitrogen, oxygen or hydrogen, at source and substrate temperatures of 600°C and 460°C respectively. The deposition time was 2min, leading to a layer thickness of ~6μm for all devices. A 200nm $CdCl_2$ layer was then deposited on the CdTe back surface by vacuum evaporation before

the 5 x 5cm structures were broken into 2.5 x 2.5cm quarters. The device quarters were subjected to a 20min anneal in air but for a range of temperatures (390°C, 400°C, 410°C and 500°C) in order to ensure the treatment was optimized for each device. The cell quarters were then subjected to a 10s NP etch, before a series (~25) of 2mm diameter circular gold back contacts were applied by vacuum evaporation.

8.3.2 SEM/EDX analysis

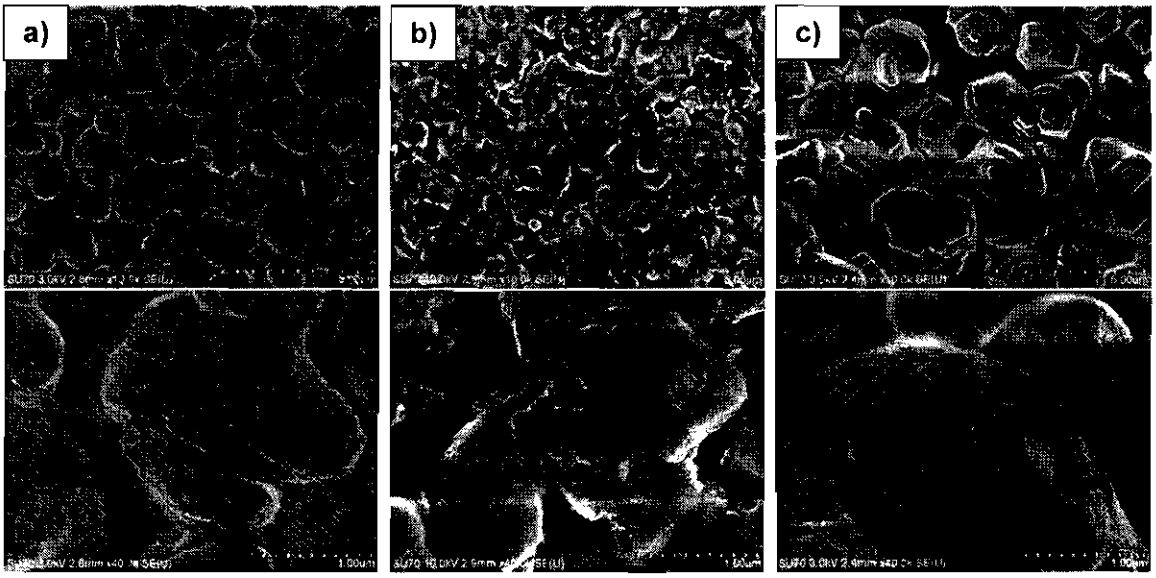

Figure 8.8: SEM images of CdTe layers deposited under three different gas ambients: a) 2Torr of nitrogen, b) 2Torr of oxygen and c) 2Torr of hydrogen.

Fig.8.8 shows SEM images of the CdTe back surface, with images being shown at two different magnifications for each of the three deposition ambients used. The images reveal a change in both the grain size and morphology of the films for the different ambients. The film grown in a nitrogen ambient (fig.8.8a) was expected to display large grains with distinct crystal facets, as observed in work on the early stages of growth (Section 7.3.2). However, although grains were still of a reasonable size (1.3 - 2.0μm diameter), they were seen to be rounded with no apparent faceting. This is believed to have been caused by residual traces of oxygen in the CdTe source material, as CdTe growth runs prior to the deposition of this sample had been carried out in oxygen. However, other devices with CdTe layers deposited under nitrogen where found to display a more typical morphology (large grains with well defined crystal facets), but

showed little difference in the level of device performance from the cell being discussed here (Section 8.3.3). The device results presented here for the nitrogen grown cell are therefore considered as typical for a device deposited in this manner.

The CdTe layer grown in an oxygen ambient (fig8.8b) shows a densely packed grain structure, with grains appearing slightly smaller (0.8 - 1.5μm diameter) than those deposited under a nitrogen ambient. The individual grains are difficult to discern and show no evidence of crystal faceting. An explanation for this change in morphology may be found in Section 7.2.5.

For CdTe growth under hydrogen (fig.8.8c) the layer morphology has altered significantly. The film displayed grains with crystal facets and the largest typical size (2.5 - 3.7μm diameter) observed for the three ambients examined. High resolution images reveal the grains to be constructed of stacked "plates" of material, all having the same apparent shape. Individual grains are isolated by deeply incised boundary regions, giving grains the appearance of an isolated stack, rather than being part of a dense film having a cohesive grain structure. This represents a marked change from the grain structure of the other two devices, and for that observed in other CdTe devices examined by SEM (e.g. ANTEC and CBD CdS based devices had CdTe films with large grain size and well defined crystal facets). It is clear from these results that the presence of hydrogen had altered the CdTe growth process. Results presented in Section 7.2.4 had also demonstrated that growth under hydrogen could potentially lead to the formation of non-CdTe phases on the surface. Although the substrate being used here did not contain indium, concerns were still raised that the observed deposit may not be CdTe, but rather some alternative compound. EDX analysis of all three samples was performed at a series of random locations, to identify the composition of the layers. All samples were found to be CdTe with no other elements being strongly detected. The deposit formed under hydrogen was therefore confirmed to be CdTe with an unusual morphology, rather than an alternative material resulting from a substrate reaction.

8.3.3 J-V analysis

J-V curves were recorded under AM1.5 illumination for all contacts from each of the 2.5 x 2.5cm device plates annealed at different temperatures (i.e. ~100 *J-V* measurements

for each deposition ambient). Typical *J-V* curves for samples annealed at 410°C are shown in fig.8.9, while extracted device parameters η, *FF*, V_{oc} and *FF* are plotted as a function of annealing time for each ambient in fig.8.10.

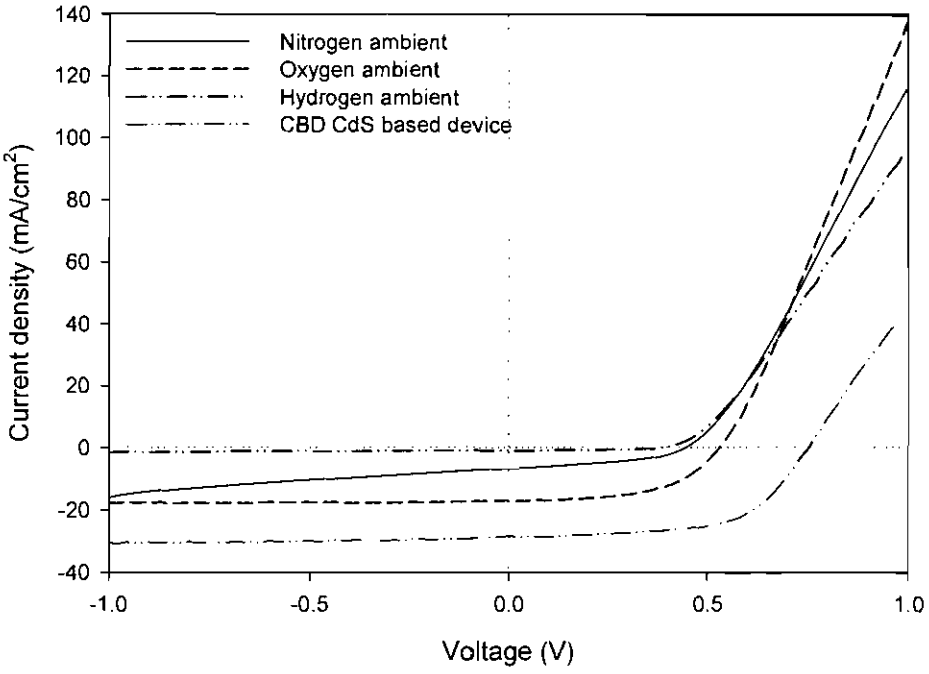

Figure 8.9: Typical *J-V* curves for cells with CdTe layers deposited under different gas ambients (2Torr of either nitrogen, oxygen or hydrogen) on CSS CdS. A comparative curve for a device based on CBD CdS is also included.

The results presented in fig.8.10 reveal the device with CdTe deposited under oxygen to have the highest performance for all annealing times. All devices show a large variation in performance as a function of annealing time, but with all devices displaying the peak performance for quarters treated at a temperature of 410°C. The subsequent discussion will therefore focus primarily on these devices quarters.

The oxygen grown cell displays an average efficiency of 4.78% (peak of 6.07%), while the nitrogen and hydrogen cells give only 1.13% (peak of 2.03%) and 0.22% (peak of 1.90%) respectively. This variation in efficiency seems to be primarily due to the change in J_{sc}, and it can be seen from the *J-V* curves in fig.8.9 that there is a large discrepancy in the current generated under reverse bias. The oxygen grown device displays reasonably high J_{sc} values (an average of 17.54mA/cm^2), while in the case of nitrogen growth this is significantly reduced (an average of 5.99mA/cm^2). In the case of

the cell with CdTe deposited under hydrogen, hardly any current is generated and the J_{sc} value is very low as a result (an average of 1.08mA/cm^2). A similar trend is seen for the V_{oc} values determined, with the oxygen grown cell having a higher value (an average of 0.54V) than the nitrogen (an average of 0.45V) or hydrogen grown (an average of 0.41V) cells. However, it should be noted that whilst very little current is generated, the hydrogen grown device does show a good *J-V* shape and as a result has a relatively high *FF* (an average of 49.54%). The *FF* is comparable to that determined for the oxygen grown cell (an average of 50.46%), and is far superior to that of the nitrogen grown cell (an average of 41.39%). The *FF* of the hydrogen grown cell is also superior to that of the other two devices at the other anneal times examined.

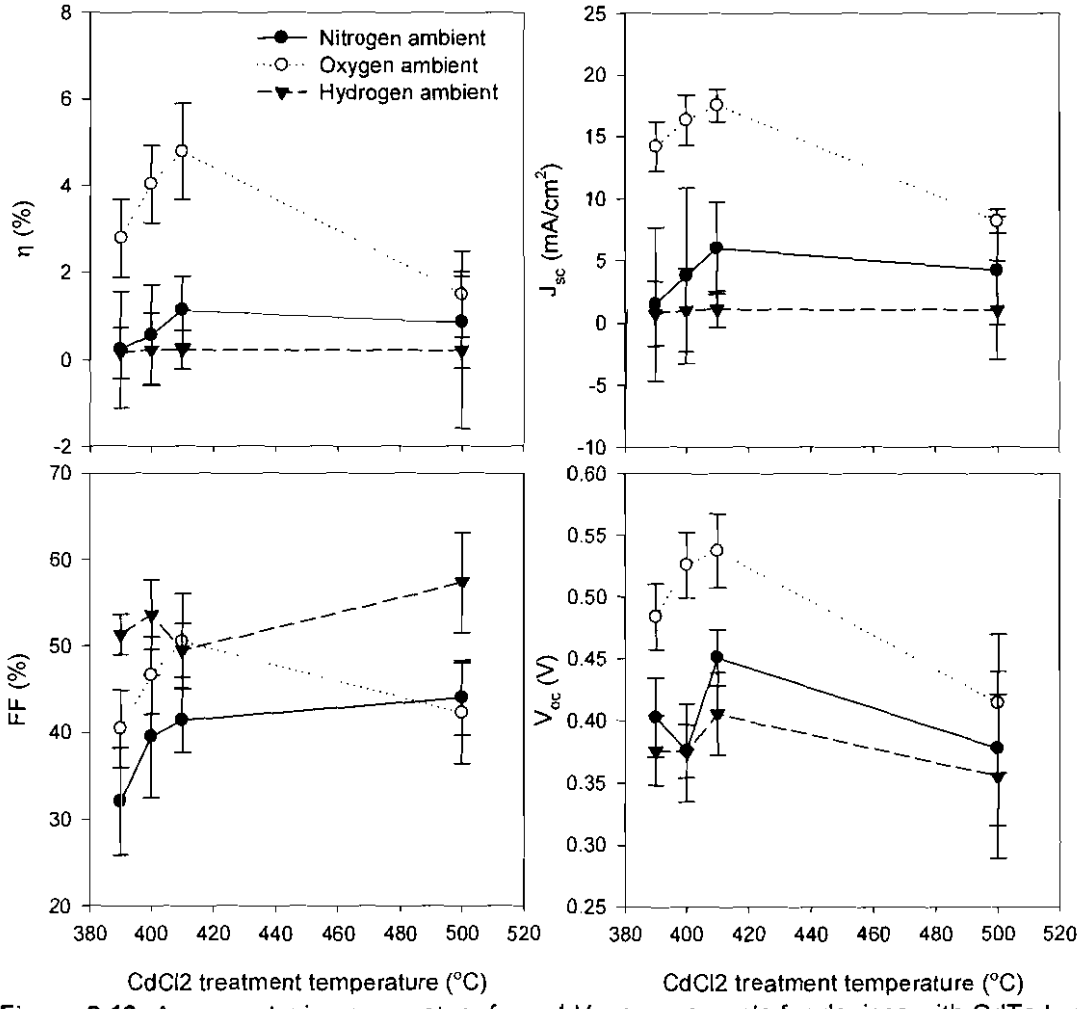

Figure 8.10: Average device parameters from *J-V* measurements for devices with CdTe layers deposited under different gas ambients (2Torr of either nitrogen, oxygen or hydrogen) as a

function of $CdCl_2$ treatment temperature. Each point represents an average of ~25 contacts with error bars being +/- 1 S.D.

8.3.4 EQE and cross section SEM/EBIC analysis

A typical contact from each device plate was selected for examination by EQE measurement, generating four curves (one from each annealing temperature) for each device. Fig.8.11 shows normalised EQE curves recorded for each of the device plates annealed at 410°C. Normalisation was performed by scaling each set of data with a coefficient such that the maximum *EQE* value was 1.0.

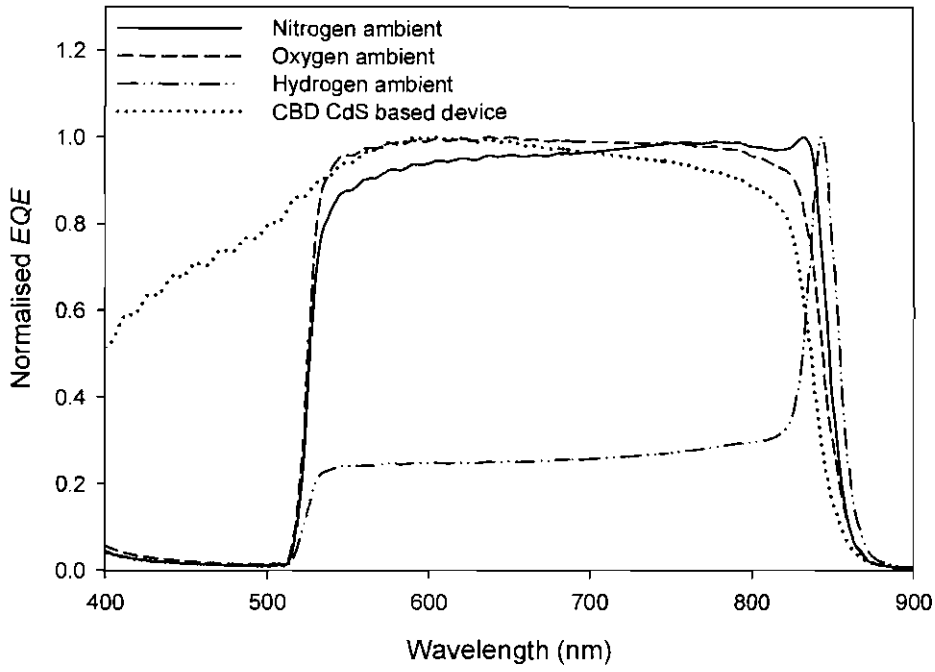

Figure 8.11: Normalised EQE curves for devices with CdTe layers deposited under different gas ambients (2Torr of either nitrogen, oxygen or hydrogen). A comparative curve for a device based on CBD CdS is also included. The periodic oscillations observed in the 520 – 600nm range may possibly result from optical interference fringes.

The EQE curves provide insight into the low performance of the devices with CdTe layers grown in hydrogen and nitrogen ambients. Both show the characteristic shape of a buried homo-junction (the peak response being close to the CdTe bandgap), with the shape being far more pronounced in the case of the hydrogen deposited cell, indication that the junction is further from the CdTe/CdS interface. By contrast the cell with CdTe

deposited under oxygen displays a typical hetero-junction response, showing a reasonably uniform level of response in the 520-840nm wavelength range.

In order to further probe the position of the p-n junctions in these devices, a series of cross sectional EBIC measurements (Section 5.4.3) were performed using a SEM. A representative contact was selected from the devices with CdTe deposited under hydrogen and under oxygen. The cells were then mounted and contacted in the cross-sectional geometry, as described in Section 5.4.3, with the electron beam being incident on the CdTe/CdS interface. For comparison, a high efficiency device (η = 11.3%), with the CdTe deposited under oxygen and the CdS layer deposited by CBD, was also examined. Fig.8.12 shows the cross sectional secondary electron images of the CdTe/CdS structures which have been overlaid with the EBIC current signal (coloured). The location of the EBIC current signal indicates the p-n junction position of the device.

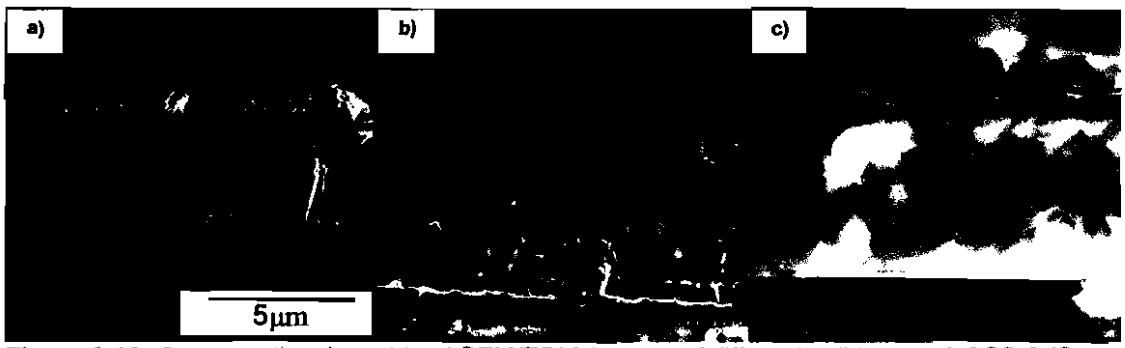

Figure 8.12: Cross sectional combined SEM/EBIC images of different cell types: a) CSS CdS with CSS CdTe deposited in an oxygen ambient, b) CSS CdS with CSS CdTe deposited in a hydrogen ambient and c) CBD CdS with CdTe deposited in a oxygen ambient. All images have been rotated so that the CdS layer is located at the bottom of the image and the CdTe layer is located towards the top. The coloured region on each image represents a region of high collection of excited carriers, indicating the junction position (see Section 5.4.3).

Fig.8.12a shows that despite the good EQE curve shape observed the junction position of the device with the CdTe layer deposited under oxygen is not ideally situated, with the junction being towards the CdTe back surface. The junction appears to be some distance (~1-2μm) from the CdS layer, implying it is in fact a CdTe homo-junction rather than a CdTe/CdS hetero-junction as expected from EQE analysis. However, due to the reasonable efficiency of this device, it seems likely that it may contain a hetero-junction which is simply not visible here (possibly due to the relative weakness of the hetero-

junction in comparison to the homo-junction, making EBIC imaging of the weaker junction difficult). For the cell with the hydrogen deposited CdTe layer (fig.8.12b), the junction is seen to be deeply buried and located towards the CdTe back surface. Unlike the previous device, where the junction was located towards the centre of the CdTe layer, the junction in this device is fixed at the back surface. The strength of the observed EBIC signal was also considerably weaker than for the oxygen grown device, with a much greater signal amplification required in order to image the generated EBIC current. For the CBD CdS based device (fig.8.12c) the detected EBIC signal is very strong and is seen to be located directly at the CdTe/CdS interface, indicating the presence of a strong hetero-junction. Comparison between this device and the two CSS CdS based devices reveals a marked change in the junction positioning for the different deposition conditions. Whilst the oxygen grown device did show reasonable levels of device efficiency, and the inclusion of oxygen into the CdTe deposition ambient improved the junction position slightly (in comparison to other deposition ambients), the junction is clearly far from being optimized.

8.3.5 OBIC analysis

OBIC measurements were made to determine the uniformity of PV response for the devices deposited under the three different ambients. For each device a representative contact was selected from the 2.5 x 2.5cm device plates which had undergone annealing at a temperature of 410°C. OBIC measurements were performed at a series of 6 wavelengths (427.5nm, 525nm, 600nm, 705nm, 825nm and 847.5nm) over a 0.6 x 0.6μm area and at a resolution of 12.5μm. Maps of the device response for two of the wavelengths (600nm and 847.5nm) are shown in fig.8.13, while the device *EQE* variation ((max *EQE* – min *EQE*)/average *EQE*) is plotted as a function of wavelength for each device in fig.8.14. The maps have been normalised to allow direct comparison between devices at each illumination wavelength. Normalisation was performed by scaling each set of data with a coefficient such that the maximum *EQE* value was 1.0.

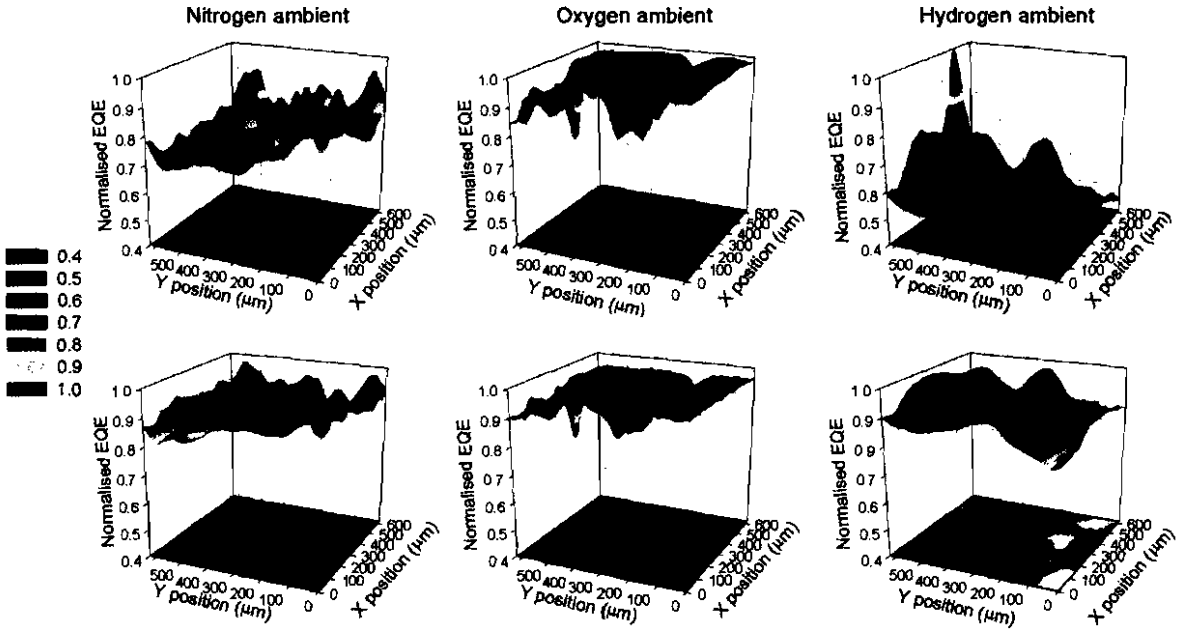

Figure 8.13: Normalised OBIC maps of cells with CdTe layers deposited under 2Torr of either nitrogen, oxygen or hydrogen. Maps were determined using two different wavelengths 600nm (top) and 847.5nm (bottom) and at a resolution of 12.5μm.

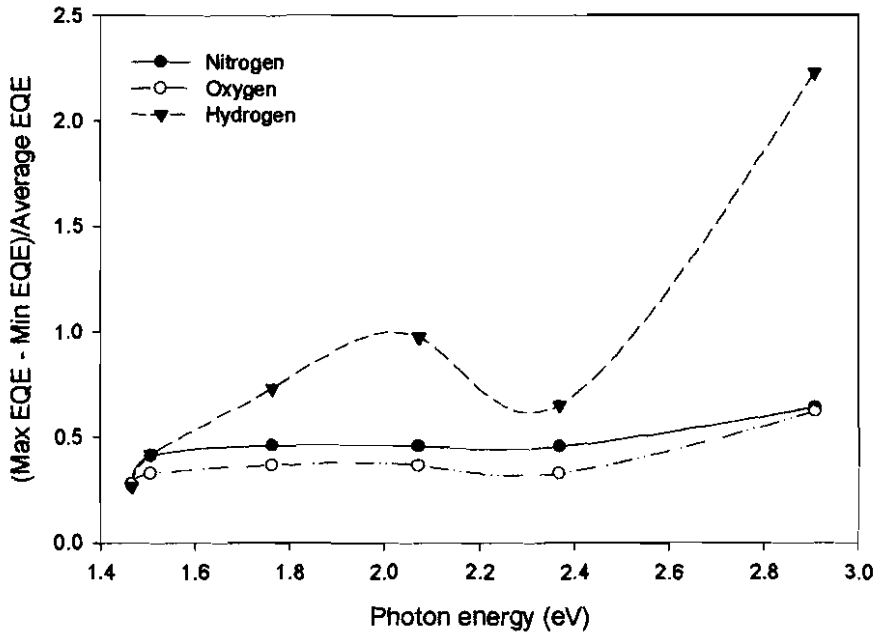

Figure 8.14: *EQE* variation as a function of incident photon energy as determined by OBIC for devices with CdTe layers deposited under 2Torr of either nitrogen, oxygen or hydrogen.

It can be seen in fig.8.13 that the device with CdTe deposited under oxygen shows the most homogenous response at a 600nm incident wavelength. The majority of the area examined performs close to the peak level of response detected, with there being only a few small areas performing poorly. Very little change is observed in this distribution for a longer incident wavelength (847.5nm), with the poorly performing regions noticeable at 600nm still being apparent. As a result the device uniformity remains reasonably constant as a function of wavelength (fig.8.14), with the oxygen grown device showing the lowest variation response of the three devices considered. The 600nm OBIC maps of the devices with CdTe layers deposited under nitrogen or hydrogen, show regions that perform better than the majority of the examined area. This implies that only small regions of the device are performing optimally, whilst the majority of the device performs at a substandard level. The device grown under nitrogen displays a number of these regions that perform at ~10-20% above the bulk of the response. For the hydrogen grown device there is a single response peak that performs at ~30-40% above the bulk of response. As a result the variation in response is high in both cases, with the hydrogen grown device showing the highest degree of variation over the majority of the wavelength range. These regions of high performance are less pronounced in the map recorded at 847.5nm than that recorded at 600nm, in which the device uniformity is significantly better. This change demonstrates there is wavelength dependence of the *EQE* and as a result implies these defects are not simply as a result of optical defects, as this would introduce a constant attenuation over all wavelengths. Instead these peak positions must relate in someway to the cell structure, presumably related to a localised variation in the CdTe badgap (Section 6.2.2). To further probe the nature of these positions, localized EQE measurements were made at these points and compared to EQE measurements from positions representing the bulk of the response. Two examples of normalised EQE plots are shown in fig.8.15. These curves were recorded from the cell with a CdTe layer deposited under nitrogen, from the region shown in fig.8.13.

Localised EQE measurement revealed that the better performing regions of the hydrogen and nitrogen grown devices have junctions that, whilst still being homo-junctions, were less deeply buried than other positions. This can be seen in fig.8.15, where the better performing position examined shows an improved response in the 520-

840nm range. The curves come into coincidence toward the peak of response, demonstrating why the peak positions appear less pronounced at longer wavelengths in the OBIC maps. Similar behaviour was observed for the device deposited under hydrogen, whereby the better performing positions appeared to correspond to those points that had junctions located closer to the device front surface.

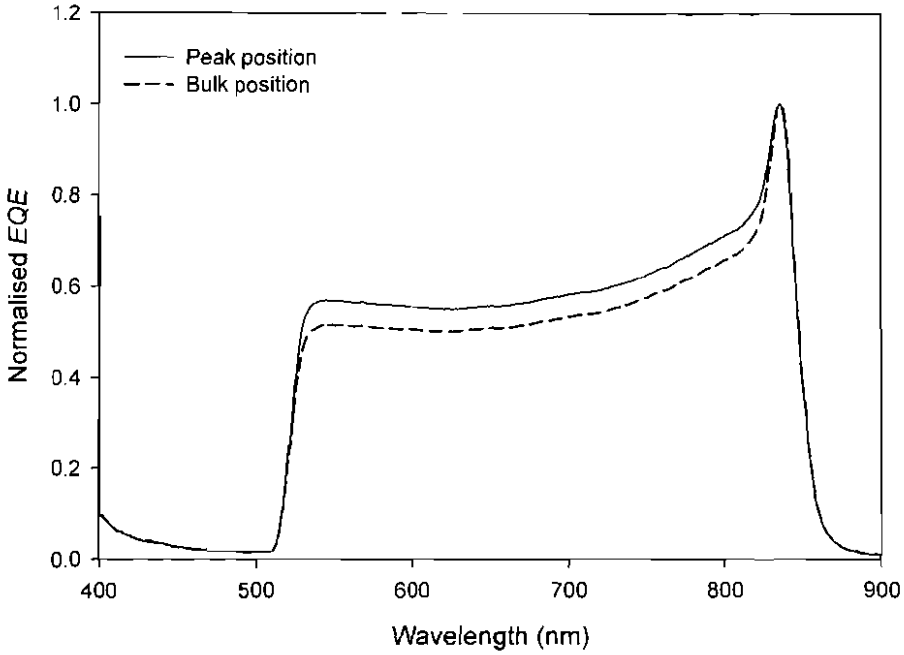

Figure 8.15: Localised EQE curves for a cell with CdTe layer grown under nitrogen. The curves are taken from areas identified as peak and bulk response positions by OBIC measurements shown in fig.8.13.

8.3.6 Discussion

It appears from the results presented in this section that inclusion of oxygen in the CdTe deposition ambient increases the device efficiency by reducing the tendency for the formation of buried homo-junctions, as indicated by EQE results. Use of EBIC to determine the junction position supported this finding, but it is recognized the devices reported here have at least partly homo-junction character, rather than being fully optimised hetero-structures. It appears that inclusion of oxygen simply serves to move the homo-junction closer towards the front surface, thus making it indistinguishable from a hetero-junction under EQE measurement. Without oxygen a buried homo-junction is always formed, with the junction being most deeply buried for devices grown under a

reducing ambient. There is an important distinction to be made between the homo-junctions observed here and those discussed previously in Chapter 6, where CSS CdS was deposited on ITO. In that instance it was found that buried homo-junctions were formed regardless of the CdTe deposition conditions, with oxygen being found to have no effect. For such devices the homo-junction formation was considered to result from indium diffusion from the ITO layer, which produced *n*-type doping of the CdTe layer[13]. However, as no indium was present in the FTO substrate employed throughout this chapter, the homo-junction formation must result from other factors. It seems clear that the strongest driver for buried homo-junction formation is the lack of oxygen present during the device fabrication, either in the CdS or CdTe layers. Similar results were found by Tyan *et al*[14] who reported the formation of buried homo-junction devices when CdTe layers were deposited in the absence of oxygen. They concluded that oxygen enhanced the *p*-type doping of the CdTe layer, leading to the formation of a correctly working junction, an assertion supported by wavelength modulation reflectance spectroscopy analysis of CSS CdTe films reported by Hsu *et al*[15]. However, these results have been contradicted by Rose *et al*[12] who reported that there is no direct observable link between the inclusion of oxygen in the processing ambient and the formation of homo-junction devices. They found that whilst homo-junctions were occasionally formed, high efficiency devices (>13%) were able to be fabricated without oxygen. However, the devices fabricated by Rose *et al* were based upon CBD CdS (which contains oxygen), rather than on CSS CdS as being reported here and by Tyan *et al*. Results presented within this thesis (Section 6.4) have also demonstrated that for deposition on CBD CdS, oxygen is not required during CdTe growth in order that high efficiency devices may be produced. The requirement for oxygen to be included during CdTe deposition therefore seems to be limited to devices based upon CSS deposited CdS. This may be due to the high oxygen concentration of CBD deposited CdS films, negating the need for oxygen to be intentionally included during CdTe deposition to affect the *p*-type doping of the CdTe layer. It may therefore be possible to omit or exclude oxygen from the CdTe deposition ambient if the CdS layer were to be made oxygen rich. This would therefore allow the formation of a hetero-junction without the reduction in CdTe grain size that accompanies growth with oxygen.

Whilst inclusion of hydrogen in the deposition ambient achieves an improved grain size, it has been shown to have a catastrophic effect on the device performance. Devices fabricated in hydrogen display deeply buried homo-junctions, suggesting the reducing nature of the ambient removes any residual oxygen species that may have been present during deposition. It is interesting to note that whilst the cells deposited under hydrogen display low efficiency, the *J-V* curves maintain a good shape. This may be indication that whilst the junction is positioned towards the back surface of the device, the quality of the junction is still high. However, results presented here show that CdTe deposition under hydrogen is not a suitable technique for the fabrication of high efficiency devices.

8.4 Influence of nitrogen pressure on CdTe growth and device performance

It was demonstrated in Section 7.4.6 that increasing the pressure of nitrogen used during CSS CdTe deposition may produce films with a significantly larger grain size at the early stages of growth. The section describes an investigation into the effect of nitrogen pressure on the CdTe grain structure in completed CdTe/CdS devices, along with its effect on the device performance.

8.4.1 Cell fabrication conditions

A series of four devices, with CdTe layers deposited under different pressures of nitrogen, were fabricated using commercial FTO Tec8 substrates (2.5 x 2.5cm) bought from Pilkington. 150nm thick CdS films were deposited by CSS under 2Torr of oxygen at source and substrate temperatures of 650°C and 520°C respectively. Prior to CdTe deposition the CdS films were annealed under 3Torr of hydrogen, at a temperature of 400°C, for a period of 2mins in the CdTe deposition chamber. CdTe films were then deposited by CSS under various pressure of nitrogen (2, 50, 100 and 200Torr), at source and substrate temperatures of 600°C and 460°C respectively, with a layer thickness of ~8μm for all devices. Due to the sublimation rate being reduced with increased pressure the CdTe deposition time had to be varied in order to generate equal layer thickness for each pressure, with deposition time being 2min for 2Torr and 90min for 200Torr. After CdTe deposition, a 200nm $CdCl_2$ layer was deposited on the CdTe back surface before

cells were subjected to annealing in air at a temperature of 400°C, with the treatment time being optimized for each device (in the range 5-20min). The cells were then subjected to a 10s NP etch, before a series (~25) of 2mm diameter circular gold back contacts were applied by vacuum evaporation.

8.4.2 SEM and AFM analysis of grain morphology

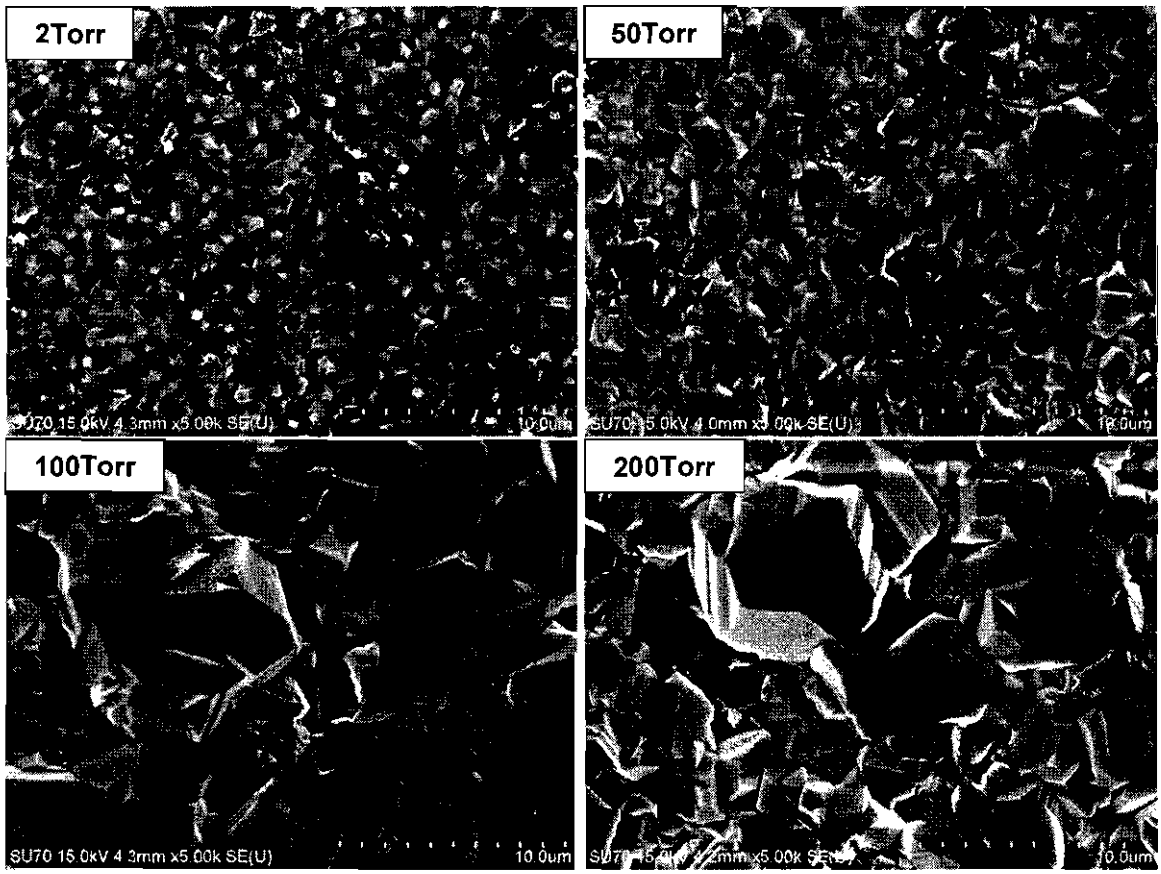

Figure 8.16: SEM images of CdTe layers deposited under different pressures of nitrogen.

Fig.8.16 shows SEM images of the CdTe films deposited under pressures of nitrogen in the range 2-200Torr. Grain diameter values were determined by manual measurement from SEM images, with the average grain diameter (being determined from the measurement of 100 individual grains) plotted against deposition pressure in fig.8.17, whilst histograms of grain size for the various pressures are shown in fig.8.18.

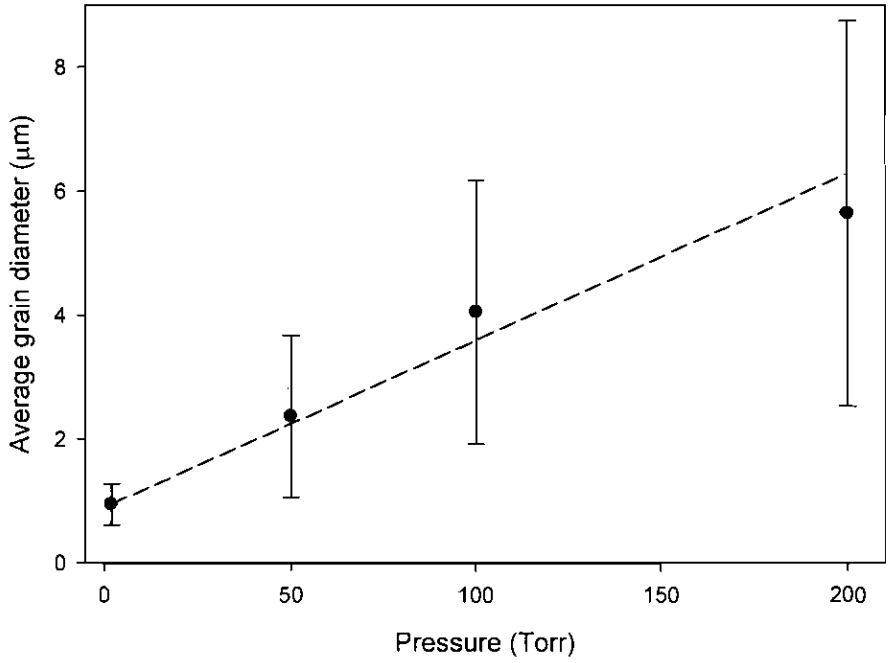

Figure 8.17: Average grain diameter for CdTe layers deposited under different nitrogen pressures. The linear fit $D = mP + c$ is subject to considerable uncertainty. The best fit and the associated error in the gradient and intercept values were determined using the χ^2+1 method. The determined values were m = 0.027 +/- 0.011 and c = 0.90 +/- 0.31.

It can be clearly seen from the SEM images in fig.8.16 that the change in deposition pressure has had a dramatic effect on the grain structure of the deposited CdTe films. The grain size is noticeably larger in the films deposited under higher pressure, as shown in the graph of average grain size (fig.8.17) and the histogram distributions (fig.8.18). For the lowest deposition pressure used (2Torr) the average grain diameter was relatively small, 0.94μm, whilst the maximum diameter observed was only 2.01μm. As the pressure was increased the typical grain diameter became larger (following the straight line equation; grain diameter = [0.027 P +0.9]μm, where P is the pressure), reaching an average of 5.63μm and a peak of 17.60μm for a pressure of 200Torr. As can be seen from the histograms in fig.8.18 the range of grain sizes observed at high pressure was also increased with there still being a number of smaller grains (~1-2μm). All films displayed well defined crystal facets, regardless of the deposition pressure.

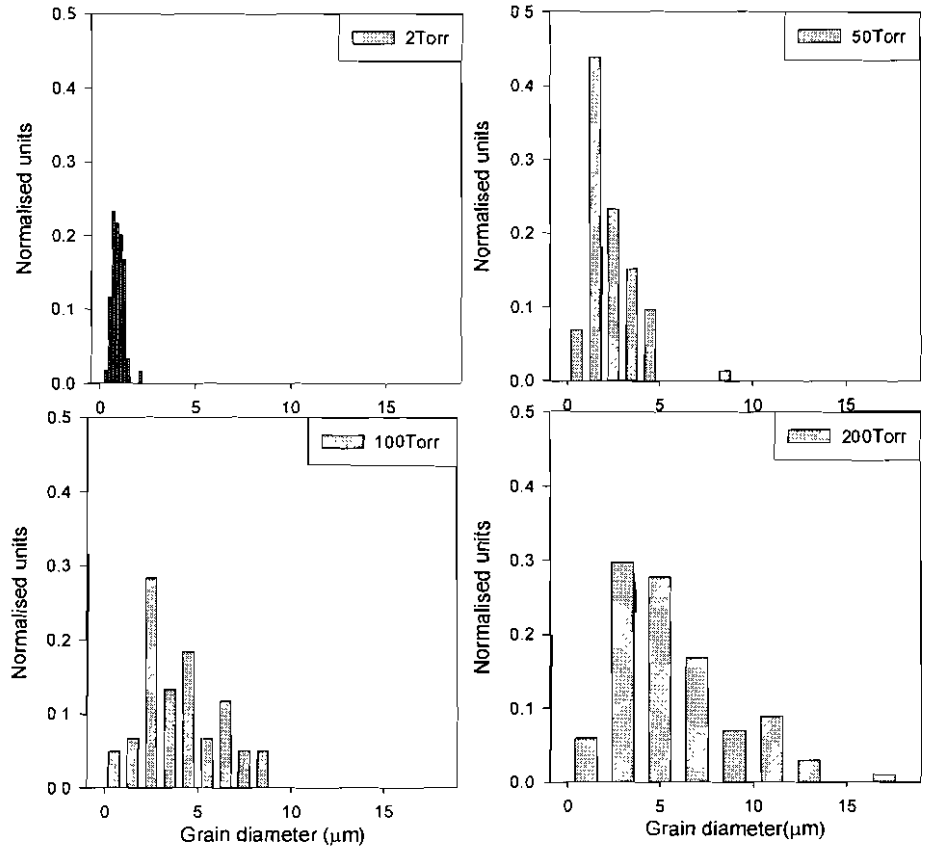

Figure 8.18: Grain diameter histograms (100 grains) for CdTe layers deposited under different nitrogen pressures. Average values are 0.94μm for 2Torr, 2.36μm for 50Torr, 4.04μm for 100Torr and 5.63μm for 200Torr.

In addition to the SEM investigation (and extraction of grain size information) above, an AFM investigation of the same samples was undertaken, the results being shown in fig.8.19. All images have the same *Z*-axis scale, so as to allow direct comparison of the change in the layer microstructure. These images confirm the findings of the SEM measurements, emphasising the increased grain size for higher deposition pressures. The roughness and height range of the samples has also visibly increased, with the film deposited at 2Torr appearing relatively flat in comparison to the large peaks and troughs displayed in the other films. Roughness and height range values determined from these measurements reveal that the average roughness increases from 236.1nm (2Torr) to

965.1nm (200Torr), with the maximum height range of the films increases from 2.58μm (2Torr) to 7.07μm (200Torr).

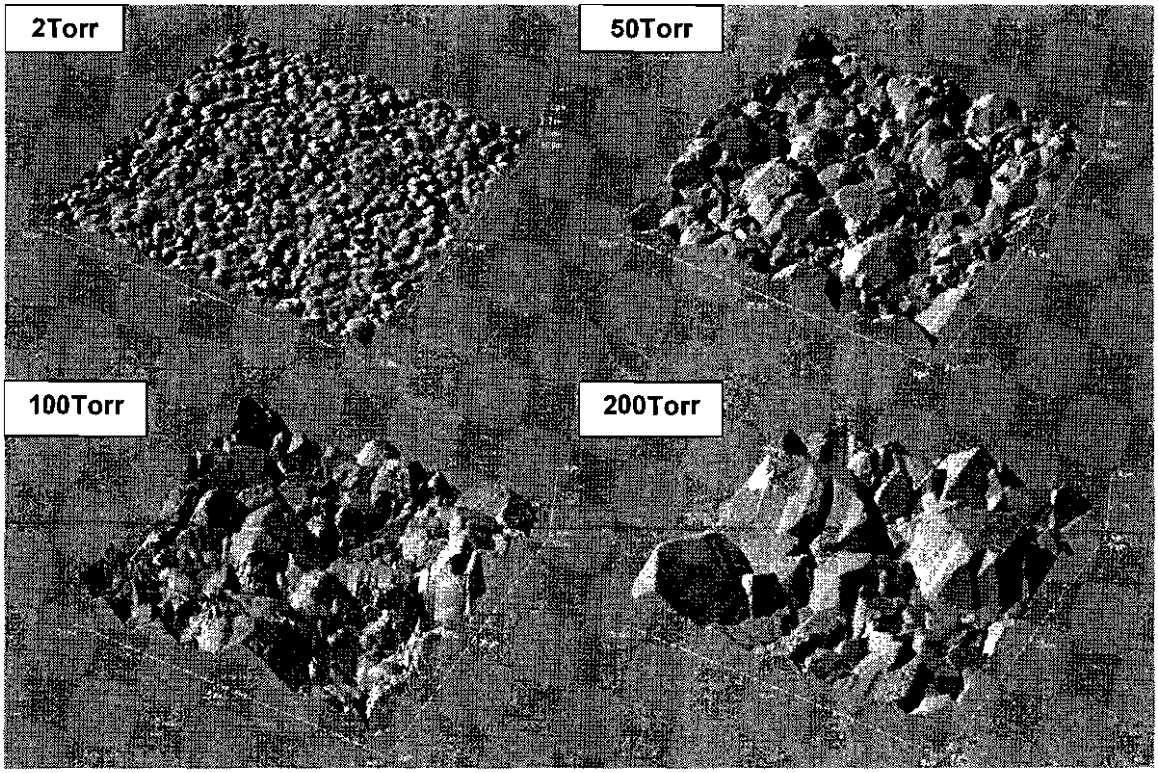

Figure 8.19: AFM images of CdTe layers deposited under different pressures of nitrogen. In all images the field of view is 50 x 50μm and the Z axis scales are equivalent (6μm full scale).

8.4.3 XRD and EDX analysis

Fig.8.20 shows the XRD patterns determined for CdTe layers deposited under various nitrogen pressures (2 - 200Torr), whilst table 8.2 summarises the texture coefficient and preferred orientation values (details of the calculations of these values can be found in Section 5.3.1) for each sample.

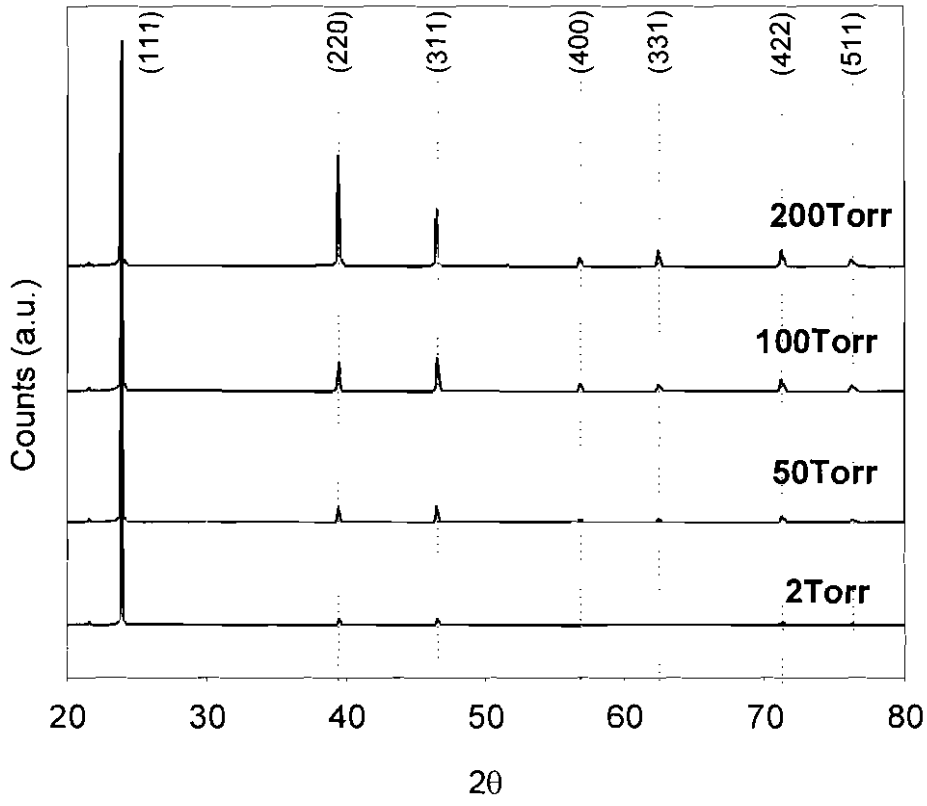

Figure 8.20: XRD spectra of CdTe/CdS devices with CdTe layers deposited under different nitrogen pressures.

Nitrogen pressure (Torr)	C_{111}	C_{220}	C_{311}	C_{400}	C_{331}	C_{422}	C_{511}	σ
2	4.58	0.22	0.40	0.00	0.00	0.58	1.21	***0.78***
50	2.95	0.31	0.72	0.77	0.45	0.76	1.03	***0.61***
100	2.01	0.38	0.91	1.02	0.50	1.02	1.16	***0.42***
200	1.26	1.05	1.18	0.83	0.89	0.92	0.86	***0.24***

Table 8.2: Values of texture coefficients, C_{hkl}, and degree of preferred orientation, σ, for CdTe layers deposited under various pressure of nitrogen (2 - 200Torr).

It can be seen that the sample deposited at the lowest pressure (2Torr) displays the strongest preferred orientation, with the [111] orientation being prevalent. For samples deposited under higher pressure the level of preferred [111] orientation is decreased (with

C_{220} and C_{311} coefficients increasing with pressure) whilst [400] and [311] orientations emerge. For the highest deposition pressure utilised (200Torr) the [111] orientation is only slightly favoured ahead of the other observed orientations, resulting in a decreased range of C_{hkl} coefficient values (see table for standard deviations) and a reduction in texture coefficient value (σ). The cells with CdTe layers deposited at higher pressure, therefore display a more randomised structure than those with CdTe layers deposited at a lower pressure.

EDX analysis of the samples revealed no change in the Cd:Te ratio as a function of deposition pressure, with the ratio remaining at ~1:1 for all cells.

8.4.4 J-V and EQE analysis

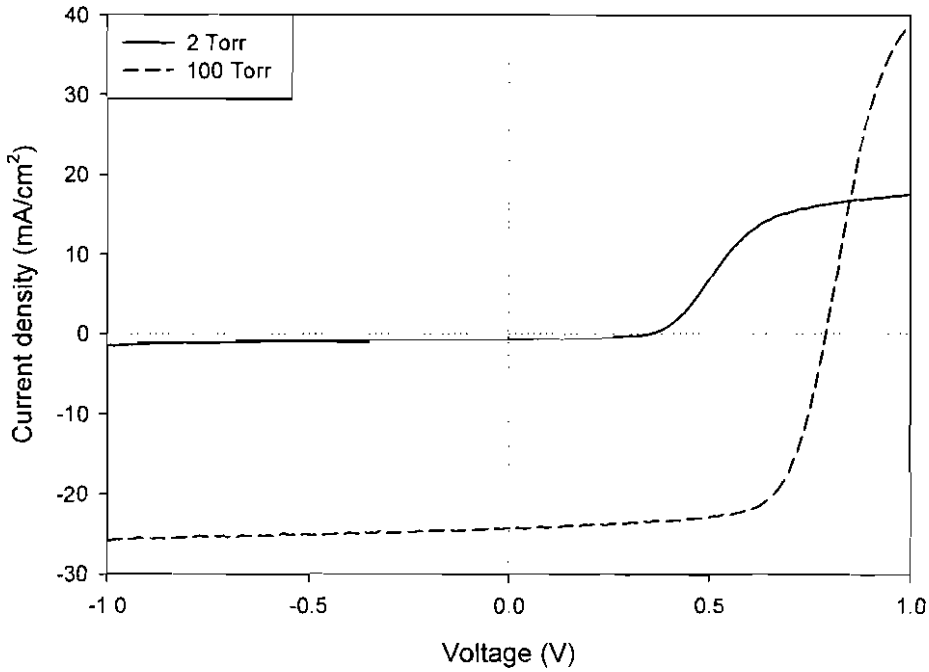

Figure 8.21: *J-V* curves recorded under AM1.5 illumination for cells with CdTe layers deposited under 2Torr and 100Torr of nitrogen.

J-V curves were recorded under AM1.5 illumination for all back contacts from each device (i.e. ~25 *J-V* measurements for each deposition pressure used). Typical *J-V* curves for samples with CdTe layers deposited under 2 and 200Torr nitrogen pressures are

shown in fig.8.21, while extracted device parameters η, FF, V_{oc} and FF are plotted for all contacts as a function of pressure in fig.8.22.

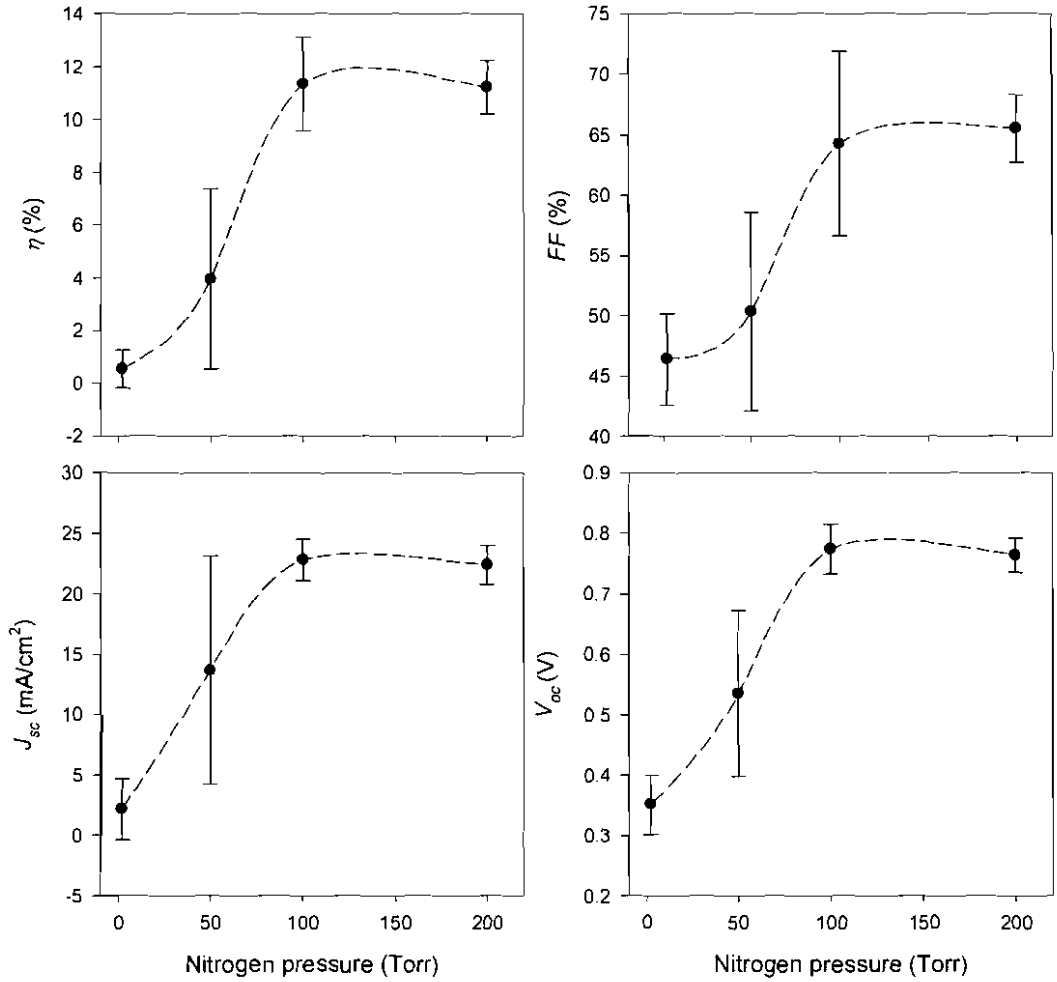

Figure 8.22: Average device performance parameters extracted from *J-V* curves as a function of nitrogen deposition pressure. Each point represents an average of ~25 contacts with error bars being +/- 1 S.D.

The *J-V* curves (fig.8.21) reveal a gulf in performance between the devices deposited at low (2Totrr) and high (100Torr) pressures. The device deposited at higher pressure shows an obvious improvement in both J_{sc} and V_{oc}. Both curves show similar gradients under reverse bias implying little difference in their shunt resistances (see Section 2.3). However, there is significant change in the gradients of the curves under forward bias (the roll-over portion of the 2Torr curve not being considered), with the 100Torr device showing a steeper gradient, indicating a reduced series resistance. An estimate for the

series resistance (R_s) of each device was made from dark *J*-V curves by fitting a line to the straight line portion of the curve under forward bias (as discussed in Section 2.4.2.3). The resultant values are plotted as a function of the deposition pressure in fig.8.23. It shows that the series resistance is vastly reduced for the larger grained devices, with a minimum being reached for pressures ≥ 100Torr.

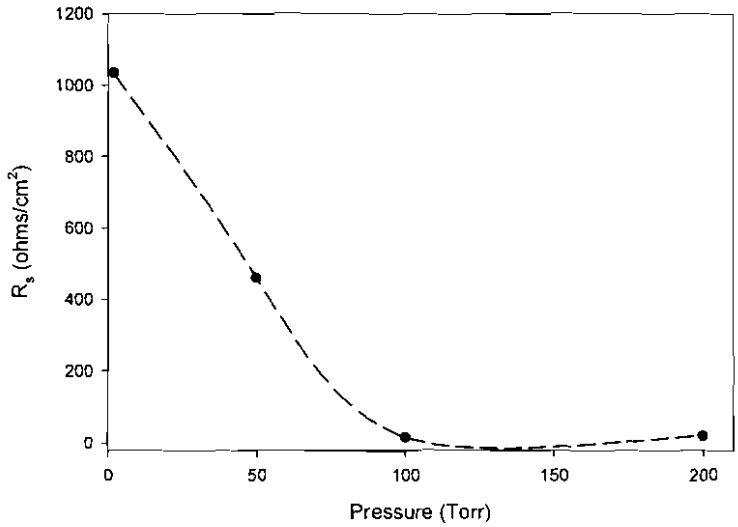

Figure 8.23: Series resistance values determined from dark *J-V* curves for cells with CdTe layers deposited under various pressures of nitrogen (the line is a guide to the eye).

The extracted performance parameters shown in fig.8.22 highlight the variation in performance, revealing the device efficiency to increase from an average 0.54% (peak of 2.12%) at 2Torr to an average of 11.34% (peak of 13.17%) at 100Torr. All device parameters are seen to increase in accordance with the increase in efficiency, with there being a notably large change in the average J_{sc} (2.17mA/cm^2 at 2Torr to 22.80mA/cm^2 at 100Torr). Of particular note however, is the change in the V_{oc} with increased pressure, with the average being found to increase from 0.35V (peak of 0.44V) at 2Torr to 0.77V (peak of 0.80V) for a deposition pressure of 100Torr. Whilst equivalent levels for the short circuit current density were found to be attainable by other methods (i.e. CdTe deposition under 2Torr of oxygen yielded J_{sc} values in the 20-25mA/cm^2 range, see Section 8.3), the V_{oc} values obtained for higher pressure depositions were significantly greater, with the best V_{oc} obtained for a device deposited under a "normal" deposition pressure (i.e. in the range 0-5Torr) being 0.68V. Further refinement of the $CdCl_2$

treatment step led to efficiencies of up to 14.1% being achieved for deposition under 100Torr.

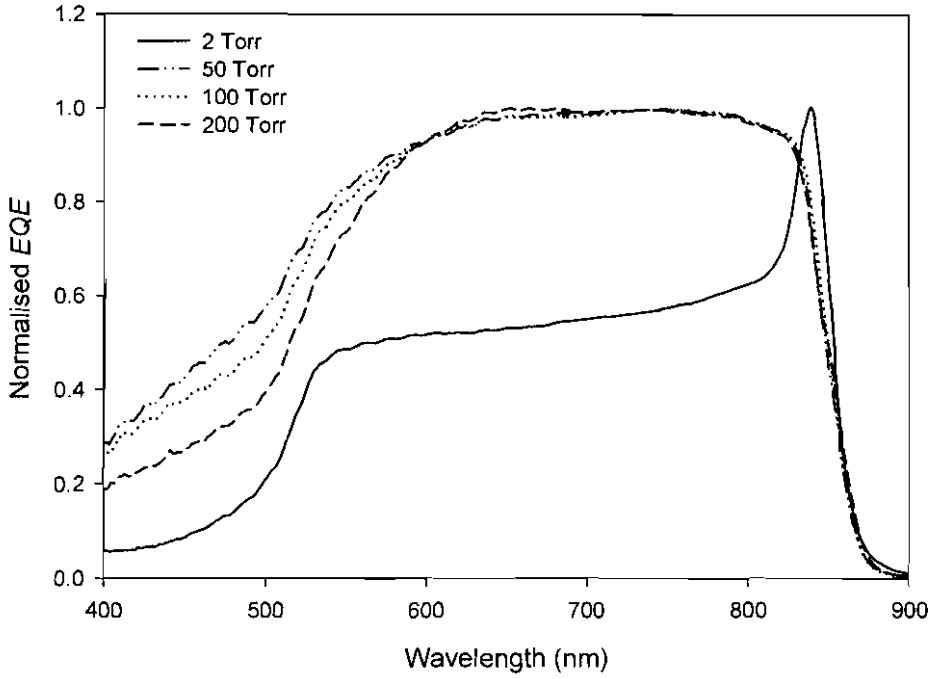

Figure 8.24: Normalised EQE curves for devices with CdTe layers grown under various pressures of nitrogen. The periodic oscillations observed in the 520 – 600nm range may possibly result from optical interference fringes.

Fig.8.24 shows normalised EQE curves taken from a representative contact for devices deposited under each nitrogen pressure. The cell with CdTe deposited under 2Torr of nitrogen shows the characteristic shape of a buried homo-junction, providing an explanation for the poor performance of the device. Cells deposited at higher pressures (50 - 200Torr) all display a more typical hetero-junction shape, with a uniform response in the 520-840nm range. There is little variation observed in the shape of the EQE curves between these higher pressure devices, except for in the 400-520nm region, which can be attributed to variation in the CdS thickness. There is also a slight change in the *EQE* within the 520-600nm region, indicating a variation in the level of intermixing, however no associated shift of the CdTe cutoff (~845nm) is observed. Any change in the level of intermixing level has therefore had little effect on the CdTe bandgap.

8.4.5 Discussion

By utilizing higher than normal nitrogen pressures during CSS deposition, a notable increase in the grain size of CdTe films has been achieved. From a consideration of the mechanism of nucleation and growth for a polycrystalline film (reviewed in Chapter 4) it is possible to postulate a microscopic mechanism for this effect: The change in pressure alters the arrival rate of adatoms at the surface, with the rate being reduced for higher pressure. Even though the adatom surface lifetime is expected to be unaltered by pressure, its population is nevertheless reduced, hence diminishing the probability of stable nuclei being formed as a result of adatom surface collisions. This leads to a smaller number density of islands being formed, meaning that islands grow to larger sizes, resulting in a completed film with a larger grain size. Very little work has previously been reported on the effect of CSS deposition pressure upon CdTe film microstructure. Falcao *et al*[10] reported a small increase in grain size (0.92-1.64μm) upon using argon pressures of up to 10Torr, but they concluded that at pressures above 10Torr no further size increase could be achieved. This result was not explained further, moreover they did not report the effect of deposition pressure on device performance. The results presented in this chapter contradict their findings, demonstrating that grain size continually increases for nitrogen deposition pressures of up to 200Torr. It should also be noted that this work does not necessarily indicate the upper limit of grain size that may be achievable. Although not yet investigated it does seem probable that the use of nitrogen pressures >200Torr may result in even larger grain sizes, although there will inevitably be a pressure limit (for a given deposition temperature) after which no nucleation will occur. The ultimate grain size achievable may not be limited by the deposition pressure, but rather by the nature of the deposition surface. Under extremely high pressure conditions nucleation, although unlikely by the homogenous route may nevertheless occur heterogeneously i.e. at surface defect sites (e.g. kinks, steps and grain boundaries- see Section 4.4.3). In this case the minimum density of nucleation occurring, and by extension the maximal grain size, will be dependant upon the density of these defect locations and hence the substrate type and quality. The grain size may therefore be expected to reach a plateau, for deposition pressures above a certain threshold value. Also, it is widely accepted that higher substrate temperatures may also yield larger

grains[9,10]. It therefore seems probable that combining an increased deposition pressure with higher substrate and source temperatures may yield further gains in the grain size.

The device performance was found to improve significantly for deposition under higher pressure, with the efficiency reaching a peak of 13.17% at 100Torr in comparison to only 2.12% at 2Torr (fig.8.22). However, while the overall conclusion is that grain size is responsible, for the cell grown under 2Torr of nitrogen the junction position at least contributes to low performance as EQE results (fig.8.24) revealed this device to contain a buried homo-junction. It seems likely therefore that the poor performance of this particular device relates principally to its junction position, rather than to any grain size or grain boundary effects. For deposition at pressures of 50Torr and above, EQE measurements showed all devices contained hetero-junctions. The exact explanation for the switch between homo and hetero-junction formation in these devices is not completely understood, nevertheless the following explanation is proposed: The longer deposition times required for growth under higher pressures (i.e. 2min at 2Torr, 90min at 200Torr) may effectively act as an in-situ annealing step and may enhance the intermixing between the layers. Also, results in Section 8.3 indicated that the formation of a deeply buried CdTe homo-junction in all-CSS deposited cells was due to the lack of oxygen during CdTe deposition. In order to form a good quality device, the presence of oxygen was essential either from the deposition ambient or the from the CdS layer (in the case of deposition on CBD CdS). Whilst no oxygen was included during CdTe deposition in the devices being reported here (due to oxygen being expected to reduce the CdTe grain size), the CdS layers were deposited in the presence of oxygen. Whilst the oxygen concentration in the CdS films was not measured during this work, Tyan *et al*[14] report oxygen concentrations of 2×10^{19} cm^{-3} for similar CSS CdS deposited in the presence of oxygen. It may therefore be possible that the longer deposition times allowed oxygen diffusion from the CdS to the CdTe layer, thus providing *p*-type doping of the CdTe layer. If this supposition is correct then hetero-junctions may be formed in the cells deposited at lower pressure by the addition of a post-growth annealing step at deposition level temperatures.

If the cell deposited at 2Torr is discounted, due to it containing a buried homo-junction, then the effect of the grain size on device performance may be evaluated by

comparison of the cells deposited at 50, 100 and 200Torr pressures. There is a large increase in the level of device performance between 50 and 100Torr, with average efficiency increasing from 4.0% to 11.3%, and the average grain size increasing from 2.4μm to 4.0μm. In contrast, the device performance was found to remain reasonably constant for 100 and 200Torr pressures (the average efficiency being 11.2% at 200Torr), despite there again being a significant increase in grain size (average 4.0-5.6μm) for the 200Torr device. This suggests that above a certain grain size the polycrystallinity of the film is no longer the limiting factor of device performance. However, it seems unlikely that increasing the grain size would have no beneficial effects on device performance. Indeed the peak efficiency recorded for these devices (14.1% for 100Torr deposition pressure) was far superior to that recorded for any other CSS deposited cells fabricated during this work that had a much larger grain size (devices with CdTe layers deposited in high concentrations of oxygen only achieved a maximum efficiency of ~10%). It is also widely accepted that grain boundaries are deleterious to device performance and it has been estimated by Sites *et al*[16]that two-thirds of the excess performance loss of polycrystalline devices is directly attributable to their polycrystallinity, with these losses being minimized by a large grain structure. Sites *et al* also made the assertion that the principle loss mechanism due to polycrystallinity is through excess recombination due to trapping states in the depletion region, introduced as a result of the high defect density at the grain boundaries. They conclude that the principal effect of this enhanced recombination is to lower the device V_{oc} and *FF*. It is interesting to note therefore that the principal improvement observed for devices with large grain size in this work was in the V_{oc} and *FF*, with V_{oc} of up to 0.8V and *FF* of 71.9% being recorded for high pressure deposition. This was a significant improvement, with the previous maximum V_{oc} being 0.68V and *FF* being 61.0%, achieved for a device deposited under 2Torr of oxygen.

The reason no improvement was observed between the 100Torr and 200Torr devices may be explained by reference to the determined series resistance values (fig.8.23). The series resistance is reduced as a function of pressure but reaches a minimum for deposition pressures ≥100Torr, at which point no further improvement in device performance is observed. It is believed that for deposition at pressures ≥100Torr the grain boundary contribution to the series resistance has been reduced by the increased grain

size, to the extent where it is no longer the limiting factor to device performance. Instead some other series resistance term, presumed to be the back contact resistance, now provides the limit to performance. Consequentially it is believed that to achieve further gains in device performance the contact series resistance must be reduced, at which point increasing the CdTe grain size may once again have a beneficial effect.

Whilst there is a clear relationship between grain size and efficiency, there appears to be no relationship between the preferred orientation of the CdTe film and the device performance. In this work the device performance was found to decrease with an increase in the level of preferred orientation (fig.8.20) whilst other authors (Ferekides *et al*[9]) have reported contradictory findings, with higher efficiency devices showing an increase in the preferred orientation. However, in both instances the device performance is improved by a larger CdTe grain size and it therefore appears that it is the grain size rather than the orientation of the film that limits device performance.

It is also worth noting that no increase in shunting was observed for the devices with larger grain size. A decrease in shunt resistance may have been expected, due to the larger grains leading to voids in the film. However, as the shunt resistance was found to be relatively constant, this implies that the level of film coverage is maintained for larger grain size.

Overall it is most likely that the increase in grain size is the cause of enhanced performance observed. Nevertheless other causes should also be considered. For example, considerable variation in performance can be achieved by enhanced intermixing of the layers or from oxygen diffusion as a result of the prolonged deposition times associated with the use of higher pressures. Further work is therefore needed to separate the effect of the grain size from the deposition time. This may be most easily achieved by subjecting the cells deposited at lower pressure to a post growth period of annealing at the deposition temperature. This would allow the same period of high temperature treatment for cells deposited at different pressures and would allow the effect of the grain size upon device performance to be isolated.

8.5 Conclusions

Techniques to control the growth of thin films based on nucleation and early growth studies of CdTe thin films, have been successfully applied to the fabrication of complete solar cells. The impact of the manner of CSS CdS deposition, the CdTe deposition ambient and the CdTe nitrogen deposition pressure upon device performance has been evaluated, and the optimal growth conditions identified in each case. The results presented in this chapter demonstrate a practical application for the fundamental understanding of the CdTe film formation developed from the results presented in Chapter 7.

The results in Section 8.2 demonstrated that CSS deposited CdS, whilst not an ideal window layer for CdTe/CdS devices, may be used to fabricate good quality devices by careful selection of the deposition conditions. The use of thinner CdS layers (whilst providing an increase in J_{sc}) was found to hinder device performance due to a loss in the V_{oc}. However, reduction of the CdS nucleation temperature and the inclusion of oxygen in the deposition ambient was shown to increase the device V_{oc} from 0.51V to 0.68V. This was thought to be due to better coverage of the substrate and a reduction in the pinhole density of the films.

The growth of CdTe under different ambients (N_2, O_2, H_2), showed oxygen to be vital to the formation of a hetero-junction device. It is believed that in the absence of an oxygen-rich CdS layer (i.e. CBD deposited), oxygen must be added to the CdTe deposition ambient in order for a reasonable device efficiency to be achieved. However, it appears that a shallow homo-junction rather than a hetero-junction is still formed under these deposition conditions. The inclusion of hydrogen in the deposition ambient was found to be unsuitable for CdTe deposition, as the devices produced under these conditions were found to contain deeply buried homo-junctions.

Significant increases in both the CdTe grain size and device performance were achieved by the use of higher nitrogen pressures during CdTe deposition. Device efficiencies of up to 14.1% were achieved for deposition under 100Torr of nitrogen, whilst the CdTe grain size was found to increase continually with pressure, reaching an average of 5.6μm at a pressure of 200Torr. These results provide evidence that high efficiency devices with a large CdTe grain size are achievable, without the need for very

high (>550°C) substrate temperatures. Analysis of *J-V* curves showed this increased grain size led to a reduction in the series resistance, presumably due to the reduced contribution of grain boundaries. For large grain sizes the series resistance was minimised and the grain structure was deemed to no longer be the limiting factor to performance.

The results presented in this chapter, whilst not presented in chronological order, represent an ongoing process of device optimization. Approximately 200 2.5x2.5cm CdTe/CdS samples were produced during this investigation, leading to the production and analysis of approximately 5000 dot contact devices. During this period the maximum device efficiency was increased from <1% to 14.1%. For the purpose of brevity this chapter represents a summary of the principal findings from this larger work.

8.6 References

1 A. R. Davies, J. R. Sites, R. A. Enzenroth, W. S. Sampath, and K. L. Barth, Materials Research Society Symposium Proceedings **1012,** 157-162 (2007).

2 C. S. Ferekides, D. Marinskiy, S. Marinskaya, B. Tetali, D. Oman, and D. L. Morel, in *Conference Record of the Twenty Fifth IEEE Photovoltaic Specialists Conference*, (Washington D.C., 1996), 751-756.

3 B. E. McCandless and S. S. Hegedus, in *Conference Record of the Twenty Second IEEE Photovoltaic Specialists Conference*, (Las Vegas, 1991), 967-972.

4 K. Ohata, J. Saraie, and T. Tanaka, Japanese Journal of Applied Physics **12,** 1641-1642 (1973).

5 C. S. Ferekides, K. Dugan, V. Ceekala, J. Killian, D. Oman, R. Swaminathan, and D. L. Morel, in *IEEE First World Conference on Photovoltaic Energy Conversion/Conference Record of the Twenty Fourth IEEE Photovoltaic Specialists Conference*, (Vienna, 1994), 99-102.

6 D. Albin, D. Rose, R. Dhere, D. Levi, L. Woods, A. Swartzlander, and P. Sheldon, in *Conference Record of the Twenty Sixth IEEE Photovoltaic Specialists Conference*, (Anaheim, 1997), 367-370.

7 C. Ferekides and J. Britt, Solar Energy Materials and Solar Cells **35,** 255-262 (1994).

8 D. S. Albin, Y. Yan, and M. M. Al-Jassim, Progress in Photovoltaics **10,** 309-322 (2002).

9 C. S. Ferekides, D. Marinskiy, V. Viswanathan, B. Tetali, V. Palekis, P. Selvaraj, and D. L. Morel, Thin Solid Films **361-362,** 520-526 (2000).

[10] V. D. Falcao, W. A. Pinheiro, C. L. Ferreira, and L. R. Cruz, Materials Research **9,** 29-32 (2006).

[11] C. S. Ferekides and D. L. Morel, in *NREL Phase I Annual Technical Report October 2005 - September 2006* (National Renewable Energy Laboratory, Golden, Colorado, 2007), 1-20.

[12] D. H. Rose, D. H. Levi, R. J. Matson, D. S. Albin, R. G. Dhere, and P. Sheldon, in *25th Photovoltaics Specialists Conference*, (Washington D.C., 1996), 777-780.

[13] D. Bonnet, Thin Solid Films **361-362,** 547-552 (2000).

[14] Y. S. Tyan, F. Vazan, and S. Barge, in *Seventeenth IEEE Photovoltaic Specialists Conference* (Kissimmee, Florida, 1984), 840-845.

[15] T. M. Hsu, R. J. Jih, P. C. Lin, H. Y. Ueng, Y. J. Hsu, and H. L. Hwang, Journal of Applied Physics **59,** 3607-3609 (1986).

[16] J. R. Sites, Solar Energy Materials and Solar Cells **75,** 243-251 (2003).

9 Conclusions

This thesis has provided a detailed investigation into the growth and microstructure of CdTe thin films and CdTe/CdS solar cells deposited by close space sublimation (CSS). Routes to controlling the CdTe grain structure were developed from studies of thin film development, with these techniques being implemented in making complete devices and leading to significant improvements in device performance. In-depth characterisation of CdTe/CdS solar cells was also performed using a spectrally resolved OBIC/EQE system, constructed during the course of this work.

In Chapter 6 the design, construction and operation of the combined OBIC and EQE system was described. The system utilised a monochromated light source and so was able to produce OBIC maps at wavelengths across the entire response range of CdTe/CdS devices. Computer control of the system's objective lens via a stepper motor allowed for fine focussing of the beam, leading to a resolution of up to 12.5μm being achieved. The capabilities of the system were first demonstrated on a test cell (Section 6.4.1). Both high (12.5μm) and low (100μm) resolution OBIC maps were recorded as a function of wavelength, with the variation in *EQE* across the examined area being used to access the device uniformity. Detailed examination of the CdTe absorber band edge was performed, with intermixing of the CdTe and CdS layers being shown to increase the non-uniformity of the device response. The system was also shown to be capable of identifying defective areas of the device by OBIC measurement and allowed these areas to be assessed by spatially resolved EQE analysis.

A number of studies of CdTe/CdS devices utilising the OBIC system were then reported:

- In Section 6.4.2 the impact of the N-P etching process on the back contact and the device performance, was evaluated by comparison of cells subjected to a range of etch times (0-480s). *J-V* results initially suggested that device performance was significantly improved as a result of prolonged periods of

etching, with cell efficiency being found to increase by over 4%. However, this improvement was manifested via a large increase in the device J_{sc}, with values of >50mA/cm^2 being recorded for 2mm diameter dot contacts. OBIC analysis of the devices revealed that significant amounts of photocurrent was being generated from regions outside the bounds of the device back contact as a result of lateral conduction. This meant that the effective area of the contact was vastly increased, thus leading to the erroneously high J_{sc} values. Correction of the *J-V* data, using the information determined from OBIC measurements, revealed that device performance was in fact decreased as a result of prolonged etching, rather than improved.

- In Section 6.4.3 the uniformity of cells with layers deposited by a range of techniques was compared by OBIC analysis. Results showed that the commercial ANTEC solar device (in which both CdS and CdTe layers were deposited by CSS) displayed the highest level of uniformity, despite not being the highest efficiency of those evaluated. The cell with CBD CdS and CSS CdTe also displayed a high level of uniformity, whilst the all-MOCVD deposited cell was reasonably uniform with highly localised areas of low performance. The all-CSS cell fabricated at Durham was found to perform at a significantly lower level, with only isolated areas of reasonable performance. EQE measurements of these devices also yielded interesting information. Firstly, the all-CSS deposited cell displayed the characteristics of a buried homo-junction, this being attributed to indium diffusion form the ITO layer, producing *n*-type doping of the CdTe layer, hence accounting for the low performance. Secondly, the MOCVD grown device displayed evidence of a reduction in the CdTe bandgap; this was attributed to the high concentrations of arsenic used during deposition of the CdTe layer.

- In Section 6.4.4 the effect of the CdTe layer thickness upon the device performance was evaluated for all-CSS deposited cells with oxygen free CdS. *J-V* results showed that the device performance was improved by reducing the

CdTe layer thickness from 6μm to 2μm, with the efficiency increasing from an average of 1.7% to 5.9%. OBIC analysis of these devices showed that the device with the thinnest absorber layer (2μm) had the most uniform response at all wavelengths examined. EQE analysis revealed that the devices with thicker absorber layers contained buried homo-junctions, whilst the thinner absorber layer device displayed a response typical of a shallow homo-junction or hetero-junction device. This accounted for the improvement in device efficiency observed and may suggest that the junction position was related to a diffusion length effect from the back surface (i.e. as a result of the $CdCl_2$ treatment). For cells in which oxygen *was* included in the CdS (CBD or CSS), the junctions were usually shallow: this indicated that oxygen in the CdS plays a role in junction formation.

Chapter 7 presented investigations into the early stages of the growth of CdTe thin films upon both ITO (Section 7.3) and CdS (Section 7.4). Prior to describing the results both the experimental and interpretative methodologies shall be commented on. In order to allow investigation of the film morphology to take place, the CSS growth was slowed by using higher pressures (100-200Torr) than is normal (1-20Torr). The results are therefore for the higher rather than the lower pressure. Interruption of the growth allowed samples to be extracted for ex-situ AFM and SEM analysis. The validity of this approach depends on the ability to terminate the growth abruptly, this being achieved by inserting the growth shutter, switching off the heaters and further increasing the deposition pressure via a high flow of nitrogen. Hence it is unlikely that any significant post-interrupt growth occurs. The interpretative methodology is based on a wide range of previous work (reviewed in Chapter 4) in which the morphologies of films are interpreted and thereby associated to the most plausible model available. Three examples are i) island growth (rather than complete wetting) indicates that the film-film bonding is stronger than the film-substrate bonding, ii) formation of singular facets on islands indicates the process of uninterrupted step flow and iii) formation of rounded facets on islands indicates the co-deposition of impurities has led to the interruption of step flow. It is this framework of understanding – particularly the work of P. Barna – that has been

used not only to interpret the results, but to design the experiments described in this thesis. For example, the use of oxidizing and reducing gases was intended to demonstrate step flow interruption and grain size control.

CdTe layers were deposited by CSS for a range of growth times, with above average (100-200 Torr) nitrogen pressures being used to slow the rate of growth. Films were assessed by post-growth AFM and SEM, with the shape, size and density of CdTe islands formed being analysed as a function of the growth time. This allowed a mechanism for the CdTe film formation to be proposed, based upon the accepted models of thin film growth. For CdTe deposition onto CdS, a film formation process of nucleation and island growth, followed by complete coalescence of islands to form single larger islands was deduced. This was followed by a channel formation stage, after which the remaining substrate gaps were filled by subsequent bouts of nucleation to form a completed film. A similar process was deduced for growth on ITO, although no evidence of channel formation or secondary nucleation was observed.

The impact of including different ambient gasses (i.e. O_2 and H_2) upon the CdTe thin film formation was also studied. Oxygen was shown to significantly reduce the CdTe grain size and increase the substrate coverage for deposition on ITO (Section 7.3.3). This result was explained with reference to a step flow model and by treating oxygen as an impurity species that preferentially bonded at the step sites. However, owing to problems with source oxidation, and thus variations in the material deposition rate, the effect of oxygen upon CdTe growth was not evaluated in depth. No such problems were encountered with deposition under hydrogen and time dependant growth studies were performed on both ITO and CdS utilising a hydrogen ambient. In both cases the level of substrate coverage was found to be improved by the inclusion of hydrogen in the processing ambient. For deposition on ITO (Section 7.3.4), the use of high partial pressures of hydrogen was found to lead to the reduction of the substrate and the formation of indium telluride phases on the surface. As a result it was concluded that hydrogen was not a suitable ambient for the deposition of CdTe onto ITO. For deposition on CdS (Section 7.4.4), inclusion of hydrogen was shown to increase the island number density and increase the substrate coverage. By the use of a two stage deposition ambient

(Section 7.4.5), it was shown that the principle effects of hydrogen upon growth were to: a) increase the deposition rate and b) to alter the initial nucleation of the films.

In Section 7.4.6 the effect of the nitrogen deposition pressure upon film formation was demonstrated. It was shown that increasing the pressure led to a significant increase in the island/grain size of CdTe thin films deposited on CdS. This finding was interpreted using the nucleation theory, as outlined in Chapter 4, with the increase in island size being attributed to a decreased likelihood of stable nuclei forming due to adatom surface collisions, on account of the impingement rate being reduced.

All of the interpretations given are fully consistent with the interpretative methodology described earlier and in general these are satisfactory. However, the limitation of the approach is recognised, particularly in explaining complex phenomena such as channel filling. Another approach might be modeling, but this is likely to be difficult due to the large number of competing growth processes occurring and the author is not aware of any such work being reported for CdTe thin films.

To the author's knowledge the results presented in this chapter represented the first such study on the early growth mechanisms of polycrystalline CdTe thin films.

In Chapter 8 performance and characterisation results for all-CSS CdTe/CdS solar cell devices fabricated at Durham were presented. Attempts were made to control the structure of the thin film layers using the knowledge developed from the materials studies presented in Chapter 7. A number of different device studies were reported:

- In Section 8.2 attempts were made to improve the suitability of CSS deposited CdS layers for CdTe device fabrication. Initial results showed that thickness reduction of the CdS layer led to loss of device performance through a decrease in the V_{oc} and FF. This was attributed to the large CdS grain size (i.e. low nucleation density) resulting from the high deposition temperature, leading to pinholes in the CdS and formation of CdTe/TCO junction regions. By reducing the substrate temperature at the point of film nucleation (achieved by omitting the growth shutter) and by the addition of oxygen to the deposition ambient, significant gains in V_{oc} were achieved. This was believed to be due to

a reduction in grain size and an associated increase in the coverage, thus reducing the pinhole density in the CdS layer.

- In Section 8.3 the impact of using different gas ambients (N_2, O_2 and H_2) during CdTe deposition on both the layer morphology and device performance was assessed. Considerable morphological changes were seen by SEM and *J-V* analysis of the completed devices showed that the cell with a CdTe layer grown in the presence of oxygen performed significantly better than the other devices. *EQE* analysis of the devices showed the N_2 and H_2 grown cells to have a buried homo-junction response, whilst the O_2 grown cells displayed a shallow or hetro-junction type response. However, cross-sectional EBIC analysis revealed that whilst the cell with the CdTe layer deposited in oxygen had a shallower junction than for H_2 deposited device, it was not ideally located at the CdTe/CdS interface. In contrast devices deposited on CBD CdS were shown to have ideally positioned hetero-junctions. The conclusion was made that the *p*-type doping of CdTe by oxygen is vital to the formation of a good hetero-junction. In cells where the CdS layer is oxygen rich, such as in CBD CdS, hetero-junctions form naturally. However, for CdS layers that contain lower oxygen concentrations, oxygen must be added to the CdTe deposition ambient in order to achieve reasonable device performance.

- A large amount of work has been reported in this thesis on the role of oxygen in the formation of hetero-junctions in CdTe/CdS solar cells. This work may be briefly summarised as follows: i) for devices containing CSS CdS layers deposited in the absence of oxygen a buried homo-junction was typically formed ii) devices based on CBD CdS were always found to contain hetero-junctions, regardless of the CdTe deposition conditions, iii) CSS CdS layers deposited with oxygen, were typically found to contain hetero-junctions (or shallow homo-junctions) if the CdTe was deposited in oxygen or at high nitrogen pressures, but buried homo-junctions were found to form if deposited was performed under low nitrogen pressures. From these results it is inferred

that oxygen is required within the CdS layer in order to produce a highly efficient (hetero-junction) device. This is most effectively achieved by methods such as CBD, where the oxygen content is naturally high. In the case of CSS deposited CdS the inclusion of oxygen is no guarantee of hetero-junction formation, but rather a longer growth time (presumably on account of increased oxygen diffusion from the CdS) or the inclusion of oxygen during CdTe deposition is required in order to achieve the formation of a hetero-junction.

- In Section 8.4 the CdTe grain structure was altered by the use of different pressures of nitrogen during CSS deposition in the range 2-200Torr. A large increase in the grain size was observed as a function of pressure, with the average grain diameter increasing linearly with pressure from ~1μm (2Torr) to ~6μm (200Torr). This represented a significant finding, as no work on the effect of nitrogen pressure upon CdTe deposition on CdS has been reported which shows this large increase in the CdTe grain size. The devices containing these large grained CdTe films showed significant gains in performance. The V_{oc} and FF values of devices with large CdTe grain sizes represented a vast improvement on previous device results. Analysis of the device series resistance showed a minimum to be reached for grains above a certain size (those deposited at pressures ≥ 100Torr). This implied that the contribution of the grain structure to series resistance had been minimized by the reduced contribution of the grain boundaries. It is believed that the device performance instead became limited by other factors, in particular the series resistance arising from the back contact. This was an important finding as it clearly demonstrated the impact of grain boundaries upon device performance and also highlighted the need to determine the principle factors limiting device performance. For cells with a small CdTe grain size, the device performance is controlled by the impact of grain boundaries and to improve the device performance it seems necessary to reduce their contribution. In cells with a

large CdTe grain size, alternative factors limit the performance and work to further identify and reduce the impact of these limiting factors is needed.

Suggestions for further work

Following on from the work presented in this thesis, a number of further studies may yield important information:

Improvement to the OBIC/EQE system:

The OBIC/EQE system could be enhanced by the addition of:

i) Light biasing. Biasing with light of AM1.5 intensity would ensure the accuracy of EQE curves, as the cell would then be measured under 'standard' operating conditions.

ii) Electrical biasing. Highly spatially resolved measurements would then be able to be recorded as a function of both wavelength and of bias voltage. This would mean EQE and OBIC measurements could be made for different cell bias, allowing the separation of electrical and optical defects (as optical defects should have no bias related component), and also the extraction of localised *J-V* curves for different illumination wavelengths. However, due to the small photo-currents recorded during OBIC measurements (nA), some form of current pre-amplification and very stable biasing equipment would be required.

Further nucleation/growth mechanism studies:

Further to the thin film growth work reported, a number of additional studies may yield useful information about the mechanism of CdTe thin film formation. For example the effect of the substrate temperature was not investigated, but is known to have a pronounced effect upon the CdTe microstructure. Studying the film development as a function of time but for a range of substrate temperatures may allow the effect of temperature upon the nucleation and coalescence processes of CdTe films to be determined. Also, whilst briefly touched upon in this work, the effect of the substrate type upon the nucleation and growth of films warrants further investigation. For example

the CdTe island size was shown to be far greater for deposition on ITO than on CdS. The dependence of CdTe growth on different TCO and CdS types may reveal further ways to control the CdTe grain size and hence benefit device performance.

Large grain CdTe thin films:

As has previously been mentioned, the CdTe grain size achieved in devices reported in Chapter 8 as a result of increased nitrogen pressure, does not necessarily represent the largest grain size achievable by this method. Further work is required utilising even higher pressures in order to ascertain if there exists an upper limit of pressure that may be successfully used. It seems probable there will be a point at which nucleation ceases to occur altogether, but prior to this point being reached further gains in the CdTe grain size may be expected.

High performance CdTe solar cells:

The results reported in Section 8.4 suggested that the device performance was limited by the series resulting from the back contact, once the series resistance resulting from grain boundaries had been minimized. Impedance analysis may resolve this issue by separating the individual resistance terms that contribute to the overall device series resistance. This work will offer the potential to identify the limiting factors in device performance, thus indicating how more efficient devices may be produced.

The work presented in this thesis has provided insights into numerous areas of CdTe/CdS device research. The basic growth and structure of CdTe films has been investigated as well as the performance and characterisation of CdTe/CdS devices. New techniques designed to control the grain structure of CdTe/CdS devices have been established and significant gains in device performance have been achieved. This work may provide a basis for future work on the structure of CdTe and CdS films and for the production of higher efficiency CdTe/CdS solar cells.

Appendix A: AFM analysis of substrates

Atomic force microscopy (AFM) analysis was performed on the substrates used for the nucleation and early growth work presented in Chapter 7. Typical AFM images for both ITO and CdS/ITO substrates are shown in fig.A.1, while roughness and average height values are given in table A.1.

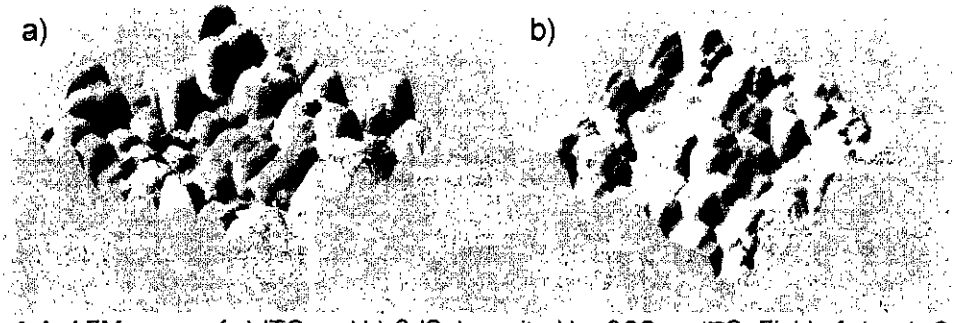

Figure A.1: AFM scans of a) ITO and b) CdS deposited by CSS on ITO. Field of view is 2x2μm for both images with Z axis scale being 0.15μm in a) and 0.13μm in b)

	ITO	CdS/ITO
R_a	22.1 nm	19.9nm
R_{rms}	29.22 nm	25.31 nm
Ave height	81.55 nm	91.05 nm

Table A.2: Roughness and average height values for ITO and CdS/ITO substrates used for nucleation studies.

Whilst only one type of ITO was used for the work reported in Chapter 7, the effect of different ITO types upon film growth was compared. Films were grown under the same conditions on commercial ITO from both Merck Technologies and Visiontek Systems and analysed by AFM. However, little difference was observed in the nucleation density or island size for these different substrates and the specific ITO type was deemed to have little effect on the film growth.

Appendix B: List of publications

J. D. Major, Y. Y. Proskuryakov, K. Durose and S. Green, Thin Solid Films **515**, 5828-5832 (2007).

V. Barrioz, Y. Y. Proskuryakov, E. W. Jones, J. D. Major, S. J. C. Irvine, K. Durose, and D. A. Lamb, Materials Research Society Symposium Proceedings **1012,** 367-372 (2007).

Y. Y. Proskuryakov , J. D. Major, K. Durose , V. Barrioz, S. J. C. Irvine, E. W. Jones and D. Lamb, Applied Physics Letters **91**, 153505 (2007).

J. D. Major and K. Durose, "Use of a combined OBIC and spectrally resolved EQE system to evaluate the impact of buried homojunctions in CdTe/CdS solar cells", Thin Solid Films, In Press.